BERGISCHE UNIVERSITÄT
GESAMTHOCHSCHULE WUPPERTAL
FACHBEREICH PHYSIK

Open Charm Production in Deep Inelastic Electron-Proton Scattering with the H1 Detector at HERA

Dissertation zur Erlangung des Doktorgrades
vorgelegt von

Catherine Adloff

WUB-DIS 2001-14
Wuppertal, Oktober 2001

Gutachter der Dissertation:	Prof. Dr. Hinrich Meyer Prof. Dr. Karl-Heinz Becks
Gutachter der Disputation:	Prof. Dr. Hinrich Meyer Prof. Dr. Karl-Heinz Becks Prof. Dr. Peter Kroll Dr. Dr. Wolfgang Rhode
Schriftführer der Disputation:	Dr. Dr. Wolfgang Rhode
Vorsitzender des Promotionsausschusses:	Prof. Dr. Karl-Heinz Mütter
Datum der Disputation:	12. Dezember 2001

For my parents

Abstract

A measurement of the inclusive D^{*+} single and double differential cross sections in deep inelastic electron-proton scattering is presented in the kinematic range $1\ \mathrm{GeV}^2 < Q^2 < 100\ \mathrm{GeV}^2$ and $0.05 < y < 0.7$. Additionally, the D^{*+} cross sections are restricted to the visible range of the analysis given by $-1.5 < \eta_{D^*} < 1.5$ and $p_{\perp D^*} > 1.5$ GeV/c. The measurement is based on the data collected at HERA by the H1 detector in 1996 and 1997. The D^{*+} mesons are reconstructed in the $D^{*+} \rightarrow D^0\pi_s^+ \rightarrow (K^-\pi^+)\pi_s^+$ decay channel, where the charged decay particles are measured in the central jet chambers of the H1 detector. In the studied kinematic range the scattered electron is detected in the new backward calorimeter SpaCal.

In Quantum Chromodynamics (QCD) the production of D^{*+} mesons in deep inelastic electron-proton scattering originate from the fragmentation of charm quarks which are the outgoing particles of the boson-gluon fusion perturbative process. The presented measurement allows therefore to test our understanding of QCD within the frame of charm production by the confrontation with perturbative QCD calculations combined with charm fragmentation models.

In addition the extraction of the gluon density in the proton within the leading order DGLAP formalism was attempted and reveals the necessity of taking into account the QCD next-to-leading order terms for the feasibility of this measurement.

Zusammenfassung

In der vorliegenden Arbeit werden inklusive D^{*+} einfach und doppelt differenzielle Wirkungsquerschnitte in tiefinelastischer Elektron-Proton Streuung präsentiert. Der kinematische Bereich der Messung erstreckt sich auf $1\ \mathrm{GeV}^2 < Q^2 < 100\ \mathrm{GeV}^2$, $0.05 < y < 0.7$ und beschränkt sich auf den zugänglichen Bereich der Datenanalyse, welche durch $-1.5 < \eta_{D^*} < 1.5$ und $p_{\perp D^*} > 1.5$ GeV/c gegeben ist. Die Daten für die durchgeführte Messung wurden am H1 Experiment des Beschleunigers HERA in den Jahren 1996 und 1997 gesammelt. Die D^{*+} Mesonen werden dabei über den Zerfallskanal $D^{*+} \rightarrow D^0\pi_s^+ \rightarrow (K^-\pi^+)\pi_s^+$ rekonstruiert, wobei der Nachweis der auftretenden geladenen Zerfallsteilchen in der zentralen Jetkammer des H1 Detektors stattfindet. Das im betrachteten kinematischen Bereich gestreute Elektron wird im neuartigen, rückwärtsgerichteten Kalorimeter SpaCal detektiert.

Im Rahmen der Quantenchromodynamik (QCD) wird die Produktion von D^{*+} Mesonen in tiefinelastischer Elektron-Proton Streuung durch die Fragmentation von Charm Quarks beschrieben, welche die auslaufenden Teilchen des QCD störungstheoretischen Boson-Gluon Fusionsprozesses sind. Die vorliegenden Messungen erlauben deshalb, das bisherige Verständnis der Quantenchromodynamik zu überprüfen. Dies wird durch die Gegenüberstellung von den Messungen mit den störungstheoretischen QCD Berechnungen zusammen mit verschiedenen Fragmentationsmodellen erreicht.

Weiterhin wurde versucht, die Gluondichte im Proton mit Hilfe der ersten Ordnung der DGLAP QCD Störungsrechnung zu extrahieren. Die Analyse zeigt die Notwendigkeit, die zweite Ordnung der QCD Störungstheorie mit einzubeziehen, um die Extraktion der Gluondichte durchführen zu können.

Résumé

La mesure des sections efficaces différentielles de la production inclusive de mésons D^{*+} auprès des collisions électron-proton profondément inélastiques est présentée dans le domaine de cinématique 1 $\mathrm{GeV}^2 < Q^2 < 100\ \mathrm{GeV}^2$ et $0.05 < y < 0.7$. Les sections efficaces sont de plus réstreintes dans le domaine accesible à la sélection de mésons D^{*+} qui est donné par $-1.5 < \eta_{D^*} < 1.5$ et $p_{\perp D^*} > 1.5$ GeV/c. La mesure se base sur les données collectées à HERA par le détecteur H1 en 1996 et 1997. Les mésons D^{*+} sont reconstruits dans le mode de désintégration $D^{*+} \rightarrow D^0\pi_s^+ \rightarrow (K^-\pi^+)\pi_s^+$ à partir des particules chargées mesurées dans les chambres centrales à jets. Dans le domaines de cinématique étudié, l'électron diffusé est detecté dans le nouveau calorimètre SpaCal situé dans la partie arière du détecteur H1.

Dans la chromodynamique quantique (QCD) la production de mésons D^{*+} auprès des collisions électron-proton profondément inélastiques a pour origine la fragmentation des quarks charmés qui sont les particules sortantes du processus perturbatif de la fusion d'un boson (ici un photon) et d'un gluon. La mesure présentée permet donc de tester notre compréhension de la QCD dans le cadre de la production de quarks charmés par la confrontation avec les calculs de la QCD perturbative combinés avec des modèles de fragmentation.

Pour finir, l'extraction de la densité de gluons dans le proton a été tentée dans le cadre du formalisme DGLAP au premier ordre. Cette étude a révélé la nécéssité de prendre en compte les termes du second ordre dans les développements perturbatifs de la QCD afin de pouvoir évaluer la densité de gluons dans le proton à partir de la mesure des mésons D^{*+}.

Contents

Appendix

Introduction

Until now the so-called Standard Model is the most successful theory in describing the fundamental constituents of matter and their interactions. This Model has been intensively tested during the course of the last decade. Nevertheless, the Standard Model describes the strong interaction only in part because of a rising strong coupling constant with decreasing momentum transfer. This in turn restricts the validity of the perturbative calculations only when the strong coupling constant is small.

The HERA electron(positron)-proton collider was built for the purposes of studying the structure of the proton. Indeed, the electron with its point-like structure at the HERA energy level acts as an ideal probe. On the other hand, the proton, which is composed of partons - the quarks and the strong force mediators called gluons, represents a very complex system. The measurements of the *ep* collision products at HERA provide a very interesting and precise insight into the partonic composition of the proton, and at the same time allow the intimately coupled Quantum Chromodynamics (QCD) theory of the interaction between partons to be tested. Due to the high HERA centre of mass energy the proton components are resolved and the type of interactions which are taking place are described by perturbative QCD (pQCD).

The study of heavy quark production is an especially interesting means to demonstrate both the success achieved and the complications encountered when applying pQCD in order to predict production dynamics [1, 2]. This thesis focuses on the study of charm production in Deep Inelastic Scattering (DIS) because the charm quark, being the *lighter* of the heavy quarks, is the most abundantly produced heavy quark. In QCD, charm production in DIS near threshold takes place at the first order via the Boson-Gluon Fusion (BGF) perturbative process where the charm is regarded as a massive particle. This is the basic reason why pQCD can be tested using charm production measurement. Another apparent advantage of testing pQCD using charm production is that charm quarks must appear in the detector as charmed hadrons. However, in order to delve deeper into charm production processes one must understand the fragmentation which describes the soft processes by which the charm quark develops into a charmed hadron.

In pQCD the charm cross section is directly proportional to the gluon density as the charm is produced at the perturbative level via the BGF process. The D^{*+} measurement thus provides the opportunity to extract the gluon density within the pQCD theory. This is a very interesting subject as it opens up the the possibility of testing the factorisation scheme and the universality of the non pQCD parton density.

The thesis presented here deals with the identification of DIS charm events in the data collected by the H1 experiment during the years 1996 and 1997 by means of reconstructing

D^{*+} mesons in the $D^{*+} \to D^0\pi_s^+ \to (K^-\pi^+)\pi_s^+$ decay channel[1]. The charged decay particles are measured in the central jet chambers of the H1 detector and the scattered electron in the backward calorimeter. In order to confront the measurement and the theory predictions, two different approaches are possible. Firstly, one can rely on fragmentation models in order to calculate the total charm cross section from the measured D^{*+} events. In this case the reconstruction efficiency within the D^{*+} visible range and the purely theoretical extrapolation from the visible to the total range have to be taken into account. The D^{*+} visible range corresponds to the detector acceptance ($-1.5 < \eta_{D^*} < 1.5$) and a minimum transverse D^{*+} momentum ($p_{\perp D^*} > 1.5$ GeV/c). The second possibility is to rely on fragmentation models to predict the D^{*+} cross section within the visible range from the theoretical charm cross section. The latter has been chosen here since the D^{*+} measured cross section is less prone to theoretical uncertainties. Moreover, it leaves the possibility open to later comparisons with future predictions probably using improved fragmentation models.

Although the first results on D^{*+} production in DIS at HERA were based on fairly modest event samples [3, 4], they already demonstrated the dominance of the BGF process in charm production. The statistics and the quality of the data used in this work were considerably improved by the increase of the HERA luminosity together with the better performances of the central tracker and of the backward region of H1. Therefore, the D^{*+} cross sections presented here permit a closer and finer comparison, in a larger kinematic range, with the predictions of available pQCD calculations combined with fragmentation models. At the leading order in α_s (LO), the predictions of the AROMA and the new coming CASCADE event generators using the DGLAP and CCFM formalism respectively were studied. In addition, the next to leading order (NLO) predictions carried out within the DGLAP and provided by the HVQDIS programme formalism were also confronted to the presented measurement.

After a general description of electron-proton scattering at HERA in chapter 1 and of the H1 detector in chapter 2, the theoretical framework will be discussed in chapter 3. The complete D^{*+} analysis, ranging from the online selection to the final D^{*+} reconstruction, is dealt with in chapter 4. The D^{*+} total cross section within the visible range as well as single and double differential cross sections are presented in chapter 5 together with a comparison with the three above-mentioned theoretical predictions. Finally, in chapter 6 the different ways to determine the gluon density at HERA are described. With the D^{*+} events selected in this analysis, the attempt has been made to extract the gluon density in the proton by means of LO pQCD calculations. The encountered difficulties and possible explanations are discussed.

---

[1] Charge conjugate states are always implicitly included.

Chapter 1

Electron-Proton Scattering at HERA

1.1 The Electron-Proton Ring HERA

The HERA (**H**adron **E**lectron **R**ing **A**nlage) particle collider at the research institute DESY (Hamburg) is the first ever constructed electron-proton storage ring. Since 1992, two independent accelerators housing in the same tunnel have provided counter circulating proton and electron[1] beams with energies of 820 GeV and 27.5 GeV respectively[2]. The accelerating complex DESY and the former storage ring PETRA were modified to serve as pre-accelerators. They provide HERA injection energies of 12 GeV for electrons and 40 GeV for protons. Both rings of HERA show a four fold symmetry and have a circumference of 6.3 km. Four high energy physics experiments are carried out in the four straight sections. The H1 and ZEUS detectors are located in the North and South Halls where the electron and proton beams are brought to head on collisions with a centre of mass energy of $\sqrt{s} \approx 300$ GeV (318 GeV in case of a 920 GeV proton beam). The HERMES detector (East Hall) studies the scattering of the polarised electron beam on polarised gas targets. In the fourth hall, the HERA-B experiment where the HERA protons collide on several possible wire targets, was originally dedicated to CP violation measurement in the decay of neutral B particles. However, the tremendous effort necessary to reach the required radiation hard detector and the difficulty to face background 12 orders of magnitude larger than the investigated signal forced the HERA-B physicists to revise the research programme toward general questions in strong interaction physics and rare decays of charm quarks.

The maximum reachable energy of the stored beams is given by two different means. The electron energy is limited by the available accelerating power which has to compensate the strong increase of synchrotron radiation losses, while the proton energy is limited by the strength of the magnetic field which is required to keep the heavy particles on their orbit. In the years 1996 and 1997, when the data were taken for this analysis, 175 colliding bunches were filled into each HERA rings. A few non colliding electron and proton bunches were additionally injected as so-called pilot bunches. Those are used to

---

[1] Electrons have been replaced by positrons in August 1994 since electron beams showed a much shorter lifetime. In 1998 till mid 1999 HERA switched back to electrons. Positron running was resumed from mid 1999 on.

[2] From 1998 on the proton beam energy was risen to 920 GeV.

determine background processes like interactions with residual gas and with the beam pipe. The time lapse between two bunch crossings at the collision points totals 96 ns ($\approx$ 10.4 MHz). The above mentioned background processes normally occur with rates of more than 10 kHz while the rate of genuine ep events is in the order of below 1 kHz. Therefore, it is necessary to operate detectors like H1 with sophisticated trigger systems to suppress the high background rates.

1.2 Kinematic Quantities in Electron-Proton Scattering

The inclusive electron-proton scattering process $ep \rightarrow lX$ ($l = e$ or ν) is taking place at the lowest order via the exchange of a gauge boson between the electron and a quark in the proton (see figure 1.1). One generally distinguishes two different classes of events. The first one - $ep \rightarrow eX$- where the exchanged boson is neutral (a virtual photon or a Z^0 boson) is called Neutral Current (NC). The second event class called Charged Current (CC) - $ep \rightarrow \nu X$- has the particularity to have a neutrino as outgoing lepton and the $W^{\pm}$ boson mediates the exchange. Most physical processes and quantities studied at HERA are functions of the event kinematics x, y and Q^2 (Lorentz invariant quantities) and it is therefore important to define them here:

$$\begin{aligned} Q^2 &= -q^2\mathrm{c}^2 \quad = (k-k')^2\mathrm{c}^2 \\ x &= \frac{Q^2}{2\,P\cdot q\ \mathrm{c}^2} \\ y &= \frac{P\cdot q}{P\cdot k} \quad . \end{aligned} \tag{1.1}$$

The four-momentum of the exchanged boson is noted q and its invariant mass squared is given by $-Q^2$. The value of Q^2 represents the degree of the boson virtuality. At the lepton vertex the variable Q^2 can be described in terms of the difference of the incoming lepton momentum (k) and the outgoing lepton momentum (k'). In a frame where the proton mass is very small compared to the proton energy (called infinite momentum frame) the Bjorken scaling variable x is interpreted as the fraction of proton momentum carried by the struck quark within the assumption of the Quark Parton Model (QPM, see subsection 3.1.1). The four-momentum of the incoming proton is denoted by P. In the incident proton rest frame y represents the fraction of the incident electron energy transfered to the proton.

It is also important to notice that for fixed beam energies there are only two independent variables among the three defined in equation 1.1. The variables x, y and Q^2 are related via the centre of mass energy $\sqrt{s}$ of the ep collision as follows:

$$Q^2 = xys, \tag{1.2}$$

where:

$$s = (k+P)^2\mathrm{c}^2. \tag{1.3}$$

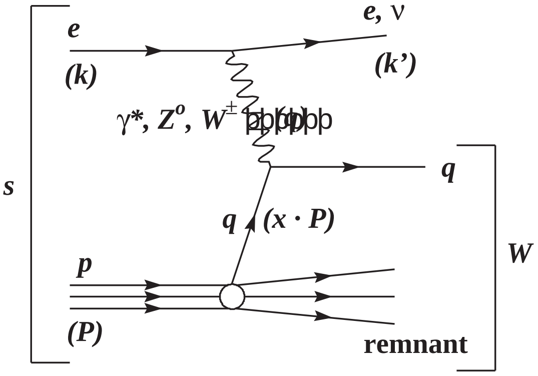

Figure 1.1: Representation of the inclusive electron-proton scattering process $ep \rightarrow lX$ ($l = e$ or ν) in the Quark Parton Model.

Equation 1.2 is valid when the electron and proton masses are neglected because in this case s is given by:

$$s = 2\ k \cdot P\ \mathrm{c}^2 = 4E_e E_p, \tag{1.4}$$

where $E_e = 27.6$ GeV and $E_p = 820$ GeV are the electron and proton beam energy respectively.

Another important quantity is the energy of the boson-proton centre of mass W which is equal to the invariant mass of the hadronic final state:

$$W^2 = (q + P)^2 \mathrm{c}^2 = Q^2 \left(\frac{1}{x} - 1 \right) + m_p^2 \mathrm{c}^4 = ys - Q^2 + m_p^2 \mathrm{c}^4. \tag{1.5}$$

1.3 Accessible Kinematic Range at HERA

In figure 1.2 the (x, Q^2) domains reached by HERA experiments and previous experiments are shown. In NC process the cross section decreases rapidly with Q^2 because the value zero for Q^2 corresponds to the pole of the photon propagator. In the Quark Parton Model, for a given moderate Q^2 value a struck quark with large x will stay in the proton direction (forward). A smaller x struck quark will loose its initial direction and therefore be more deviated from the proton direction. Usually three different kinematic domains are defined by the virtuality of the exchanged boson.

- The commonly named **photoproduction** domain for $Q^2 \approx 0$ GeV^2 corresponds to an exchanged photon almost on-shell. The very small virtuality allows the photon to fluctuate into a hadronic state. Those resolved processes are distinguished from the direct case where the photon is point like. They are important for light quark production.

- For 0.35 GeV$^2 < Q^2 < 100$ GeV^2 one enters already the Deep Inelastic Scattering regime (DIS). This Q^2 range is called **DIS at low and moderate Q^2** and is dominated by NC photon exchange events. Smaller values of x are accessed which allows extensive tests of QCD. The present analysis is done in a subregion of this domain which can be seen in figure 1.2.

- The so called **DIS at high Q^2** domain for $Q^2 > 100$ GeV^2 corresponds to events where in most of the case the quark involved in the process is a valence quark. For Q^2 above 5000 GeV^2 cross sections for NN and CC are of comparable size. Moreover in NC process where $Q^2 \approx m_Z^2 c^4$ the contributions due to Z^0 exchange become important. Therefore in this domain it is possible to evaluate the effect of the electroweak sector of the Standard Model and to pin down any indication of physics beyond the Standard Model.

1.4 Heavy Quark Production at HERA

Charm quarks are revealed by identifying their fragmentated hadrons. The D^{*+} and D^0 mesons or the Λ_c baryon are representatives of open charm production whereas J/ψ mesons allow to tag charmonium production[3]. Generally the hadrons are reconstructed from their decay particles measured in tracker devices.

Open charm photoproduction in NC is accessible with the H1 detector (see figure 2.1) by identifying the scattered electron in calorimeters situated far down-stream[4] and very close to the beam direction. Different Q^2, y, W ranges are accessible depending how far the device is situated from the interaction point. They deliver detailed information about the production mechanism.

In DIS open charm production the electrons are scattered at larger angles than in photoproduction and are identified in the backward region of the main body of H1. First measurement at HERA [3] has confirmed the EMC collaboration results on muon nucleon scattering [5], showing that charm production is dominated by the boson-gluon fusion process (see figure 3.3).

The object of the present analysis is to study open charm production in DIS where the scattered electron is identified in the new backward components of H1 (see section 2.3). In figure 1.2 the parallelogram shows the domain in which the cross sections are be measured (1 GeV$^2 < Q^2 <$ 100 GeV^2 and $0.05 < y < 0.7$). The points correspond to the 1996 selected D^{*+} candidates (see chapter 4). The D^{*+} candidates can only be reconstructed in the so-called visible range which corresponds to the detector acceptance ($-1.5 < \eta_{D^*} < 1.5$) and to the way of extracting the D^{*+} signal which requires $p_{\perp D^*} > 1.5$ GeV/c. The accessible W range, which is essentially given by the y range, goes from 70 to 250 GeV. The steeply falling cross section with Q^2 together with a small reconstruction efficiency restricts the accessible kinematics to $Q^2 < 100$ GeV^2. The accessible larger kinematic range as well as the improvement of the scattered electron selection and kinematics resolution allows a better confrontation between the data and the available theories.

Up to now it was not possible to identify charm within CC events. At moderate Q^2 the CC cross section is suppressed due to the high mass of the $W^\pm$ boson. At very high Q^2 both NC and CC cross sections are small though of the same order of magnitude.

---

[3] Charge conjugate states are always implicitly included.

[4] Backward with respect to the centre of mass direction.

At HERA, beauty production, which is two order of magnitude smaller than charm production, is enhanced in events containing two jets where one of the jet is accompanied by a muon. The contribution of $b\bar{b}$ events is determined from a simultaneous fit of the impact parameter δ and the transverse momentum $p_{\perp}^{rel}$ relative to the jet axis. Within the detector muon acceptance, $p_{\perp\mu} > 2$ GeV/c and $35^\circ < \theta_\mu < 130^\circ$, the H1 collaboration has already given preliminary results for $b\bar{b}$ cross sections:

- $\sigma_{vis}^{b\bar{b}}(ep \rightarrow e\mu X) = (170 \pm 25(\mathrm{stat}) \pm 29(\mathrm{syst}))\,\mathrm{pb}$
  for $Q^2 < 1$ GeV^2 and $0.1 < y < 0.8$ [6],
- $\sigma_{vis}^{b\bar{b}}(ep \rightarrow e\mu X) = (39 \pm 8(\mathrm{stat}) \pm 10(\mathrm{syst}))\,\mathrm{pb}$
  for 2 GeV^2 $< Q^2 <$ 100 GeV^2 and $0.05 < y < 0.7$ [7].

For $Q^2 < 1$ GeV^2 the predicted cross section based on the NLO calculations by Frixione *et al.* [8] is 104 ± 17 pb. This prediction undershoots clearly the data. In deep inelastic scattering (2 GeV^2 $< Q^2 <$ 100 GeV^2), the measured $b\bar{b}$ cross section is roughly three times larger than the prediction of the HVQDIS NLO calculations (see subsection 3.3.5) which amounts only (11 ± 2)pb.

Studying charm production at HERA with improved experimental conditions can therefore significantly contribute to the understanding of heavy quark physics. Beauty measurements are also very important as they show large discrepancies with the available theories.

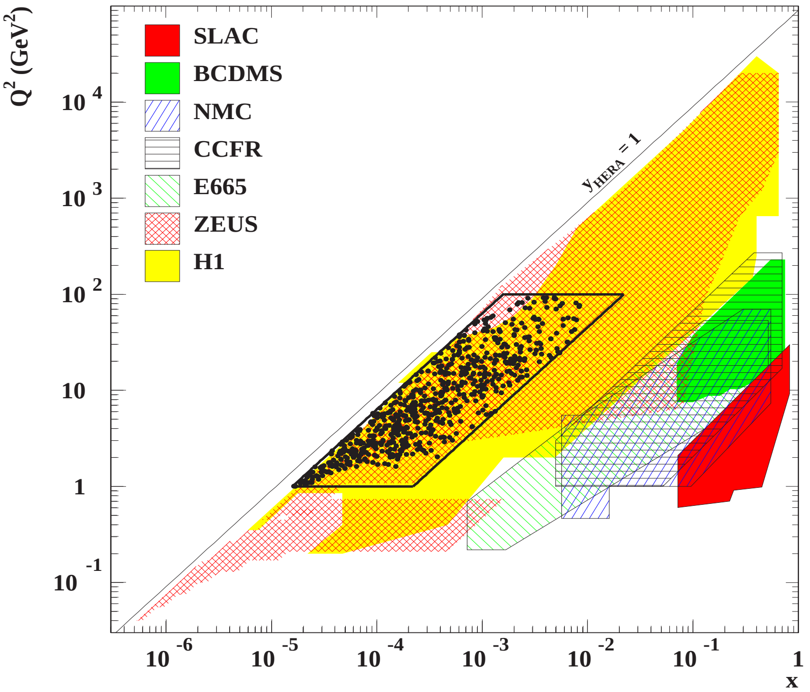

Figure 1.2: x, Q^2 range covered by fixed target experiments (SLAC, BCDMS, NMC, CCFR and E665) and collider deep inelastic scattering experiments (H1 and ZEUS) carried out until 1997. The parallelogram shows the domain in which the cross sections presented in this analysis are measured and the points correspond to the 1996 selected D^{*+} candidates (after selection described in chapter 4).

Chapter 2

The Detector H1

2.1 Overview of the Experimental Setup

The H1 spectrometer [9], one of the two devices built to study the electron-proton collisions provided by HERA, is schematised in figure 2.1. A cut along the beam axis is shown in figure 2.2. Although H1 is composed like all modern collider experiments, it presents the specificity of an enhanced instrumentation in the proton direction (frequently called the forward direction). This is the consequence of the fact that the centre of mass of the collision is not at rest in the laboratory frame but progressing in the proton direction (with a velocity $\beta_{\rm CM}{\rm c} = 0.935{\rm c}$) due to highly asymmetric beam energies (see chapter 1.1). For the understanding of all the figures in this chapter, one has to know that the coordinate system attributed to H1 has the z-axis parallel and in the same direction as the proton momentum. The origin is at the nominal interaction point inside H1 and the x-axis is pointing towards the centre of the accelerator ring. Emphasise has been put on basic requirements in order to fully exploit the physics available at the HERA *ep* collider. Indeed, the measurement of the proton structure functions (F_2, F_L, F_3, F_2^c) in deep inelastic scattering requires a clean identification of the scattered electron as well as a good resolution in the measurement of its energy and scattering angle (see equation 4.4). To attain this, an adequate segmentation of the calorimeters in depth, θ and φ over the full kinematic range has been achieved. In the case when the event kinematics are determined via the $E - p_z$ measurement (see subsection 4.3.2), a high degree of hermiticity as well as a good reconstruction of the hadronic final state are necessary. The previous requirements are also important to identify missing transverse momentum resulting in a positive $E - p_z$ value, a usual signature of events involving energetic neutrinos. A highly efficient central tracking system and a good muon identification are essential to heavy flavour physics and search for new particles.

The H1 detector is summing up approximately 270,000 channels coming from a number of complex, highly-segmented subdetectors. It is composed as follows.

- A tracking system is providing track triggering, momentum reconstruction and particle identification, adequate to the event topology particular to HERA electron-proton collisions. It is mechanically distinct into the central and forward tracking devices (CTD, FTD) in order to maintain a good efficiency for triggering and reconstruction over the whole polar angle. This is necessary because of the event topology when colliding two beams asymmetric in energy (high density of particles at small polar angle). The central tracking device is described in details in section 2.2.

The forward tracking device consists of a dense assembly of three nearly identical super-modules and was designed to provide an accurate measurement of charged particle momenta in the forward direction (momentum resolution $\sigma_p/p^2 < 0.003$ GeV^{-1}c and track angular resolution $\sigma_{\theta,\varphi} < 1$ mrad). Each super-module is composed of the following devices (starting from the device closest to the vertex):

  - Three planar drift chambers are composed respectively of 32 cells. Within one chamber the wires are strung in the (x, y) plane parallel with one another and with four layers of sense wires deep in z. The wires in one chamber are tilted by 60° in azimuthal angle with respect to the wires of the neighbouring planar chamber. The drift velocity lies as well in the (x, y) plane but perpendicular to the wires (in case of no magnetic field). The drift time coordinate is determined from the pulse profile (Q, t) analysis (described in appendix A.1).
  - One multi-wire proportional chamber (FWPC) is a sandwich in z of three layers of concentric cathodes separated by two layers of dense parallel wires perpendicular to the beam line (dense y orientated wires). The bad space resolution is compensated by a very small time response (≈ 20 ns) which turns the FWPC into the forward device used in the general track triggering.
  - A transition radiator (TR) consisting of 400 polypropylene foils is enclosed in his own helium-ethane mixture gas envelope and provides an adequate number of dielectric interfaces to enhance the X-ray emission of crossing electrons. To allow the transition radiation photons to pass through, a thin mylar window is making the separation between the TR and the radial chamber.
  - The radial chamber produces up to 12 accurate space points determined by the drift coordinates perpendicular to the sense wire (using pulse profile (Q, t) analysis) and by the radial position (using charge division method). The radial chamber gas is optimised for efficient X-ray detection of the TR photons. This allows an electron-pion discrimination at the level of 90% electron acceptance with less than 10% pion contamination for tracks up to 80 GeV passing through all three super-modules of the FTD.

- Two Silicon detectors were installed between the beam pipe and the central tracker device. The central silicon tracker (CST) implemented partially in 1996 and completed in in 1997 consists of two concentric cylindrical layers of silicon sensors. It will be of use in the determination of the heavy meson secondary vertices and in the improvement of the central track measurement. A backward silicon tracker (BST) has been mounted in 1996 downstream in the electron direction and before the BDC in order to improve the measurement of the scattered electron. The BDC consists of four planes of silicon wafers with p-type strips concentric around the beam axis.

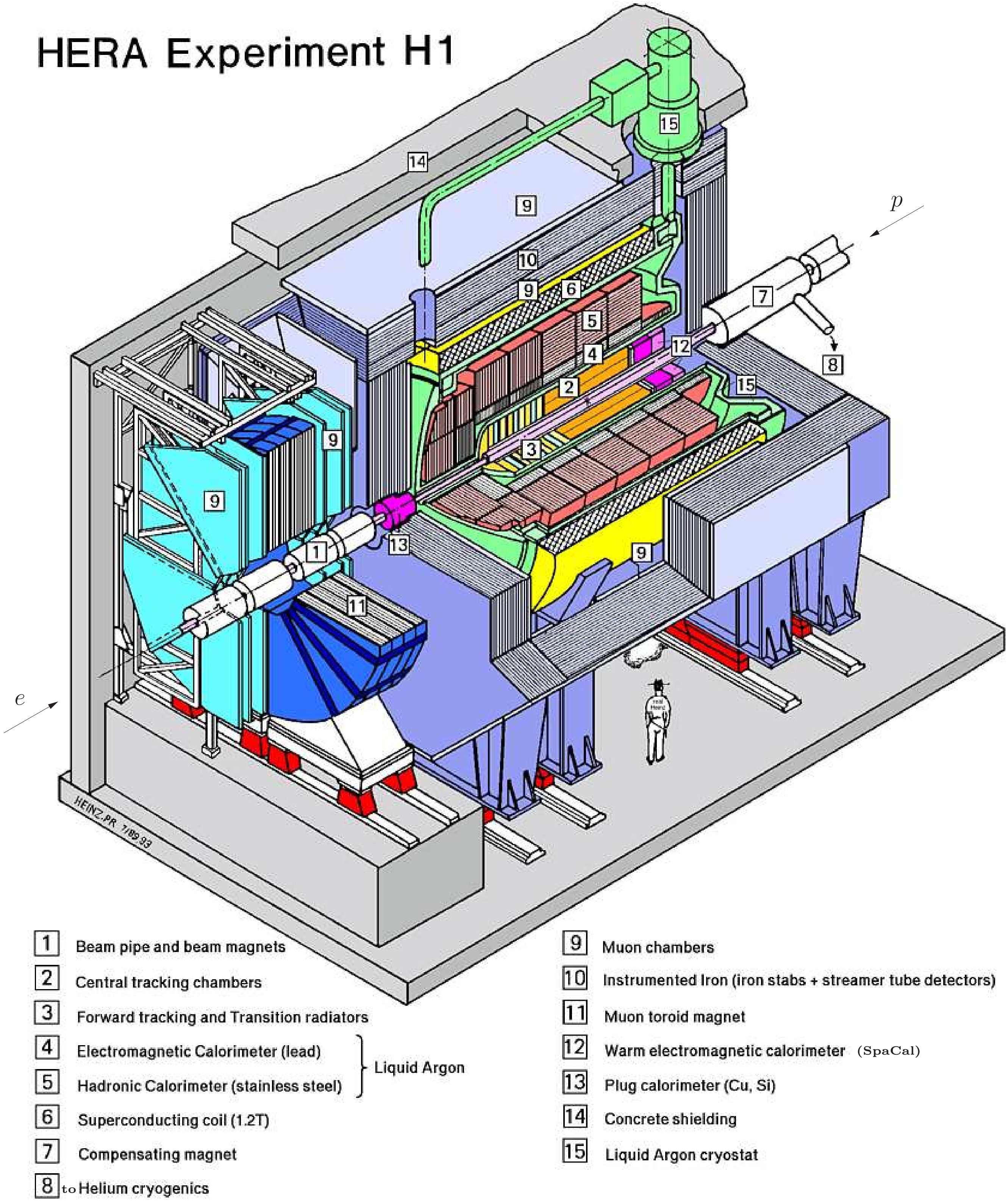

Figure 2.1: The main body of the H1 detector.

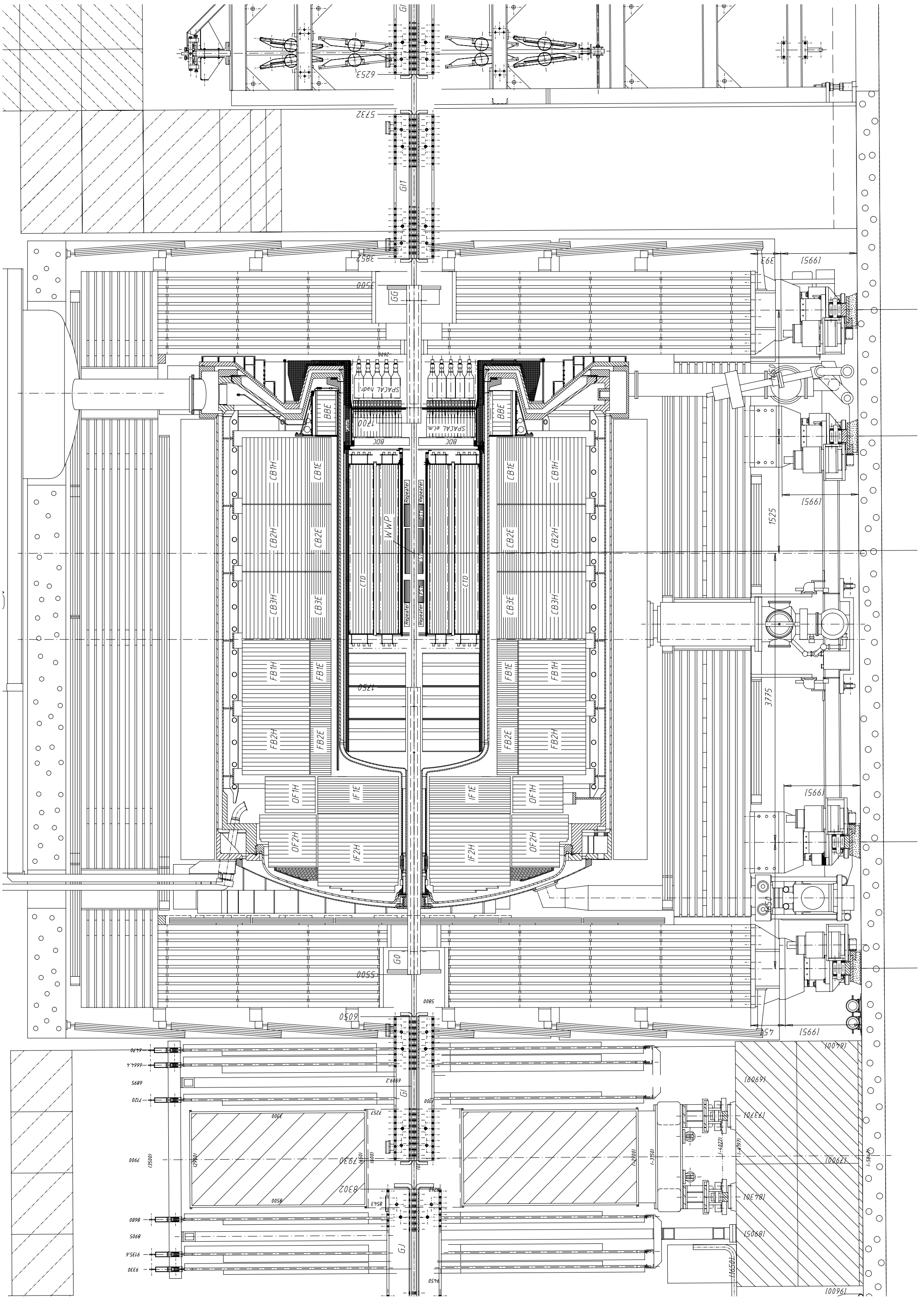

Figure 2.2: Longitudinal cut through the H1 detector along the beam axis.

- A central calorimeter is surrounding the central and forward tracking devices. The liquid argon (LAr) technique has been chosen in order to profit from its excellent stability, its good resistance to radiation and its relatively well off calibration as well as its fine granularity necessary to separate electrons from pions. The homogeneity in its response as well as the best hermiticity have been sought after in order to achieve a precise measurement of the energy flux and thus of the missing energy. The calorimeter is divided into two functional parts. Right after the central trackers stands the electromagnetic part which will be used to detect the electrons while the hadronic part is dedicated to the hadron energy measurement.

- The backward region is hermetically covered by a thin drift chamber (BDC) and a spaghetti calorimeter (SpaCal) with an electromagnetic and a hadronic section. More details on the SpaCal and on the BDC are given in sections 2.3 and 2.4 respectively.

- Encircling the LAr calorimeter a superconducting solenoid produces a uniform and longitudinal magnetic field of 1.15 T which allows the measurement of the transverse momentum in the trackers.

- An iron yoke consisting of an octagonal barrel around the solenoid plus two flat end caps ensures the guidance of the returning magnetic flux and the uniformity of the internal field. The iron yoke is instrumented with limited streamer tubes (LST) which are placed in gaps between alternate layers of iron. Two additional muon chambers are situated at the inside and outside of the iron yoke. This so called instrumented iron serves a dual purpose. At first, it is used as a tail catcher (TC) calorimeter to detect and measure the hadronic energy leaking from the LAr and backward calorimeters. At second, it acts as a detector of penetrating muon tracks.

- The forward muon detector is situated outside of the iron yoke in the forward direction and consists of six layers of muon chambers, three either side of a toroidal magnet.

- Electron and photon taggers are placed well downstream in the electron direction. They are used to measure the luminosity and in addition, in the case of the electron tagger, to tag photoproduction. A precise description of the luminosity system is given in section 2.5

- Time of flight (ToF) counters and two double scintillator veto walls have been installed to reject proton-beam associated background at the first trigger level with the help of the SpaCal calorimeter. The Forward ToF (FToF) is situated at $z \approx 7.0$ m in between the forward muon system. The Plug ToF (PToF) is installed in the region of the Plug calorimeter at $z \approx 5.3$ m. The Backward ToF (BToF) is mounted at $z \approx -3.3$ m. The veto wall system consists out of two devices: the big veto wall or outer veto wall (seen in figure 2.2) covering nearly the entire surface of H1 and installed at $z \approx -6.5$ m; the small veto wall or inner veto wall located very close to the beam line in between some HERA magnets at $z \approx -8.1$ m. An event is rejected when activity arrives out of time with respect to the bunch crossing or when the determined z position of the *ep* interaction (determined with 30 cm precision) is not in the expected region.

- The supression of the high background due to the non point-like characteristic of the proton and the restriction to keep only dedicated physics is realised through a very sophisticated trigger system described in section 2.6.

In the following a detailed description of the H1 detector components which are particularly relevant to this analysis is given.

2.2 The Central Tracking System

The Central Tracking System, centred at the nominal interaction point in the region of z between -1.25 and 1.25 m, covers the polar angular range between 15° and 165°. It is composed of two concentric cylindrical drift chambers - the central jet chamber 1 and 2 (CJC1 and CJC2) - which provide the trajectory measurement in the transverse plane (x, y). The trajectory along the z-axis is measured by two supplementary drift chambers named central inner (CIZ) and central outer (COZ) z-chambers. Despite of the very good spacial resolution these chambers with their large time response ($\approx 1\ \mu$s) are not adequate to provide time resolution better than the separation of two successive bunch crossings. Therefore two proportional chambers, the central inner proportional (CIP) and the central outer proportional (COP) chamber, with a very small time response have been implemented. They provide in combination with the forward and backward multiwire proportional chambers a fast trigger decision which is used to distinguish between successive bunch crossings. A particle created at the interaction point will cross the elements of the central tracking system in the order CIP, CIZ, CJC1, COZ, COP, CJC2 as seen in figure 2.3.

2.2.1 The Central Jet Chambers

The two concentric central jet chambers are the main devices used in the track reconstruction. They allow the measurement of particle transverse momenta as well as particle identification. The latter is accomplished via the measurement of $\frac{dE}{dx}$, the loss of energy with distance travelled. The large time response ($\approx 1\ \mu$s) requires a fast algorithm based on the recognition of special track configurations to allow the use of the CJC at the first trigger level. The CJC1 chamber consists of 30 cells, each containing 24 sense wires, whilst the CJC2 chamber consists of 60 cells of 32 sense wires each. The cells are separated by cathode planes, made of wires, shaping the drift field. The anode sense wire direction is parallel to the z-axis so that the drift velocity (being around 50 mm$\cdot\mu$s^{-1}) is in the (x, y) plane. The drift time information is used to determine the $r\varphi$-coordinate with a resolution of approximately 170 μm. A rough estimation of the z-coordinate (25 mm resolution) is available from the charge division (see appendix A.2). To account for the magnetic field all drift cells are tilted by 30° to the radial direction. The electric drift

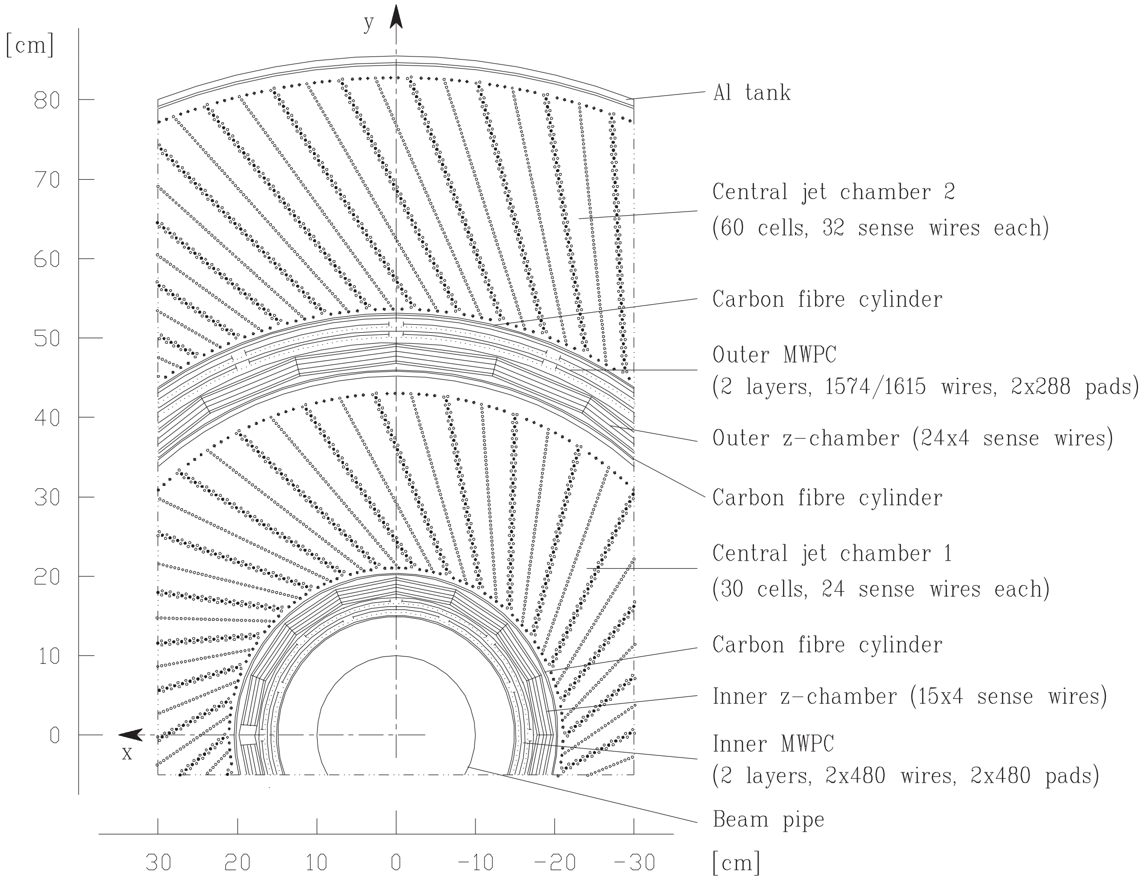

Figure 2.3: r-φ view of the Central Tracking System.

field compensates the effect of magnetic field on the ionising electrons so that, for a stiff track originating at the z-axis, the ionising electron will drift perpendicular to the track direction. This configuration gives an optimum track resolution. The usual drift chamber ambiguity (mirror track) is resolved by combining track segments from different cells.

2.2.2 Complementary Trackers

The Central z-Chambers

The central inner and outer z-chambers (CIZ and COZ) complement the measurement of the CJC chambers by a precise measurement of z. Their wires are perpendicular to the radial direction with a drift velocity parallel to z. Both chambers give a z-resolution of typically 300 μm. Whenever CIZ and COZ track elements can be linked to a CJC track an additional fit will be performed including the CIZ and COZ track elements and resulting in an improved track momentum measurement. This treatment is limited by the low linking efficiency. Therefore the z-chambers do not improve the detector performance considerably.

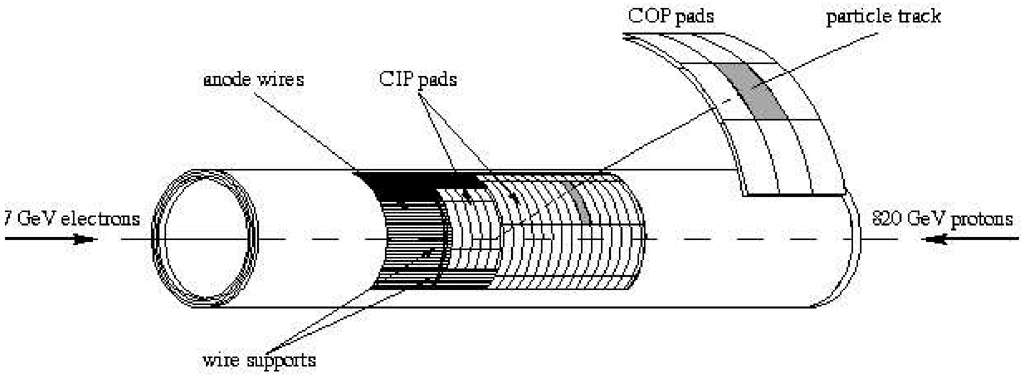

Figure 2.4: Schema of the CIP and COP geometry.

The Central Proportional Chambers

The central inner and outer proportional chambers (CIP and COP) are also complementary trackers but have no impact on the final track measurement. Their main role is to provide, in combination with the FWPC (see section 2.1), a fast information on the primary vertex z-position usable at the first trigger level. Like for the CJC trackers the CIP and COP have their wire parallel to the z-axis. Both detectors consist of 2 layers (chambers) delimited by three concentric cylinders. The CIP (COP) chambers are segmented in z by 60 (18) pads of 36 (120) mm for each of the 8 (16) φ sectors. The wires are running over the pads along the z-axis. The two CIP chambers are rotated by $\pi/8$ in φ thus both CIP and COP are providing a 16-fold segmentation in φ. An overview of the central proportional chambers is shown in figure 2.4.

2.2.3 Track Reconstruction

The presence of an external longitudinal magnetic field in the area of the CJC results in Lorentz forces on charged particles. The trajectory of a charged particle can be described by a helix which is determined by a set of five parameters.

- The signed curvature $\kappa = \pm r^{-1}$.
- The signed closest distance from the z-axis in the (x, y)-plane d_{ca}.
- The azimuth angle Φ at the point of the closest approach: angle between x-direction and the transverse momentum (tangent to the helix in the r, ϕ-plane) at the closest approach.
- The polar angle θ at the point of the closest approach: angle between z-direction and the momentum at the closest approach.
- The z-position z_{ca} at the point of the closest approach.

The sign of κ is positive if the propagation of the particle from the closest approach is counter-clockwise. The transverse momentum of the track is directly parametrised through the curvature of the helix in the (x, y)-plane, $\kappa \propto 1/p_\perp$. The distance d_{ca} is chosen positive if the vectors $(d_{ca}, p_\perp)$ build up a right-handed system. The first three parameters are determined by projecting the trajectory into the (x, y)-plane and fitting the resulting circle. The polar angle θ and the z-position z_{ca} are then the result of a linear least-square fit in the (r, z)-plane. The track reconstruction is implemented in two different versions. A fast version, on the trigger Level 4, is the input for an online event classification and background rejection. It only reconstructs tracks origin from a primary vertex. The second version, the so called standard version, reconstructs all kind of tracks on trigger level 5 (offline reconstruction).

The Fast Track Reconstruction on L4

The reconstruction is carried out in different phases. In the first phase, the algorithm looks for short track elements in each angular drift cell independently. For this the time of the interaction T_0 of the event is determined from the threshold in the so-called drift time histogram where all first electrons arival times from all wire signals (see appendix A.1) are added. Then the algorithm calculates the drift distances (including mirror hits since the drift distance is ambiguous) for each wire signal. It searches for triple hits (short track elements) which belong together. Here, only wires with a wire distance of two are taken into account. This limits the search to tracks with negligible curvature. Regions with many hits are not analysed at this reconstruction stage. Based on the three hits, a circle fit is done with the preliminary assumption $d_{ca} = 0$ and the parameters κ and Φ are determined. Thus parameters of triplets belonging to the same track cluster in the plane (κ, Φ). A first track definition is achieved. In the next phase a circle is fitted again with all triplets of one track but now allowing $d_{ca} \neq 0$. Mirror triple hits are usually excluded at this stage since tracks based on those hits are not continuous across neighbouring drift cells. After the track reconstruction is finished in the r, ϕ-plane the hits are fitted in the r, z-plane where z_{ca} was obtained by the charge division method (see appendix A.2).

The Standard Track Reconstruction on L5

The standard track reconstruction on trigger level 5 uses the results which are obtained with the fast reconstruction method. First of all, it tries to improve the value of the interaction time T_0. This is achieved by calculating the differences between the measured and expected drift lengths of long tracks. An expression is fitted to these differences and results in a much more accurate determination of T_0 than obtained on Level 4. After this the standard track finding searches for triple hits as before but now on all adjacent wires. An iterative merging algorithm combines track elements with similar helix parameters and builds up new longer track elements. New fits are then performed to these longer track elements and lead to more accurate helix parameters if the fit was accepted. Up to now all reconstructed tracks are not vertex fitted. The run vertex coordinates (x_{vtx}, y_{vtx}), which can vary over a few hundred μm from run to run, is determined by minimising the rms value of the distances between run vertex and several hundred long tracks with high momentum. The z_{vtx} value of the primary interaction vertex is determined for each event from all tracks fitting to the (x_{vtx}, y_{vtx}) vertex. Finally, the standard track reconstruction algorithm also looks for secondary vertices coming from the decay of neutral particles. Here, simple geometrical cuts and kinematic constraints are applied for the search of two oppositely charged particles. The reconstruction programme provides a list of track properties. It collects the parameters of the helix, the reconstructed momentum but also a set of quality criteria:

- the number of hits used in the fit in the CJC1 and in CJC2
- the so called track length which represents the total length of the track measured segment.
- The radius at the first hit used in the fits, track starting radius.
- The energy loss due to ionisation, $\frac{dE}{dx}$.

2.3 The Backward Detector SpaCal

Under the constant worry of improving the performance of the H1 detector, it had been decided to use the winter shutdown 1994/95 to accomplish heavy changes in the structure of H1. The implementation of a new backward Spaghetti Calorimeter, the SpaCal [10], fronted by a new drift chamber (BDC) was the major change. This was motivated by the interest in the physics at low Q^2 where the gluon density dramatically increases. To compare with the previous backward calorimeter (BEMC [9]), the SpaCal increases the polar angular range from 176° to 177.5° which allows to access Q^2 values down to 0.4 GeV^2 and x values down to 10^{-5}. It also provides a better granularity as well as a big improvement in the resolution of the electromagnetic and hadronic energy measurements. In photoproduction, a process several order of magnitude more abundant than DIS scattering, the scattered electron often escapes in the beam pipe. In this case the SpaCal, with an excellent electrons to charged hadrons separation, is able to suppress fake electron which could be considered as the scattered one. The overall calibration uncertainty of less than 1% allows to reduce the already dominant systematic error on the kinematic variables relevant in the determination of the proton structure function. Finally a time resolution of less than 1 ns gives the possibility to reject upstream beam-induced background events which have a time-of-flight delay of approximately 10 ns compared to ep scattering events.

The SpaCal calorimeter consists of an inner electromagnetic and an outer hadronic section covering the polar angle range from 153° to 177.5°. The 1192 electromagnetic cells and the 136 hadronic cells provide an extremely fine granularity. Both electromagnetic and hadronic parts use the same spaghetti type technology. For the electromagnetic section a 2-cell module, represented in figure 2.5, is composed of 52 lead matrices where a total of 4680 fibres are embedded. The cross section of one cell is 40.5×40.5 mm^2 and contains 2340 fibres which are bundled at the cell end and read by a single photomultiplier after mixing the scintillation light with the help of an acrylic light mixer. Eight 2-cell modules are grouped to form a 16-cell module. The orientation of the 2-cell modules within a 16-cell module is either horizontal or vertical (figure 2.6) to minimise channelling[1]. The electromagnetic cells are less dense and smaller than the hadronic ones as represented in figure 2.6. The section of a hadronic cell is 119.3×119.3 mm^2 and consists of 65 lead plates, each filled with 54 fibres. As in the electromagnetic section, the fibres of one hadronic cell are bundled and coupled via an 80 mm long acrylic light mixer to a photomultiplier. Both electromagnetic and hadronic parts have an active length of 25 cm which corresponds to 27.8 radiation lengths for the electromagnetic section and 29.4 for the hadronic section. The two sections, each representing approximately one interaction length, provide a longitudinal calorimetry which is the key point of a good electron-hadron separation. The main SpaCal parameters are summarised in table 2.1.

	Electromagnetic Section	Hadronic section
Total length of the section	500 mm	500 mm
Active length	250 mm	250 mm
Number of cells	1192	136
Fibre type	Bicron BCF-12	Bicron BCF-12
Fibre diameter	0.5 mm	1.0 mm
Lead to fibre ratio	2.3 : 1	3.4 : 1
Standard cell size	40.5×40.5 mm^2	119.3×119.3 mm^2
Number of lead plates/cell	52	65
Number of fibres/plate	45	54
Total number of fibres/cell	2340	3510
Radiation length X_0	9.0 mm	8.5 mm
Active length in X_0	27.8	29.4
Interaction length Λ	250 mm	246 mm
Active length in Λ	1.00	1.02

Table 2.1: Design parameters of the backward calorimeter SpaCal.

The test realised with the PS and SPS beam at CERN and at DESY [11] have allowed to measure the energy resolution of the electromagnetic section:

$$\frac{\sigma_E}{E} = \frac{(7.1 \pm 0.2)\%}{\sqrt{E/\mathrm{GeV}}} \oplus (1.0 \pm 0.1)\% \tag{2.1}$$

where the term in $\sqrt{E/\mathrm{GeV}}$ comes from the fluctuation of the number of generated electron in the photomultipliers. This resolution was one of the main requirements for a new backward calorimeter in order to improve the x resolution at small values of y.
Later, when SpaCal was operated within H1, studies of the scattered electron energy spectrum at the kinematic peak have been performed [12] using both electron and double

---

[1] The channelling effect is a degradation of the energy resolution which occurs if fibres or lead sheets are aligned with the particle trajectory.

angle methods (see equations 4.4 and 4.15). They resulted in a 1% energy resolution for 27.5 GeV electrons. QED Compton events were used to measure a 2.5% energy resolution for scattered electrons of 7 GeV [13]. Finally, since a straight line can well describe the behaviour of the equation 2.1 , the SpaCal energy resolution can be taken as linear from 2.5% at 7 GeV to 1% at 27.5 GeV.

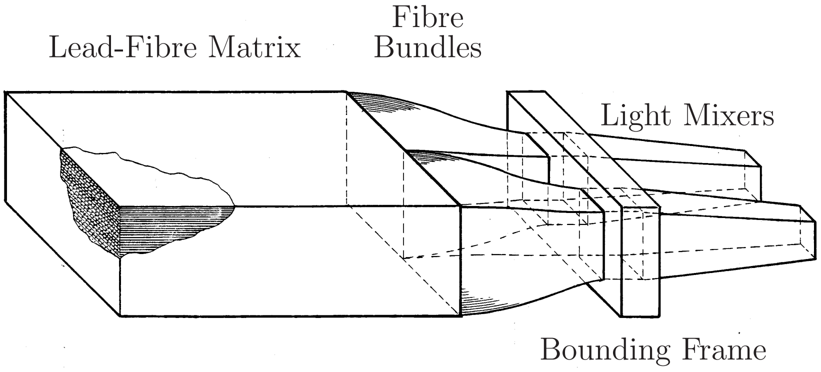

Figure 2.5: SpaCal Electromagnetic 2-cell module.

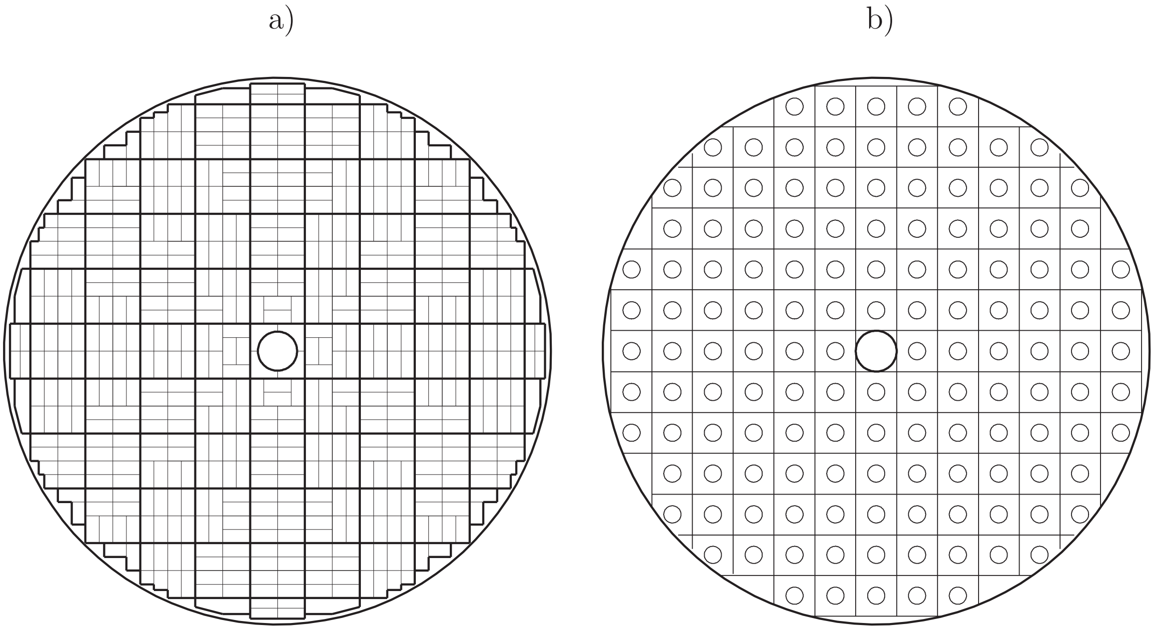

Figure 2.6: r-ϕ view of the SpaCal a) electromagnetic section with its 16-cells delimited by bold lines and b) the hadronic section where the circle represents cells read out by a photomultiplier.

For the hadronic part, measurements were performed at the ITEP proton synchrotron at Moscow [14] and result in a hadronic resolution of

$$\frac{\sigma_E}{E} = \frac{(56.0 \pm 3.0)\%}{\sqrt{E/\mathrm{GeV}}} \tag{2.2}$$

compared to the $\frac{100\%}{\sqrt{E/\mathrm{GeV}}}$ obtained with the previous BEMC calorimeter.
The fine granularity of the electromagnetic section gives a polar angle resolution of:

$$\sigma_\theta = 2 \text{ mrad} \tag{2.3}$$

which corresponds to a few mm resolution in the position measurement. Such a good resolution is essential to achieve a precise measurement of Q^2 at large scattering angle.

2.4 The Backward Drift Chamber

The Backward Drift Chamber (BDC) [15] is mounted in front of the SpaCal. Thanks to its similar angular acceptance it provides an accurate measurement of the scattered electron polar and azimuthal angles. The BDC is subdivided in eight octants. One octant consists of four double layers of drift chambers which are superposed along the z direction. The sens wires (2048) are strung perpendicular to the beam pipe and in a way that an almost radial drift direction is produced. This geometry optimises the spacial resolution in the polar angle. Moreover, the wire spacing decreases towards the inner region of the chamber, such that a uniform resolution in the polar angle is obtained. The left and right ambiguity on the ionisation point is solved by shifting each double layer by half a cell width. In addition, the double layers are rotated by 11.5° with respect to one another which allows to measure the azimuthal angle.

2.5 The Luminosity System

The luminosity system is forseen to provide a fast online luminosity measurement necessary for the HERA machine group to steer the electron beam and to detect problems. Offline, it gives an accurate luminosity measurement used to calculate precise cross sections at H1. The luminosity is determined from the rate of the Bethe-Heitler process, $ep \rightarrow ep\gamma$, because this process is insensitive to the internal proton structure. The Bethe-Heitler events represent the dominant part of the bremsstrahlung process which corresponds to the poles in both the virtual electron and photon propagators. The outgoing electron and photon leave the central detector collinear to the incoming electron. The Bethe-Heitler cross section is large and precisely calculable within the quantum electrodynamics theory. It amounts to 70 nb in the visible range of the luminosity system [16].

The luminosity system is based on two dedicated detectors: the Electron Tagger (ET) for detecting the scattered electron and the Photon Detector (PD) for detecting the outgoing photon. The kinematic of the Bethe-Heitler process favours scattered electrons

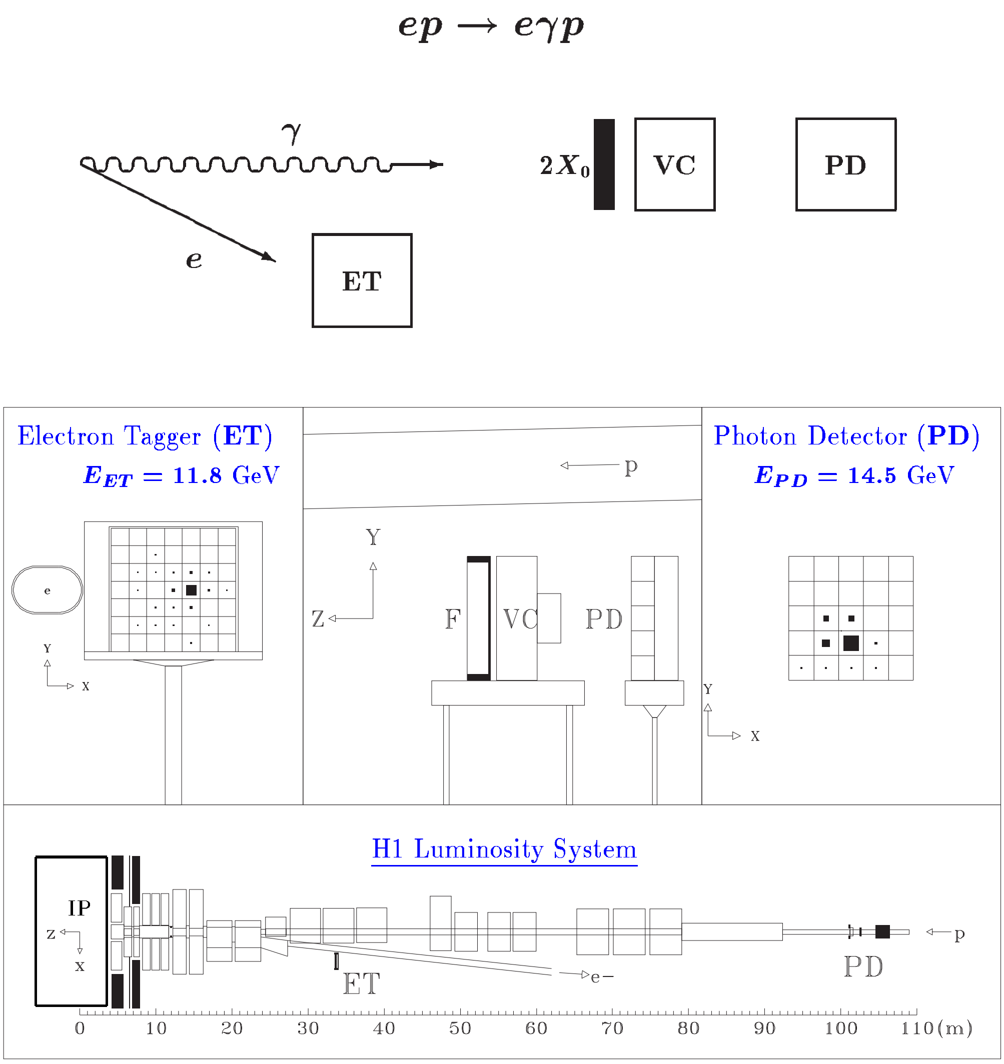

Figure 2.7: Layout of the luminosity system.

staying inside the beam pipe. Therefore the ET is situated very close to the beam pipe and far from the interaction point ($z = -33$ cm) in order to access electrons with scattered polar angles close to 180°. Like for the electron of the beam the scattered electron is deflected by the system of magnets used to isolate the electron beam from the proton beam. On the contrary, the outgoing photon will continue straight and will reach the PD which is centred on the proton beam axis at $z = -103$ m. Figure 2.7 shows the layout of the luminosity system.

A two radiation length long lead filter, followed by a one radiation length long water Čerenkov counter is located in front of the PD and protects the PD against low energetic synchrotron radiations. The water Čerenkov counter serves as a veto counter to tag and reject early photons and events with photons interacting already in the filter. Total absorption KRS-15 cristal Čerenkov counters have been chosen for both the ET and PD detectors to reach high radiation resistance, good energy, coordinates and time resolutions. The high energy resolution of the ET and PD is essential for the determination of the event rate within a given energy window.

The instantaneous luminosity is determined from the total rate of bremsstrahlung events R_{tot}, the rate of bremsstrahlung events coming from electron pilot bunches R_0 (see subsection 1.1), the corresponding electron currents I_{tot}, I_0 and the visible part of the Bethe-Heitler cross section σ_{vis} taking into account acceptance and trigger efficiency. The instantaneous luminosity is then given by:

$$L = \frac{R_{tot} - (I_{tot}/I_0)R_0}{\sigma_{vis}}. \tag{2.4}$$

The event rate from the electron pilot bunches allows a good estimation of the amount of bremsstrahlung events coming from electron interactions with residual gas in the beam pipe ($eA \to eA\gamma$), the main background source affecting the Bethe-Heitler rate determination. More details on the luminosity measurement in the H1 experiment can be found in [16] and [17].

2.6 The Trigger System and Data Acquisition

The H1 detectors like most of the particle physics collider experiments has a very sophisticated trigger system. This is mandatory to reduce the large total interaction rate which exceeds the data readout and storage capabilities. Initially the raw data size per event is approximately 3 MBytes and is reduced at the front end to 50-100 KBytes per event. Only a small fraction of events coming from physics processes with high rate should be kept whereas events coming from rare or hitherto unobserved physics processes should be recorded with maximum possible efficiency.

The H1 trigger system consists of four levels out of which three are extensively used for the online event selection. An event is written to tape after having passed with success all three trigger levels.

With the increasing luminosity delivered by HERA over the years 1994 to 1999 the H1 trigger system was continuously improved and refined. This section gives an overview of the three trigger levels for the years 1996 and 1997.

2.6.1 Trigger Level 1

The HERA *ep* collider is providing one bunch crossing every 96 ns. Although an *ep* interaction is not expected at every bunch crossing it is necessary to be able to detect a genuine *ep* collision for each of the bunch crossings. Therefore the first trigger level has been designed to provide a trigger decision according to the HERA clock signal of 10.4 MHz without causing deadtime. This is performed by feeding all subdetector data into front-end pipelines for the time of 2.4 μs (25 bunch crossings) during which fast informations about the general properties of the event will be generated. These informations are delivered under the form of trigger elements to the central trigger logic (CTL). Each subdetector is approximatively producing 8 trigger elements.The CTL builds up 128 logical combinations of these trigger elements called subtriggers. At this level the subtrigger bits are named raw subtrigger bits. For a better reduction of the L1 *keep* rate all subtriggers can be downscaled by a so called prescale factor. If a subtrigger i is downscaled by a prescale factor d_i, only one event out of d_i events which have been fired by this subtrigger will keep the subtrigger i bit set. The subtrigger bits after downscaling are named actual subtrigger bits. A logical OR of the actual subtrigger bits will form the L1 *keep* signal. After a positive L1 *keep* no data is taken from H1, all front end-pipelines are stopped, the data of the event which has produced the positive L1 *keep* will be read and transferred to the memories of the readout processors. When all front-end buffers have been read the CTL resets the L1 *keep* signal and news events can feed again the pipelines. Due to the deadtime introduced by the pipelines readout (1-2 ms) the subtriggers have to be enough performant in order to keep the L1 *keep* rate under 50-100 Hz. In this case the primary deadtime will stay under 5-10%.

2.6.2 Trigger Level 2

The second level of the H1 triggering is based on the output of two independent systems. The L2 Topological Trigger (L2TT) and the L2 Neural Net (L2NN) are producing in parallel L2 trigger elements (L2TE) in a time of 20 μs. Each non set L2 TE is resetting one or several defined Subtriggers. L1 raw subtriggers with L2 condition can therefore run with rates up to few hundred Hertz without affecting the primary dead time. Many of the subtriggers however, are not affected by the L2 TE. The L1 subtrigger bits after the Level 2 are named final subtrigger bits. If none of the final subtrigger are set then the readout is aborted and the data taking starts immediately after.

2.6.3 Trigger Level 4

A farm of RISC processors is running at the fourth trigger level parallel to the data taking. The events arriving with a rate of 30 to 40 Hz will be distributed among the processors, each running a reduced version of the offline reconstruction. An event will be written to tape as soon as one of the Level 4 condition is satisfied. A final logged event rate of 5-10 Hz is reached. Until the year 1996 the trigger Level 4 was only used to select genuine *ep* collisions. Since beginning of 1997, because of the higher luminosity delivered by HERA, the use of the trigger Level 4 was compulsory to reduce the rate of recorded *ep* collisions. All physics interests have to be explicitely saved as well as corner of phase space with potential of underlying unknown physics.

In addition the trigger Level 4 has the double feature of monitoring the performance of all subdetectors necessary to detect problems during H1 operation.

Chapter 3

Theoretical Framework

3.1 Quantum Chromodynamics in Electron-Proton Scattering

Quantum Chromodynamics (QCD) is the field theory of strong interaction. Quarks and gluons, which are the components of the hadrons, get an additional non classical internal degree of freedom, the so called colour. There are only three fundamental colours (red = r, green = g and blue = b). Quarks carry only one type of colour whereas gluons are "bicoloured" ($b\bar{r}$ for example). The strong force between two quarks is mediated by the exchange of a gluon. Since the gluons themselves carry colours they can also couple to other gluons. This is a fundamental difference from QED where photon self-coupling cannot occur (photons are electrically neutral). A consequence of the gluon self-coupling is the logarithmic increase of the strong coupling constant α_s with decreasing momentum transfer. It is therefore difficult to apply the Feynman procedure to QCD. But experience has shown that for many, if not all high energy processes involving a large momentum transfer, it is possible to factorise the process into one part which only includes the hard interaction and a second part characterised by smaller momentum transfers. The hard interaction part can then be treated in perturbative QCD theory (pQCD) when α_s is small enough. The second part requires detailed non perturbative information like how hadrons are built up out of quarks and gluons. Nevertheless, this part is not energy dependant and can be applied to all interation processes after having been measured in simple cases. Electron-proton scattering is a very fine method to test QCD because the electron is a well known electromagnetic probe.

3.1.1 *ep* Scattering and the Proton Structure Functions

In deep inelastic ep scattering the general expression of the differential cross section for the reaction $ep \rightarrow eX$ at the Born approximation in QED can be written in function of the structure functions $F_1(x, Q^2)$ and $F_2(x, Q^2)$:

$$\frac{d^2\sigma_{NC}^{ep}}{dxdQ^2} = \frac{4\pi\alpha_{em}^2}{xQ^4}\left(xy^2F_1(x, Q^2) + (1-y)F_2(x, Q^2)\right), \tag{3.1}$$

where α_{em} is the electromagnetic coupling constant. The quantities x, y and Q^2 are defined in subsection 1.2. The contributions from Z_0 exchange and from the interference terms between photon exchange and Z_0 exchange yield an additional structure function F_3. However, for $Q^2 < 1000$ GeV^2 those contributions are negligible ($m_Z^2 \mathrm{c}^4 \approx 8100$ GeV^2) and are therefore neglected in equation 3.1.
The differential cross section can also be written in function of the structure function $F_2(x, Q^2)$ and the longitudinal structure function $F_L(x, Q^2)$:

$$\frac{d^2\sigma_{NC}^{ep}}{dxdQ^2} = \frac{4\pi\alpha_{em}^2}{xQ^4}\left((1-y+\frac{y^2}{2})F_2(x,Q^2) - \frac{y^2}{2}F_L(x,Q^2)\right), \tag{3.2}$$

where $F_L(x, Q^2)$ is defined as:

$$F_L(x,Q^2) = F_2(x,Q^2) - 2xF_1(x,Q^2). \tag{3.3}$$

The structure functions is related to the cross section of the virtual photon with the proton $\sigma^{\gamma^* p}$ and the separated cross section $\sigma_\perp^{\gamma p}$ and $\sigma_\parallel^{\gamma p}$ corresponding to a transversely and longitudinally polarised photon:

$$F_L(x,Q^2) = \frac{Q^2}{4\pi^2\alpha_{em}}\sigma_\parallel^{\gamma p} \tag{3.4}$$

$$2xF_1(x,Q^2) = \frac{Q^2}{4\pi^2\alpha_{em}}\sigma_\perp^{\gamma p} \tag{3.5}$$

$$F_2(x,Q^2) = \frac{Q^2}{4\pi^2\alpha_{em}}(\sigma_\perp^{\gamma p} + \sigma_\parallel^{\gamma p}) = \frac{Q^2}{4\pi^2\alpha_{em}}\sigma^{\gamma p}. \tag{3.6}$$

The differential cross section then takes the following form:

$$\frac{d^2\sigma_{NC}^{ep}}{dxdQ^2} = \frac{\alpha_{em}}{xQ^2\pi}\left((1-y+\frac{y^2}{2})\sigma_\perp^{\gamma p} + (1-y)\sigma_\parallel^{\gamma p}\right). \tag{3.7}$$

In *ep* interaction, QCD factorisation leads to the decomposition of the proton structure functions F_1 and F_2.

The simplest factorisation is done in the Quark Parton Model (QPM) where no QCD hard scale process is considered. The quarks are point-like and defined as quasi free in the proton (all gluon initiated processes are neglected) and are represented by quark and antiquark distribution functions $q_i(x)$ and $\bar{q}_i(x)$ respectively. In this formalism the function F_2 is written as:

$$F_2(x) = \sum_{i=1}^{n_f} e_i^2 x\left(q_i(x) + \bar{q}_i(x)\right), \tag{3.8}$$

where the sum $i = 1, ..., n_f$ runs over all active quark flavours ordered by increasing quark masses. The idea of F_2 scaling behaviour (i.e. F_2 depends only on x) was proposed by Bjorken in the limit of Q^2 and $\nu = (E_e - E_e')^{\gamma p}$ approaching infinity [19]. It was first observed in deep inelastic electron-proton scattering experiments at SLAC [20].

In the QPM model the virtual photon is exchanged between the electron and an on-shell massless spin 1/2 quark. This results in a vanishing cross section for longitudinally polarised photon $\sigma_{\parallel}^{\gamma p} = 0$ and is expressed in the Callan-Cross relationship:

$$F_L(x) = F_2(x) - 2xF_1(x) = 0. \tag{3.9}$$

The evidence of non free quarks in the proton is modelled in the DIS scheme where all QCD orders are contained in the long range quark distribution functions $q_i(x, Q^2)$ and where F_2 keeps the same form as in the Quark Parton Model:

$$F_2(x, Q^2) = \sum_{i=1}^{n_f} e_i^2 x \left(q_i(x, Q^2) + \bar{q}_i(x, Q^2) \right). \tag{3.10}$$

Experimentally at a fixed value of x the Q^2 dependence of F_2 can be observed by increasing Q^2. Indeed, when Q^2 rises, the electron probe can distinguish finer and finer fluctuations within the proton. From the F_2 measurement at HERA it can be seen that the smaller the fractional proton momentum x the earlier the Q^2 dependence appears.

As soon as the leading order is considered in pQCD, each quark is no longer considered as free but surrounded by a cloud of partons. F_2 will therefore also be directly connected to the gluon density in the proton. The structure function F_2 is then the sum over all quarks, antiquarks and gluon of the convolution of the coefficient functions $C^{V,i}$ and the parton distribution functions f_i ($f_i = q_i$ for quarks and $f_{n_f+1} = g$ for gluon):

$$F_2(x, Q^2) = \sum_{i=1}^{n_f+1} \int_x^1 C^{V,i}(x/x', Q^2/\mu_R^2, \mu_F^2, \alpha_s) f_i(x', \mu_R^2, \mu_F^2, \alpha_s) dx'. \tag{3.11}$$

The scale μ_F is known as the factorisation scale and defines the boundary between the perturbative ($\alpha_s(\mu_F^2) \ll 1$) and the non-perturbative QCD regimes. For $Q^2 \geq \mu_F^2$, pQCD can be applied. The hard interaction part is factorised in the coefficient function $C^{V,i}$. The function $C^{V,i}$ describes how a parton i with fractional proton momentum x evolves from pQCD radiative processes (via the exchange of virtual partons) out of the initial parton with fractional proton momentum x'. Nowadays most of the pQCD calculations are performed at the leading order (LO) or at the next to leading order (NLO). All non calculated higher orders are absorbed in the parton density functions. When $Q^2 \leq \mu_F^2$ pQCD does not hold and all QCD orders are then absorbed in the parton density functions. The renormalisation scale μ_R is present in every perturbative theory [21]. In pQCD, when calculating the $(\alpha_s)^n$ coefficients, various divergencies arise. These divergencies must be regulated via a particular renormalisation scheme which requests the introduction of the mass scale μ_R. The renormalisation scale depends on the chosen renormalisation scheme. The renormalisation procedure also affects our way to look at the strong coupling constant. Here we deal with the effective QCD coupling constant, a renormalised running coupling constant with scale dependence controlled by the renormalisation group equation:

$$\mu \frac{\partial \alpha_s}{\partial \mu} = \alpha_s \left(-\frac{\beta_0}{2\pi} \alpha_s - \frac{\beta_1}{4\pi^2} \alpha_s^2 - \frac{\beta_2}{64\pi^3} \alpha_s^3 - ... \right). \tag{3.12}$$

Only the first two coefficients (β_0, β_1) are independent of the choice of the renormalisation scheme as shown below:

$$\begin{aligned} \beta_0 &= 11 - \ 2/3 \, n_f & (3.13) \\ \beta_1 &= 51 - \ 19/3 \, n_f, & (3.14) \end{aligned}$$

where n_f is the number of active flavours (number of quarks with mass smaller than μ). Usually μ is chosen to be the typical energy scale of the hard process.

To completely solve the differential equation of α_s a constant of integration is introduced. This constant is determined from experiment and is chosen to be the value of α_s at a fixed reference scale. The preferred reference scale is the Z_0 boson mass m_Z. For example, at the leading order this gives:

$$\alpha_s(\mu^2) = \frac{\alpha_s(m_Z^2 c^4)}{1 - \beta_0 \dfrac{\alpha_s(m_Z^2 c^4)}{4\pi} \ln\left(\dfrac{\mu^2}{m_Z^2 c^4}\right)}. \tag{3.15}$$

An other way to take into account the integration constant is to introduce the dimensional parameter $\Lambda_{QCD}^{(n_f)}$. The parameter $\Lambda_{QCD}^{(n_f)}$ always depends on n_f and for higher order also on the renormalisation scheme. One of the most used way is to write a solution of equation 3.12 as an expansion of inverse power of $\ln(\mu^2)$ as shown in the following equation:

$$\begin{aligned} \alpha_s(\mu^2) = \frac{4\pi}{\beta_0 \ln(\mu^2/\Lambda_{QCD}^{(n_f)\,2})} \Bigg[1 &- \frac{2\beta_1}{\beta_0^2} \frac{\ln[\ln(\mu^2/\Lambda_{QCD}^{(n_f)\,2})]}{\ln(\mu^2/\Lambda_{QCD}^{(n_f)\,2})} + \frac{4\beta_1^2}{\beta_0^4 \ln^2(\mu^2/\Lambda_{QCD}^{(n_f)\,2})} \\ &\times \left((\ln[\ln(\mu^2/\Lambda_{QCD}^{(n_f)\,2})] - \frac{1}{2})^2 + \frac{\beta_2 \beta_0}{8\beta_1^2} - \frac{5}{4} \right) \Bigg]. \end{aligned} \tag{3.16}$$

Here $\Lambda_{QCD}^{(n_f)}$ can be interpreted as the strength of the strong coupling constant (α_s increases to infinity when Q^2 approaches $\Lambda_{QCD}^{(n_f)}$). This solution nicely illustrates the asymptotic freedom property of QCD.

At the leading order it reduces to:

$$\begin{aligned} \alpha_s(\mu^2) &= \frac{4\pi}{\beta_0 \ln\left(\mu^2/\Lambda_{QCD}^{(n_f)\,2}\right)} & (3.17) \\ \ln(\Lambda_{QCD}^{(n_f)\,2}) &= \ln(m_Z^2 c^4) - \frac{4\pi}{\beta_0 \alpha_s(m_Z^2 c^4)}. & (3.18) \end{aligned}$$

3.1.2 The DGLAP Equations

The first calculation of the structure function in equation were done in the beginning of the seventies by V.N. Gribov, L.N. Lipatov, G. Altarelli and G. Parisi (GLAP). The non perturbative part in equation 3.11 is represented by the parton densities noted $f_i(x', \mu_R^2, \mu_F^2, \alpha_s(Q^2))$. The pQCD part is treated like a power series in α_s which is justified when $\alpha_s(Q^2) \ll 1$. Unfortunately the LO QCD calculation shows an $\ln(Q^2)$ dependence in the $\alpha_s(Q^2)$ coefficient term. This rules out the use of power series in $\alpha_s(Q^2)$ because the smallness of $\alpha_s(Q^2)$ is compensated by the large size of $\ln(Q^2)$ ($\alpha_s(Q^2)\ln(Q^2) \approx 1$). To solve this problem, the $\ln(Q^2)$ can be absorbed (factorised) into modified parton distributions:

$$C^{V,i}(x/x', Q^2/\mu_R^2, \mu_F^2, \alpha_s) = C^{V,i}(x/x', \ln\left(\frac{Q^2}{\mu_R^2}\right), \mu_F^2, \alpha_s) \quad\rightarrow\quad C^{V,i}_{\gamma q\rightarrow q}(x/x') \tag{3.19}$$

$$f_i(x', \mu_R^2, \mu_F^2, \alpha_s) \quad\rightarrow\quad q_i(x', \ln\left(\frac{Q^2}{\mu_R^2}\right), \alpha_s). \tag{3.20}$$

The factorisation is possible because the $\ln(Q^2)$ divergency (also known as collinear singularity) has a universal character in the way that it is independent of the high energy interactions. This procedure is in fact similar to the renormalisation procedure of the strong coupling constant since finally not only the LO collinear singularity is absorbed but also all $(\alpha_s(Q^2)\ln(Q^2))^n$. At the LO in α_s the same formalism is kept as it is in the simple Quark Parton Model. But the parton distributions have now a dynamical behaviour also called parton evolution which is determined by the pQCD calculations. The Q^2 dependence of F_2 at fixed x, also known as F_2 scaling violation, is entirely contained in the parton density function. This gives a better understanding of what happens when Q^2 increases, namely the quark densities are shifted to lower x because of the coupling $g \rightarrow q\bar{q}$. The first signs of F_2 scaling violation were observed in the middle of the seventies in muon-hadron and neutrino hadron scattering at Fermilab [22] and in electron-proton scattering at SLAC [23]. The Q^2 evolution of the parton density functions is then fixed by the DGLAP[1] evolution equations [24] at the LO in α_s:

$$\begin{aligned} q_i(x,Q^2,\alpha_s(Q^2)) = \quad & q_i(x,Q_0^2) \quad + \\ \frac{\alpha_s(Q^2)}{2\pi}\int\limits_x^1 \frac{dx'}{x'}\Bigg(\quad & q_i(x',Q_0^2) \quad P_{qq}\left(\frac{x}{x'}\right) + g(x',Q_0^2)P_{qg}\left(\frac{x}{x'}\right)\Bigg)\ln\left(\frac{Q^2}{Q_0^2}\right) \\ g(x,Q^2,\alpha_s(Q^2) \quad = \quad & g(x,Q_0^2) \quad + \\ \frac{\alpha_s(Q^2)}{2\pi}\int\limits_x^1 \frac{dx'}{x'}\left(\sum_{i=1}^{n_f}\right. & \left.(q_i(x',Q_0^2)+\bar{q}_i(x',Q_0^2))P_{gq}\left(\frac{x}{x'}\right) + g(x',Q_0^2)P_{gg}\left(\frac{x}{x'}\right)\right)\ln\left(\frac{Q^2}{Q_0^2}\right). \end{aligned} \tag{3.21}$$

These equations relate the parton distribution at the scale Q^2 to the parton distribution at the scale Q_0^2 where $\alpha_s(Q_0^2) < 1$. To get a prediction of F_2 one needs to parametrise the parton densities at the single input scale Q_0^2. The scale Q_0^2 can be considered as the final factorisation scale. When $Q^2 \approx Q_0^2$ the quark are quasi free. When Q^2 is larger than Q_0^2, pQCD can be applied and appears in the $\ln(Q^2)$ dependence of the parton density functions.

The splitting functions P_{ab} give the probability that a parton a with fractional proton longitudinal momentum x' will radiate a parton b with fractional proton longitudinal momentum x. The ratio x/x' is the fraction of the longitudinal momentum of the parton a carried by the parton b. The splitting functions are the results of the pQCD calculations

---

[1] Dokshitzer, Gribov, Lipatov, Altarelli, Parisi.

and so far they have been determined up to the NLO in α_s [25].
However, a hidden problem appears for very small x where P_{gg} grows as x'/x. This brings a second dominant term of the form $\ln(1/x)$ in the coefficient of α_s. Therefore, in the DGLAP approach x must be sufficiently large to ensure that $\ln(Q^2)$ remains the only dominant term in the coefficient of α_s and thus represents the only divergency which needs to be "resummed" in the parton densities. This condition is known as the collinear Leading Logarithmic Approximation (LLA) or LLA in $\ln(Q^2)$ and is represented by the following relations:

$$\begin{aligned} \alpha_s(Q^2) &\ll 1 \\ \alpha_s(Q^2)\ \ln(Q^2) &\approx 1 \\ \alpha_s(Q^2)\ln(1/x) &\ll 1. \end{aligned} \tag{3.22}$$

With the increase of the centre of mass energy available at high energy colliders a new perturbative regime opens up where the leading $\ln(Q^2)$ approximation might show its limits. However, up to now the NLO DGLAP evolution formalism is able to describe the F_2 data down to the smallest x value observed ($x \approx 5 \cdot 10^{-5}$ for $Q^2 \approx 2$ GeV^2, see figure 1.2) with an appropriate choice of the input parton distributions [26] [27] .
The DGLAP formalism at the LO is equivalent to "resumming" ladder diagrams (figure 3.1) whose rungs are strongly ordered in transverse momenta [28]:

$$\begin{gathered} Q^2/\mathrm{c}^2 \gg k_{\perp n}^2 \gg ... \gg k_{\perp 2}^2 \gg k_{\perp 1}^2 \\ x < x_n < ... < x_2 < x_1, \end{gathered} \tag{3.23}$$

where $k_i = (\vec{k}_{\parallel i} + \vec{k}_{\perp i}, E_i^{int}/\mathrm{c})$ is the four-momentum of the intermediary parton i in the ladder and the scalar $k_{\perp i}$ represents the norm of its transverse momentum $k_{\perp i} = |\vec{k}_{\perp i}|$.

3.1.3 The BFKL Equations

At very low x and low Q^2 the $\ln(Q^2)$ term is no longer the divergent part in the coefficient of α_s. In this case the divergency comes from the $\ln(1/x)$ term and (3.22) becomes:

$$\begin{aligned} \alpha_s(Q^2) &\ll 1 \\ \alpha_s(Q^2)\ \ln(Q^2) &\ll 1 \\ \alpha_s(Q^2)\ln(1/x) &\approx 1. \end{aligned} \tag{3.24}$$

The "resummation" of the $(\alpha_s \ln(1/x))^n$ terms independently of Q^2 was developed in the BFKL[2] theory [29]. Gluon ladders are considered with strong ordering in longitudinal momenta and soft ordering in transverse momenta:

$$\begin{gathered} Q^2/\mathrm{c}^2 > k_{\perp n}^2 > ... > k_{\perp 2}^2 > k_{\perp 1}^2 \\ x \ll x_n \ll ... \ll x_2 \ll x_1. \end{gathered} \tag{3.25}$$

---

[2] Balitsky, Fadin, Kuraev, Lipatov.

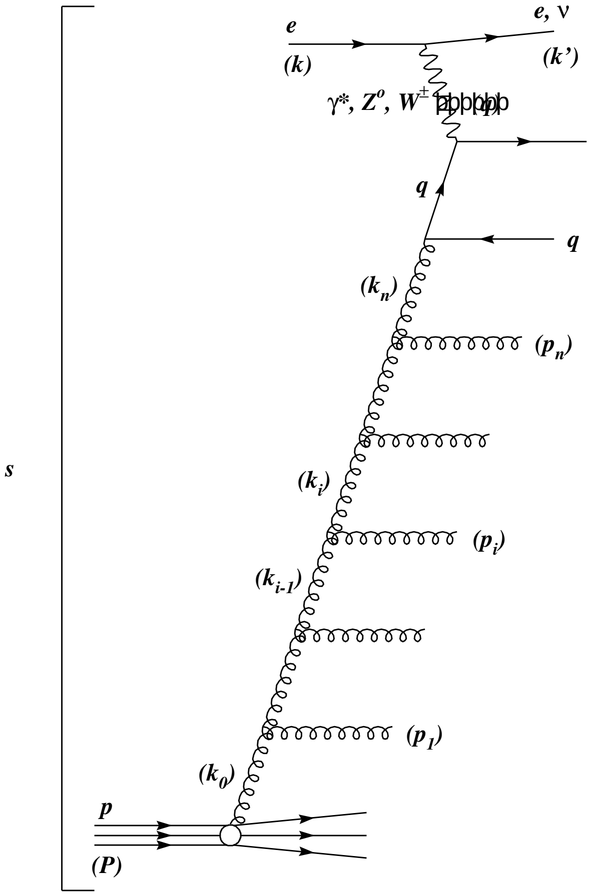

$$\begin{aligned} \vec{k}_{\parallel i} &= x_i \vec{P} \\ &= z_i \vec{k}_{\parallel i-1} = z_i x_{i-1} \vec{P} \\ \rightarrow &\qquad x_i = z_i x_{i-1} \end{aligned}$$

$$\begin{aligned} \vec{p}_{\parallel i} &= y_i \vec{P} \\ &= \vec{k}_{\parallel i-1} - \vec{k}_{\parallel i} = x_{i-1}\vec{P} - z_i x_{i-1}\vec{P} \\ \rightarrow &\qquad y_i = (1 - z_i) x_{i-1} \end{aligned}$$

Figure 3.1: Schematic representation of a ladder diagram for *ep* scattering. The t-channel intermediary gluon i carries the momentum $k_i = (\vec{k}_{\parallel i} + \vec{k}_{\perp i}, E_i^{int}/\mathrm{c})$ and the emitted gluon i carries the momentum $p_i = (\vec{p}_{\parallel i} + \vec{p}_{\perp i}, E_i^{emi}/\mathrm{c})$. The parameter x_i is the fraction of longitudinal proton momentum carried by the exchanged gluon i and y_i is the fraction of longitudinal proton momentum carried by the emitted gluon i. The longitudinal momentum transfer between the exchange gluons $i-1$ and i is given by z_i.

This results in the BFKL evolution equation [29] which fixes the x evolution of the the unintegrated gluon distribution $\mathcal{F}(x, k_\perp^2, Q_0^2)$. The unintegrated gluon distribution can be related to the conventional DGLAP gluon distribution as follow:

$$xg(x, Q^2) = \int_0^{Q^2} \mathcal{F}(x, k_\perp^2, Q_0^2) \frac{dk_\perp^2}{k_\perp^2}. \tag{3.26}$$

The region of very low x and low Q^2 could be reached for the first time at HERA experiments ZEUS and H1 (see figure 1.2). Although there exists some reasonable agreement with the F_2 data [30], the BFKL approach results in a diffusion phenomena on the transverse momentum transfer $k_\perp$ which turns out in an unreliable description of inclusive quantities like the structure function F_2 [31]. Moreover recent work on BFKL in the NLO approximation has shown that the corrections to the LO are large [32], reducing the predicted rise of F_2. The stability of the BFKL perturbative expansion is still under study.

3.1.4 The CCFM Equations

In the intermediary region where

$$\begin{aligned} \alpha_s(Q^2) &\ll 1 \\ \alpha_s(Q^2)\ \ln(Q^2) &\approx 1 \\ \alpha_s(Q^2)\ln(1/x) &\approx 1 \end{aligned} \tag{3.27}$$

both logarithms yield divergencies and have therefore to be taken into account. This approach is called double leading logarithmic approximation (DLLA). A general treatment of the gluon ladder within the DLLA is given by the CCFM[3] equation [33] which is based on an angular ordering of the gluon emission:

$$\xi_0 < \xi_1 < ... < \xi_n, \tag{3.28}$$

where ξ_i is connected to the angle of the emitted gluon i with respect to the incoming proton. The definition of ξ_i comes from the Sudakov decomposition of the four-vector p_i of the emitted gluon:

$$p_i = (\vec{p}_{\|i} + \vec{p}_{\perp i}, E_i^{emi}/\mathrm{c}) = \tilde{y}_i(P + \xi_i k) + \bar{p}_{\perp i}, \tag{3.29}$$

where P and k are the four-vectors of the incident proton and electron respectively and $\bar{p}_{\perp i} = (\vec{p}_{\perp i}, 0)$. The emitted gluons are considered to be massless therefore:

$$p_i^2 = 2\tilde{y}_i^2 \xi_i P \cdot k + \bar{p}_{\perp i}^2 = \tilde{y}_i^2 \xi_i s - \vec{p}_{\perp i}^2 = 0 \quad \text{which gives} \quad \xi_i = \frac{\vec{p}_{\perp i}^2 \mathrm{c}^2}{\tilde{y}_i^2 s} = \frac{p_{\perp i}^2 \mathrm{c}^2}{\tilde{y}_i^2 s}, \tag{3.30}$$

where the proton and electron masses are neglected. The scalar $p_{\perp i}$ is defined as follows:

$$p_{\perp i} = -\sqrt{\bar{p}_{\perp i}^2} = |\vec{p}_{\perp i}|. \tag{3.31}$$

The scalar $\tilde{y}_i$ is related to the fraction of the longitudinal proton momentum y_i carried by the emitted parton i:

$$\tilde{y}_i = \frac{y_i}{1 + \dfrac{p_{\perp i}^2 \mathrm{c}^2}{y_i^2 4 E_p^2}}. \tag{3.32}$$

When $p_{\perp i} \to 0$ the scalar $\tilde{y}_i$ becomes equal to y_i.
Usually the angular ordering (see equation 3.28) is equivalent to the following condition on the rescaled transverse momentum $q_{\perp i}$:

$$z_{i-1} q_{\perp i-1} < q_{\perp i}, \tag{3.33}$$

where z_i is defined in figure 3.1 and $q_{\perp i}$ is given by:

$$q_{\perp i} = x_{i-1}\sqrt{s\xi_i} = \frac{p_{\perp i}}{1 - z_i}. \tag{3.34}$$

---

[3] Ciafaloni, Catani, Fiorani, Marchesini.

In the CCFM formalism the $\ln(Q^2)$ and $\ln(1/x)$ are "resummed" in the parton densities therefore it is forseen to be valid for all values of x and Q^2. Indeed, when one of the two logarithms become negligible one can still take all its power into account. For $x \to 0$ the CCFM evolution equation is equivalent to the BFKL evolution equation and for large x it reproduces the standard DGLAP equations. Finally the CCFM evolution equation of the non integrated gluon distribution $\mathcal{A}(x, k_\perp^2, q_\perp)$ are written in an integral form as:

$$\begin{aligned}\mathcal{A}(x, k_\perp, q_{\perp max}) = \quad & \mathcal{A}^0(x, k_\perp, q_{\perp max}) \quad + \\ \int\limits_x^1 \frac{dx'}{x'} \int\limits_0^{q_{\perp max}} \frac{dq_\perp^2}{\pi q_\perp^2} & \Theta(q_{\perp max} - \frac{x}{x'} q_\perp) \Delta_s(q_{\perp max}, \frac{x}{x'} q_\perp) \tilde{P}(\frac{x}{x'}, q_\perp, k_\perp) \mathcal{A}(x', k'_\perp, q_\perp),\end{aligned} \tag{3.35}$$

where $k'_\perp = |\vec{k}'_\perp| = |\vec{k}_\perp + \vec{p}_\perp| = |\vec{k}_\perp + (1-z)\vec{q}_\perp|$ and where $q_{\perp max}$ corresponds to the maximum angle allowed for any emission. The latter is in fact the angle at the photon side end of the ladder because of the equivalent orderings:

$$\begin{gathered}\xi_{max} > \xi_n > \dots > \xi_1 \\ q_{\perp max} > z_n q_{\perp n}, \; \dots \; , \; q_{\perp 2} > z_1 q_{\perp 1}.\end{gathered}$$

The CCFM evolution equation, depending on the choice of Δ_s and $\tilde{P}$, allows several solutions for the unintegrated gluon density $\mathcal{A}(x, k_\perp, q_{\perp max})$. There exist succesfull fits to a wide range of F_2 data using the CCFM formalism [35].

3.2 Charm in Electron-Proton Scattering

The discovery of the charm quark played an important role in the elaboration and in the consolidation of the Standard Model. Since then, charm physics continues to contribute in the understanding of the physics of elementary particles. Experimentally only charmed hadrons can be observed via their decay particles. The observation of charm is therefore split in three different steps, first the production of charm quarks, then the transition from charm quarks to charmed hadrons known as charm fragmentation and finally the decay of charmed hadrons. Studying one of those steps requires a perfect knowledge of the two others. This section will highlight how charm production in electron-proton scattering is described within pQCD. A second part will give an overview on charm fragmentation.

3.2.1 Charm Production

Four main approaches exist to answer the question: how is charm production in electron-proton scattering considered within QCD?

The Massive Approach

In the massive approach there are three active flavours (u, d, s) in the proton. The charm quark is considered as massive and is produced at the perturbative level in QCD.

In this approach the dominant pQCD process is the boson-gluon fusion (BGF) in which a $c\bar{c}$ pair is produced (see figure 3.3). The proton structure function is then split as follow:

$$F_2(x,Q^2) = \sum_{i=1}^{n_f=3} e_i^2 x \left(q_i(x,Q^2) + \bar{q}_i(x,Q^2)\right) + F_2^c, \tag{3.36}$$

where at the LO in α_s:

$$F_2^c = \frac{Q^2\alpha_s}{4\pi m_c^2 \mathrm{c}^4} \int_{x_{min}}^{1} \frac{dx'}{x'} e_c^2 g(x_g,\mu^2) C_{2,g}^0(\frac{x}{x'}, Q^2, m_c^2, \mu^2). \tag{3.37}$$

The charm contribution F_2^c to the structure function F_2 is the convolution of the gluon density $g(x_g,\mu^2)$ and the coefficient function $C_{2,g}^0$. This later corresponds to the cross section of the BGF process in the photon-gluon system. The lower boundary of the integration x_{min} is given by $x(Q^2+4m_c^2\mathrm{c}^4)/Q^2$. The massive approach is valid for $Q^2 \approx m_c^2\mathrm{c}^4$. It breaks down for $Q^2 \gg m_c^2\mathrm{c}^4$ where the term $\ln(Q^2/m_c^2\mathrm{c}^4)$ is not anymore negligible. As the number of active flavours is fixed, the massive approach is defined as Fixed Flavour Number Scheme.

The Massless Approach

In the massless approach or Flavour Excitation approach, four active flavours (u, d, s, c) are considered in the proton. Like for the light quarks, the charm mass is neglected. The charm quark is then treated as the fourth active flavour in the proton. As a consequence, charm will be described by a parton density and it can initiate a hard scattering. The decomposition of the proton structure function is then quite obvious:

$$F_2(x,Q^2) = \sum_{i=1}^{n_f=4} e_i^2 x \left(q_i(x,Q^2) + \bar{q}_i(x,Q^2)\right) = \sum_{i=1}^{3} e_i^2 x \left(q_i(x,Q^2) + \bar{q}_i(x,Q^2)\right) + F_2^c. \tag{3.38}$$

This approach is also done in the Fixed Flavour Number Scheme and is appropriate for $Q^2 \gg m_c^2\mathrm{c}^4$.

The Variable Flavour Number Scheme Approach

The Variable Flavour Number Scheme approach does the matching between the two previous approaches. Until now only the total cross section and inclusive F_2^c are predicted by calculations within the Variable Flavour Number Scheme approach [34]. Recently also differential charm cross section predictions were published [36].

Intrinsic Charm

An alternative mechanism for charm production is intrinsic charm production [37] which is introduced to explain some special features of charm at large x. In this approach a $c\bar{c}$ pair is considered as a non perturbative component in the proton bound state. The proton wave function $|uuc\bar{c}\rangle$ contains a small, but finite probability for a quantum fluctuation into two valence charm quarks.

The kinematic range of the present analysis (1 GeV^2 $< Q^2 <$ 100 GeV^2) lies within the massive approach validity scope.

3.2.2 Charm Fragmentation

The final hadron formation, starting with partons and usually after taking into account initial and final state QED and QCD radiations, is called fragmentation. The fragmentation processes are characterised by small momentum transfers ensuing the failure of perturbative QCD. These processes are usually described with the help of the fragmentation function $D_q^h(Z_h)$ which represents the unnormalised probability density for a quark q to produce a hadron h where the variable Z_h is defined as:

$$Z_h = \frac{E_h + |\vec{p}_{h\|q}|\mathrm{c}}{E_q + |\vec{p}_q|\mathrm{c}}. \tag{3.39}$$

The variable Z_h has the advantage to be invariant under any boost parallel to the initial quark direction. There exist several parametrisations of the fragmentation function.

Only rarely do the light hadrons in a jet contain the primary quark. Therefore, the differential hadron production cross section is related to the fragmentation functions of all quarks through a set of rather complicated equations (ref). In the case of hadron production containing a heavy quark Q, the heavy quark is necessarily the primary quark because the probability of extracting a $Q\bar{Q}$ pair during the fragmentation is very small. Therefore, the cross section of heavy-flavoured particles is directly related to the unique fragmentation function $D_Q^h(Z_h)$ [38].

Electron-Positron Collision

A short overview of charm fragmentation observed at electron-positron colliders is given below because the data allow a detailed and direct experimental investigation of the fragmentation process and a decisive confrontation with models. In electron-positron collision, charm production via s-channel (the boson mediator momentum squared is $(p_{e^-} + p_{e^+})^2\mathrm{c}^2 = s = 4E_{beam}^2$) results in the ideal case where at the leading order the laboratory frame is the centre of mass of the $c\bar{c}$ system (see figure 3.2). In other words, at the leading order, both charm quarks have the energy of the beam $E_{beam} = \sqrt{s}/2$ respectively. When D mesons are observed in e^+e^- the quantity Z_D (see equation 3.39) is then approximated by the experimentally accessible quantity x_{pD} or x_{ED} defined as:

$$x_{pD} = \frac{|\vec{p}_D|}{|\vec{p}_{Dmax}|}, \tag{3.40}$$

$$x_{ED} = \frac{E_D}{E_{beam}}, \tag{3.41}$$

where E_D is the D meson energy, $\vec{p}_D$ its momentum and $|\vec{p}_{Dmax}|\mathrm{c} = \sqrt{E^2_{beam} - m^2_D \mathrm{c}^4}$. The inclusive differential D meson cross section $(1/\sigma) \cdot d\sigma/dZ_D$ measured in the laboratory frame, after correction for higher states cascades and QED and QCD radiative effects, describes the genuine fragmentation function $D^D_c(Z_D)$ of the charm in a D meson.

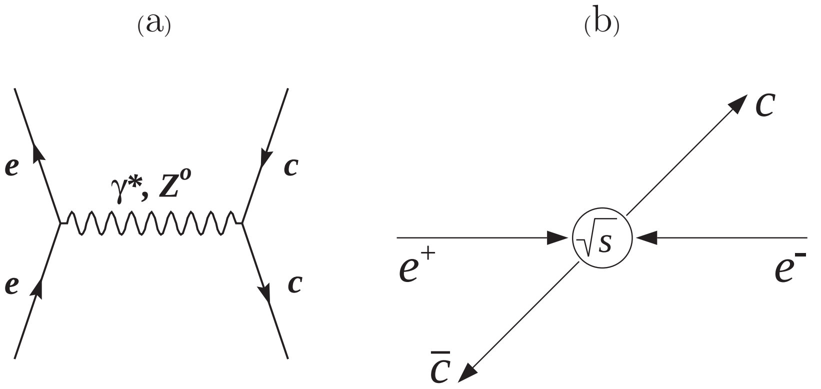

Figure 3.2: (a) Generic Feynman diagram and (b) configuration in the laboratory rest frame of charm production in the case of electron-positron collisions.

At CLEO and ARGUS experiments the D meson cross sections have been measured as a function of the heavy quark fragmentation variable x_{pD} at $\sqrt{s} \approx 10$ GeV for inclusive D^0 and D^{*+}. The experimental data were fitted with the Peterson fragmentation function [39]:

$$D^D_c(Z_D) = \frac{1}{Z_D \left[1 - \frac{1}{Z_D} - \frac{\epsilon}{1 - Z_D}\right]^2}. \tag{3.42}$$

Here ϵ is a free parameter. The combined fit of the two experiments gives [40]:

$$\epsilon(D^0) = 0.135 \pm 0.010$$
$$\epsilon(D^{*+}) = 0.078 \pm 0.008.$$

The fits have been performed within the Monte Carlo scheme in which the charm quarks are first subject to parton showers in order to take into account QCD radiation before applying the fragmentation function. No corrections for higher states were performed, thus the direct fit of the D^0 spectrum results in a higher value of ϵ.

The experiments DELPHI [41] and ALEPH [42] at LEP have performed the same measurement for $\sqrt{s} = 90$ GeV:

$$\langle x_{ED^*} \rangle = 0.504 \pm 0.009, \quad \epsilon(D^{*+}) = 0.0372 \pm 0.0014 \quad \text{(DELPHI)}$$
$$\langle x_{ED^*} \rangle = 0.488 \pm 0.008, \quad \epsilon(D^{*+}) = 0.0339 \pm 0.0037 \quad \text{(ALEPH)}.$$

However, the value of $\epsilon(D^{*+})$ has to be taken cautiously as it depends on the choice of the Monte Carlo scheme for the parton shower, on the choice of Λ_{QCD} and on the beauty contribution ($b \to c \to D^{*+}$). Therefore, the lower $\langle x_{ED^*} \rangle$ value measured at ALEPH does not correspond to a higher value of ϵ. The fits performed by the DELPHI collaboration shows that the value of ϵ is stable against different models of the QCD radiative corrections.

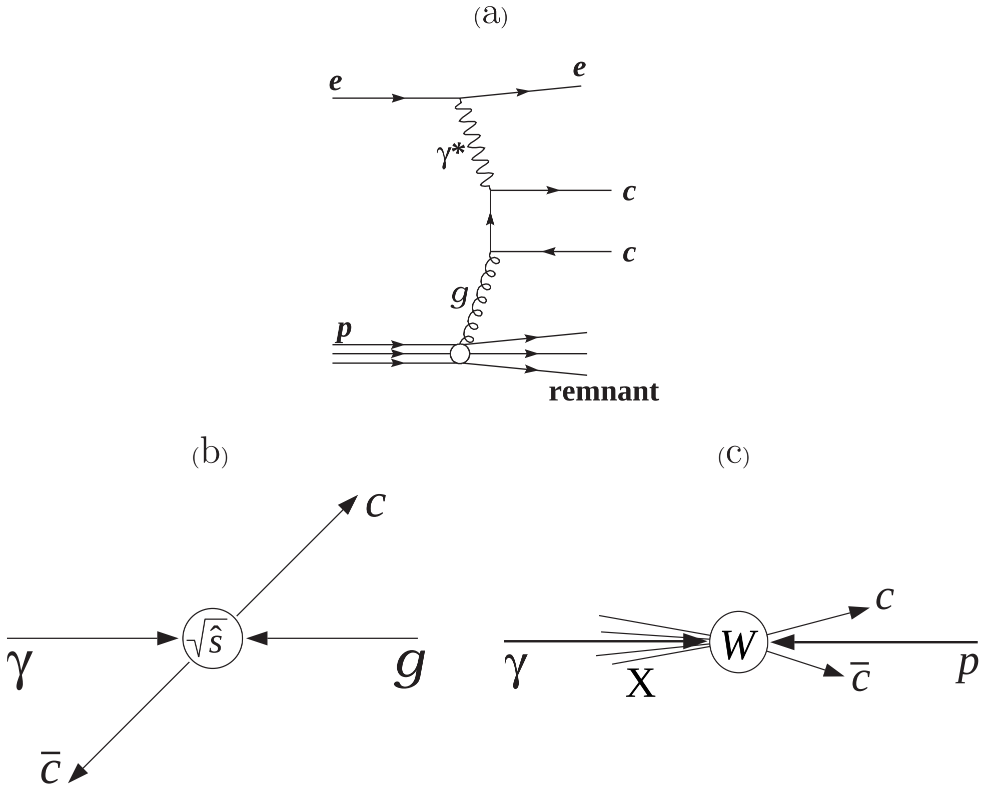

Figure 3.3: (a) Feynman diagram for ep scattering in case of boson-gluon fusion (BGF), (b) configuration of the BGF process in the γg rest frame and (c) configuration of the photon-proton interaction in the γp rest frame.

Electron-Proton Scattering

In electron-proton scattering, charm production occurs via t-channel (the boson mediator momentum squared is $(p_{e'} - p_e)^2\mathrm{c}^2 = t = -Q^2$) and is dominated by the boson-gluon fusion process (see figure 3.3). In this representation the most appropriate frame is the boson-proton centre of mass system noted by γp (figure 3.3.(c)) which is also commonly called hadronic system. The boson-gluon frame stays inaccessible to the experiment although it is the frame where the kinematics is the simplest (figure 3.3.(b)). There the two quarks are back to back and both carry half of the boson-gluon centre of mass energy $\hat{s}$. The sum of the two quarks momenta is obviously zero:

$$\vec{p}_c^{\,\gamma g} + \vec{p}_{\bar{c}}^{\,\gamma g} = 0. \tag{3.43}$$

This is also verified in the boson-proton frame (part c), figure 3.3) but only for the transverse quark momenta with respect to the γp axis:

$$\vec{p}_{\perp c}^{\,\gamma p} + \vec{p}_{\perp \bar{c}}^{\,\gamma p} = 0. \tag{3.44}$$

This holds because the boost from the boson-gluon frame to the boson-proton frame is parallel to the gluon momentum, assuming $\vec{p}_g = x_g \cdot \vec{p}_p$. Therefore, the transverse momenta of the two quarks are conserved.

Moreover, in this frame, the two $c\bar{c}$ quarks share only half of the centre of mass energy W, the other half is taken by the proton remnant (see appendix B).
In a similar way as in electron-positron collision the variable x_D is defined by:

$$x_D = \frac{|\vec{p}_D^{\,\gamma p}|\mathrm{c}}{W/2}, \tag{3.45}$$

where $\vec{p}_D^{\,\gamma p}$ is the momentum of the D meson in the γp frame.
The energy squared of the γp system is given by:

$$W^2 = (q+P)^2\mathrm{c}^2 = -Q^2 + 2E_\gamma^{\gamma p} \cdot E_p^{\gamma p} + 2\sqrt{(E_\gamma^{\gamma p})^2 + Q^2} \cdot E_p^{\gamma p}. \tag{3.46}$$

In the case where Q^2 can be neglected (for example 10 GeV^2 $< Q^2 <$ 100 GeV^2 results in $(Q^2)_{mean} \approx 25$ GeV^2, $(E_\gamma^{\gamma p})^2_{mean} \approx 3745$ GeV^2 and $(E_p^{\gamma p})^2_{mean} \approx 3720$ GeV^2), the quantities W and x_D can be approximated by:

$$W \approx 2E_p^{\gamma p} = 2|\vec{P}^{\,\gamma p}|\mathrm{c}, \qquad x_D \approx \frac{|\vec{p}_D^{\,\gamma p}|}{|\vec{P}^{\,\gamma p}|}. \tag{3.47}$$

In appendix B it is shown that $m_{c\bar{c}}$ and m_X are negligible in the γp system and therefore half of the γp energy is distributed among the two charm quarks. Thus it makes sense to define x_c and $x_{\bar{c}}$:

$$x_c = \frac{|\vec{p}_c^{\,\gamma p}|\mathrm{c}}{W/2}, \qquad\qquad x_{\bar{c}} = \frac{|\vec{p}_{\bar{c}}^{\,\gamma p}|\mathrm{c}}{W/2}, \tag{3.48}$$

so that x_c ($x_{\bar{c}}$) represents the fraction of $W/2$ carried by the c ($\bar{c}$) quark and satisfies:

$$x_c + x_{\bar{c}} \approx 1. \tag{3.49}$$

The D^* inclusive normalised differential cross section $1/\sigma\ d\sigma/dx_D$ measured in the γp frame is then the convolution integral of the charm production spectrum $\Phi^{\gamma p}(x_c)$ with the genuine fragmentation function $D_c(Z_D)$:

$$1/\sigma\ d\sigma/dx_D = \int_{x_D}^{1} \Phi^{\gamma p}(x_c) D_c(Z_D)\, dx_c, \tag{3.50}$$

where $Z_D \approx x_D/x_c$ is the fraction of the charm energy carried by the meson D. At HERA the average momentum in the γp frame of the quark and of the fragmentated D meson amounts to 10 GeV/c and the D meson transverse momentum with respect to the charm direction is negligible, therefore:

$$Z_D = \frac{E_D^{\gamma p} + |\vec{p}_{D\|c}^{\,\gamma p}|\mathrm{c}}{E_c^{\gamma p} + |\vec{p}_c^{\,\gamma p}|\mathrm{c}} \approx \frac{E_D^{\gamma p}}{E_c^{\gamma p}} \approx \frac{|\vec{p}_D^{\,\gamma p}|}{|\vec{p}_c^{\,\gamma p}|} = \frac{x_D}{x_c}. \tag{3.51}$$

The value of Z_D varies from x_D (when $x_c = 1$) to 1 (when $x_c = x_D$). Note that the quantity Z_D is different from $z_D = \dfrac{P \cdot p_D}{P \cdot q} = \dfrac{E_D - p_{D\|}\mathrm{c}}{2yE_e} \approx x_D$ which is often used instead of x_D. The charm production spectrum $\Phi^{\gamma p}(x_c)$ is given by the differential cross section in the γp frame $d\sigma(\gamma g \to c\bar{c})/dx_c$.

Unlike electron-positron collision where monochromatic charm quarks are produced, the charm quarks produced in electron-proton scattering have a broad energy spectrum which is moreover inaccessible to the experiment. Therefore, the modelisation of the fragmentation in *ep* scattering is one of the biggest theoretical systematic error in the estimation of the measured absolute D^* cross section via efficiency calculations. Moreover the uncertainty in the fragmentation process brings an uncertainty in the theoretical predictions which will be confronted to the measurement. This makes difficult a direct study of charm production in QCD.

Theoretical calculations are linked to experimental measurements with the help of Monte Carlo generators. In the next section the generators which were used in this work are briefly described.

3.3 Monte Carlo Generators for Charm Production

Monte Carlo generators are important tools which allow to calculate the efficiencies of the detector and of the cuts necessary to identify a given physical process. A direct confrontation between the data and the theory is then possible.

In the kinematic region of this analysis, charm in electron-proton scattering is produced at the perturbative level in QCD. Leading order and also next to leading order calculations in the massive approach are available. The longitudinal structure function F_L^c becomes sizeable at high y and is estimated to contribute to less than 2 percent for the whole range $0.05 < y < 0.7$ and $1 \text{ GeV}^2 < Q^2 < 100 \text{ GeV}^2$ [44] so that all calculations are based on the evaluation of the transverse cross section $\sigma_\perp^{\gamma p}$. Perturbative fixed order calculations can give reliable quantitative predictions of observables for which multiple emission effects and non-perturbative contributions are small. Unfortunately they fail to predict details of the structure of multi-particle final states as observed experimentally, in particular in the case of D meson production. A complementary approach to the perturbative calculations which allow to describe the properties of the hadronic final state is performed via parton shower models (QCD radiative corrections) matched to phenomenological models of fragmentation together with the decay of the non stable particles. Up to now only the LO calculations allow the implementation of the complete chain of hadronisation and thus the input to the detector simulation programme. In the case of charm production in electron-proton scattering, the corresponding available LO generators are AROMA [45], HERWIG [43], RAPGAP [46] and CASCADE [35] which are used in this work.

Two different approaches describe parton showers. The first uses a coherent LLA parton shower model (AROMA, HERWIG, RAPGAP and CASCADE) while the second is based on colour dipoles cascade (RAPGAP and ARIADNE [47]).

Fragmentation can be performed with the cluster fragmentation model [48] (HERWIG) or with the Lund string model [49] (AROMA, RAPGAP, CASCADE). Both models perform the hadronisation locally in phase space. In addition, the charm in D meson fragmentation function can be either the Lund string fragmentation function or the Peterson fragmentation parametrisation.

Higher order QED processes are not negligible at HERA. They influence the cross sections, the kinematics and the boost in the γp rest frame. Real photon emissions from the incoming lepton and virtual contributions at the leptonic vertex are included in the HERACLES [50] programme which is directly interfaced in the RAPGAP generator.

The following subsections are devoted to a brief description of the Monte Carlo event generators AROMA, HERWIG, RAPGAP and CASCADE in the context of our analysis for charm production. The HVQDIS Monte Carlo integration package which is the only available NLO DGLAP calculation of charm and beauty production is also described.

3.3.1 AROMA

AROMA [45] is a programme to simulate the production of heavy quarks (charm and bottom) in *ep* collisions. The boson-gluon fusion hard process is calculated including the full electroweak structure and the heavy quark masses. The heavy quark cross section is obtained by the convolution of the gluon density and the pQCD subprocess. The value of $\Lambda_{QCD}^{(n_f)}$ is fixed to the value used in the chosen set of parton densities. The number of active flavour is set to three. Both mass scales for the gluon density and for α_s are set to $\hat{s}$ which is the invariant mass square of the quark antiquark system. It is possible to choose other hard scales.

In AROMA the parton showers and fragmentation is performed using the JETSET package [38]. Parton showers evolution in initial and final states approximates higher order QCD radiations. The algorithm used is a coherent Leading Log Approximation (LLA) where the probability for a parton to branch is given by the DGLAP evolution equation. A strict angular ordering is required in order to avoid that branching at the end of the iteration give partons at large angles. The shower evolves in the parton centre of mass frame and satisfies energy and momentum conservation at each step. The evolution is stopped at a mass scale Q_0 where the fragmentation takes over.

The fragmentation is performed using the Lund string scheme implemented in the JETSET package. This is an iterative procedure where strings stretch between quark and antiquark via gluon colour charges. The string model is "infrared" and collinear safe[4]. The latter is achieved by merging the collinear emitted gluon and the the initial parton to the parton carrying their total momentum. In the case of charm production in electron-proton scattering via the BGF process a string is built between each charm quark and the proton resulting in two independent jets. Moreover, the long evolution of the string leads to a charmed hadron nearly independent of the proton.

The transverse momenta of the hadrons are determined from the $p_\perp$ values of their constituents which are chosen from a tunnelling process. This leads to a Gaussian $p_\perp^2$ behaviour. The longitudinal momentum fraction Z of a hadron is determined by the Lund symmetric fragmentation function:

$$f(Z) = \frac{(1-Z)^a}{Z} \cdot \exp^{-\left(\frac{b \cdot m_\perp^2}{Z}\right)} \tag{3.52}$$

where $m_\perp$ is the transverse mass of the hadron ($m_\perp^2 \mathrm{c}^4 = m^2 \mathrm{c}^4 + p_\perp^2 \mathrm{c}^2 = E^2 - p_\parallel^2 \mathrm{c}^2$). The parameter b is universal and a can depend on the quark flavour. For heavy quark it is

---

[4] No soft gluon and collinear gluon divergencies.

possible to use the Peterson fragmentation function (see equation 3.42) which depends only on the parameter ϵ. The quark flavour fragmentation dependency is reflected by different values of ϵ.

3.3.2 RAPGAP

The Monte Carlo generator RAPGAP [46] was written to generate diffractive events[5] with an elastic proton ($ep \rightarrow eXY$ with $m_Y = m_p$). The developements of this generator ended up with a general-purpose Monte Carlo programme. In this work RAPGAP is used to investigate the change in the efficiencies due to the QED radiative effects calculated by the HERACLES programme which is directly interfaced in RAPGAP. For this investigation charm is produced like in AROMA via the LO boson-gluon fusion process (without any diffractive process contributions) but QED radiations are additionally taken into account. QCD radiative effects are simulated by a LLA parton shower model. Higher order QCD corrections can also be taken into account using the colour dipole model. This lets possible systematic studies due to QCD corrections in the future. In RAPGAP the final fragmentation is performed using the Lund string fragmentation model implemented in the JETSET programme [38].

3.3.3 HERWIG

HERWIG (Hadron Emission Reaction With Interfering Gluons) [43] is a general-purpose event generator for high energy hadronic processes. It suits particularly high momentum transfer processes giving rise to hadron jets emission. Hard pQCD processes are calculated from the exact matrix element. Heavy quarks are produced via the dominant photon-gluon fusion mechanism. Colour coherence of partons (initial and final) in hard subprocesses is respected.

The parton showers are generated using a branching formalism based on an extension of the coherent Leading Log Approximation. The parton shower is based on the "resummation" of the pQCD expansion taking into account all leading logarithmic terms and the dominant part of sub-leading contributions arising from soft and collinear gluon emission. The parameters which play the biggest role in the parton shower algorithm are the strength of the strong coupling constant $\Lambda_{QCD}^{(n_f)}$ and the shower cut-off Q_i for the parton i: $Q_i = m_i c^2 + Q_0$ where m_i is the mass of the parton i and Q_0 the quark or gluon virtualily cut-off. At the end of the parton shower non perturbative gluon splitting into $q\bar{q}$ is performed.

Hadronisation of parton jets is calculated via a cluster fragmentation model based on the preconfinement characteristic of QCD. The colour charge of a quark or diquark is compensated by the colour of a antiquark or antidiquark which is nearby in phase space. Low mass colour-neutral clusters are in this way constructed. Hadrons are formed in two-body cluster decay according to phase space and spin factors. The hadron transverse momenta are thus produced dynamically as a consequence of the cluster mass spectrum.

---

[5] Diffractive events are events characterised by a large rapidity gap which contained no final state hadrons.

For the decay of a cluster containing a quark from the perturbative phase, the quark direction is remembered but a Gaussian smearing is applied to this direction. Finally, QCD coherence effects are taken into account for the production and decay of heavy hadrons.

3.3.4 CASCADE

The Monte Carlo generator CASCADE [35] is a backward evolution scheme with respect to the hard QCD process based on the CCFM formalism (see subsection 3.1.4). The solution of the unintegrated gluon density was determined with a modified version of the parton-level forward evolution scheme programme SMALLX [51]. The unintegrated gluon density was fixed by requiring a good description of both the structure function F_2 and the cross section of the forward jet prodution as measured by the HERA experiments [52]-[55]. In the kinematic region studied in this work the CCFM formalism is equivalent to the DGLAP formalism but for the boson-gluon fusion process both the photon and the gluon are virtual. In the CASCADE code the package JETSET [38] is used to perform the parton showers and the quark fragmentation like in AROMA. CASCADE is therefore a complete hadron level event generator.

3.3.5 HVQDIS

The HVQDIS programme [56] calculates charm and beauty production in the massive approach up to the NLO in α_s. This is a fixed order pQCD calculation (FOPT) where the heavy quark mass is not neglected. Only the three light quarks are considered as active flavours in the proton. The heavy quarks are produced at the perturbative level where the BGF process is dominant. In addition a very small contribution of light quark induced processes with an emitted gluon splitting into a charm and anticharm quark appears via the NLO calculations. The imprecisely determined charm quark mass and the renormalisation and factorisation scales lead to the primary sources of uncertainty. Since the calculation is fully differential, the four-momenta of the partons involved in the pQCD hard process are available. Charm quarks can therefore be hadronised in D^{*+} mesons as an independent process according to the Peterson fragmentation function (see equation 3.42). This is done by scaling the charm three-momentum by Z_D. The D^{*+} meson predicted differential cross sections depends on the frame in which the fragmentation function is applied. We performed the fragmentation in the γp rest frame which seems to be the most appropriate choice (see subsection 3.3.6). The charmed hadron acquires a transverse momentum with respect to the charm quark direction following an exponential $\alpha p_\perp^2$ behaviour. In this work the parameter α was fixed to 6. This value corresponds to an average transverse momentum in the γp rest frame of 350 MeV/c (see figure 3.6) as observed in electron-positron data. The smearing of the D^{*+} meson transverse momentum is also performed in the hadronic centre of mass frame which allows the same drag effect in the proton direction as observed in the laboratory frame in the case of JETSET based Monte Carlo programmes. This effect arises due to the boost from the hadronic frame to the laboratory. Finally the energy componment is fixed such that the D^{*+} rest mass amounts the experimentally measured mass of 2.01 GeV/c^2. Introducing this simple fragmentation algorithm in the HVQDIS programme allows us to predict NLO differential cross sections in any final state variable depending on the D^{*+} meson and scattered electron momenta. Particularly it allows to study the predicted cross sections in the D^{*+} meson transverse momentum and angular ranges accessible with the H1 detector.

3.3.6 Predicted Charm Production in DIS

To close this chapter we explore the kinematics of charm production in electron-proton deep inelastic scattering predicted by several Monte Carlos within the kinematic range: 1 GeV^2 $< Q^2 <$ 100 GeV^2 and $0.05 < y < 0.7$.

In this work charm production will be studied by measuring the D^{*+} meson cross sections from the reconstruction of D^{*+} mesons in the decay channel $D^{*+} \to D^0\pi_s^+ \to (K^-\pi^+)\pi_s^+$. Thus, in this section, we will directly present the predicted D^{*+} cross sections. This is achieved by converting the charm cross section into the D^{*+} cross section using the measured probability $P(c \to D^{*+})$ that a charm quark fragments in a D^{*+} meson:

$$\sigma(ep \to eD^{*+}X) = 2 \cdot P(c \to D^{*+}) \cdot \sigma(ep \to ec\bar{c}X), \tag{3.53}$$

with $P(c \to D^{*+}) = (23.3 \pm 1.5)\%$ [57]. From the branching ratio point of view the studied channel allows to observe only 1.2% of the produced charm events. This fraction is described by the following probability relation:

$$P(c \to (K^-\pi^+)\pi_s^+)) = 2 \cdot P(c \to D^{*+}) \cdot BR(D^{*+} \to D^0\pi_s^+) \cdot BR(D^0 \to K^-\pi^+) = 1.2\%, \tag{3.54}$$

where the branching ratios are given in table 3.1.

	Particle Data Book 1998	Particle Data Book 2000
$D^{*+} \to D^0\pi_s^+$	0.683 ± 0.014	0.677 ± 0.005
$D^0 \to K^-\pi^+$	0.0385 ± 0.009	0.0383 ± 0.009

Table 3.1: Charm and D meson branching ratios from the Particle Data Book edited in 1998 and 2000 [58] [40].

Additionally to the total D^{*+} cross sections, the predicted cross sections in the D^{*+} visible range will also be presented. The visible range is given by the detector acceptance (-1.5 $< \eta_{D^*} <$ 1.5) and by the minimum D^{*+} transverse momentum necessary to extract the D^{*+} signal ($p_{\perp D^*} >$ 1.5 GeV/c). These limits bring an additional loss of 69% estimated with the MC generator HVQDIS.

Finally, within the visible range, an efficiency of approximately 25% (see chapter 4) to reconstruct D^{*+} mesons reduces the ratio of the observed D^{*+} events to the produced charm events down to 0.1%. This is indeed a very small fraction of the total charm cross section. However, the biggest difficulty to extract the cross sections from the observed

D^{*+} mesons is not due to the fact that they represent such a small fraction of the charm events but comes from the large uncertainty on the extrapolation from the D^{*+} visible range to the total range. This extrapolation, which is evaluated from the theoretical calculations, depends on the predicted D^{*+} transverse momentum spectrum and the D^{*+} pseudorapidity distribution. Moreover, the uncertainty on the extrapolation increases when Q^2 decreases. It amount ±8% at $Q^2 = 65$ GeV^2 and ±20% at $Q^2 = 1.5$ GeV^2. These errors were calculated by taking into account:

- the difference from the two main approaches HVQDIS and CASCADE,
- the factorisation and renormalisation scale,
- the uncertainty on the charm quark mass,
- the uncertainty on the gluon density,
- the poor knowledge on the charm fragmentation in *ep* scattering.

The present analysis is extended down to $Q^2 = 1$ GeV^2 in comparison to previous published measurements [3] which started only at $Q^2 = 10$ GeV^2. Therefore the measured cross section will be given in the D^{*+} visible range in order to minimise the theoretical uncertainties coming from the extrapolation. This justifies why not only the predicted cross sections are presented here but also the cross sections within the D^{*+} visible range.

Figures 3.4 and 3.5 show the inclusive D^{*+} differential cross sections versus W, $logx$, Q^2, $logx_g$, $p_{\perp c}$, η_c (θ_c in the icon), η_{D^*} (θ_{D^*} in the icon) and $\hat{s}$ predicted by the HVQDIS and CASCADE Monte Carlo generators respectively. The full line histograms show the cross sections in the total D^{*+} range while the dashed line histograms indicate what is left within the visible range.

The W distributions in figures 3.4.(a) and 3.5.(a) are limited by the y range because W^2 is nearly proportional to y for 1 GeV$^2 < Q^2 <$ 100 GeV^2. It is interesting to note that the full W range is accessible within the visible range.

Figures 3.4.(c) and 3.5.(c) show clearly the steep rise of the cross section when Q^2 decreases. Therefore the model uncertainties, which occur when the measured cross section is extrapolate from the visible range to the total range, is dominated by the large uncertainties at low Q^2.

Most of the charm is produced backward as seen in the differential cross sections versus θ_c (figures 3.4.(f) and 3.5.(f)). This is due to the strong boost, when x_g is small, from the γg frame to the γp frame. In the γg frame both charm quarks are produced back to back isotropically. After boosting in the γp frame, the charm quarks are collimated in the proton oposit direction. Both charm quarks stay close one to another because their total invariant mass $\sqrt{\hat{s}}$ ($\langle\sqrt{\hat{s}}\rangle \approx 6$ GeV, see figures 3.4.(a) and 3.5.(a)) is negligible in front of the γp invariant mass W which ranges from 66 to 251 GeV (see figures 3.4.(h), 3.5.(h)). In the laboratory frame, the charm quarks approximatively keep the direction of the photon which is emmited backward when x_g is small. However, the enhancement of charm in the backward direction is smoother for the CASCADE prediction. Indeed in the CASCADE code the gluon involved in the BGF process can be highly virtual and this results in an increase of the $c\bar{c}$ invariant mass. This can be observed in the differential cross section as a function of $\hat{s}$ where CASCADE shows a harder $\hat{s}$ spectrum.

On figures 3.4 and 3.5 it can be seen that the loss from the total range to the visible range of (69% for HVQDIS and 61% for CASCADE) is mainly due to the $p_{\perp D^*}$ cut of 1.5 GeV/c because of a relatively soft $p_{\perp c}$ spectrum resulting in a soft $p_{\perp D^*}$ spectrum. It is now clear that the predicted $p_{\perp c}$ spectrum as well the fragmentation of charm in D^{*+} mesons influence the predicted D^{*+} cross section within the visible range. For the same reason the θ_c distribution and the correlation between the charm and the D^{*+} meson resulting in the θ_{D^*} distribution (figures 3.4.(g) and 3.5.(g)) determine what remains after the angular cut: -1.5 < η_{D*} < 1.5.

The differential cross section as a function of x_g calculated with HVQDIS and shown in figure 3.4.(d) is more shifted toward lower x_g than the CASCADE predicted distribution shown in figure 3.5.(d). This occurs despite the fact that for the HVQDIS prediction an NLO gluon density is used (GRV 98 HO). However, the quantity x_g doesn't play the same important role in CASCADE as in the DGLAP formalism used in the HVQDIS code (see subsections 3.1.2 and 3.1.4). The visible range, mainly the $p_{\perp D^*}$ cut, produced a cross section loss which increases when x_g decreases. This effects is more pronounced in the case of HVQDIS precisely because it predicts more cross section at low x_g. Within the visible range the two models give quite similar prediction for the x_g distribution. For both model the x_g distribution leads to a broader x distribution shifted towards larger values (figures 3.4.(b) and 3.5.(b)).

Some clear differences in the differential cross sections appear for the prediction of the two models studied which are however softened within the visible range except for D^{*+} angular distribution. However, the CASCADE prediction which is 27% larger than the HVQDIS prediction in the total D^{*+} range becomes 56% larger in the visible range (see table 3.2). This is due to the difference in the parton distributions predictions, but can also be the consequence of the different correlations between the charm quark and the D^{*+} meson. Indeed the HVQDIS programme allows only for a very simple fragmentation algorithm which is less complete than the JETSET hadronisation used in CASCADE. The end of this section will give more details on how well the HVQDIS fragmentation algorithm is able to reproduced the hadronisation used in CASCADE.

Model	Parton Density	$\sigma(ep \rightarrow eD^{*+}X)$	$\sigma_{vis}(ep \rightarrow eD^{*+}X)$
HVQDIS	GRV 98 HO	17.22 nb	5.40 nb
CASCADE	H1 fit	21.85 nb	8.42 nb

Table 3.2: Predicted inclusive D^{*+} total cross sections in the electron kinematics 1 GeV^2 < Q^2 < 100 GeV^2 and 0.05 < y < 0.7 for $m_c = 1.5$ GeV/c^2 and ϵ(Peterson) = 0.078. The scale has been fixed to $Q^2 + 4m_c^2$c^4. The D^{*+} visible range is given by -1.5 < η_{D^*} < 1.5 and $p_{\perp D^*} > 1.5$ GeV/c.

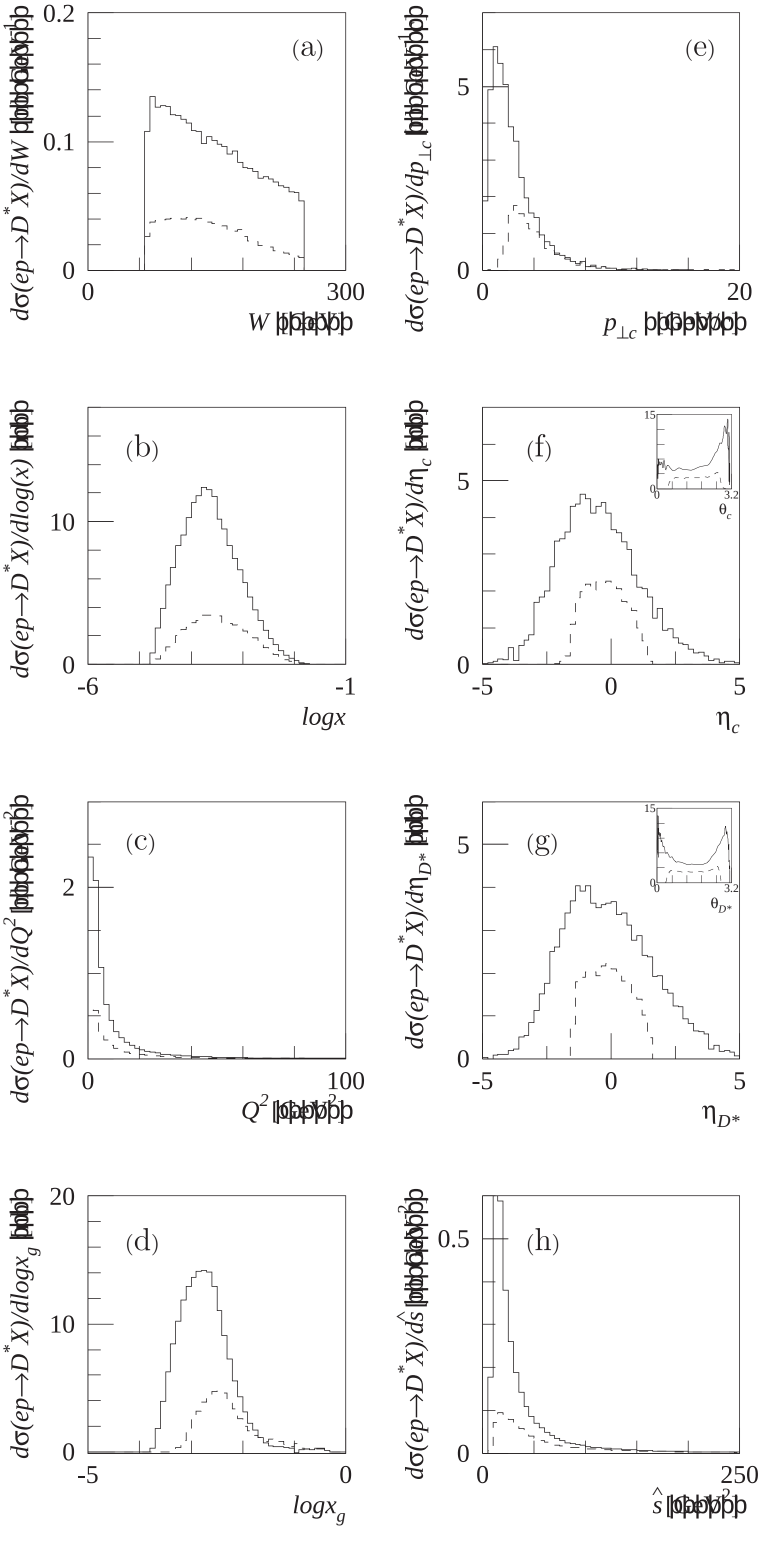

Figure 3.4: Predicted inclusive D^{*+} differential cross sections versus W, x, Q^2, x_g, $p_{\perp c}$, η_c (θ_c in the icon), η_{D^*} (θ_{D^*} in the icon) and $\hat{s}$ using the HVQDIS NLO DGLAP calculations with $m_c = 1.5$ GeV/c^2 and ϵ(Peterson) = 0.078. The dashed histograms represent the predicted cross sections in the visible range -1.5 $< \eta_{D^*} <$ 1.5 and $p_{\perp D^*} >$ 1.5 GeV/c.

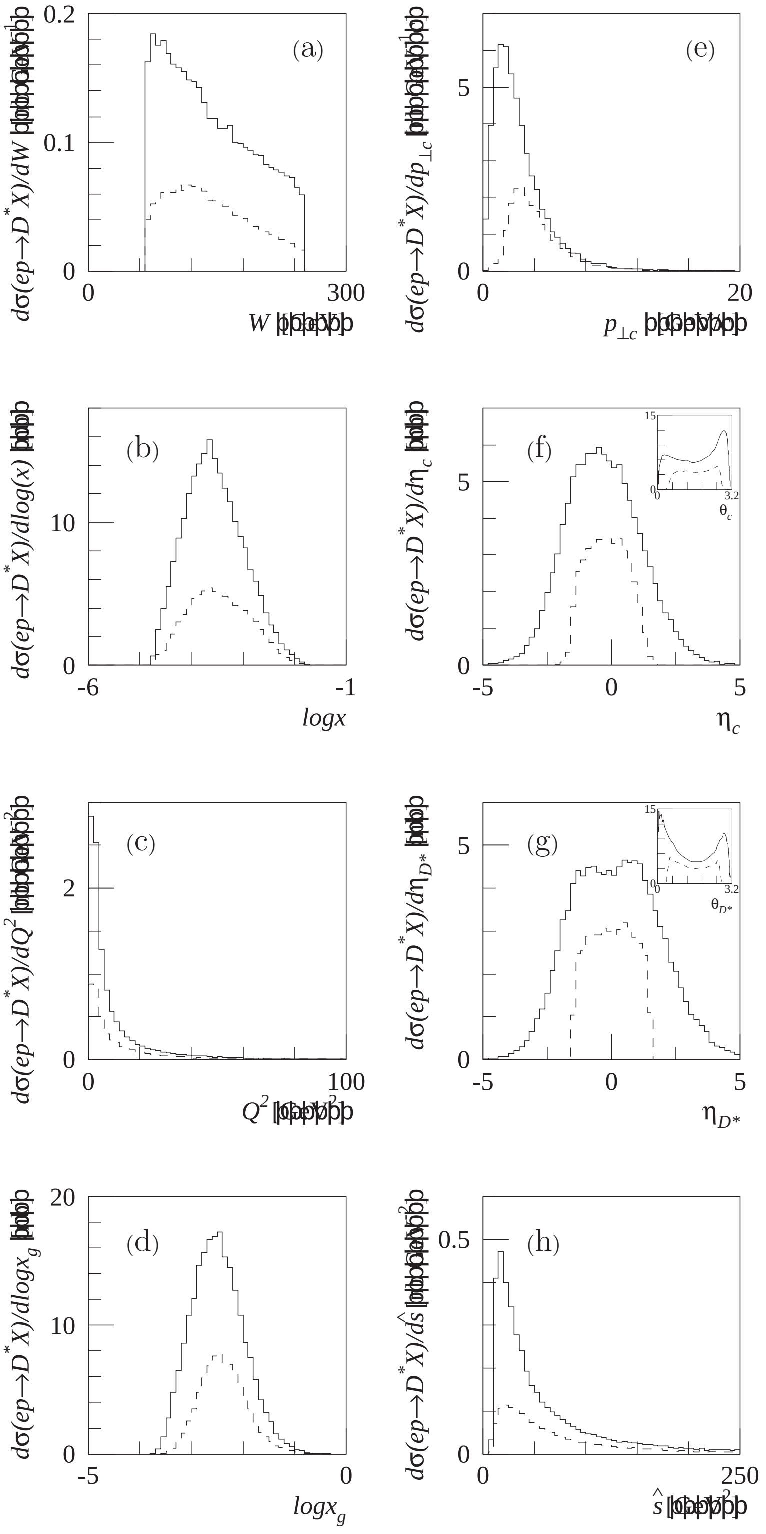

Figure 3.5: Predicted inclusive D^{*+} single differential cross sections versus W, x, Q^2, x_g, $p_{\perp c}$, η_c (θ_c in the icon), η_{D^*} (θ_{D^*} in the icon) and $\hat{s}$ using the CASCADE LO CCFM calculations with m_c = 1.5 GeV/c^2 and ϵ(Peterson) = 0.078. The dashed histograms represent the predicted cross sections in the visible range -1.5 $< \eta_{D^*} <$ 1.5 and $p_{\perp D^*} >$ 1.5 GeV/c.

The Monte Carlo CASCADE is used to study how different manners of considering the charm fragmentation can influence the D^{*+} transverse momentum and angular distributions. In the CASCADE code the parton showers and the charm fragmentation are performed with the JETSET package. This package produces a fairly realistic description of the hadronisation.

Figure 3.6 shows the predicted CASCADE D^{*+} differential cross sections versus η_c (doted histograms), η_{D^*}, $p_{\perp D^*}$, $Z_{D^*}^{\gamma p}$ and $p_{\perp D^*}^{\gamma p}$. Here $p_{\perp D^*}^{\gamma p}$ is the D^{*+} transverse momentum *with respect to the charm direction* in the γp frame. Each row represents a different way to perform the charm fragmentation in a D^{*+} meson. All approaches use the Peterson fragmentation function with $\epsilon(\text{Peterson}) = 0.078$.

In the case of figure 3.6.(a) the fragmentation function is applied within the Lund string scheme of JETSET. This is the standard way used in CASCADE. In all other approaches the D^{*+} three-momentum is calculated by simply scaling the charm momentum by Z_D according to the fragmentation function as done in HVQDIS. A transverse momentum with respect to the charm direction following an exponential $\alpha p_\perp^2$ behaviour is added to the D^{*+} momentum and results in the predicted cross sections of figure 3.6.(c) and 3.6.(e). In this case, the value of α is fixed to 6 which corresponds to an average transverse momentum with respect to the charm direction of 350 MeV/c. Figures 3.6.(b) and 3.6.(c) show the predicted cross sections when the D^{*+} momentum is made up in the γp frame whereas for figures 3.6.(d) and 3.6.(e) this was performed in the laboratory frame.

For standard JETSET fragmentation (figure 3.6.(a)) a clear positive shift from the η_c to the η_{D^*} distribution is observed. The same effect is also produced when the fragmentation is performed in the γp frame (figures 3.6.(b)) and 3.6.(c)) whereas the charm and D^{*+} angular distributions are the same when the fragmentation is performed in the laboratory frame (figures 3.6.(d)) and 3.6.(e)). The differential cross sections as a function of η_{D^*}, $p_{\perp D^*}$ and $Z_{D^*}^{\gamma p}$ in figures 3.6.(b) and 3.6.(c) are very similar to the standard JETSET fragmentation predictions of figure 3.6.(a). However, the distribution of the D^{*+} transverse momentum with respect to the charm direction in the γp frame in figure 3.6.(a) is better reproduced by the fragmentation approach used in figure 3.6.(c). Consequently this latter has been chosen to produce D^{*+} mesons from the charm quarks generated by the NLO programme HVQDIS.

To conclude it is important to note that the prediction of the D^{*+} visible cross section changes only by ± 3% for the different studied fragmentation approaches despite of fairly different predicted angular distributions. The increasing difference between the CASCADE and HVQDIS cross section predictions when restricting the cross section to the visible range is therefore not due to the different fragmentation approaches but is only due to the different charm predictions as a function of $p_{\perp c}$ and η_c. However, if the value of $\epsilon(\text{Peterson})$ is changed from 0.078 to 0.035 like measured in e^+e^- experiments, the prediction for the visible cross section increases by 10% for both models CASCADE and HVQDIS.

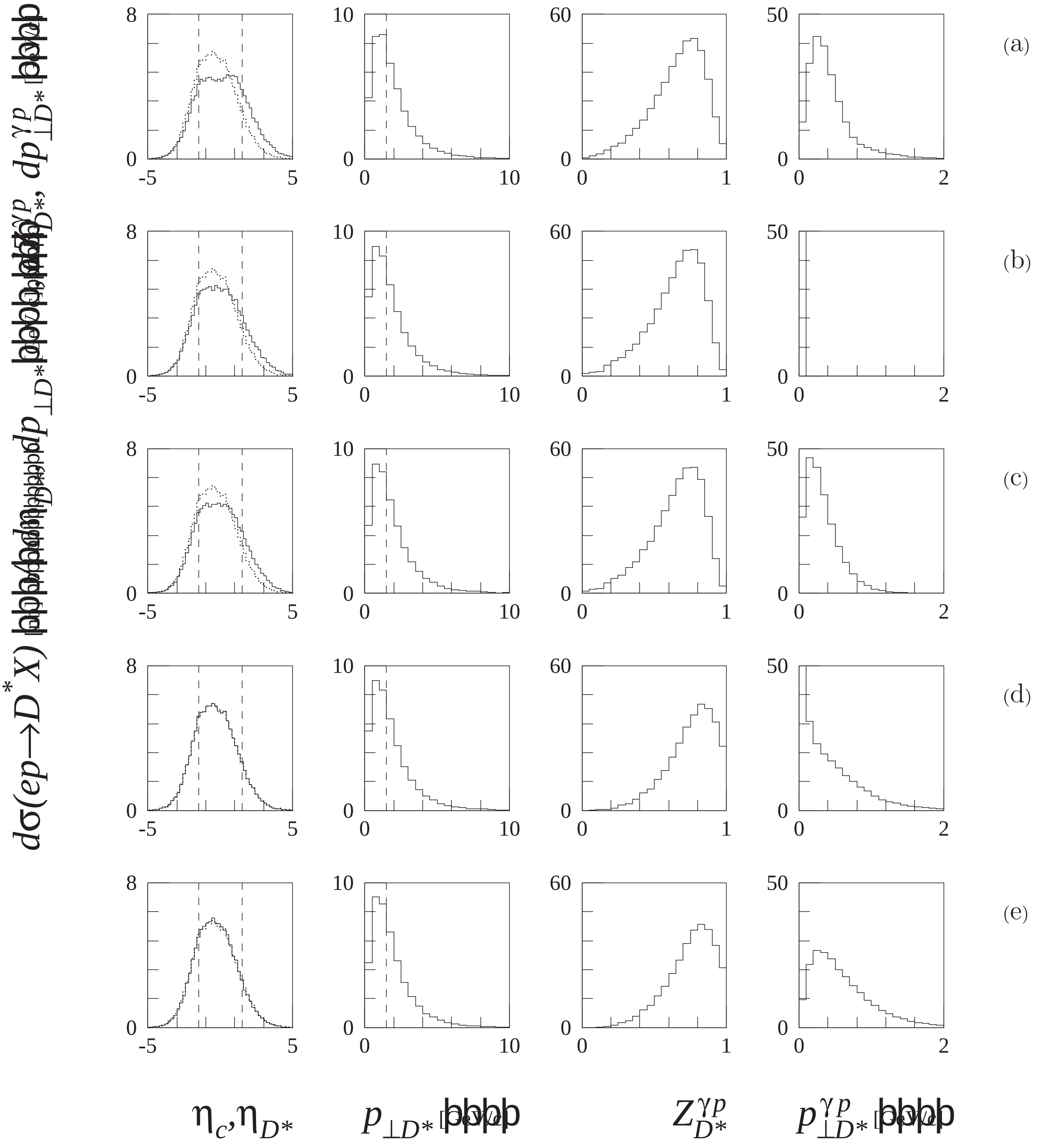

Figure 3.6: Predicted inclusive D^{*+} differential cross sections versus η_c (doted histograms), η_{D^*}, $p_{\perp D^*}$, $Z^{\gamma p}_{D^*}$ and $p^{\gamma p}_{\perp D^*}$ using the LO CCFM calculation CASCADE with $m_c = 1.5$ GeV/c^2 and ϵ(Peterson) = 0.078. Here $p^{\gamma p}_{\perp D^*}$ is the D^{*+} transverse momentum *with respect to the charm direction* in the γp frame. Each row represents the predicted cross sections with the following different ways of performing the charm fragmentation:
(a) within the Lund string scheme but using the Peterson fragmentation function,
(b) Peterson fragmentation function applied in the γp frame,
(c) Peterson fragmentation function applied in the γp frame and $\langle p^{\gamma p}_{\perp D^*}\rangle \approx 350$ MeV/c,
(d) Peterson fragmentation function applied in the laboratory frame,
(e) Peterson fragmentation function applied in the laboratory frame and $\langle p_{\perp D^*_{w.r.t.\,charm}}\rangle$ ≈ 350 MeV/c.

Chapter 4

D^{*+} Analysis

The objective of the present analysis is to tag charm events from *ep* collisions with D^{*+} mesons in the decay $D^{*+} \rightarrow D^0\pi_s^+ \rightarrow (K^-\pi^+)\pi_s^+$. The D^{*+} decay particles are measured in the central tracker of H1. This chapter will describe the complete D^{*+} analysis. The first section will give an overview of the online selection which was performed by the use of a dedicated subtrigger and a rough selection of $(K^-\pi^+)\pi_s^+$ events using online reconstructed tracks. Then the complex offline selection will be presented. The quality criteria which allow to build the considered data sample will be explained together with the resulting luminosity measurement. Special emphasis will be placed on the DIS selection and on the kinematic reconstruction as they are of big importance for the reconstruction of x_g. Finally the D^{*+} selection resulting in the D^{*+} rate is given in section 4.4.

4.1 Online Selection

The continuous luminosity increase of the HERA machine as well as the wish to record all physics processes independently of their rates were the reasons to constantly improve the online trigger system throughout the running years. The D^{*+} in DIS events were also affected by the HERA luminosity increase and therefore had to be saved online by more and more highly efficient means. Refining the dedicated Level 1 subtrigger as well as performing a rough online D^{*+} selection at the last trigger level (Level 4) was the obvious way to follow. Nowadays, a D^{*+} neural net at the second trigger level has been added in order to continue the investigation of charm physics using one of its best servant, the D^{*+} meson.

4.1.1 Subtrigger Selection

The D^{*+} analysis in the DIS regime makes use of one single dedicated Level 1 subtrigger (ST 2 replaced by ST 61 from beginning of July 1997 onwards). The concerned subtrigger is a combination of information coming from several essential subdetectors. It has been completed and refined between the 1995 and 1996 data taking. During the 1995 running period, the D^{*+} in DIS subtrigger was mainly requiring a minimum energy deposition in the SpaCal together with a veto on the *out of time* trigger elements and the weak zVtx_t0 condition of the z-vertex trigger system. In 1996 the DCr-φ trigger system was used to require at least one track with a minimum transverse momentum. The stronger zVtx_sig condition was used in order to guarantee a significant z-vertex determination. Later during the 1997 running period, the subtrigger has been completed by limiting the number of track candidates found by the *DCr-φ* trigger system and by rising the SpaCal energy threshold. The time evolution, in terms of trigger elements, of the D^{*+} in DIS subtrigger is summarised in appendix A.3. At that point it should be noticed that the Monte Carlo simulation has to follow as closely as possible this evolution in order to describe the trigger behaviour for the whole running period. The description of the different trigger subsystems as well as the definition of the trigger elements necessary to build ST 2 and ST 61 is given in the following.

- The so called *DCrϕ* trigger subsystem makes use of the CJC answer. The signals of 10 out of 56 wire layers are digitised. The obtained drift time information is compared with 10000 different masks. Those masks contain the bit pattern of tracks with transverse momentum range larger than 400 MeV/c. Two different kinds of masks are defined for positive or negative low transverse momentum tracks ($p_\perp$ <1 GeV/c). A special class of masks (t0 masks) is defined by synchronising and shifting the first seven layer signals. This allows to improve the time resolution which is usually spoiled by a layer per layer drift time comparison. Several trigger elements are available. A short description can be found in table 4.1.

DCrϕ Trigger Element	*DCrϕ* Trigger Condition
DCRPh_T0	at least one validated t0 mask fired
DCRPh_Ta	at least one mask fired
DCRPh_Tb	at least b (=2) masks fired
DCRPh_Tc	at least c (=3) masks fired
DCRPh_TPos	at least x (=1) positive masks
DCRPh_TNeg	at least x (=1) negative masks
DCRPh_THig	at least x (=1) $p_\perp$ > 800 MeV/c masks fired
DCRPh_TLow	at least x (=1) 400 MeV/c < $p_\perp$ < 800 MeV/c masks fired
DCRPh_NL_many	at least 20 negative low momentum track candidates
DCRPh_NH_many	at least 20 negative high momentum track candidates
DCRPh_PL_many	at least 20 positive low momentum track candidates
DCRPh_PH_many	at least 20 positive high momentum track candidates

Table 4.1: Description of the trigger elements delivered by the *DCrϕ* trigger subsystem. The number of masks b, c and x are programmable.

- The z-vertex trigger subsystem is built from the answers of the the MWPC (CIP, COP and the first two layers of the FWPC). Thanks to the good time resolution of these components (≈ 20 ns) it is possible to know which HERA bunch crossings an event belongs to. This allows to stop all pipelines at the front-end electronics at the right time. The z-vertex trigger reconstructs all possible tracks from all combinations of 2x2 signals. Nevertheless, these tracks must have a transverse momentum larger than 150 MeV/c in order to cross both CIP and COP or CIP and FWPC. The z coordinate of each track will cluster for a collision event. The z-vertex trigger element zVtx_sig will be set as soon as a significant peak is found and is used to fight against proton beam induced background.

- The rz trigger subsystem can reconstruct track segments found in the CIZ and COZ. It provides two trigger informations. RZ_sig1 trigger element corresponds to a significant peak in the rz vertex histogram. RZ_non_vtx trigger element indicates the accumulation of track segments far from the nominal interaction region and is used as a veto condition. Here, the veto is effective only if at the same time no significant peak in the rz vertex histogram is found (see table A.1 and A.2). Thus upstream proton background is rejected.

- The SpaCal Inclusive Electron-Trigger subsystem (IET) is the trigger system used to detect scattered electron events with high efficiency in the backward region of H1.
  The first step of this trigger system is to determine all cluster bits. The comparison of the summed deposited energy of 4x4 electromagnetic cells (trigger tower) with three defined thresholds results in three cluster bits for one trigger tower. The trigger towers overlap each other by half size in both directions x and y, thus avoiding trigger inefficiencies as a function of the impact point. For each level (energy threshold) the Local IETs (LIET) are calculated by a logical OR of 4x4 cluster bits. In addition, a central IET named LIET_CENT is the result of a logical OR of 5x5 cluster bits. The electromagnetic SpaCal is divided in 5x5 LIET plus the central one. Finally, a logical OR of the LIET bits (excluding the LIET_CENT), which is calculated for the three energy levels separately, will give three electromagnetic SpaCal trigger elements (SPCLe_IET>0, SPCLe_IET>1, SPCLe_IET>2). The SPCLe_IET_Cen trigger element is simply the LIET_CENT.
  Till August 1996 only the level 3 of the SPCLe_IET_Cen bit was available as trigger element. Then the three energy levels were defined as trigger elements (SPCLe_IET_Cen_1, SPCLe_IET_Cen_2, SPCLe_IET_Cen_3) and the level 2 was implemented for ST2. The IET energy thresholds are given in table 4.2.

	all SpaCal	Central SpaCal	Energy Threshold
level 1	SPCLe_IET>0	SPCLe_IET_Cen_1	0.5 GeV
level 2	SPCLe_IET>1	SPCLe_IET_Cen_2	2.0 GeV
level 3	SPCLe_IET>2	SPCLe_IET_Cen_3	6.0 GeV

Table 4.2: IET energy thresholds for the SpaCal trigger elements in 1996 and 1997

- The time of flight trigger subsystem provides trigger elements which are used to get rid of non genuine ep collision events. In general two time slots are defined and correspond to two trigger elements. The first trigger element (noted _BG) is set when a subdetector answer is coming outside of the ep interaction time. The second trigger element (noted _IA) indicates subdetector answers within the interaction time. The devices contributing to the time of flight trigger system are the Forward ToF (FToF), Backward ToF (BToF), the big inner veto wall (VETO_inner), the outer veto wall (VETO_Outer), the Plug ToF (PToF) and the hadronic SpaCal (SPCLh).

4.1.2 Subtrigger Efficiencies

For both years 1996 and 1997, the SpaCal IET thresholds used by the D^{*+} in DIS subtrigger were checked using events triggered by lower IET thresholds. The efficiency of the SpaCal IET thresholds is given by:

$$\varepsilon(D^{*}\text{–ST IET}) = \frac{N(\text{lower IET \& } E'_e > 8 \text{ GeV \& } D^{*}\text{–ST IET})}{N(\text{lower IET \& } E'_e > 8 \text{ GeV})}. \tag{4.1}$$

A total efficiency of 100% has been found for the events considered in this work. This reveals the full efficiency of the IET for scattered electrons with energy greater than 8 GeV as required in this analysis. A remaining uncertainty of 1.5% has to be quoted here to take in account events which might be lost for all SpaCal IET thresholds.

The tracker components efficiency of the D^{*+} in DIS subtrigger is checked with a set of events triggered by all available subtriggers using any SpaCal IET thresholds (SpaCal subtriggers) on which the full D^{*+} analysis was performed. This was done in order to improve statistics after checking consistency when only events triggered by the subtrigger ST1 (same SpaCal IET as the D^{*+} subtrigger but no track requirements) were considered. The tracker components efficiency is therefore given by:

$$\varepsilon(D^{*}\text{–ST track}) = \frac{N(\text{ref \& } D^{*}\text{analysis \& } D^{*}\text{–ST track})}{N(\text{ref \& } D^{*}\text{analysis})}. \tag{4.2}$$

Here "ref" represents the reference sample which can be either events triggered by all SpaCal subtriggers or events triggered by ST1. The efficiencies are summarised in table 4.3. The harder track requirements of the D^{*+} analysis applied to the 1997 data (see table 4.7) result in a higher efficiency of the subtrigger track conditions. The detector simulation describes the data efficiency fairly well. The bin wise description of the efficiency was also checked. The few bins which show indication of a wrong description will carry an additional systematic error. The simulated subtrigger efficiencies can therefore be used bin wise in all relevant quantities of the D^{*+} analysis.

4.1.3 Online D^{*+} Selection

In 1997 an open charm finder (HQSEL for Heavy Quark SELection) was implemented at the fourth level of the H1 trigger system. However, the Level 4 kept all events with online reconstructed Q^2 larger than 6 GeV^2 so that the open charm finder finder was effective only for online reconstructed Q^2 smaller than 6 GeV^2. Several decay channels were analysed with up to 5 decay particles. Two different sets of cuts were defined for the photoproduction and the DIS regime. Two track qualities were available: Normal and

	Subtrigger ST1	all SpaCal Subtriggers
Data 1996	$(83.9 \pm 2.2)\%$	$(85.4 \pm 1.6)\%$
Aroma D^{*+} MC 1996		$(85.4 \pm 0.6)\%$
Data 1997	$(90.0 \pm 1.7)\%$	$(92.4 \pm 1.5)\%$
Aroma D^{*+} MC 1997		$(92.0 \pm 0.5)\%$

Table 4.3: Efficiencies due to the tracker requirements of the D^{*+} in DIS subtrigger. The first column uses the subtrigger ST1 as reference sample. The SpaCal IET conditions of ST1 are very similar to the one of the D^{*+} subtrigger but ST1 has no track requirements. To improve statistics the second column gives the efficiencies calculated from a reference sample defined by all subtriggers with SpaCal IETs conditions.

High. The corresponding cuts are summarised in table 4.4. During the 1997 run period it has been necessary to require softer track qualities because of two unfortunate holes (very low efficiency cells) in the CJC detector.
For the particular $D^{*+} \rightarrow D^0\pi_s^+ \rightarrow (K^-\pi^+)\pi_s^+$ channel in DIS the following was required:

- a π_s^+ and π^+ candidate with "HQSEL Normal Quality" (see table 4.4)
- a K^- candidate with "HQSEL High Quality" (see table 4.4)
- Reconstructed masses from the satisfying $K^-\pi^+\pi_s^+$ candidates: $|m_{K\pi} - m_{D^0}| < 100$ MeV/c^2 and $m_{K\pi\pi_s^+} - m_{K\pi} < 0.17$ GeV/c^2
- a built D^{*+} candidate with $p_{\perp D^{*\pm}} > 1.0$ GeV/c
- an electron cluster in the SpaCal with energy greater than 5.5 GeV and with a linear cluster radius smaller than 4 cm.

4.2 Run Selection, Event Selection and Luminosity Determination

From all H1 recorded data, only runs which fulfil precise quality criteria are selected in order to have a good quality data sample and to avoid an overestimation of the integrated luminosity. The sum of the integrated luminosity of these runs, corrected for HV status and subtrigger prescale factors, represents the total integrated luminosity of the selected data sample.

4.2.1 Run Selection

Each run is subject to a severe control before being accepted as a good quality run. This control consists of the following run condition requirements:

	HQSEL Normal Quality
Transverse Momentum	> 120 GeV/c, > 100 GeV/c if π_s^+
Track Length	> 10 cm
Track Starting Radius	< 30 cm (run$<$199078), < 35 cm
d_{ca}	< 2.0 cm
$\lvert z_{ca} - z_{vtx} \rvert$	< 20 cm
	HQSEL High Quality
Transverse Momentum	> 200 GeV/c
Track Length	> 25 cm
Track Starting Radius	< 25 cm (run$<$199078), < 75 cm
d_{ca}	< 0.5 cm
$\lvert z_{ca} - z_{vtx} \rvert$	< 10 cm (run$<$183000), < 12 cm

Table 4.4: Track quality definitions used by the online heavy quark finder HQSEL in the 1997 running period.

- The electron and proton beam energies as well as the magnetic field have to lie in a reasonable range.

$$\begin{array}{rcccc} |E_e - 27.5| & \text{GeV} & < & 0.5 & \text{GeV} \\ |E_p - 820| & \text{GeV} & < & 5.0 & \text{GeV} \\ |B - 11.5| & \text{T} & < & 0.5 & \text{T} \end{array} \tag{4.3}$$

- The run phase (which characterises how far the run is taken in the luminosity fill) has to be larger than one. A run phase larger than one generally means good background conditions allowing to have the trackers on and not too large subtrigger prescale factors (for each phase a specific set of subtrigger prescale factors is defined).
- The run quality flag, determined online with respect to the amount of operational devices, has to be in the class good or medium.
- The luminosity related informations (like run time for example) have to be present and coherent among the H1 banks.
- The luminosity fraction carried by the satellite bunches has to be less than 20% of the integrated run luminosity.
- The integrated run luminosity, coming from colliding bunches, corrected for HV status, has to sum up more than 0.1 nb^{-1}.
- During the 1996 running time a certain period was affected by problems at the trigger Level 4. The corresponding runs have been rejected for this analysis. In addition, runs taken with SpaCal problems which are not simulated in the Monte Carlo and runs with too poor $\frac{dE}{dx}$ measurement, have not been considered in order to guarantee the best agreement between the data and the Monte Carlo simulation.

The main problem affecting the SpaCal appears for runs where the HERA clock (T_0) does not correspond to the interaction time (T_{int}): $T_{int} < T_0$. In this case the SpaCal answers at $T_{SpaCal} \approx T_{int} + 14$ ns will occur earlier than the defined SpaCal time window $[T_0 + 5 \text{ ns}, T_0 + 25 \text{ ns}]$ and no IET trigger elements will be fired. Those runs have a very low SpaCal IET efficiency which is not reproduced by the simulation, therefore they are not considered here.

4.2.2 General Event Selection

Within one run only events coming from colliding bunches are accepted (no pilot-gas interaction, no satellite interaction). During data taking, a run is not stopped when minor problems occur for any of the devices. Therefore it is also required, for each event, that the vital devices for this analysis are operational (Trackers, Luminosity system and SpaCal, BDC). This is done by checking all alarms affecting these devices as well as the high voltage status (all high voltages set to operational values) which is coded in the so called slow control bits. The considered devices are not only the ones directly used in the analysis (CJC, Luminosity system, SpaCal, BDC) but also those necessary to build up the D^{*+} in DIS subtrigger. Despite the fact that only tracks measured in the CJC are used in this analysis, it is required that the forward proportional chambers are operational. This is necessary because the D^{*+} in DIS subtrigger is based on a good quality vertex reconstruction which uses information of both central and forward proportional chambers (see subsection 2.2.2).

4.2.3 Luminosity Determination

The integrated luminosity is determined for each run by the H1 luminosity system described in section 2.5. The principle of the measurement can be found in references [16] and [17]. A layout of the luminosity system is shown in figure 2.7. The luminosity has to be corrected for the amount of time in the run where slow control bits indicate a problem in one of the devices used directly or indirectly in this analysis (see 4.2.2). The integrated luminosity is also corrected for subtrigger prescale factors as described in appendix C. The integrated luminosity for the 1996 and 1997 running period respectively is given in table 4.5.

	year 1996	year 1997
Integrated Luminosity	6.48 pb^{-1}	12.07 pb^{-1}

Table 4.5: Integrated Luminosity corrected for HV status and subtrigger prescale factors for the 1996 and 1997 selected data.

4.3 DIS Sample

In the elaboration of the DIS sample the scattered electron has to be identified in the detector. Within the Q^2 range considered in this analysis, the incident electron is scattered at small angles in the backward calorimeter SpaCal.

In this section the scattered electron selection will be presented as well as three different methods to reconstruct the kinematic variables which all require knowledge of the scattered electron. The offline calibration of the SpaCal is performed with the help of one of these methods and control plots are presented here. The efficiency of the BDC tracker in front of the SpaCal is studied in detail in subsection 4.3.3. Finally, the QED radiation contributions are explained together with the manner they are treated in this analysis.

4.3.1 Scattered Electron Selection

The DIS sample is selected using the backward SpaCal calorimeter where the scattered electron is detected. The SpaCal energy and angle resolution allows a very precise measurement of the kinematics. But above all, it has the power to select the true scattered electron and therefore rejects photoproduction background. The high cross section of photoproduction interaction brings a non negligible number of events where a hadron can be miss-identified as the scattered electron. The main criteria of the scattered electron candidate can be found in table 4.6.

Most of these requirements fight against photoproduction background. Very few hadrons which move backwards have an energy larger than 8 GeV. This is mainly due to the fact that for $y < 0.5$ the scattered electron energy and angle are larger than the hadronic jet energy and angle. Indeed, $\tan\frac{\theta_e}{2}$ is equal to $\frac{1-y}{y}\tan\frac{\theta_{jet}}{2}$. Moreover, a true electron is seldom showering in the hadronic SpaCal. It has a more condense electromagnetic shower than a hadron and therefore a smaller cluster radius. By asking for a track in the BDC with a small projected distance from the centre of the SpaCal cluster, background coming from π^0 decay photons is rejected. Before the collision, the quantity $E - p_z$ (defined in equation 4.8) is equal to $2 \cdot E_e$. A lost scattered electron close to the beam pipe will result in a small total reconstructed $E - p_z$ value after the interaction. Therefore the cut on $E - p_z$ increases the purity of the scattered electron sample by rejecting photoproduction background events. Moreover, it reduces as well the contribution of QED radiative events.

Independently of the trouble to get rid of photoproduction background, some additional care is necessary. In order to have a fully contained shower, part of the inner most SpaCal region has to be suppressed. For this the variable $r_\theta = (z_{\text{cluster}} - z_{vtx}) \cdot tan(\theta)$ was used instead of simple geometrical cuts because it allows beam displacements between data and Monte Carlo simulation. Events with high value of $\rho_{\text{cluster}} = \sqrt{x^2_{\text{cluster}} + y^2_{\text{cluster}}}$ have to be rejected because the detector simulation results in too large a BDC inefficiency.

Scattered Electron Candidate	
Energy E'_e	> 8 GeV
Hadronic SpaCal Energy	< 0.5 GeV
Hadronic SpaCal Energy/E_e	< 0.03
Linear Cluster Radius	< 4 cm
Reweighted Cluster Radius	< 4 cm
Number of BDC hits	> 3
Distance Cluster-BDCtrack	< 1.5 cm
$E - p_z$	> 35 GeV
SpaCal Acceptance Cut r_θ	> 8.9 cm
ρ_{cluster}	< 74 cm

Table 4.6: Scattered electron selection criteria applied to the highest energetic cluster in the electromagnetic SpaCal.

4.3.2 Reconstruction of the Kinematics

There are several empirical methods to determine the kinematics of the ep collision [59]. The accuracy of the kinematic measurement over the entire kinematic range is of importance for the precise measurement of single and double differential cross sections and for the determination of x_g. For the final cross sections presented in this work the kinematic variables are calculated with the so called electron method. The double angle method allows us to check the SpaCal energy calibration. The full analysis is also performed with the sigma method to estimate systematic errors due to the event kinematic determination but also to QED radiations. The three methods are described and discussed below.

The Electron Method

The energy E'_e and the polar angle θ_e of the scattered electron allow to fully determine the event kinematics. After neglecting the electron and proton masses the kinematic variables are given by:

$$Q^2_e = 4E_eE'_e\cos^2\left(\frac{\theta_e}{2}\right) \qquad y_e = 1 - \frac{E'_e}{E_e}\sin^2\left(\frac{\theta_e}{2}\right)$$
$$x_e = \frac{Q^2_e}{y_e s} = \frac{\cos^2\left(\frac{\theta_e}{2}\right)}{1-\frac{E'_e}{E_e}\sin^2\left(\frac{\theta_e}{2}\right)}\frac{E'_e}{E_p}. \tag{4.4}$$

The advantage of the electron method comes from its simplicity. Moreover, for relative small Q^2 it is based exclusively on the SpaCal detector. Nevertheless, it requires a very good resolution of the scattered electron energy and polar angle measurements. As a matter of fact, The Q^2 resolution is identical to the scattered electron energy resolution for small polar angle:

$$dQ_e^2 = \frac{Q_e^2}{E_e'} dE_e' + Q_e^2 \tan(\theta_e/2) d\theta_e \quad \rightarrow \quad \frac{dQ_e^2}{Q_e^2} \approx \frac{dE_e'}{E_e'} \text{ for small } \theta_e. \tag{4.5}$$

The x and y resolutions degrade towards lower y where the calibration of the energy scale becomes essential as shown by the relations:

$$\begin{aligned} \frac{dx_e}{x_e} &= \frac{1}{y_e} \frac{dE_e'}{E_e'}, & (4.6) \\ \frac{dy_e}{y_e} &= \frac{1}{y_e} \frac{E_e'}{E_e} \sin^2\left(\frac{\theta_e}{2}\right) \frac{dE_e'}{E_e'}, & (4.7) \end{aligned}$$

for θ_e constant. However, this effect is restricted in this analysis since y is asked to be larger than 0.05.

In addition, contributions from collinear QED radiation of the incident electron get large at high y and low x. This results in migrations in the kinematic variables when they are calculated with the electron method. Usually QED radiative corrections are applied to the data to take this effect into account (see subsection 4.3.5).

The Sigma Method

The sigma method takes care of the possible QED radiations emitted by the incoming electron. To account for these radiations, the electron beam energy E_e is replaced by the energy of the electron at the photon vertex. This energy is measured as $(E - p_z)/2$ where:

$$E - p_z = \sum_{h=hadrons} (E_h - p_{z,h}) + E_e'(1 - \cos\theta_e) = (E - p_z)_{had} + E_e'(1 - \cos\theta_e). \tag{4.8}$$

Technically, to get y_Σ and Q_Σ^2 with the sigma method, the beam energy E_e has to be replaced by $(E - p_z)/2$ in equation 4.4:

$$y_\Sigma = 1 - \frac{E_e'}{\frac{E - p_z}{2}} \sin^2\left(\frac{\theta_e}{2}\right) = \frac{E - p_z - E_e'(1 - \cos\theta_e)}{E - p_z} = \frac{(E - p_z)_{had}}{E - p_z} \tag{4.9}$$

$$\begin{aligned} Q_\Sigma^2 &= 4\frac{E - p_z}{2} E_e' \cos^2\left(\frac{\theta_e}{2}\right) = (E - p_z) E_e'(1 + \cos\theta_e) \\ &= \frac{(E_e' \sin\theta_e)^2}{\frac{E_e'(1 - \cos\theta_e)}{E - p_z}} = \frac{(E_e' \sin\theta_e)^2}{1 - y_\Sigma}. \end{aligned} \tag{4.10}$$

The choice for x is more ambiguous. Using equation 1.2 the purist way would be to take $s = 2(E - p_z)E_p$. However, the $E - p_z$ measurement relies on quantities with relative large systematic errors. Thus, it is more appropriate to choose $s = 4E_eE_p$. In this work the second case has been used. Finally, the following definitions are obtained:

$$Q^2_\Sigma = \frac{(E'_e \sin\theta_e)^2}{1-y_\Sigma} \qquad y_\Sigma = \frac{(E-p_z)_{had}}{E-p_z}$$
$$x_\Sigma = \frac{Q^2_\Sigma}{y_\Sigma s} = \frac{Q^2_\Sigma}{y_\Sigma 4E_eE_p}. \tag{4.11}$$

Here appears another physical interpretation of Q^2. The variable Q^2 represents here how much transverse momentum p_t^{had} is involved in the process scaled by the inverse of the incident electron energy carried by the scattered electron in the proton rest frame as expressed in the following equation:

$$Q^2 = \frac{p_t^{had}}{(E'_e/E_e)^{proton}_{rest\ frame}}. \tag{4.12}$$

In this work $(E-p_z)_{had}$ is obtained experimentally with the simultaneous use of the trackers and the calorimeters. The quantitiy $(E-p_z)_{had}$ is built up from all well measured tracks found in the central and forward tracking system and from all clusters without any corresponding tracks. The energy measured in the calorimeter cells around the impact point of a good track is ignored thus avoiding double counting. The y_Σ resolution is better than the one obtained with the electron method especially for very small values of y, as given by:

$$\frac{dy_\Sigma}{y_\Sigma} = (1-y_\Sigma)\sqrt{\left(\frac{dE'_e}{E'_e}\right)^2 + \left(\frac{d(E-p_z)_{had}}{(E-p_z)_{had}}\right)^2} \quad \text{for } \theta_e \text{ constant.} \tag{4.13}$$

Moreover, the sigma method does not suffer from kinematic migration due to QED radiations. However, the resolution for Q^2 is poorer than the one obtain with the electron method. This latter is confronted to the sigma method by looking at the ratio y_e/y_Σ in different y_e ranges as presented in figure 4.1. The figure shows that in the low y_e region, the data y_e/y_Σ distribution reveals the energy resolution of the scattered electron which degrades the y_e resolution by a factor $1/y_e$ (see equation 4.7). At large y_e the two methods show better agreement as the r.m.s. of the y_e/y_Σ distribution decreases. The tail at high y_e/y_Σ shows an enhancement of events with $y_e > y_\Sigma$ and is more pronounced at high y_e. From the Monte Carlo studies, this corresponds to a reconstructed y_Σ smaller than the true y. A very good agreement between the data and the Monte Carlo is observed in figure 4.1 with however a small shift for $0.05 < y_e < 0.25$ in the case of the 1997 data.

The sigma method allows us to estimate the systematic error coming from the use of the electron method in the calculation of the final cross section given in this work. This is done by performing the complete analysis with the sigma method instead of the electron method (see section 5.2). The small shift in figure 4.1 between data and Monte Carlo for the 1997 sample is far below the error due to the energy scale. The difference between the cross sections where the kinematic variables are determined with one or the other method thus correctly describes the kinematic method dependency.

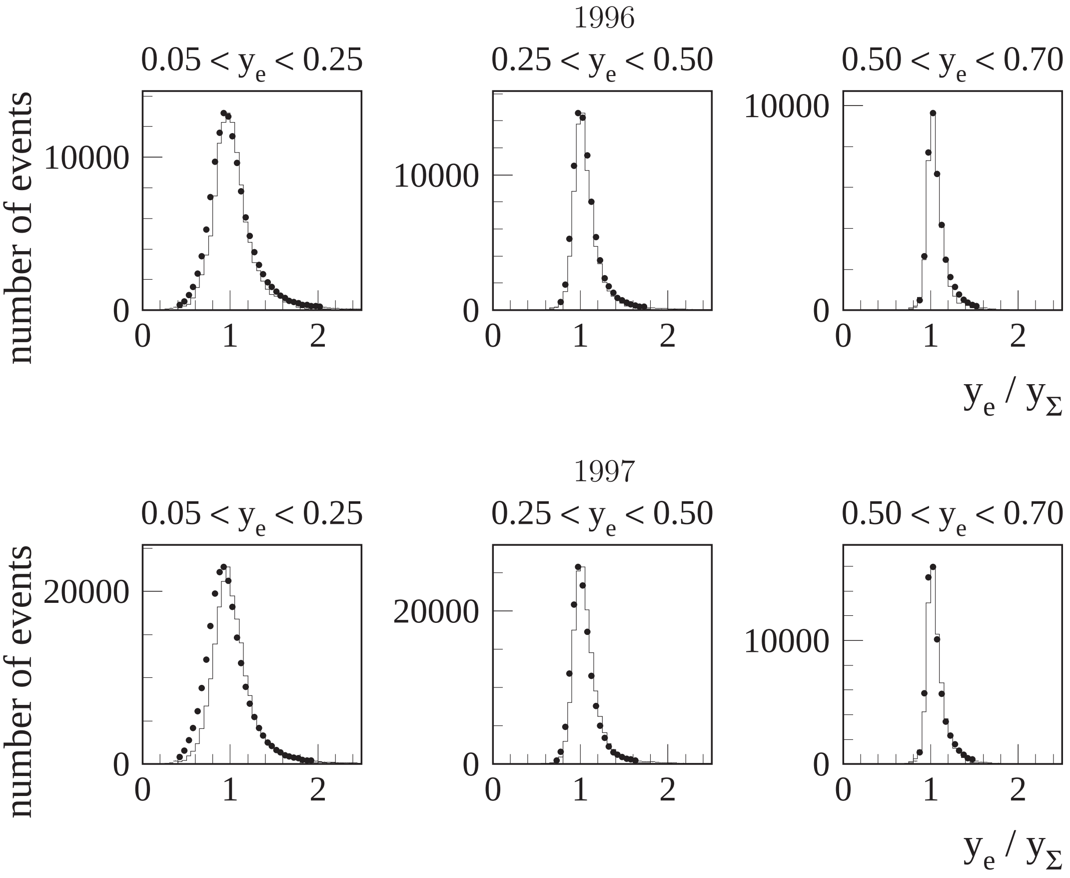

Figure 4.1: Ratio y_e/y_Σ in different y_e ranges for the two running periods 1996 and 1997 after the complete electron selection. Data is represented by points and the detector simulation using the AROMA Monte Carlo generator by open histograms.

The Double Angle Method

The double angle method is based on the angle measurements of the hadrons and of the scattered electron. This method is at first order independent of the hadron energy resolution and not in the least dependent on the scattered electron energy measurement. Therefore the double angle method is be used to improve the energy calibration of the scattered electron in the SpaCal (see subsection 4.3.3).

The hadronic final state polar angle γ is defined as:

$$\cos\gamma = \frac{(\sum\limits_h p_{x,h})^2 + (\sum\limits_h p_{y,h})^2 - (\sum\limits_h (E_h - p_{z,h}))^2}{(\sum\limits_h p_{x,h})^2 + (\sum\limits_h p_{y,h})^2 + (\sum\limits_h (E_h - p_{z,h}))^2}. \tag{4.14}$$

In the quark parton model the angle γ represents the polar angle of the struck quark. The definitions of the double angle kinematics can be derived by using the four-momentum conservation, they are given by:

$$Q^2_{DA} = \frac{4E_e^2 \sin\gamma \cdot (1+\cos\theta_e)}{\sin\gamma + \sin\theta_e - \sin(\gamma+\theta_e)} \qquad y_{DA} = \frac{\sin\theta_e \cdot (1-\cos\gamma)}{\sin\gamma + \sin\theta_e - \sin(\theta_e+\gamma)}$$
$$x_{DA} = \frac{Q^2_{DA}}{y_{DA} s} \tag{4.15}$$

For scattered electrons within the SpaCal acceptance ($153^\circ < \theta_e < 177.5^\circ$) the double angle method gives good results at intermediate y ($0.05 < y < 0.3$) and $x > 0.01$. For very low y the hadronic final state polar angle approaches zero degree ($\frac{1-y}{y} \tan\frac{\gamma}{2} = \tan\frac{\theta_e}{2}$) and therefore the fraction of undetected transverse momentum increases. This results in a bad resolution of γ. In the SpaCal acceptance for θ_e the hadronic final state polar angle gets close to 180° already for $y > 0.3$ leading to a bad resolution of γ again.

4.3.3 Energy Calibration

Various calibration methods provide multiplicative calibration constants for each SpaCal cell [60]. Within the frame of this analysis the scattered electron energy carries an additive calibration. It consists of a cell dependent calibration [61] determined when the measured cluster energy differs of more than a few percent from the scattered electron energy E'_{DA} deduced from the double angle method:

$$E'_{DA} = \frac{E_e(1-y_{DA})}{\sin^2\left(\dfrac{\theta_e}{2}\right)}. \tag{4.16}$$

The improvement of the energy scale when using this additive calibration is checked within a kinematic range where the double angle method gives good results:

$$0.05 < y < 0.2. \tag{4.17}$$

This is illustrated in figure 4.2 where the ratio of E'_{DA} over the measured energy of the scattered electron E'_e is plotted with and without the calibration for both data and Monte Carlo simulation. The ratio is shown for three radial regions of the SpaCal. An improvement in the SpaCal energy resolution is observed as well as a good agreement in the behaviour of the simulation.

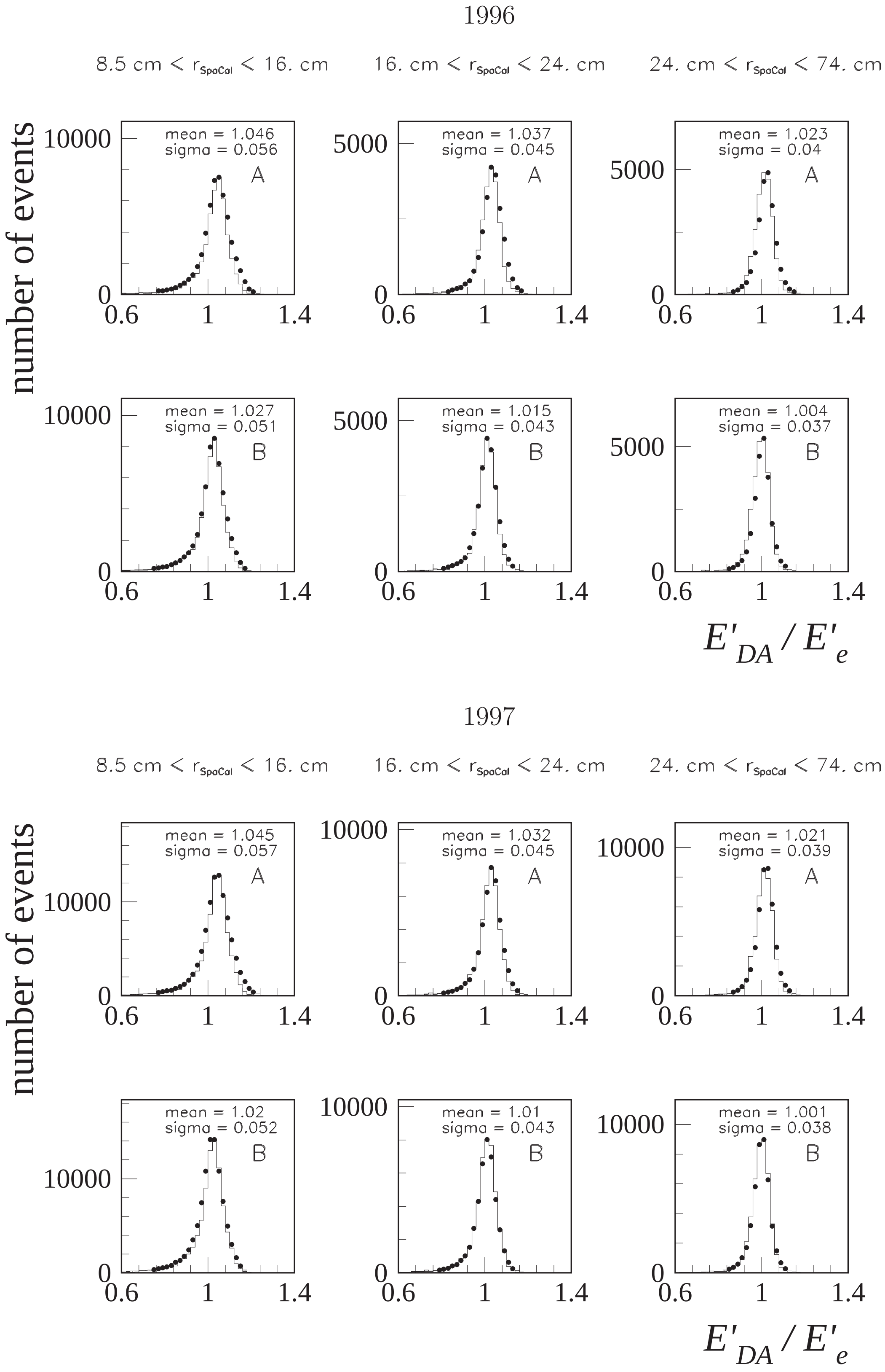

Figure 4.2: Ratio of the deduced scattered electron energy E'_{DA} using the Double Angle method (DA) over the scattered electron energy E'_e measured in the SpaCal for 1996 and 1997 data (points) and detector simulations using the AROMA Monte Carlo generator (open histograms). A: without DA SpaCal energy calibration, B: with DA SpaCal energy calibration.

4.3.4 BDC Efficiency

The BDC algorithm to find the *BDC electron track* is quite elaborated [62] because up to thirty BDC tracks can be reconstructed in a cylinder of 1.5 cm around the electron impact point. The main reason for this is the electron pre-shower where the scattered electron interacts with the dead material between the interaction point and the BDC. In the following the BDC efficiency is defined as the probability of finding the *BDC electron track* with 1.5 cm around the electromagnetic cluster in the SpaCal. The left plots of figure 4.3 show the BDC inefficiency as a function of the radial position ρ_{cluster} of the SpaCal cluster centre of gravity. For the 1996 and 1997 data an inefficiency of 2% is found. At $\rho_{\text{cluster}} \approx 27cm$, region between small and large BDC cells, the inefficiency reaches 8% for the 1996 data and 10% for the 1997 data. This behaviour is not described by the Monte Carlo simulation therefore it has been tuned to reproduce the data behaviour. This can be appreciated in the right plots of figure 4.3.

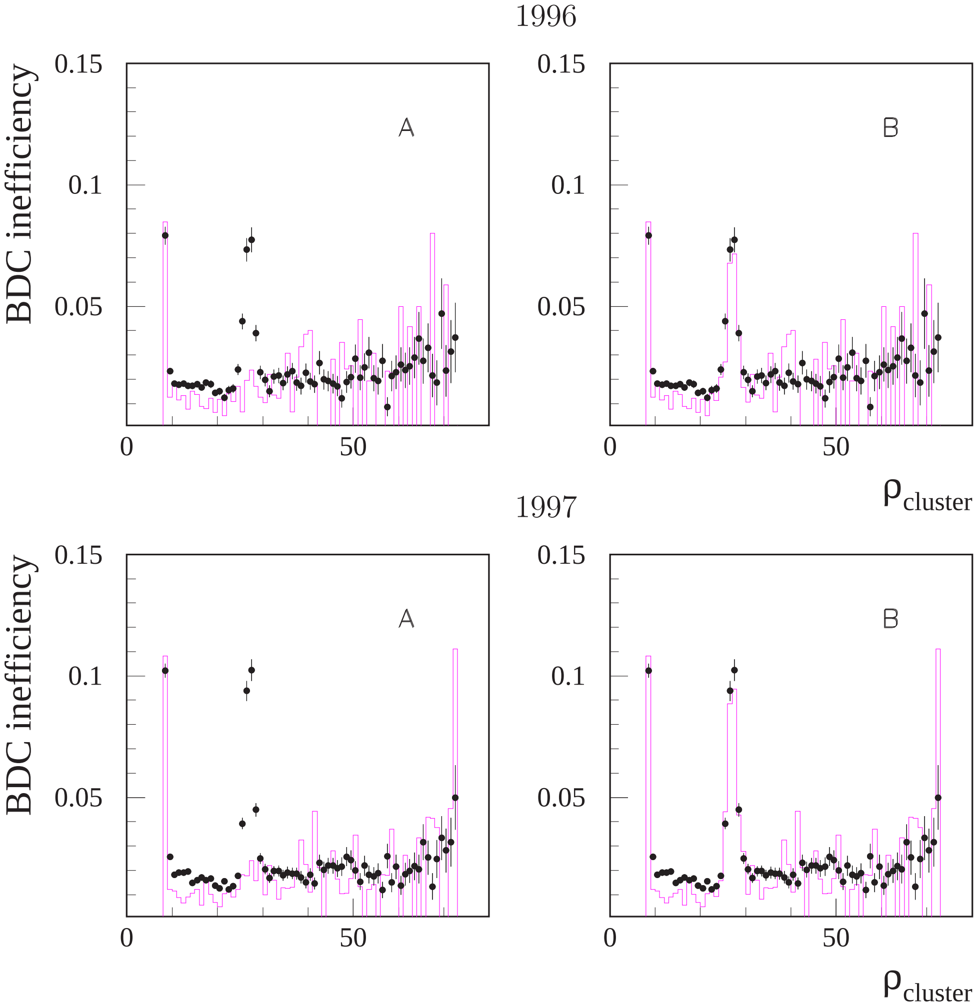

Figure 4.3: BDC inefficiency as a function of the radial position of the SpaCal cluster centre of gravity in 1996 and 1997 for data (points) and the detector simulations using the AROMA generator (open histograms). On the left plots (A) the standard detector simulation is shown. On the right plots (B) the simulation is tuned to reproduce the data.

4.3.5 QED Radiative Corrections

The experimentally measured cross sections can be fully described by perturbative theory only when all orders are included. Higher orders of the electroweak interaction are seldomly included within calculations. Therefore, in order to compare the measurement with the Born cross section predicted by theory, it is necessary to subtract to the measurement contributions from higher order processes. This is also compulsory for the extraction of the gluon density (see chapter 6).

Within the Q^2 range considered in this work (1 GeV^2 $< Q^2 <$ 100 GeV^2) the weak interaction processes can be neglected since their matrix elements are suppressed by the inverse of the squared boson mediator mass. The quarkonic QED radiations are also negligible (matrix element $\propto q_q^2/m_q^2$).

The QED radiative events at HERA are usually classified in three categories:

- The bremsstrahlung process corresponds to the poles in both the virtual electron and photon propagators. It is dominated by the Bethe-Heitler process $ep \rightarrow ep\gamma$ where the proton remains intact (elastic scattering). This process does not contribute to the D^{*+} cross section for $Q^2 > 1$ GeV^2.

- Process where Q^2 is close to zero and where the invariant mass squared of the virtual electron is large can be assimilated as a quasi real QED Compton process. The corresponding events are characterised by an empty detector except for two electromagnetic clusters in the backward region. Since a track reconstructed vertex is required in this analysis no QED Compton events enter the selected sample.

- Radiative DIS events are defined as events with large Q^2 and with small virtual electron invariant mass. Those events contribute to the measured D^{*+} cross section so that a correction is necessary to be able to quote the Born cross section.

QED Radiative Corrections in DIS

To come back to the Born cross section only radiative DIS events have to be considered. Moreover for final state radiations the radiated photon is collinear to the scattered electron so that they contribute to the same electromagnetic cluster. In this case the kinematics are not affected. The QED initial state radiations in DIS are characterised by a radiated photon collinear to the incoming electron. When calculating the kinematics at the exchange photon vertex with the electron method an error is introduced. This results in migration in the kinematics.

In this work radiative corrections are applied by reweighting the data depending on the reconstructed Q_e^2 and y_e. However, no weight is applied when the kinematic variables are determined with the sigma method which in a good approximation already take into account the QED radiation effects. The weighting function is obtained from the programme HECTOR [63].

4.4 D^{*+} Offline Selection

For the reconstruction of the D^{*+} meson using the $D^{*+} \rightarrow D^0\pi_s^+ \rightarrow (K^-\pi^+)\pi_s^+$ channel, particle mass assumptions were applied to all combinations of three tracks taken from a selected sample of tracks measured in the CJC. This restricts the analysis to the central rapidity region from the start. When the hypothetic K^- and π^+ result in a D^0 meson with reconstructed invariant mass $m_{K\pi}$ close to the mass of the D^0 meson m_{D^0} all possible π_s^+ candidates will be considered to reconstruct the D^{*+} meson. In the studied channel one takes advantage of the fact that the mass of the D^{*+} meson is nearly the sum of the D^0 meson and pion mass. The D^0 and π_s^+ direct daughters of the D^{*+} are therefore produced nearly at rest in the D^{*+} rest frame. Boosting from the D^{*+} rest frame to the laboratory frame will give to the D^0 meson most of the D^{*+} momentum because of its larger mass compared to the pion mass. The pion π_s^+ coming directly from the D^{*+} has consequently the smallest momentum among the three decay particles ($K^-\pi^+\pi_s^+$). The best resolution can be achieved in a mass distribution dominated by the π_s^+ momentum resolution ($\Delta p_\perp/p_\perp \propto p_\perp$). This is the case of the Δm distribution:

$$\Delta m = m_{K\pi\pi_s} - m_{K\pi}. \tag{4.18}$$

The number of reconstructed D^{*+} is the result of a fit in the Δm distribution.

4.4.1 Tracks Selection

In order to reach a good mass resolution as well as a good signal to background ratio, a selection of well measured tracks has to be considered as input for $K^-\pi^+\pi_s^+$ candidates. The analysis is performed on the vertex fitted track bank. Thus, only tracks which can be linked to a vertex within the nominal interaction in z are considered. The detailed list of the track requirements can be found in table 4.7. They are different for the three candidates and for the two year measurements because of different detector behaviour. The quantities which characterise a track are described in subsection 2.2.3. A good combination of track segments in the inner and outer chambers of the CJC is achieved by asking a maximum track length and a minimum starting radius. A minimum number of hits, used in the final fit of a track, is required in order to reduce the probability that some very short track segments are linked together by chance. Both the cuts on the track length and the number of hits allow to select tracks with accurate measurement of the helix parameters. Cuts on the d_{ca} reject tracks coming from proton beam pipe interactions, cosmics or tracks resulting from random fits.

Some other important points have to be considered and result in the motivation of the transverse momentum cut values and in an additional weight for the Monte Carlo tracks. The CJC simulation is suffering from a simplified description of the energy loss in the chambers. Only an energy loss as a whole is generated per cell and the drift distance to the wire is simply smeared with a Gaussian. Moreover, no dependence either on particle type, track angle with respect to the cell or momentum and gas amplification is taken into account. As a consequence, the CJC simulation results in perfectly fitted tracks even when track efficiency is low. The simplified CJC simulation leads also in a wrong description of bad CJC regions and of low $p_\perp$ tracks in general. In this work the Monte Carlo tracks have been subject to an additional weight which improve the description of the bad regions of the CJC [64]. Recent studies have shown that in 1997 the ϕ region where the data revealed an abnormal lower number of reconstructed tracks was in fact suffering of a readout problem. The consequence was that part of the readout information was mixed with the next event. The *ad hoc* correction performed by applying an empirical weight to the Monte Carlo tracks remains adequate as long as the track selection criteria are stronger than those required on the trigger Level 4 which has been carefully done here (see table 4.4 and table 4.7 [1]).

Year 1996	Kaon	Pion	Slow Pion
Transverse Momentum	> 250 GeV/c	> 250 GeV/c	> 120 GeV/c
Track Length	> 10 cm	> 10 cm	> 10 cm
Track Starting Radius	< 30 cm	< 30 cm	< 30 cm
Number of Hits in CJC1	>= 5	>= 5	>= 5
Number of Hits used for $\frac{dE}{dx}$	>= 10	>= 10	no cut
d_{ca}	< 1 cm	< 1 cm	< 1 cm
$\lvert z_{ca} - z_{vtx} \rvert$	< 20 cm	< 20 cm	< 20 cm
$\lvert d_{ca} * sin(\theta) \rvert$	< 0.5 cm	< 0.5 cm	< 0.7 cm
Particle Identification	$K1$	$\pi1$	no cut

Year 1997	Kaon	Pion	Slow Pion
Transverse Momentum	> 250 GeV/c	> 250 GeV/c	> 120 GeV/c
Track Length	> 25 cm	> 10 cm	> 10 cm
Track Starting Radius	run≤199078: < 25 cm run>199078: < 50 cm	run≤199078: < 30 cm run>199078: < 35 cm	run≤199078: < 30 cm run>199078: < 35 cm
Number of Hits in CJC1+CJC2	>= 10	>= 10	>= 10
Number of Hits used for $\frac{dE}{dx}$	>= 10	>= 10	no cut
d_{ca}	<0.45 cm	< 1.8 cm	< 1.8 cm
$\lvert z_{ca} - z_{vtx} \rvert$	run≤183000: < 9 cm run>183000: < 11 cm	< 18 cm	< 18 cm
$\lvert d_{ca} * sin(\theta) \rvert$	no cut	no cut	no cut
Particle Identification	$K2$	$\pi2$	no cut

Table 4.7: Track selection cuts for 1996 and 1997. The cuts on the normalised $\frac{dE}{dx}$ likelihood probability defining the particle identification criteria ($K1$, $K2$, $\pi1$, $\pi2$) are given in the text.

---

[1] The cuts on the track length and the track starting radius are identical at the Level 4 and in this analysis. This is justified because the CJC hits are the same at the Level 4 and after the offline reconstruction so that the track length and the track starting radius keep unchanged.

Another problem is the track efficiency for the low $p_\perp$ momentum which is quite difficult to be determined in the data (the track efficiency is 100% for tracks with $p_\perp > 200$ MeV/c). To avoid this as well as the wrong description of low $p_\perp$ tracks in the simulation a minimum transverse momentum of 250 MeV/c for the kaon and the pion coming from the D^0 is required. Unfortunately the soft spectrum of the slow pion does not allow such a cut. The difference between the data and the Monte Carlo will be taken into account in the systematics.

The Likelihood probability, LH_i, of a particle hypothesis i is calculated from an improved $\frac{dE}{dx}$ measurement based on an extensive study on the systematic dependencies of the $\frac{dE}{dx}$ measurement [65]. For a standard track selection the corrected $\frac{dE}{dx}$ value as a function of the track momentum is shown in figure 4.4 for the data and the Monte Carlo simulation. The normalised test variable LN_i for the particle hypothesis i is:

$$LN_i = \frac{LH_i}{\sum\limits_{i=p,K,\pi} LH_i}. \tag{4.19}$$

It allows particle identification in some given momentum range. For this analysis two particle identification criteria were defined for the two particle types K and π:
$K1$: for $p \leq 0.7$ GeV/c, $LN_K > 10\%$ and $LN_K > 5 * LN_\pi$
for 0.7 GeV/c $< p \leq 1.2$ GeV/c, $LN_K > 20\%$
for $p > 1.2$ GeV/c, $LN_K > 10\%$
$K2$: for $p \leq 1.2$ GeV/c, $LN_K > 5\%$
for $p > 1.2$ GeV/c $LN_K > 1\%$
$\pi1$: for $p \leq 0.7$ GeV/c, $LN_\pi > 80\%$
for 0.7 GeV/c $< p \leq 1.2$ GeV/c, $LN_\pi > 20\%$
$\pi2$: for $p \leq 1.2$ GeV/c, $LN_\pi > 1\%$
The strong criteria ($K1$, $\pi1$) were used for the 1996 data whereas the softer criteria ($K2$, $\pi2$) were used for the 1997 data. This was motivated by a worse $\frac{dE}{dx}$ description in the simulation for the 1997 detector conditions. Nevertheless, the softer particle identification requirements still allow to have a reasonable signal to background ratio while reducing systematics. The particle identification is of a big help to enhance the D^{*+} signal.

4.4.2 D^{*+} Requirements

Due to the geometrical acceptance of the detector D^{*+} candidates are limited to the pseudorapidity range:

$$-1.5 < \eta_{D^*} < 1.5. \tag{4.20}$$

Combinatorial background of low $p_\perp$ tracks is suppressed by asking

$$p_{\perp D^*} > 1.5 \text{ GeV/c and } p_{\perp K} + p_{\perp \pi} > 2 \text{ GeV/c}. \tag{4.21}$$

For previous analysis in H1 the improved $\frac{dE}{dx}$ measurement did not exist and it was compulsory to cut the low x_{D^*} region in order to reach an acceptable signal to background ratio. The present analysis is free of this cut and can therefore probe the D^{*+} cross section at low x_{D^*}, precisely were models seem to move away from the data (see figure D.16 in appendix D).

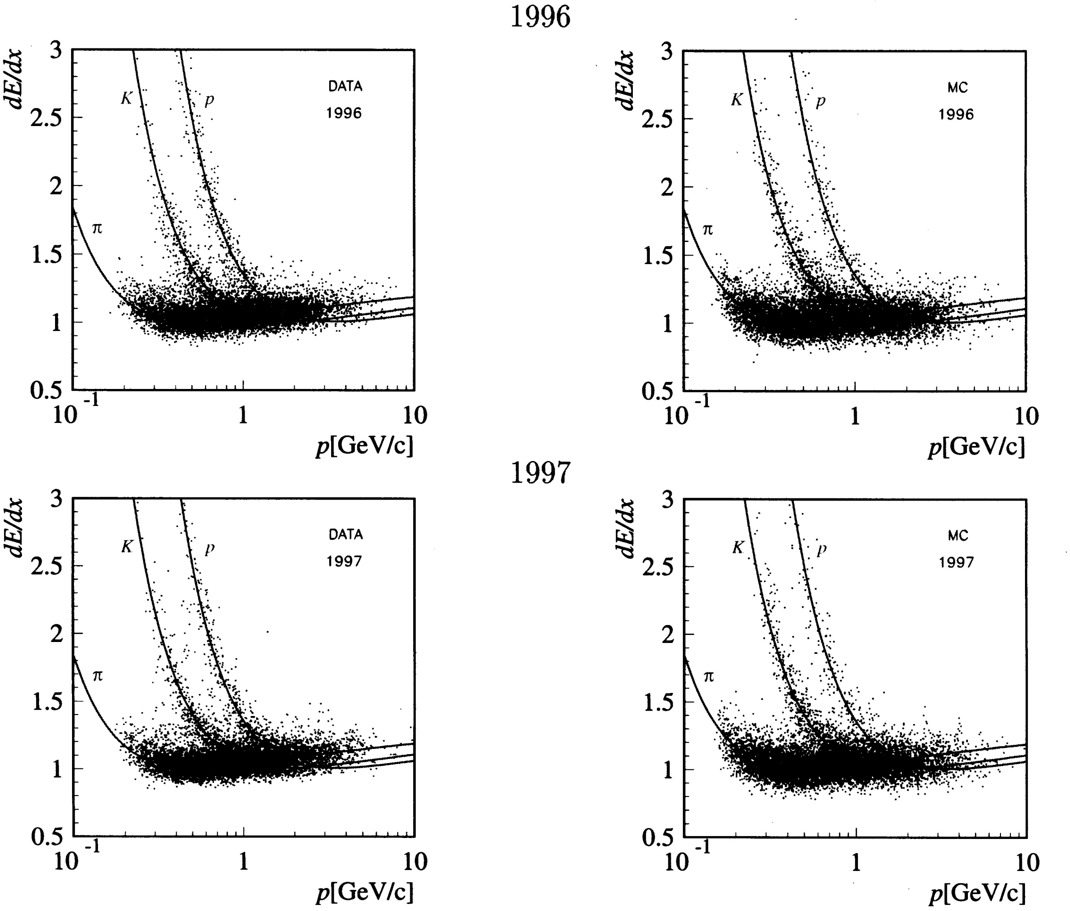

Figure 4.4: Corrected $\frac{dE}{dx}$ values as a function of the track momentum for standard tracks with number of hits used for the $\frac{dE}{dx}$ determination greater than 40. The two years are represented for both data and the AROMA Monte Carlo. The curves show the new $\frac{dE}{dx}$ parameterisation for different mass hypotheses (K, π, p)

4.4.3 Mass Reconstruction

The number of reconstructed D^{*+}, N_{D^*}, is obtained from a fit in the Δm distribution of all D^{*+} candidates within the D^0 mass window:

$$|m_{K\pi} - m_{D^0}| < 70 \text{ MeV/c}^2. \tag{4.22}$$

The Δm distribution for the D^{*+} candidates selected in this analysis is shown in the right plots in figure **??** (upper: 1996, middle: 1997, lower: 1996 and 1997 combined). The shaded histogram represents the wrong charge $(K^-\pi^-)\pi_s^+$ candidates giving a good description of the combinatorial background. The fit function is composed of a Gaussian centred at the nominal Δm mass plus the two-body phase space background:

$$\begin{aligned} f(\Delta m) &= \frac{\text{P4}}{\sqrt{2\pi}\cdot \text{P5}\cdot B}\cdot e^{-\frac{1}{2}\left(\frac{\Delta m-\text{P6}}{\text{P5}}\right)^2} \\ &+ \text{P1}\cdot\left(\frac{\sqrt{[(m_{D^0}+\Delta m)^2-(m_{D^0}+m_\pi)^2]\cdot[(m_{D^0}+\Delta m)^2-(m_{D^0}-m_\pi)^2]}}{(m_{D^0}+\Delta m)^3}\right)^{\text{P3}}. \end{aligned} \tag{4.23}$$

The free parameters of the fit are P1 to P6 and B is a bin size scaling factor so that P4 is the number of D^{*+} events in the Gaussian.

To constrain the background parameter P3, the wrong charge background given by $D^{*+} \to (K^-\pi^-)\pi_s^+$ is simultaneously fitted using the same two-body decay formula with parameter P2 instead of P1. The resulting parameters of the Δm fit are summarised in table 4.8 for 1996 and 1997 separately and combined. The fit yields in $952_{\pm 46}$ D^{*+} for the combined years with the peak position at $\Delta m = 145.50_{\pm 0.04}$ MeV/c^2 and the width of the Gaussian of $\sigma = 1.05_{\pm 0.06}$ MeV/c^2. The peak position agrees well with the Monte Carlo expectation and with the nominal value $\Delta m = 145.436_{\pm 0.016}$ MeV/c^2 [40].

Δm fit		Data 1996	Data 1997	Data 1996 & 1997
P1	Background Normalisation	749 ± 120	1217 ± 134	1756 ± 155
P2	Background Normalisation	756 ± 125	1272 ± 141	1804 ± 163
P3	Background Exponent	0.84 ± 0.05	0.84 $\pm$ 0.03	0.80 ± 0.03
P4	N_{D^*}	423 ± 30	547 ± 36	952 ± 46
P5	Width [MeV/c^2]	1.02 ± 0.08	1.09 ± 0.08	1.05 ± 0.06
P6	Mean [GeV/c^2]	0.14560 ± 0.00006	0.14542 ± 0.00006	0.14550 ± 0.00004
$c_{\Delta m}$	Fraction in Δm Window	0.966	0.956	0.964

Table 4.8: Results of the Δm fit after the D^{*+} selection for 1996 and 1997 separately and combined. The factor $c_{\Delta m}$ is the fraction of D^{*+} in the fitted Gaussian which is left when the Δm cut of equation 4.24 is performed.

The m_{D^0} window cut of equation 4.22 represents a loss $c_{m_{D^0}}$ of the number of D^{*+} contributing to the Δm peak. This loss is determined by evaluating the width of the peak in the D^0 mass distribution. The left plots in figure 4.5 (upper: 1996, middle: 1997, lower: 1996 and 1997 combined) represent the D^0 mass distribution for $(K^-\pi^-)\pi_s^+$ candidates which satisfy:

$$|m_{K\pi\pi_s} - m_{K\pi} - (m_{D^*} - m_{D^0})| < 2.2 \text{ MeV/c}^2. \tag{4.24}$$

The shaded histogram shows the $(K^-\pi^+)\pi_s^+$ candidates from the high Δm distribution (0.16 GeV/c^2 $< \Delta m <$0.17 GeV/c^2) and indicates the background expectation for $m_{D^0} >$ 2.05 GeV/c^2. Two signals can be observed. One from the decay $D^0 \to K^-\pi^+$ and the so called "S0" signal corresponding to the decay $D^0 \to K^-\pi^+\pi^0$ where the π^0 is not detected. At low m_{D^0} the high Δm background does not describe the m_{D^0} distribution. The difference indicates the background produced by D^0 decays different from $D^0 \to K^-\pi^+$. The peak width in the D^0 mass distribution is determined from a fit taking into account the two signal contributions plus an exponentially falling background. The results of the fit (N_{D^*}, mean and width of the $D^0 \to K^-\pi^+$ signal) as well as the fraction of the total signal left in the m_{D^0} window are listed in table 4.9. The differences between the data and the Monte Carlo are taken into account in the calculation of the D^{*+} cross section (see section 5.1).

After considering the loss due to the m_{D^0} and Δm windows, the D^{*+} rate obtained from the fit of the Δm distribution ($988_{\pm 48}$) agrees well with the rate from the m_{D^0} fit ($947_{\pm 49}$).

The Δm fits in bins of all quantities which are used for the differential cross sections presented in this work, are given in appendix D.1.

m_{D^0} Fit	Data 1996	MC 1996	Data 1997	MC 1997	Data 1996 & 1997
N_{D^*}	$414_{\pm 31}$	$5210_{\pm 93}$	$499_{\pm 37}$	$5788_{\pm 98}$	$913_{\pm 47}$
Mean [GeV/c^2]	$1.862_{\pm 0.003}$	$1.8704_{\pm 0.0004}$	$1.860_{\pm 0.003}$	$1.8696_{\pm 0.0003}$	$1.861_{\pm 0.002}$
Width [GeV/c^2]	$0.035_{\pm 0.003}$	$0.025_{\pm 0.001}$	$0.032_{\pm 0.003}$	$0.023_{\pm 0.001}$	$0.033_{\pm 0.002}$
$c_{m_{D^0}}$ Fraction in m_{D^0} Window	0.956	0.995	0.970	0.997	0.963

Table 4.9: Results of the m_{D^0} fit after the D^{*+} selection for 1996 and 1997 separately and combined and for the year dependent Monte Carlo simulations. The D^0 nominal mass is 1.8645 ± 0.0005 GeV/c^2 [40]. The factor $c_{m_{D^0}}$ is the fraction of D^{*+} in the fitted Gaussian which is left when the m_{D^0} cut of equation 4.22 is performed.

4.5 Reflections Contribution

To determine the number of D^{*+} decaying in the channel $D^{*+} \to D^0\pi_s^+ \to (K^-\pi^+)\pi_s^+$ from the Δm distribution within a given D^0 mass window the contributions due to other D^0 decay modes (reflections) have to be subtracted. Theses contributions are estimated with the help of Monte Carlo generator events.

All D^0 decay modes different from $D^0 \to K^-\pi^+$ will result in a D^0 reconstructed mass shifted from the nominal mass of the D^0 meson due to the kaon and pion mass assumption. Because of the D^0 mass window cut, the D^0 mass resolution affects the number of $D^{*+} \to (K^-\pi^+)\pi_s^+$ and the amount of reflections entering the Δm histogram. When fitting the Δm distribution with one Gaussian the amount of reflections contributing to the Gaussian depends on the Δm resolution. The reflections contribution depends on these two effects, therefore both the D^0 mass and Δm data mass resolution have to be described by the Monte Carlo generator.

The reflections have been studied using Monte Carlo events at the generator level. The amount of events necessary to have a statistical significant result is such that the simulation and reconstruction steps of the H1 detector cannot be envisaged. Since the number of reflections events (as well as the number of signal events) entering the D^0 mass window depends on the resolution achieved in the D^0 mass distribution, a smearing of the generated track momentum is necessary to reach a similar resolution as the one which is found with the simulation and reconstruction steps.

The smearing is carried out by taking into account the CJC momentum resolution and the multiple scattering which takes place at the beam pipe and at the detector walls.

The resolution in the transverse momentum $p_\perp$is given by:

$$\frac{\sigma_{p_\perp}}{p_\perp} = \alpha p_\perp + \frac{\beta}{p_\perp * (R_{length} + 21.8\ \mathrm{cm})^2}, \tag{4.25}$$

where R_{length} is the expected track length in cm. The multiple scattering is reproduced by applying a smearing in the polar and azimuthal angle in the following form:

$$\sigma_\theta = \sigma_\varphi = \gamma \frac{E}{p^2} \frac{1}{\sqrt{\sin\theta}}. \tag{4.26}$$

This results in a crude simulation of the momentum resolution achieved with the CJC.

The parameters α, β, γ in equations 4.25 and 4.26 have been adjusted in order to have the best description of the momentum resolution and of the Δm and m_{D^0} mass resolution. This results in $\alpha = 0.0105$ GeV^{-1}·c, $\beta = 20.0$ GeV·c^{-1}·cm^2, $\gamma = 0.0021$ GeV/c^2. With these sets of parameters the D^0 decay modes entering the m_{D^0} window were identified. They are listed in table 4.10.

	Branching Ratios JETSET 7.41	Branching Ratios Particle Data Book 2000	Contribution in the Δm peak
$K^-\pi^+$	0.03650	0.0383 ± 0.0009	97.0%
K^-K^+	0.00410	0.00425 ± 0.00016	1.2%
$\pi^-\pi^+$	0.00160	0.00152 ± 0.00009	0.4%
$\pi^-\pi^+\pi^0$	0.01500	0.0160 ± 0.0110	0.3%
$\pi^-\pi^+\pi^-\pi^+$	0.00750	0.0073 ± 0.0005	< 0.1%
$K^-e^+\nu_e$	0.034	0.0364 ± 0.0018	0.3%
$K^-\mu^-\nu_\mu$	0.034	0.0322 ± 0.0017	0.7%
$\pi^-e^+\nu_e$	0.002	0.0037 ± 0.0006	< 0.1%
$\pi^-\mu^+\nu_\mu$	0.002	not measured	< 0.1%

Table 4.10: Differences between branching ratios of the D^0 decay modes entering the D^0 window given by the JETSET programme and the Particle Data Book [40]. Contributions (predicted by the AROMA Monte Carlo after detector simulation and 1996 selection cuts) in the Δm peak after cutting in the D^0 mass window are given in the third column. This yields to a 3% contribution in the Δm peak from D^0 decays other than $K^-\pi^+$.

Restricting the Monte Carlo generator to those decay modes it was then possible to run the detector simulation. The third column of table 4.10 gives the contribution (predicted by the AROMA Monte Carlo generator after detector simulation and 1996 selection cuts) in the Δm peak after cutting in the D^0 mass window. This yields to a 3% contribution in the Δm peak from D^0 decays other than $K^-\pi^+$. The difference in the branching ratios between the Monte Carlo and the Particle Data Book [40] are not relevant for the decay modes which contribute significantly to the reflections number (K^-K^+, $\pi^-\pi^+$, $K^-\mu^-\nu_\mu$). The amount of reflections after the 1997 selection cuts are not significantly different within the fits accuracy. This as well as the differences in the branching ratios is taken into account in the error on the reflections contribution: $r = (3 \pm 1.5)\%$.

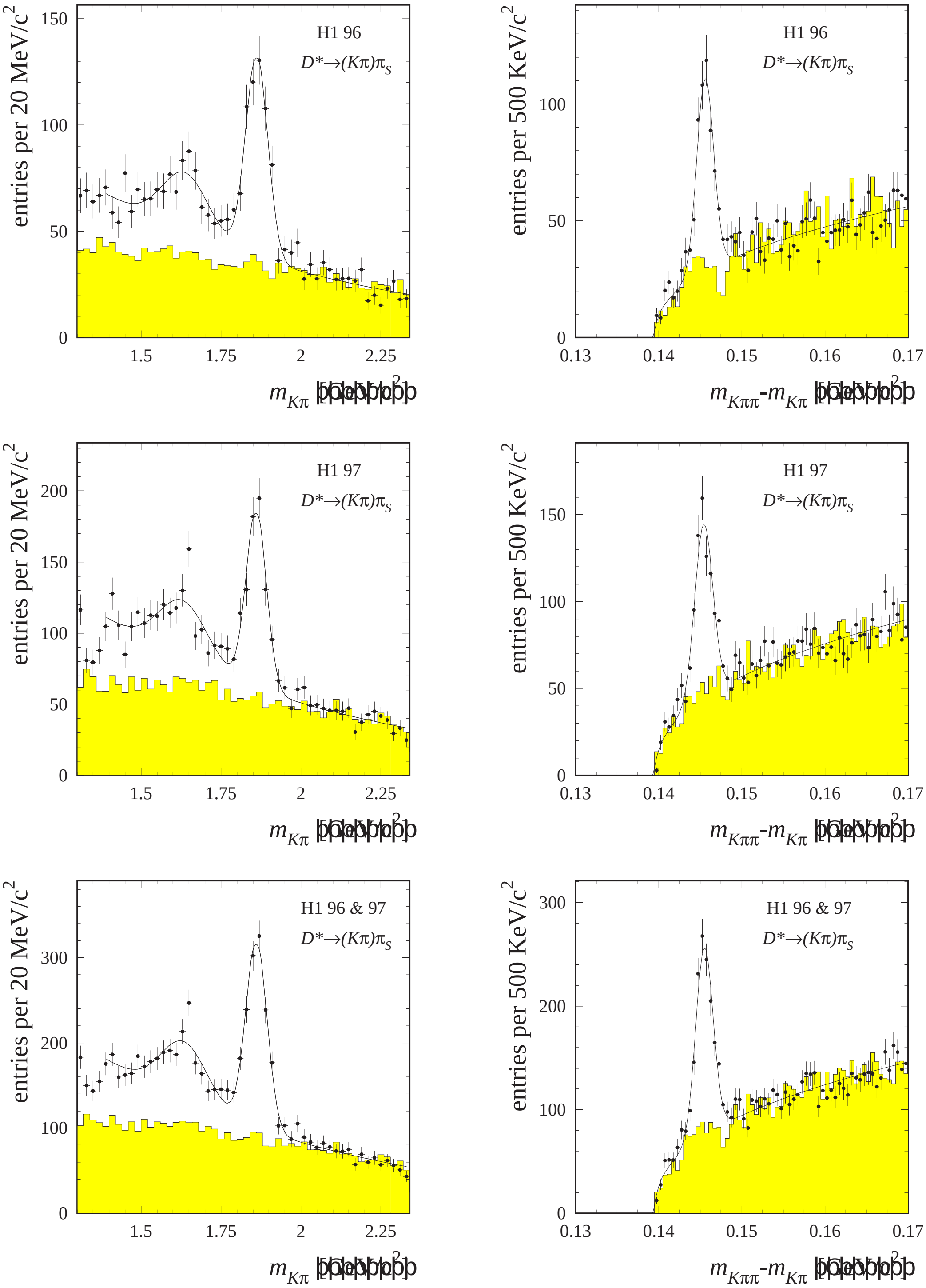

Figure 4.5: m_{D^0} (left) and Δm (right) distributions for the D^{*+} candidates selected in this analysis (upper: 1996, middle: 1997, lower: 1996 and 1997 combined). The description of the shaded histograms as well as the fit functions are given in the text.

Chapter 5

Inclusive D^{*+} Cross Sections Measurement

This chapter will present inclusive D^{*+} total, single differential and double differential cross sections deduced from the $D^{*+} \to (K^-\pi^+)\pi_s^+$ analysis. The cross sections are measured in the kinematic region 1 GeV^2 $< Q^2 <$ 100 GeV^2 and $0.05 < y < 0.7$ and in the accessible range of the D^{*+} analysis $-1.5 < \eta_{D^*} < 1.5$ and $p_{\perp D^*} > 1.5$ GeV/c. After determination of the systematics errors due to detector effects and theoretical uncertainties the cross sections measurement is compared to the NLO QCD calculations and to two differrent LO QCD Monte Carlo generators.

5.1 D^{*+} Cross Sections Calculations

The inclusive D^{*+} cross section, in the kinematic region and in the D^{*+} visible ranges, is deduced from the following quantities.

- The integrated luminosity of the two considered years $\mathcal{L} = 18.55$ pb^{-1}.
- The number of fitted D^{*+} in the data N_{D^*} corrected for QED radiation (see subsection 4.3.5). The radiative corrections δ_{rad} are estimated to 3% for the total visible cross section.
- The fraction $c^{exp}_{m_{D^0}}$ and $c^{MC}_{m_{D^0}}$ of D^{*+} mesons which are left when the m_{D^0} window cut is performed, for data and Monte Carlo respectively (see subsection 4.4.3).
- The amount of reflections r contributing to N_{D^*} (see section 4.5).
- The branching ratio $BR(K^-\pi^+\pi_s^+)$=2.59% of the decay channel $D^{*+} \to D^0\pi_s^+ \to (K^-\pi^+)\pi_s^+$ [40].
- The Monte Carlo efficiency ε_{vis}, in the kinematic and visible ranges, is the sum of the efficiencies for the two considered years scaled by the data luminosities:

$$\varepsilon_{vis} = \frac{\mathcal{L}^{96}\varepsilon^{96}_{vis}/c^{MC96}_{m_{D^0}} + \mathcal{L}^{97}\varepsilon^{97}_{vis}/c^{MC97}_{m_{D^0}}}{\mathcal{L}^{96} + \mathcal{L}^{97}}. \tag{5.1}$$

For one year measurements, the efficiency is the number of fitted D^{*+} events in the reconstructed ranges after subtrigger requirements and analysis cuts over the total number of D^{*+} in the generated ranges. This yields to an efficiency of $(27.8 \pm 0.3)\%$ and $(21.2 \pm 0.2)\%$ in 1996 and 1997 respectively, based on the AROMA Monte Carlo with $m_c = 1.5$ GeV/c^2, ϵ(Peterson) $= 0.078$, $\mu_R^2 = \mu_F^2 = \hat{s}$ and GRV 94 LO for the gluon density. The lower efficiency in 1997 is due to harder track quality requirements (d_{ca} and track length) and to the partly inefficient CJC.

In the kinematic region and D^{*+} visible ranges the inclusive D^{*+} cross section is calculated using:

$$\sigma_{vis}(ep \to eD^{*+}X) = \frac{N_{D^*} \cdot (1-r)/c^{exp}_{m_{D^0}}}{\mathcal{L} \cdot BR(K^-\pi^+\pi_s^+) \cdot \varepsilon_{vis}} \tag{5.2}$$

$$vis: \quad -1.5 < \eta_{D^*} < 1.5 \quad , \quad p_{\perp D^*} > 1.5 \text{ GeV/c} \ . \tag{5.3}$$

5.2 D^{*+} Systematic Errors

The sources of systematics on the cross sections measurement are separated in two categories. The experimental systematics sum up all systematics related to the understanding of the detector and related to the D^{*+} rate determination. The model uncertainties which change the value of the efficiency represent the theoretical systematics.

5.2.1 Experimental Systematics

- After checking the agreement for the subtrigger efficiencies between the data and the detector simulation (see subsection 4.1.2) the simulated subtrigger efficiencies are used. An overall error of 2% takes into account the errors coming from the SpaCal trigger efficiency uncertainties and the systematics when using the detector simulation subtrigger efficiencies. For the 1st and 4th $p_{\perp D^*}$ bins the systematics is risen to 5% and 4% respectively because of an only relative agreement between the data and the detector simulation.

- Track reconstruction for the detector simulation has been checked with K^0 decays on the 1994 data [66]. A similar analysis was performed on the 1996 data [64]. Using the results from the first analysis and the knowledge gained in the second analysis, an error of $+7.5\% - 3.4\%$ is estimated for the systematics related to the track reconstruction including the errors introduced by the weighting procedure described in subsection 4.4.1.

- The error on the number of D^{*+} resulting from the Δm fit is determined by changing the Δm fit procedure. The reference fit uses the wrong charge background to constrain the background parameter (see subsection 4.4.3). The fit has also been performed first without any background constraint and second using the high m_{D^0} mass background as a constraint. This results in an error of $\pm 5\%$. The same treatment has been performed in all differential distributions. Within the accuracy of the fit no bin dependency effects were found.

- An additional error on the number of D^{*+} results from the m_{D0} mass cut (see subsection 4.4.3). The Δm fit is performed for a larger m_{D0} window ($|m_{K\pi} - m_{D^0}| < 80$ MeV/c^2) and for a smaller m_{D0} window ($|m_{K\pi} - m_{D^0}| < 60$ MeV/c^2) resulting in an error of $+4\% - 2.5\%$. The reflections contribution has been taken into account when closing the m_{D^0} window ($r = 2.5\%$) or opening it ($r = 4.0\%$). No bin dependency effects were found except in the η_{D^*} distribution which reveals a polar angle dependency of the m_{D0} resolution.

- The wrong description of the low $p_\perp$ track behaviour is quantified by applying a stronger $p_\perp$ cut to the slow pion ($p_{\perp\pi_s^+} > 0.14$ GeV/c). The total cross section is then 4% larger. This systematics is applied bin wise since significant effects are observed in all distributions.

- Using the results found in [12] and [13] (see section 2.3) the scattered electron energy has been changed in the data by $\pm1\%$ at 27.5 GeV to $\pm3.0\%$ at 8 GeV assuming a linear behaviour of the energy uncertainty. Differences in the cross section ($+1.2\% - 4.0\%$) are attributed to the absolute energy scale uncertainty. Changing θ_e by ±1 mrad shows that the resolution of the polar angle induces no relevant systematics on the total cross section. Only in bins where the systematics due to the θ_e resolution approach the energy scale systematics they will be taken into account. No year dependency was observed which allows a precise estimation of the systematics after combining the two years. Finally, the systematics were estimated bin wise except in the $p_{\perp D^*}$, η_{D^*} bins where no significant changes could be observed.

- The systematics due to the event kinematic determination, here the electron method, were estimated by performing the complete analysis using the sigma method. This results in an increase of the total cross section by 4.7%. Thus, an asymmetric error of +4.7% is attributed to the systematics due to the event kinematic determination. The changes in the cross section were also taken into account bin wise except in the $p_{\perp D^*}$, η_{D^*} distributions.

- The uncertainties in the QED radiation corrections yield to a 2% systematic error for $Q^2 > 1$ GeV^2 [67].

- The contribution from photoproduction background amounts to 0.4%. This was estimated from a 132 pb^{-1} sample generated with the AROMA Monte Carlo for generated Q^2 smaller than 1 GeV^2. The photoproduction background is taken into account in the systematics.

- A systematics of ±1.5% reveals the luminosity measurement error [68].

- The subtraction of the reflections leads to a ±1.5% systematics (see subsection 4.5).

- The uncertainty in the branching ratio of the D^{*+} to $(K^-\pi^+)\pi_s^+$ from other experiments reaches ±4% [40].

The different contributions are added in quadrature which leads to a total relative error of $+13.2\% - 9.8\%$. Main contributions come from the track efficiency systematics and in the extraction of the D^{*+} signal systematics. All experimental systematics are summarised in table 5.1.

	Experimental Systematics in %	Special Treatment for Differential Cross Sections
Trigger	$+2.0 - 2.0$	1st $p_{\perp D^*}$ bin: $+5.0\%$ -5.0% 4th $p_{\perp D^*}$ bin: $+4.0\%$ -4.0%
Track Efficiency and MC Weight	$+7.5 - 3.4$	
Δm Fit	$+5.0 - 5.0$	
m_{D^0} Window	$+4.0 - 2.5$	1st η_{D^*} bin: $+0.06\%$ -0.0% 4th η_{D^*} bin: $+0.06\%$ -0.0%
$\frac{dE}{dx}$ Measurement	$+3.0 - 3.0$	
$p_{\perp\pi_s^+}$ Cut	$+4.0 - 0.0$	bin wise
E'_e, θ_e Resolution	$+1.2 - 4.0$	bin wise except $p_{\perp D^*}$, η_{D^*} bins
Event Kinematics	$+4.7 - 0.0$	bin wise except $p_{\perp D^*}$, η_{D^*} bins
Radiative Corrections	$+2.0 - 2.0$	
γp Contribution	$+0.0 - 0.4$	
Luminosity	$+1.5 - 1.5$	
Reflection Contribution	$+1.5 - 1.5$	
Branching Ratios	$+4.0 - 4.0$	
Total	$+13.2 - 9.8$	

Table 5.1: Experimental systematics in % for the inclusive D^{*+} total cross section within the visible range. Details on the systematics determination are given in the text. The third column indicates how the systematics are treated in the case of the D^{*+} differential cross sections, see text for details. Where nothing is stated the total cross section systematics is used.

5.2.2 Theoretical Systematics

In order to determine the D^{*+} cross sections, the efficiencies of the analysis are estimated with a Monte Carlo generator. Presently several Monte Carlo generators are available (see section 3.3) giving different estimations of the efficiencies. Indeed, different theoretical D^{*+} production dynamics result in different efficiencies because the efficiencies depend on $p_{\perp D^*}$, η_{D^*} etc. distributions. For the same reason, some input parameters of the generators which have an influence on the predicted cross section (see subsection 3.3.6), have also an influence on the analysis efficiencies. The theoretical systematics on the D^{*+} cross sections are given by the uncertainties on the efficiencies. Four independent sources of theoretical systematics were studied in this work.

- The D^{*+} rate in the x^*_D distribution reveals an insufficient understanding of the charm fragmentation (see figure D.16 in appendix D). The fragmentation represents the pure non perturbative part of the transition from the partons at the hard level to the final hadrons. It is described with the help of phenomenological models (see subsection 3.2.2 and section 3.3). The analysis efficiencies whithin the visible range for the different distributions were calculated for different Peterson fragmentation parameter (ϵ(Peterson) = 0.035 and 0.100) or using the standard Lund fragmentation or the HERWIG Monte Carlo instead of AROMA. The changes in the efficiency with respect to the reference (ϵ(Peterson) = 0.078) are assigned as systematics if a significant effect is observed.
- With the same procedure the systematics due to the charm mass uncertainty are estimated using $m_c = 1.3$ or 1.7 GeV/c^2.
- The factorisation and renormalisation scales in the AROMA Monte Carlo used as reference are fixed to the invariant mass of the $c\bar{c}$ system. This was changed to $Q^2 + 4m_c^2\mathrm{c}^4$ to estimate systematics due to the scale needed in the theory.
- The effect on the efficiency when including QED radiations on the lepton side, leads to a decrease of the cross section of 2.6%.

All model uncertainties are summarised in table 5.2. The model dependencies are added in quadrature which leads to a total relative error of +7.6%−4.9%. A charm mass smaller than 1.5 GeV/c^2 brings the biggest contribution to the model uncertainties (+6.7%). The second biggest contribution to the model uncertainties comes from the sensitivity of the cross section to the charm fragmentation. The last model uncertainties are of the same order.

	Model Uncertainties in %
Fragmentation	+3.5 − 3.1
Charm Mass	+6.7 − 2.3
Factorisation and Renormalisation Scale	+0.0 − 1.1
QED Radiations	+0.0 − 2.6
Total	+7.6 − 4.9

Table 5.2: Model uncertainties in % for the inclusive D^{*+} total cross section. The different theoretical models considered as well as the variations of the theoretical parameters are described in the text.

Finally, the comparison of the experimental and theoretical systematics shows that the cross section measurement is predominated by the experimental systematics. However, the systematics coming from the uncetainties on the branching ratios are not depending on the performance of the H1 detector. Taking this into account, the H1 experimental systematics are comparable to the remaining systematics.

5.3 D^{*+} Cross Sections Results

In the following, the D^{*+} total, single and double differential cross sections are given in the kinematic and visible ranges:

$$0.05 < y < 0.7 \qquad Q^2 > 1 \text{ GeV}^2 \tag{5.4}$$

$$-1.5 < \eta_{D^*} < 1.5 \qquad p_{\perp D^*} > 1.5 \text{ GeV/c}. \tag{5.5}$$

The D^{*+} visible range corresponds to the detector acceptance (-1.5 $< \eta_{D^*} <$ 1.5) and to the way of extracting the D^{*+} signal which requires $p_{\perp D^*} >$ 1.5 GeV/c.

The measurement is confronted with the predictions of the NLO DGLAP calculations implemented in the HVQDIS programme and with the predictions of two LO Monte Carlo event generators. One of them, AROMA, is based on the DGLAP QCD approach whereas in the other, CASCADE, the CCFM formalism is applied.

5.3.1 Total D^{*+} Cross Sections

The inclusive D^{*+} total cross section in the kinematic and visible ranges based on the AROMA Monte Carlo to determine the efficiency (with main parameters as given in section 5.1) is found to be:

$$\sigma_{vis}(ep \to eD^{*+}X) = \left(8.44 \pm 0.42(\text{stat.}) \begin{array}{c}+1.12\\-0.83\end{array}(\text{exp. syst.}) \begin{array}{c}+0.64\\-0.41\end{array}(\text{theo. syst.})\right) \text{nb} \tag{5.6}$$

The D^{*+} visible cross section is compared to several theoretical models in table 5.3. All programmes generate $c\bar{c}$ events but they use different values for the probability $P(c \to D^{*+})$ that a charm quark fragments in a D^{*+} meson. Therefore correction factors have been applied so that the resulting probability agrees with the most recent value measured in electron-positron collisions at LEP: $P(c \to D^{*+}) = (23.3 \pm 1.5)\%$ [57]. Prediction ranges are given by using different scales, charm mass and values of ϵ(Peterson).

The predictions of the NLO DGLAP calculations performed in the HVQDIS programme (see subsection 3.3.5) are systematically lower than the measured cross section (roughly 30%) even when assuming an extrem value for the charm mass. In the most recent publication [69] using the 1995 and 1996 H1 data a better agreement was found. This better agreement is mainly due to the fact that the predicted HVQDIS D^{*+} cross section was calculated with 27% for $P(c \to D^{*+})$ instead of the 23.3% taken here. Also the former use of a cut at low x_{D^*} supressed the corner of phase space where the data are systematically above all predictions (see subsection 5.3.2). Moreover, the analysis was performed for $Q^2 > 2$ GeV^2 instead of for $Q^2 > 1$ GeV^2 for the present analysis.

Recently the CASCADE programme based on the LO CCFM evolution equation was released (see subsection 3.3.4). Here the unintegrated gluon density is a solution of the CCFM evolution equation describing both the structure function F_2 and the cross section of forward jet production as measured by the HERA experiments. The resulting D^{*+} predicted cross sections for m_c = 1.3 GeV/c^2 and m_c = 1.5 GeV/c^2 particularly well enclose the measurement.

Like for the HVQDIS predictions the LO DGLAP AROMA Monte Carlo (see subsection 3.3.1) underestimates the D^{*+} total cross section in the visible range. For a fixed value of ϵ(Peterson), scales and charm mass, a larger cross section is predicted when the set GRV 94 LO instead of GRV 98 HO is used for the gluon density. The cross section prediction is not affected by using $\hat{s}$ or $Q^2 + 4m_c^2\mathrm{c}^4$ for the factorisation and renormalisation scales. It is interesting to note that the AROMA cross section is close to the HVQDIS prediction when using the same value of ϵ(Peterson), the same scales and the same gluon density.

The predictions of the D^{*+} visible cross section from the two DGLAP programmes HVQDIS and AROMA undershoot the data cross section whereas the CASCADE prediction agrees well with the data. The different fragmentation approaches cannot affect the predicted visible cross section as it was shown in subsection 3.3.6. Therefore, the HVQDIS and AROMA underestimation of the data can be due to an overall normalisation problem. A wrong estimation of the loss coming from the visible cuts when the predicted $p_{\perp c}$ and η_c distributions are too far from the reality is also possible. Both effects certainly contribute, because the CASCADE prediction which is 27% larger than the HVQDIS prediction in the total D^{*+} range becomes 56% larger in the visible range.

					$\sigma_{vis}(ep \rightarrow eD^{*+}X)$
Data	H1 1996 & 1997				$\left(8.44\ ^{+1.36}_{-1.01}\right)$ nb
Model	scales	ϵ(Peterson)	m_c	$g(x_g, Q^2)$	
AROMA	$\hat{s}$	0.078	1.3 GeV/c^2	GRV 94 LO	7.44 nb
AROMA	$\hat{s}$	0.078	1.5 GeV/c^2	GRV 94 LO	6.34 nb
AROMA	Q^2+$4m_c^2\mathrm{c}^4$	0.078	1.5 GeV/c^2	GRV 94 LO	6.44 nb
AROMA	Q^2+$4m_c^2\mathrm{c}^4$	0.078	1.3 GeV/c^2	GRV 98 HO	5.66 nb
AROMA	Q^2+$4m_c^2\mathrm{c}^4$	0.078	1.5 GeV/c^2	GRV 98 HO	4.85 nb
HVQDIS	Q^2+$4m_c^2\mathrm{c}^4$	0.078	1.3 GeV/c^2	GRV 98 HO	6.29 nb
HVQDIS	Q^2+$4m_c^2\mathrm{c}^4$	0.078	1.5 GeV/c^2	GRV 98 HO	5.40 nb
HVQDIS	Q^2+$4m_c^2\mathrm{c}^4$	0.035	1.3 GeV/c^2	GRV 98 HO	7.01 nb
HVQDIS	Q^2+$4m_c^2\mathrm{c}^4$	0.100	1.5 GeV/c^2	GRV 98 HO	5.17 nb
CASCADE	Q^2+$4m_c^2\mathrm{c}^4$	0.078	1.3 GeV/c^2	H1 fit	9.86 nb
CASCADE	Q^2+$4m_c^2\mathrm{c}^4$	0.078	1.5 GeV/c^2	H1 fit	8.42 nb

Table 5.3: Measured inclusive D^{*+} total cross sections in the kinematic range and D^{*+} visible range compared to different choices of theoretical models together with different factorisation and renormalisation scales, values of ϵ(Peterson), charm masses and gluon densities.

5.3.2 Single and Double Differential D^{*+} Cross Sections

The measured inclusive D^{*+} single differential cross sections in the visible range versus W, x, Q^2 and $p_{\perp D^*}$, η_{D^*}, x_{D^*} are shown in figure 5.1. The following double differential cross sections[1]

$$d^2\sigma_{vis}(ep \to eD^{*+}X)/(dp_{\perp D^*}d\eta_{D^*})$$
$$d^2\sigma_{vis}(ep \to eD^{*+}X)/(dp_{\perp D^*}dx_{D^*})$$

are shown in figure 5.2 and

$$d^2\sigma_{vis}(ep \to eD^{*+}X)/(dx_{D^*}d\eta_{D^*})$$
$$d^2\sigma_{vis}(ep \to eD^{*+}X)/(d\eta_{D^*}dQ^2)$$
$$d^2\sigma_{vis}(ep \to eD^{*+}X)/(dp_{\perp D^*}dQ^2)$$

in figure 5.3.

In these series of figures the predictions of the HVQDIS and CASCADE generators are also indicated. The same measured cross sections are compared to the predictions of the AROMA generator for two gluon density hypotheses in figures 5.4 to 5.6. The derivative of $d\sigma_{vis}(ep \to eD^{*+}X)/dlogx_g^{obs}$ with respect to the variables $\hat{s}^{obs}$, x, η_{D^*} and x_{D^*} are shown appart in chapter 6 in the context of the extraction of the gluon density.

The effects due to the detector resolution are small with respect to the chosen bin sizes in the considered distributions and are taken into account in the Monte Carlo efficiencies. The innermost error bars correspond to the statistical error. The experimental systematical errors are added in quadrature for the middle error bars. The total error bars additionally take the model systematics into account.

For the presented differential cross sections, the efficiency is determined bin wise with the AROMA Monte Carlo where the main parameters are given in section 5.1. As a check of the efficiency estimation validity the number of D^{*+} predicted by this Monte Carlo generator at the detector level and after the analysis cuts is compared, in appendix D.2, to the number of D^{*+} found in the data. A reasonable description of the D^{*+} rate is found in all distributions. However, too few D^{*+} candidates are predicted at positive η_{D^*} and low x_{D^*} and too many at negative η_{D^*} and high x_{D^*}. The corresponding efficiencies are shown in appendix D.3. The discrepancy in the rates of the η_{D^*} and x_{D^*} distributions together with a non constant efficiency could bias the cross section differentiated in the other quantities. This is controlled by the model dependency systematics.

In figure 5.1 the measured cross section within the kinematic and visible range versus x shows that the variable x is accessible between $1.6 \cdot 10^{-5}$ and 0.01. This corresponds to x_g^{obs} values between $6.3 \cdot 10^{-4}$ and 0.025 as seen in chapter 6. The cross section versus η_{D^*} has a broad structure centred at positive η_{D^*} values (D^{*+} in forward direction). It is more pronounced for low x_{D^*} values which indicates a relative soft fragmentation function.

---

[1] Single and double differential cross sections $d\sigma/dX$ and $d^2\sigma/(dXdY)$ are always meant to be *partial* differential cross sections $\partial\sigma/\partial X$ and $\partial^2\sigma/(\partial X\partial Y)$.

The double differential cross section $d^2\sigma_{vis}(ep \to eD^{*+}X)/(dp_{\perp D^*}d\eta_{D^*})$ in figure 5.2.(a) indicates a nearly flat behaviour in η_{D^*} at low $p_{\perp D^*}$ with a slight increase in the positive η_{D^*} region. For intermediate $p_{\perp D^*}$ the maximum of the cross section versus η_{D^*} is more centred. For high $p_{\perp D^*}$ this maximum is shifted to positive η_{D^*} values. Figure 5.2.(b) shows that at low $p_{\perp D^*}$ the data increase with decreasing x_{D^*}. For $p_{\perp D^*} > 2.5$ GeV/c the x_{D^*} distribution is more pronounced at intermediate x_{D^*} and is independent of $p_{\perp D^*}$. In figure 5.2.(c) the cross section in the lowest x_{D^*} bin rises with increasing η_{D^*} whereas it decreases slightly for higher x_{D^*}. This confirms the intuitive relation between low x_{D^*} and D^{*+} mesons emitted in the forward direction.

In figure 5.3.(a) the decreasing of the cross section as a function of Q^2 is nearly the same for the three η_{D^*} bins. The larger cross section for positive values of η_{D^*} in figure 5.1 is reflected in figure 5.3.(a) by a Q^2 independent rise of the double differential cross section with increasing η_{D^*}. The double differential cross section $d^2\sigma_{vis}(ep \to eD^{*+}X)/(dp_{\perp D^*}dQ^2)$ in figure 5.3.(b) is two order of magnitude higher at low Q^2 than at high Q^2 when $p_{\perp D^*}$ is small. For large $p_{\perp D^*}$ values only a factor three remains between the two extreme Q^2 bins. The steep rise of the double differential cross section in figure 5.3.(b) with decreasing $p_{\perp D^*}$ is strongly attenuated when Q^2 increases.

The experimental data are compared to the prediction of the NLO DGLAP calculations from the HVQDIS programme in figures 5.1 to 5.3 (dark shaded band). In this calculation the GRV 98 HO parton density parametrisation was used with $m_c = 1.3$ GeV/c^2, ϵ(Peterson) = 0.035 (upper limit) and $m_c = 1.5$ GeV/c^2, ϵ(Peterson) = 0.10 (lower limit). In figure 5.1 a reasonable agreement with the data is observed in the shape of the different single differential cross sections, taking into acount additional uncertainties in the other parameters of the theory (gluon density, QCD scales). However, an overall normalisation problem remains as already discussed in subsection 5.3.1. The shapes of the distributions are easier to compare in the figures of appendix E where the normalised differential cross sections are presented. Despite the good agreement with the data the HVQDIS predictions poorly describe the η_{D^*} and x_{D^*} distributions. The experimental cross section is more important in the forward direction (positive η_{D^*}) which corresponds to a softer distribution in x_{D^*}.

With a closer look on the double differential cross sections in figures 5.2.(a) and 5.2.(c) it gets clearer that the larger amount of experimental cross section at large η_{D^*} compared to the HVQDIS predictions corresponds to small $p_{\perp D^*}$ and small x_{D^*}. In figure 5.3.(a) the HVQDIS predictions are roughly 5% and 10% lower than the data for the low and intermediate η_{D^*} bin respectively and this independently of Q^2. For the highest η_{D^*} bin, the HVQDIS predictions only explain 50% of the measured cross section with a slight better agreement at high Q^2 than at low Q^2. Indeed, the HVQDIS cross section gets shifted to higher η_{D^*} when Q^2 increases. At low $p_{\perp D^*}$ the Q^2 distribution predicted by HVQDIS (see figure 5.3.(b)) is systematically too low but with a sligth different Q^2 slope as observed in figure E.3.(b) of appendix E, which stays however within the data uncertainties. At high $p_{\perp D^*}$ the HVQDIS prediction band nearly covers the data for all Q^2 bins.

The light shaded band in figures 5.1 to 5.3 is the prediction of the LO CCFM calculations implemented in the CASCADE event generator for $m_c = 1.3$ GeV/c^2 (upper limit) and $m_c = 1.5$ GeV/c^2 (lower limit). The value of ϵ(Peterson) has been fixed to 0.078. The solution of the CCFM evolution equation for the unintegrated gluon density which is used here is described in subsection 3.3.4. The predictions of CASCADE agree in shape and normalisation with the data in all the single differential cross sections shown in figure 5.1, with, however, an overestimation of the cross section at large $p_{\perp D^*}$.

From the double differential cross sections in figure 5.2 it can be observed that the overestimation of the predicted CASCADE cross section at large $p_{\perp D^*}$ is concentrated at low η_{D^*} and high x_{D^*}. Appart this small difference, the prediction of the CASACDE generator nicely follows the data behaviour in all distributions of figure 5.2.

Figure 5.3.(a) shows that already at low Q^2 the CASCADE cross section is more shifted towards larger η_{D^*} than the HVQDIS cross section. This results in an overall better description of the double differential cross section as a function of η_{D^*} and Q^2. The CASCADE prediction seems, however, to overshoot the data at large Q^2 but independently of η_{D^*}. A good agreement in the cross section versus Q^2 for the low $p_{\perp D^*}$ can be observed in figure 5.3.(b) with a slight shift towards larger Q^2 (see also figure E.3.(b)). When $p_{\perp D^*}$ is large the CASCADE predictions are systematically higher for all Q^2. Moreover, the difference between the CASCADE $p_{\perp D^*}$ slope and data seems to be more pronounced at low Q^2.

In figures 5.4 to 5.6 the cross sections measurement is compared to the LO DGLAP AROMA generator predictions. They are represented by the light and dark shaded bands when using the GRV 94 LO and the GRV 98 HO gluon density parametrisations respectively. For both shaded bands the lower limit corresponds to $m_c = 1.5$ GeV/c^2 while the upper limit corresponds to $m_c = 1.3$ GeV/c^2. The factorisation and renormalisation scales were set to $Q^2 + 4m_c^2c^4$ and ϵ(Peterson) has been fixed to 0.078.

The AROMA D^{*+} cross sections in the visible range are larger when using the GRV 94 LO parametrisation instead of the GRV 98 HO parametrisation (see table 5.3). This is the consequence of a steeper rising gluon density with decreasing x_g in the case of the LO DGLAP GRV 94 LO gluon density as seen in figure 6.1 in chapter 6. The predicted cross section is larger at high W, low x, Q^2, $p_{\perp D^*}$ and η_{D^*} values when using the LO DGLAP gluon density instead of the NLO DGLAP density. In the x_{D^*} distribution this effect is spread over the intermediate region from 0.1 to 0.5. The cross section enhancement when using the GRV 94 LO parametrisation brings a better agreement in the W, x, Q^2 distributions but a worse agreement is observed in the $p_{\perp D^*}$ and η_{D^*} distributions (see also the normalised cross sections in figure E.5). This indicates that the LO DGLAP formalism used in AROMA is not able to describe simultaneously both the kinematic dependence of the cross section and the charm production mechanism occurring predominantly in the $p_{\perp D^*}$ and η_{D^*} distributions.

The same effect is also observed for the double differential cross sections in figure 5.5. Indeed, at low $p_{\perp D^*}$ the change in the gluon density from the GRV 98 HO to the GRV 94 LO parametrisation increases the predicted cross section independently of η_{D^*} (figure 5.5.(a)) which does not improve the agreement with the exceeding data at the high η_{D^*} values. At high $p_{\perp D^*}$ the change of the cross sections when using the LO density is more pronounced at low η_{D^*} values which even more deteriorates the agreement with the shape of the data. The predicted x_{D^*} distributions in figure 5.5.(b) for the two gluon densities are nearly the same for the high $p_{\perp D^*}$ bins. Indeed, Most of the high $p_{\perp D^*}$ events correspond to large x_g values where the two gluon densities are nearly indentical. At smaller $p_{\perp D^*}$ values no improvement in the x_{D^*} distributions is observed. The cross section $d^2\sigma_{vis}(ep \to eD^{*+}X)/(dx_{D^*}d\eta_{D^*})$ in figure 5.5.(c) shows that the difference between the two bands systematically increases when η_{D^*} decreases. Therefore none of the two AROMA bands describe well the large cross section measured at high η_{D^*} and low x_{D^*}. The prediction of AROMA when using the GRV 94 LO parametrisation better describes, independently of η_{D^*}, the Q^2 dependency of the measurement as shown in figure 5.6.(a), however only at low $p_{\perp D^*}$ (figure 5.6.(b)).

From the comparison of figures 5.1 to 5.3 with figures 5.4 to 5.6 a better agreement with the data is found for the HVQDIS predictions than for the AROMA predictions when both were calculated with the GRV 98 HO parametrisation. As a matter of fact, the NLO calculations implemented in the HVQDIS programme lead to a higher cross section than the LO calculations at high W, low x and Q^2 (figures 5.1 and 5.4). The same η_{D^*} dependency is however predicted at low Q^2 (see figure 5.3.(a) and 5.6.(a)). In all $p_{\perp D^*}$ bins the HVQDIS predictions are above the AROMA predictions. This effect is even more pronounced at high $p_{\perp D^*}$ resulting in a better description of the data. These differences at high $p_{\perp D^*}$ do not affect the η_{D^*} dependency (see figures 5.2.(a) and 5.5.(a)) but a clear improvement of the Q^2 slope predicted by the HVQDIS programme compared to the AROMA results is observed in figures 5.3.(b) and 5.6.(b). The NLO calculations as a function of x_{D^*} also describe the data better than the LO calculations, independently of the D^{*+} emitted angle (figures 5.3.(c) and 5.6.(c)). The agreement is even better with increasing $p_{\perp D^*}$ as seen in figures 5.3.(b) and 5.6.(b).

To conclude, the experimental results presented here are extended down to Q^2 of 1 GeV^2 thanks to the detection of the scattered electron at smaller angles. This was achieved with the new backward components of the H1 setup. A better selection of the scattered electron and a higher precision in the kinematic variables were thus also obtained. Compared to first measurement relying on the hundred D^{*+} mesons reconstructed in the 1994 H1 data, the present work deals with one order of magnitude more D^{*+} events. The rather high number of D^{*+} mesons is the result of the increase of the luminosity delivered by HERA in 1996 and 1997 and obviously by two years measurements time. The rising cross section with decreasing Q^2 also improve the statistics. In the selection of the D^{*+} candidates further improvement was achieved by entirely suppressing the x_{D^*} cut. This was possible because of extensive use of the improved $\frac{dE}{dx}$ measurement delivered by the H1 central jet chamber.

The improvements in the experimental measurements allow for a very fine confrontation with the available theories. In parallel, progress were done in the theoretical calculations in particular the establisment of new calculations based on the CCFM formalism. The overall comparison with the three studied theoretical models shows a reasonable agreement for all of them. However, one should emphasise that the CCFM CASCADE predictions, with the settings used here, describe particularly well both the absolute cross section measurement and its behaviour as a function of the studied variables. The results of the LO and NLO DGLAP calculations in AROMA and HVQDIS generators respectively, underestimate the measurement systematically. Moreover, the AROMA calculations indicate that the use of a steep gluon density brings a better agreement in the absolute predicted cross section and on the kinematic dependencies but does not allow to correctly reproduce the charm production mechanism.

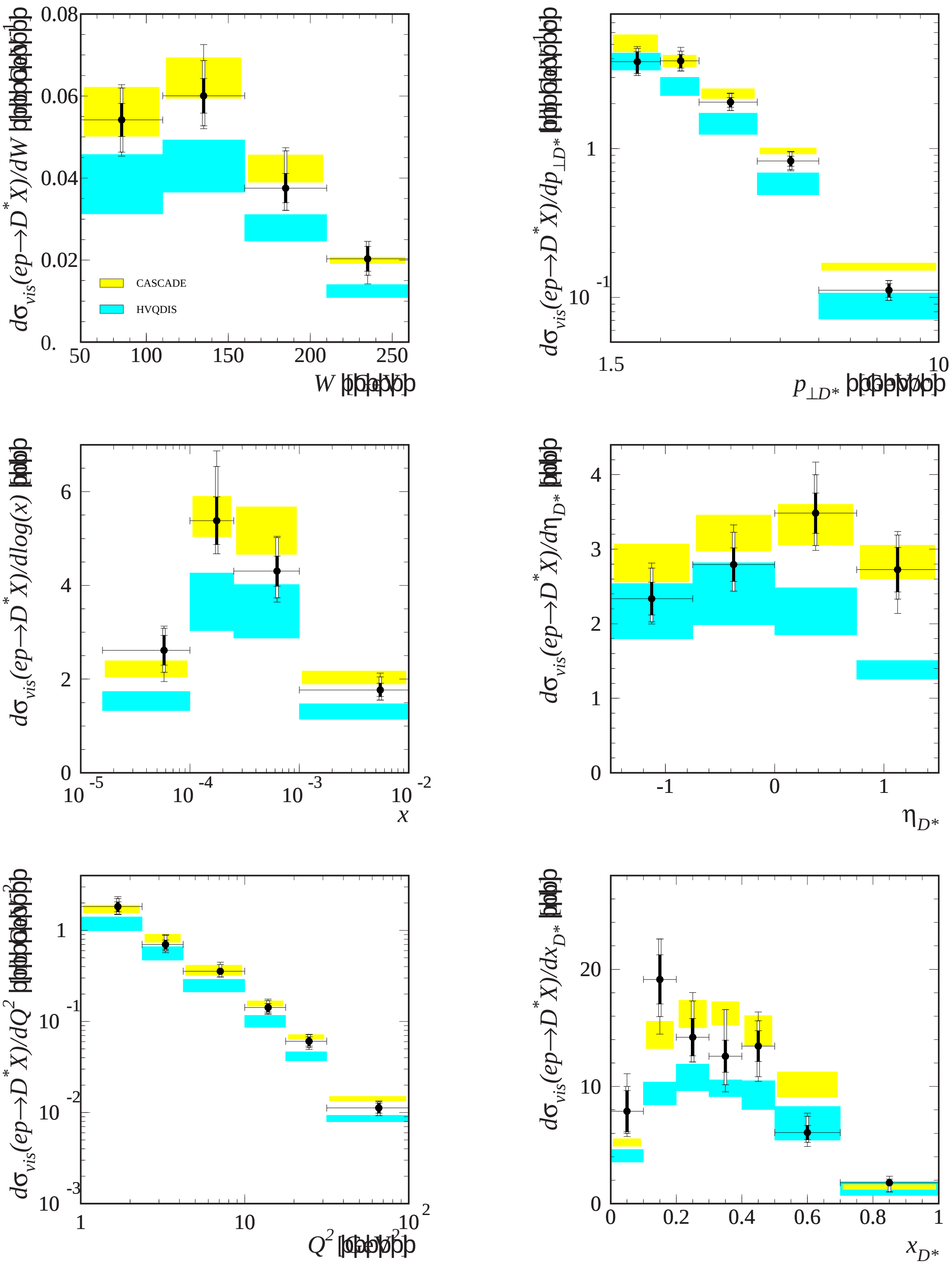

Figure 5.1: Inclusive D^{*+} single differential cross sections in the visible range versus W, x, Q^2 and $p_{\perp D^*}$, η_{D^*}, x_{D^*}. The innermost error bars correspond to the statistical error. The experimental systematical errors are added in quadrature for the middle error bars and the total error bars additionally take the Monte Carlo systematics into account. The dark shaded band is the prediction of the HVQDIS NLO DGLAP calculations for m_c = 1.3 GeV/c^2, ϵ(Peterson) = 0.035 (upper limit) and m_c = 1.5 GeV/c^2, ϵ(Peterson) = 0.10 (lower limit). The light shaded band is the prediction of the CASCADE LO CCFM calculations for m_c = 1.3 GeV/c^2 (upper limit) and m_c = 1.5 GeV/c^2 (lower limit); ϵ(Peterson) has been fixed to 0.078.

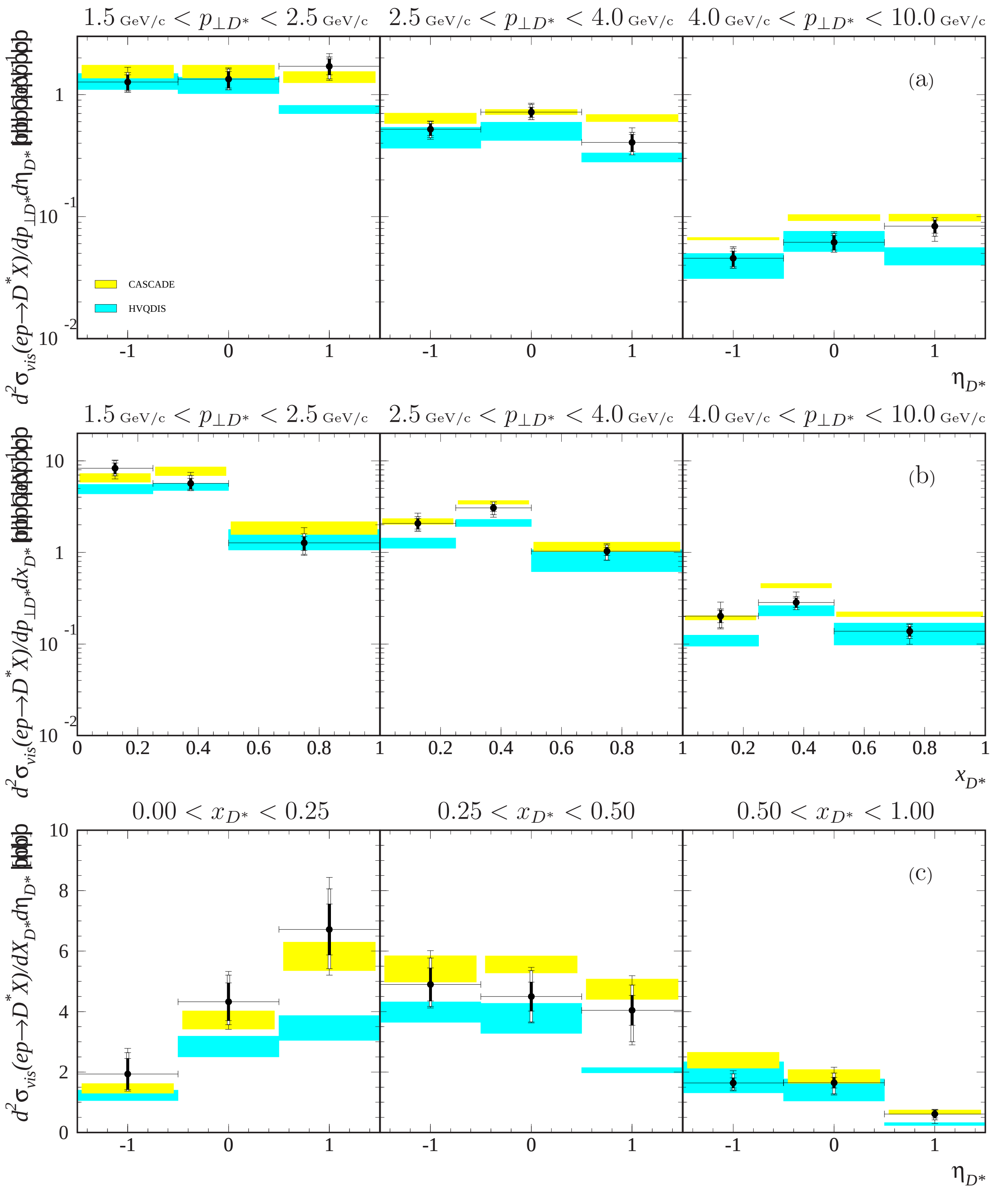

Figure 5.2: Inclusive D^{*+} double differential cross sections in the visible range for D^{*+} quantities $d^2\sigma_{vis}(ep \to eD^{*+}X)/(dp_{\perp D^*}d\eta_{D^*})$, $d^2\sigma_{vis}(ep \to eD^{*+}X)/(dp_{\perp D^*}dx_{D^*})$, $d^2\sigma_{vis}(ep \to eD^{*+}X)/(dx_{D^*}d\eta_{D^*})$. The dark and light shaded bands are described in the caption of figure 5.1.

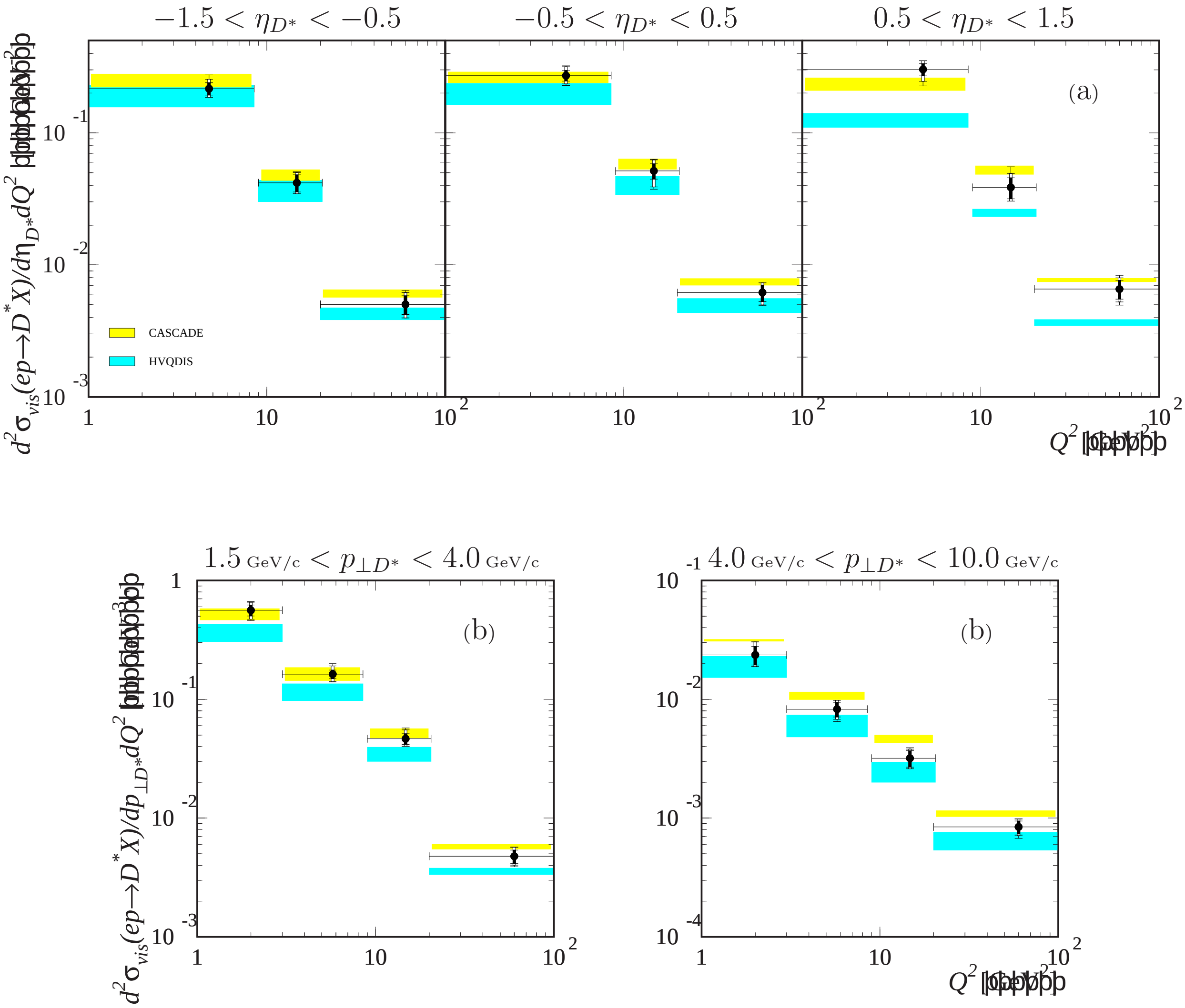

Figure 5.3: Inclusive D^{*+} double differential cross sections in the visible range $d^2\sigma_{vis}(ep \to eD^{*+}X)/(d\eta_{D^*}dQ^2)$ and $d^2\sigma_{vis}(ep \to eD^{*+}X)/(dp_{\perp D^*}dQ^2)$. The dark and light shaded bands are described in the caption of figure 5.1.

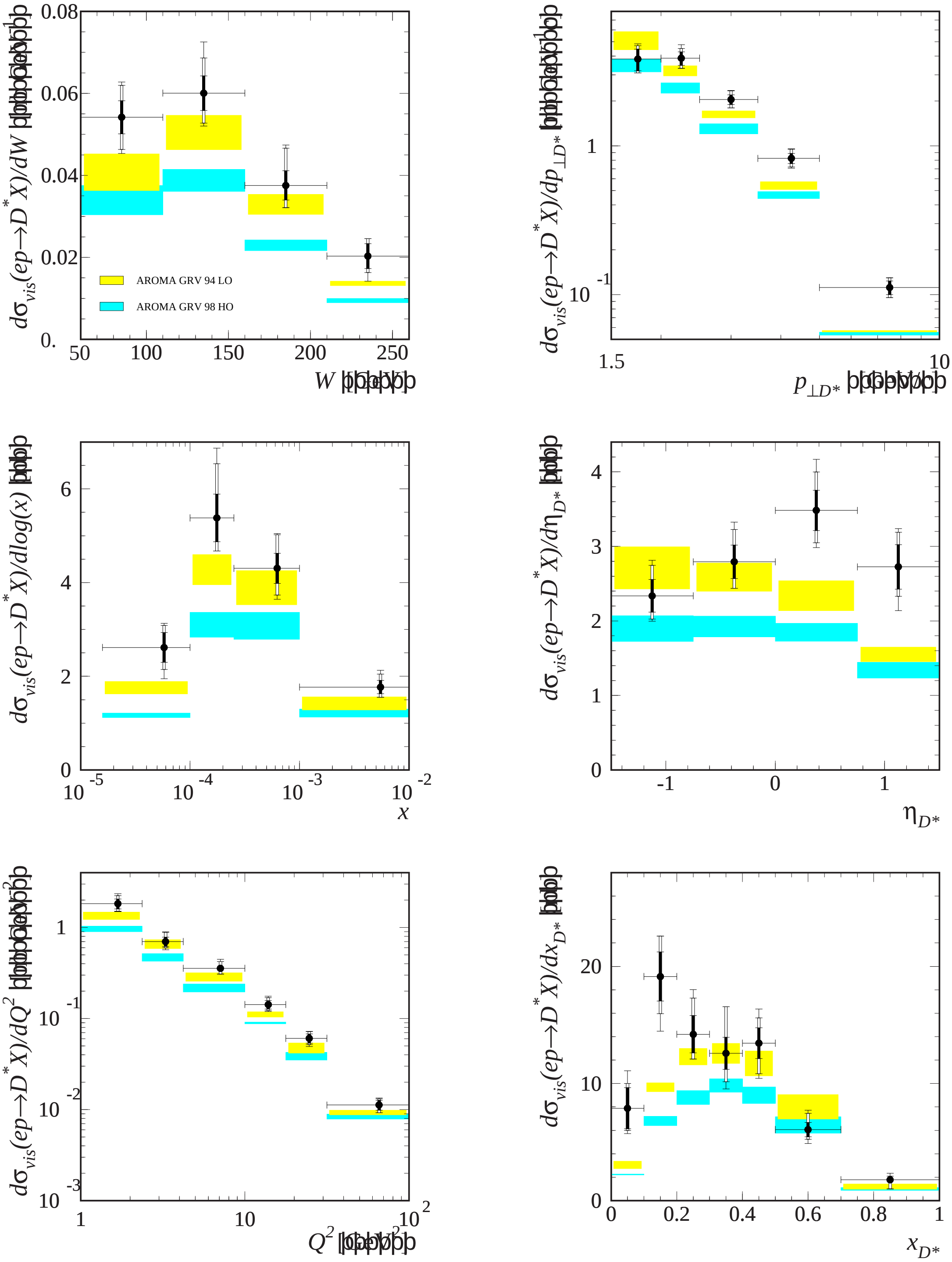

Figure 5.4: Inclusive D^{*+} single differential cross sections in the visible range versus W, x, Q^2 and $p_{\perp D^*}$, η_{D^*}, x_{D^*}. The innermost error bars correspond to the statistical error. The experimental systematical errors are added in quadrature for the middle error bars and the total error bars additionally take the Monte Carlo systematics into account. The dark shaded band is the prediction of the LO DGLAP AROMA event generator for m_c = 1.3 GeV/c^2 (upper limit) and m_c = 1.5 GeV/c^2 (lower limit) with GRV 98 HO for the parton density set. The light shaded band is the prediction of the LO DGLAP AROMA event generator for m_c = 1.3 GeV/c^2 (upper limit) and m_c = 1.5 GeV/c^2 (lower limit) with GRV 94 LO for the parton density set. In both cases ϵ(Peterson) has been fixed to 0.078.

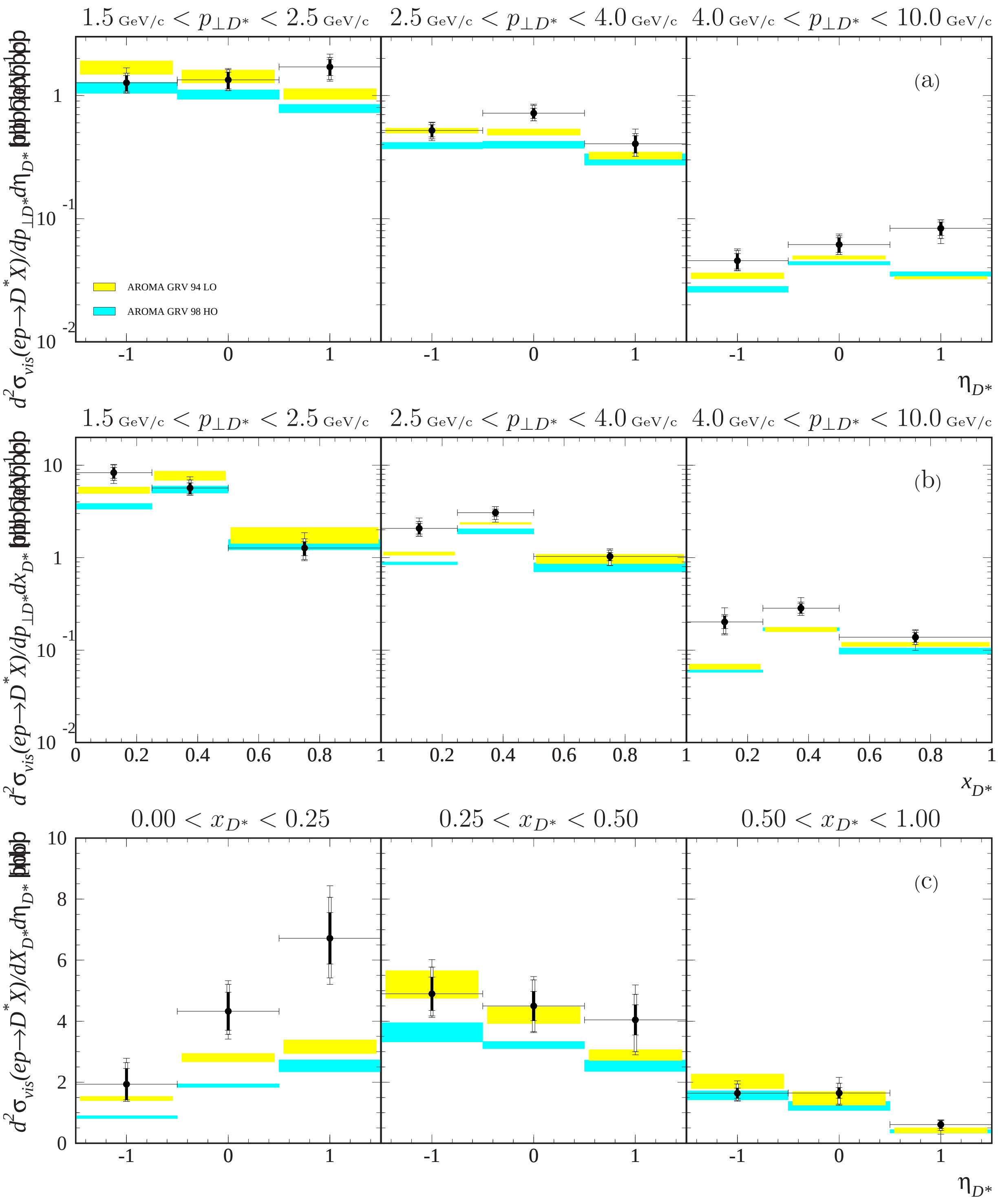

Figure 5.5: Inclusive D^{*+} double differential cross sections in the visible range for D^{*+} quantities $d^2\sigma_{vis}(ep \to eD^{*+}X)/(dp_{\perp D^*}d\eta_{D^*})$, $d^2\sigma_{vis}(ep \to eD^{*+}X)/(dp_{\perp D^*}dx_{D^*})$, $d^2\sigma_{vis}(ep \to eD^{*+}X)/(dx_{D^*}d\eta_{D^*})$. The dark and light shaded bands are described in the caption of figure 5.4.

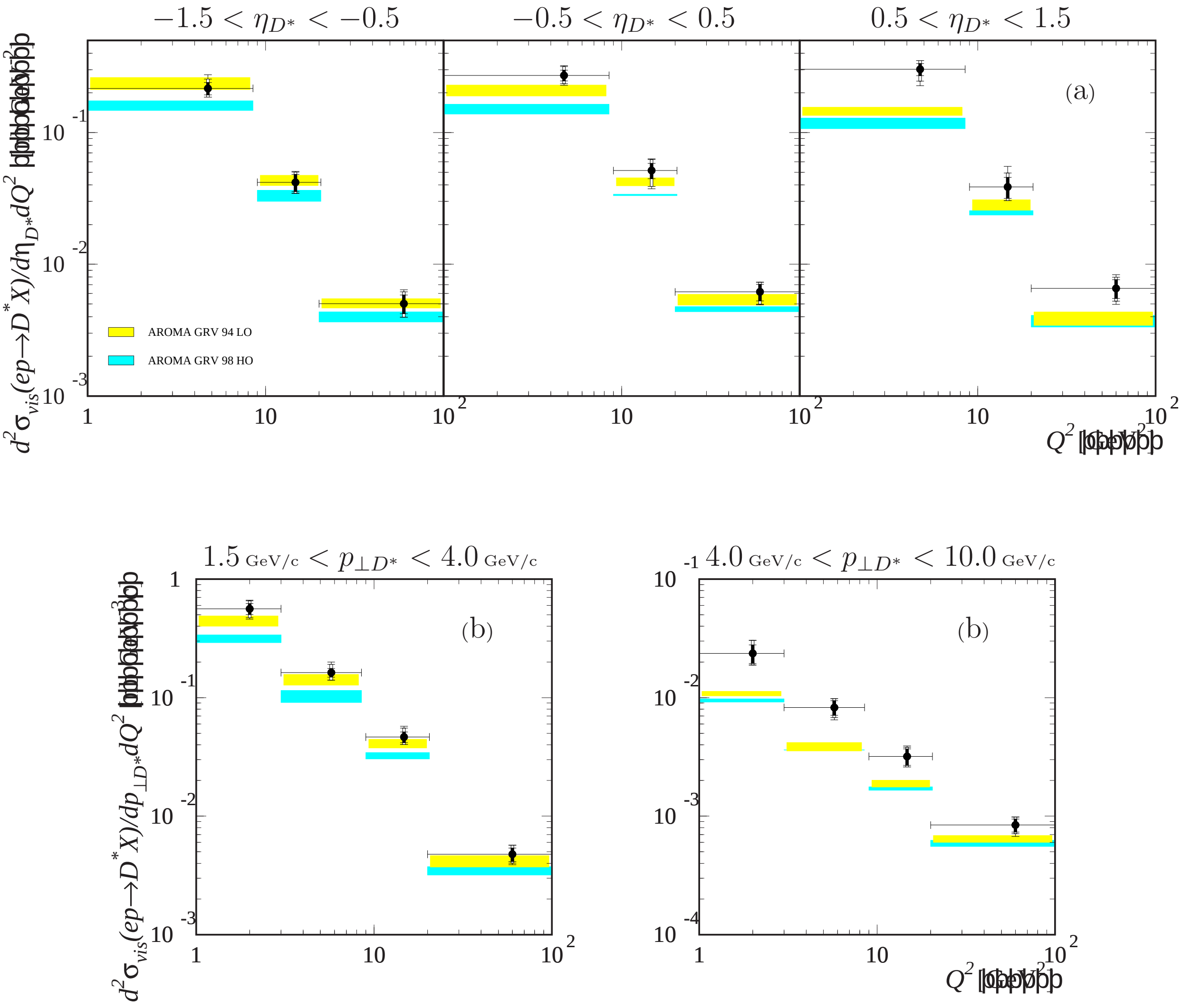

Figure 5.6: Inclusive D^{*+} double differential cross sections in the visible range $d^2\sigma_{vis}(ep \to eD^{*+}X)/(d\eta_{D^*}dQ^2)$ and $d^2\sigma_{vis}(ep \to eD^{*+}X)/(dp_{\perp D^*}dQ^2)$. The dark and light shaded bands are described in the caption of figure 5.4.

Chapter 6

Extraction of the Gluon Density at HERA

One of the main goals of HERA was to study the gluon density in the proton. The most evident and accommodating way to reach it is to measure precisely the scaling violation behaviour of the structure function F_2 as shortly described in section 6.1. In a complementary approach the gluon density can also be obtained by directly reconstructing the fraction x_g of the proton momentum carried by the gluon in events which are dominated by the boson-gluon fusion process. Experimentally, jet or tagged charm events lend themselves to this measurement. In section 6.2 the different ways to measure x_g are presented together with the features of both jet and D^{*+} meson analysis. The initial aim of this work was to extract the gluon density from the sample of D^{*+} events selected in the 1996 and 1997 H1 data. The principle of the chosen method and the encountered difficulties are given in section 6.3.

6.1 F_2 Indirect Measurement

In the DGLAP QCD formalism the Q^2 dependency of the structure function $F_2(x, Q^2)$ is determined by the evolution equations of the parton densities. Especially for $Q^2 > m_p^2 \mathrm{c}^4$ and low x the scaling violation behaviour of $F_2(x, Q^2)$ given by $\partial F_2(x, Q^2)/\partial Q^2$ is governed by the dominance of gluons in the proton (see subsection 3.1.2). The NLO DGLAP QCD fit performed in reference [27] to the H1 ep and BCDMS μp inclusive cross sections, assuming heavy flavour production within the massive scheme, allows to extract the gluon density $x_g\ g(x_g, Q^2)$ for different values of Q^2 as shown in figure 6.1. Simultaneously the strong coupling constant which also occurs in the formalism is obtained. The Q^2 range provided by H1 data extends from 3.5 GeV^2 to 3000 GeV^2. The low Q^2 data constrain the gluon density parametrisation whereas the high Q^2 data together with the BCDMS data constrain the quark densities parametrisation. In the QCD fit no data were included above 3000 GeV^2 in order to avoid the region where the electroweak interference gets large. Figure 6.1 shows that the gluon density is extracted with an impressive precision with only a few percent experimental uncertainty at low x_g. The final error bands take into account the uncertainty coming from the simultaneous fit of α_s, from the fit parameters Q^2_{min},

Q_0^2, m_c and from the choice of the parton distribution parametrisation at the initial scale Q_0^2. In the error the dependency of the fit on the theoretical description for heavy quark production (massive or massless formalism) has also been taken into account. Indeed, the relative contribution of charm is large (approximatively 25% at $Q^2 = 60$ GeV^2 and $x < 0.01$ [64]) and therefore influences the results. The fit was also performed with the H1 data alone and after fixing the strong coupling constant. The resulting gluon distribution is shown in figure 6.1 as solid lines inside the given bands.

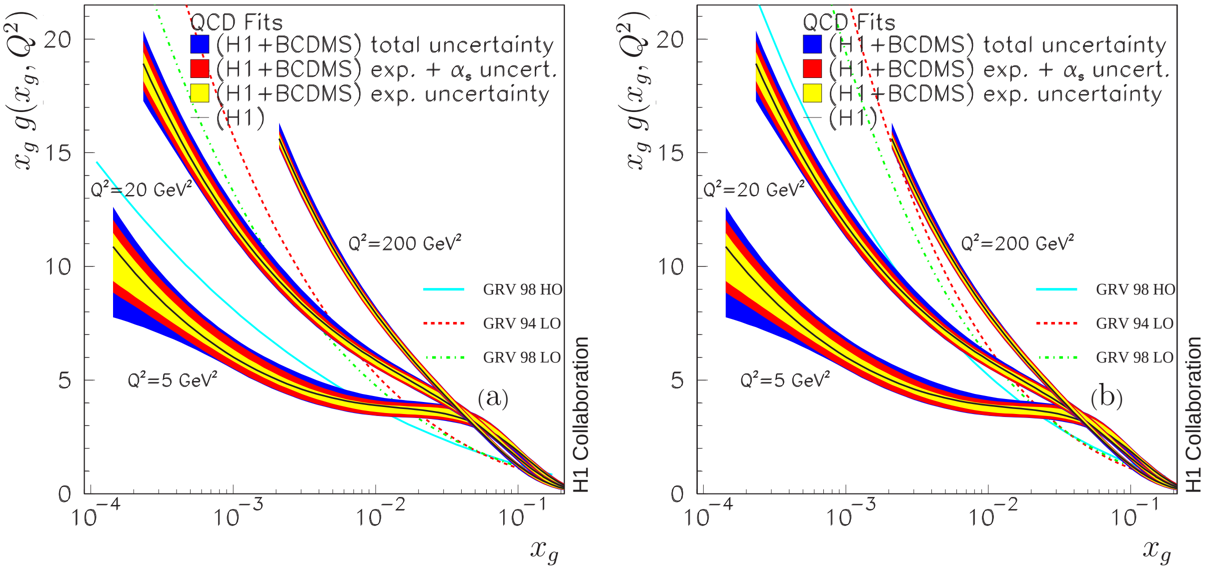

Figure 6.1: Gluon distributions $x_g\; g(x_g, Q^2)$ as a function of x_g resulting from the NLO DGLAP fit to the H1 ep and BCDMS μp inclusive cross section assuming heavy flavour production within the massive scheme. The innermost error bands represent the experimental error when $\alpha_s(m_Z^2)$ was set to 0.115 while the middle error bands take into account the simultaneous fit of α_s. The outer error bands include the uncertainties related to the theory. The results are compared to the GRV parametrisations for (a) $Q^2 = 5$ GeV^2 and (b) $Q^2 = 20$ GeV^2.

6.2 Direct Measurements

In deep inelastic electron-proton scattering, the main hard processes up to order $\alpha_{em}\alpha_s$ are the Quark Parton Model (QPM), the QCD-Compton (QCDC) and the boson-gluon fusion (BGF) processes, which are represented in figure 6.2. Experimentally the fraction of proton momentum carried by the gluon x_g can be directly measured in events where the hard interaction between the electron and the proton is taking place via the BGF process. This is the case of events containing at least two jets or a D^{*+} meson.

In the following subsection the different ways to calculate the quantity x_g are presented. Next the frames of the multi-jet and D^{*+} analysis are discussed. In the last section special emphasis on the D^{*+} analysis which was performed in this work is given.

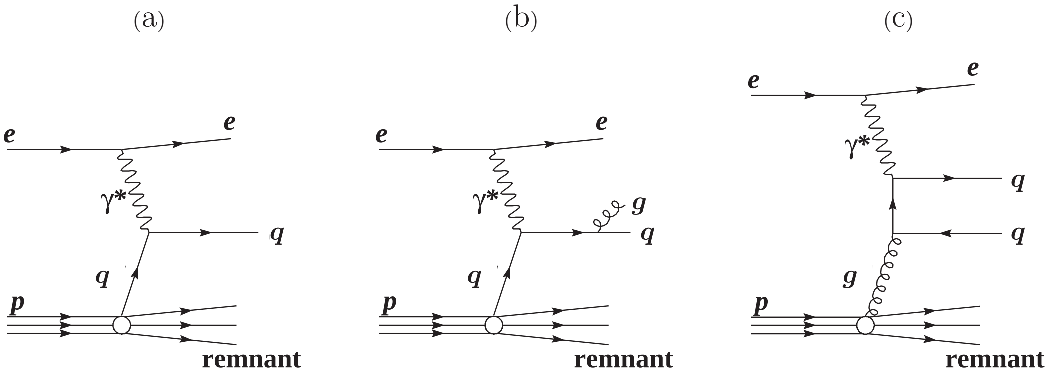

Figure 6.2: Generic Feynman diagrams for deep inelastic ep scattering up to order $\alpha_{em}\alpha_s$: (a) ep interaction of the virtual probe (γ, Z^0) with a valence or a sea quark in the proton according to the Quark Parton Model (QPM), (b) corrections to process (a) due to gluon radiation of the struck quark before or after interacting with the probe (QCD-Compton scattering), and (c) Boson-Gluon Fusion process (BGF).

6.2.1 Direct Reconstruction of x_g

In this part we describe how to reconstruct x_g from the outgoing quarks of the BGF process. However, it should be noticed that as soon as higher order are taken into account the formulas developed here are not valid anymore. For better understanding of the formulas the quark and antiquark involved in the BGF process are taken with charm flavour but it should be kept in mind that the beauty flavour is also possible. In the BGF hard sub-process the momentum conservation is given by:

$$x_g P + q = p_c + p_{\bar{c}}, \tag{6.1}$$

where P, q, p_c and $p_{\bar{c}}$ denote the proton, photon, c quark and $\bar{c}$ quark momenta respectively. Squaring equation (6.1) gives the following equation when the proton mass is neglected:

$$2x_g P{\cdot}q + q^2 = (p_c + p_{\bar{c}})^2. \tag{6.2}$$

From the definitions of the kinematic variable Q^2 and the Bjorken scaling variable x ($Q^2 = -q^2$, $x = -q^2/2P{\cdot}q$) the quantity x_g is then given by:

$$x_g = x(1 + \hat{s}/Q^2), \tag{6.3}$$

where $\hat{s} = (p_c + p_{\bar{c}})^2$ is the squared invariant mass of the $c\bar{c}$ system. Experimentally x and Q^2 are determined with one of the methods described in section 4.3.

The reconstruction of the variable x_g thus requires to have access to the quantity $\hat{s}$. Three different ways to calculate $\hat{s}$ from the two charm quark quantities are presented below.

Invariant Mass Method

The squared invariant mass of the $c\bar{c}$ system can be trivially computed from the four-momenta of the two quarks. Since in the detector only hadrons are accessible, the quantity $\hat{s}$ can be reconstructed by identifying the four-momenta of the two quarks with the four-momenta of the two main hadron jets.

Pseudorapidity Method

In the hadronic centre of mass system, $\hat{s}$ can be directly reconstructed from the pseudorapidities $\eta_c^{\gamma p}$ and $\eta_{\bar{c}}^{\gamma p}$ of the charm quarks and the squared γp invariant mass W^2 via:

$$\hat{s} = W^2 e^{-\left(\eta_c^{\gamma p} + \eta_{\bar{c}}^{\gamma p}\right)}, \tag{6.4}$$

where W^2 is defined in equation 1.5 and depends only on the kinematic variables.

Four-Momentum Method

Another method to reconstruct x_g uses the four-momentum of a single charm quark produced by the BGF process. In this case $\hat{s}$ is reconstructed by the following relations:

$$\hat{s} = \frac{(p_{\perp c}^{\gamma p})^2 \mathrm{c}^2 + m_c^2 \mathrm{c}^4}{z_c(1-z_c)} \qquad \text{and} \qquad z_c = \frac{P \cdot p_c}{P \cdot q} = \frac{E_c - p_{\parallel c} \cdot \mathrm{c}}{2yE_e}, \tag{6.5}$$

where $p_{\perp c}^{\gamma p}$ is the transverse charm momentum in the γp rest frame; E_c and $p_{\parallel c}$ are the charm energy and longitudinal momentum in the laboratory system respectively. The quantity y is the fractional energy loss of the lepton in the proton rest frame as defined in equation 1.1.

6.2.2 Jet Analysis

The multi-jet cross sections in DIS give the possibility to test our understanding of perturbative QCD and provide a direct determination of the gluon density and the strong coupling constant α_s. The hard process involved in multi-jet events is either the QCD-Compton process or the BGF process. These events are therefore directly sensitive to both the quark and gluon content in the proton.

In a former H1 analysis [70] the pseudorapidity method combined with the invariant mass method has been applied to reconstruct x_g. This was done by replacing in formula 6.4 the quantities $\eta_c^{\gamma p}$ and $\eta_{\bar{c}}^{\gamma p}$ by $\eta_{jet1}^{\gamma p}$ and $\eta_{jet2}^{\gamma p}$ in case of the pseudorapidity method. The invariant mass of the two quarks in the BGF process was calculated from the four-momentum of the two jets. The analysis was performed for 12.5 GeV^2 $< Q^2 <$ 80 GeV^2 leading to the extracion of the gluon density at a scale of 30 GeV^2. The disadvantage of

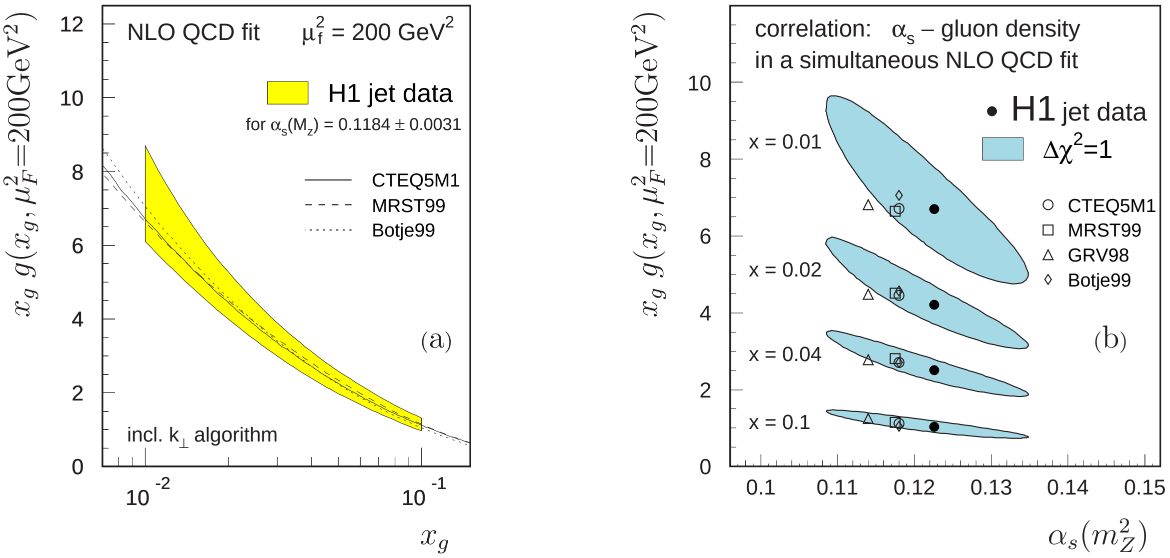

Figure 6.3: Gluon distribution $x_g\ g(x_g, \mu_F^2{=}200\mathrm{GeV}^2)$ as a function of x_g obtained from the NLO DGLAP fit to the H1 inclusive DIS cross section together with $d^2\sigma_{dijet}/d\xi dQ^2$ and $d^2\sigma_{jet}/dE_T dQ^2$, is displayed in part (a). Part (b) shows the correlation between $x_g\ g(x_g, \mu_F^2{=}200\mathrm{GeV}^2)$ and α_s as the result of a combined fit.

the two jet analysis is the large contamination of QCDC events (30%) and the explicit cut on $\hat{s}$ at 100 GeV^2, which is needed to identify the jets. The latter restricts such an analysis to a relatively large x_g: $0.002 < x_g < 0.2$. Nevertheless, the well achieved statistics already allowed an estimation of the gluon density with 35% total error which was a good achievement in view of the complexity of the involved theoretical processes.

The most recent measurements of inclusive jet and inclusive dijet cross sections in DIS by H1 [71] were performed in a higher Q^2 range. Hard QCD processes with at least one order in α_s always involve at least two jets and lead to events with high transverse jet energies in the Breit frame[1]. Therefore, even the inclusive jet cross section for high transverse jet energy is also a multi-jet cross section. The gluon density together with the quark densities in the proton are determined in [71] with a simultaneous fit of $d^2\sigma_{dijet}/d\xi dQ^2$, $d^2\sigma_{jet}/dE_T dQ^2$ within 150 GeV^2 $< Q^2 <$ 5000 GeV^2 and inclusive DIS data within 150 GeV^2 $< Q^2 <$ 1000 GeV^2 [72]. The inclusive DIS data give strong direct constraints on the quark densities. In the LO α_s picture, ξ is the fraction of the proton momentum carried by the parton. The parton can be either a quark in case of QCD-Compton hard processes or a gluon for boson-gluon hard processes. In the inclusive dijet analysis, ξ is reconstructed from the invariant mass method using the four-momenta p_{jet1} and p_{jet2} of the two jets with high transverse jet energies in the Breit frame. The quantity ξ is then given by:

$$\xi = x(1 + \hat{s}^{obs}/Q^2) \text{ with } \hat{s}^{obs} = (p_{jet1} + p_{jet2})^2 \mathrm{c}^2. \tag{6.6}$$

---

[1] The Breit frame is defined by $2x\vec{P} + \vec{q} = 0$, where $\vec{P}$ and $\vec{q}$ are the momenta of the incident proton and exchange boson respectively. In the QPM model the struck quark is back-scattered in the negative z_{BF} direction.

Figure 6.3.(a) shows the extracted gluon density while fixing $\alpha_s(m_Z^2)$ to the world average value: $\alpha_s(m_Z^2) = 0.1184 \pm 0.0031$. Like in the former analysis, the jet finding algorithm and the need of relative high transverse jet energies in the Breit frame allow to have access to the gluon density only at large x_g ($0.01 < x_g < 0.1$) in comparison with the values of x_g reached via the indirect F_2 measurement which extend down to $2 \cdot 10^{-3}$ at the scale of 200 GeV^2 (see figure 6.1). A simultaneous fit of α_s and the parton densities was also performed and indicates that the data are sensitive to the product $\alpha_s \cdot x_g \; g(x_g, \mu_F^2)$ as displayed in figure 6.3.(b).

6.2.3 D^{*+} Analysis

As a confirmation of EMC collaboration measurements [5] on muon-nucleon scattering, the 1994 data taken by the H1 detector at HERA electron-proton collider have also shown a clear dominance of the BGF process in charm production. Additional contributions where the charm quarks may come from fragmentation or gluon splitting are suppressed by heavy quark mass effects. The easiest way to tag charm events in electron-proton scattering is to reconstruct D^{*+} mesons via the decay channel $D^{*+} \to D^0\pi_s^+ \to (K^-\pi^+)\pi_s^+$ as done in this work. In this case the gluon density can be extracted directly by explicit reconstruction of the quantity x_g from the measurement of the four-momentum of the D^{*+} meson. No indirect cut on $\hat{s}$ is present in the D^{*+} analysis thus allowing the measurement of $x_g \cdot g(x_g, \mu_F^2)$ at smaller x_g than in the multi-jet analysis. Moreover, no assumption on the gluon and quark density shapes at an input scale is needed, contrary to the indirect measurement based on the F_2 scaling violation. Therefore tagged charm events are a unique way of probing the gluon density in the proton.

In the following section the problematic of the unfolding of the gluon density within the LO DGLAP formalism using D^{*+} meson events will be discussed.

6.3 Unfolding of the Gluon Density within the D^{*+} Analysis

Within the the D^{*+} analysis performed in this work, the variable x_g is reconstructed with the four-momentum method. In this case the charm momentum is approximated by the D^{*+} momentum which result in the observable quantities x_g^{obs} and $\hat{s}^{obs}$:

$$x_g^{obs} = x(1 + \hat{s}^{obs}/Q^2), \tag{6.7}$$

$$\hat{s}^{obs} = \frac{(p_{\perp D^*}^{\gamma p})^2 \mathrm{c}^2 + m_c^2 \mathrm{c}^4}{z_{D^*}(1 - z_{D^*})}. \tag{6.8}$$

A good precision of the measured quantity x_g^{obs} is obtained with the H1 detector as shown in figure 6.4.(a). However, the correlation between x_g^{obs} and the true x_g makes it impossible to directly measure $d\sigma_{vis}(ep \to eD^{*+}X)/dlogx_g$. Figure 6.4.(b) gives the correlation between $logx_g^{obs}$ and the true $logx_g$ predicted by the LO DGLAP calculations in the AROMA generator. A resolution of roughly 50% is predicted together with large bin migration at $x_g^{obs} < x_g$ (the accessible range for x_g from $6.3 \cdot 10^{-4}$ to 0.1 corresponds to values of x_g^{obs} from $6.3 \cdot 10^{-4}$ to 0.025). An unfolding of the measured distribution $d\sigma_{vis}(ep \rightarrow eD^{*+}X)/dlogx_g^{obs}$ is therefore compulsory.

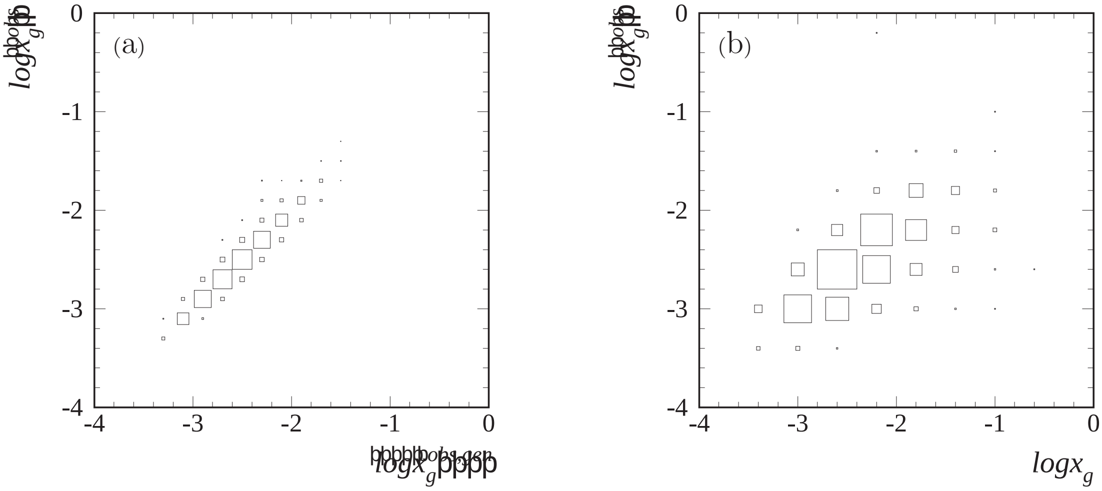

Figure 6.4: (a) correlation between the measured quantity x_g^{obs} and the generated quantity $x_g^{obs,gen}$, (b) correlation between the measured quantity x_g^{obs} and the generated x_g for LO AROMA BGF D^{*+} candidates ($m_c = 1.5$ GeV/c^2, GRV 94 LO).

In the frame of this work, the unfolding is performed with the programme *RUN* [73]. The data, background if any and Monte Carlo samples are given under the form of event ntuples. In our case an event is a D^{*+} candidate within the mass windows $|m_{K\pi} - m_{D^0}| < 70$ MeV/c^2 and $|m_{K\pi\pi_s} - m_{K\pi} - (m_{D^*} - m_{D^0})| < 2.2$ MeV/c^2. Both data and Monte Carlo simulation samples are corrected for the mass window cuts using the values of $c_{\Delta m}$ and $c_{m_{D^0}}$ determined from the Δm and m_{D^0} fit results (see subsection 4.4.3). Each ntuple contains the measured quantity $logx_g^{obs}$ and several other measured quantities which are used for the control of the unfolding result. Each Monte Carlo ntuple has to contain the corresponding true quantity $logx_g$ as well. Mathematically, the original distribution $d\sigma_{vis}(ep \rightarrow eD^{*+}X)/dlogx_g$ of the true variable x_g is related to the measured distribution[2] $d\sigma^*_{vis}(ep \rightarrow eD^{*+}X)/dlogx_g^{obs}$ of the measured variable x_g^{obs} as follows:

$$\frac{d\sigma^*_{vis}(ep \rightarrow eD^{*+}X)}{dlogx_g^{obs}} = \int A(logx_g^{obs}, logx_g)\frac{d\sigma_{vis}(ep \rightarrow eD^{*+}X)}{dlogx_g} dlogx_g + B(logx_g^{obs}). \quad (6.9)$$

The function $B(logx_g^{obs})$ represents the background contribution to the measured distribution and the function $A(logx_g^{obs}, logx_g)$ represents the smearing and bin migration due to the charm fragmentation but also to the pQCD processes from the gluon to the quark when processes of higher order than the BGF process are taken into account. The detector effects, though non dominant here, are also taken into account in $A(logx_g^{obs}, logx_g)$.

---

[2] For the measured distribution $d\sigma^*_{vis}(ep \rightarrow eD^{*+}X)/dlogx_g^{obs}$ the *asterisk* stands for non-background-substracted cross section.

The unfolding programme RUN defines internally a weighting function f_{mult} for the Monte Carlo ntuples which is parametrised by orthogonal B-spline functions. The function f_{mult} is determined by a fit to the experimentally measured differential cross section:

$$\begin{aligned}\frac{d\sigma_{vis}^{*exp}(ep \to eD^{*+}X)}{dlogx_g^{obs}} \approx & \int A^{MC}(logx_g^{obs}, logx_g)\, f_{mult}(logx_g)\, \frac{d\sigma_{vis}^{MC}(ep \to eD^{*+}X)}{dlogx_g}\, dlogx_g \\ & + B^{exp}(logx_g^{obs}).\end{aligned} \tag{6.10}$$

The background function is determined by the unfolding programme from a sample of D^{*+} with a wrong charge reconstructed D^0 candidates ($K^-\pi^-$) lying in the m_{D^0} window. The background sample is scaled down to the background contribution in the Δm window by the background normalisation factor. This number is determined from the results of the Δm fit (see section 4.4.3). The result of the unfolding is then given by:

$$\frac{d\sigma_{vis}^{exp}(ep \to eD^{*+}X)}{dlogx_g} = f_{mult}(logx_g)\, \frac{d\sigma_{vis}^{MC}(ep \to eD^{*+}X)}{dlogx_g}. \tag{6.11}$$

In this analysis the AROMA LO DGLAP Monte Carlo is used to performe the unfolding. Since the NLO DGLAP calculations were not yet available under the form of an event generator, it was not possible to use them as an input of the unfolding programme. The result of the unfolding are presented in figure 6.5 together with the non unfolded distribution. Both the HVQDIS and CASCADE predictions agree in shape with the experimental cross sections as a function of $logx_g^{obs}$. The AROMA prediction using the GRV 94 LO gluon density clearly show that this parametrisation has too steep an increase for decreasing $logx_g$. This is also observed in the result from the F_2 scaling violation in figure 6.1. After the unfolding, the D^{*+} cross section as a function of $logx_g$ shows the same behaviour. This already indicates the difficulty of extracting the gluon density from the D^{*+} analysis, at least when using LO QCD calculations.

To extract the gluon density from the cross section as a function of $logx_g$, the following proportionality within one $logx_g$ bin is used:

$$\frac{d\sigma(ep \to eD^{*+}X)}{dlogx_g} \propto x_g g(x_g, \mu_F^2). \tag{6.12}$$

This proportionality is valid only for the total cross section. Therefore, it is necessary to extrapolate the cross section which is measured in the D^{*+} visible range to the full range. Both the extrapolation factor and the proportionality factor are taken from the AROMA Monte Carlo prediction, which gives:

$$x_g g^{exp}(x_g, \mu_F^2) = x_g g^{MC}(x_g, \mu_F^2) \frac{\dfrac{d\sigma_{vis}^{exp}(ep \to eD^{*+}X)}{dlogx_g}}{\dfrac{d\sigma_{vis}^{MC}(ep \to eD^{*+}X)}{dlogx_g}}. \tag{6.13}$$

Again with the help of the Monte Carlo prediction, the extracted gluon density is additionally bin-centre corrected and given at the scale of 20 GeV^2. For heavy quark production the factorisation and normalisation scales are generally set to $\hat{s}$ or $Q^2 + 4m_c^2\mathrm{c}^4$. The mean values of these quantities within the full D^{*+} range amount 25 GeV^2 and 17 GeV^2 for the

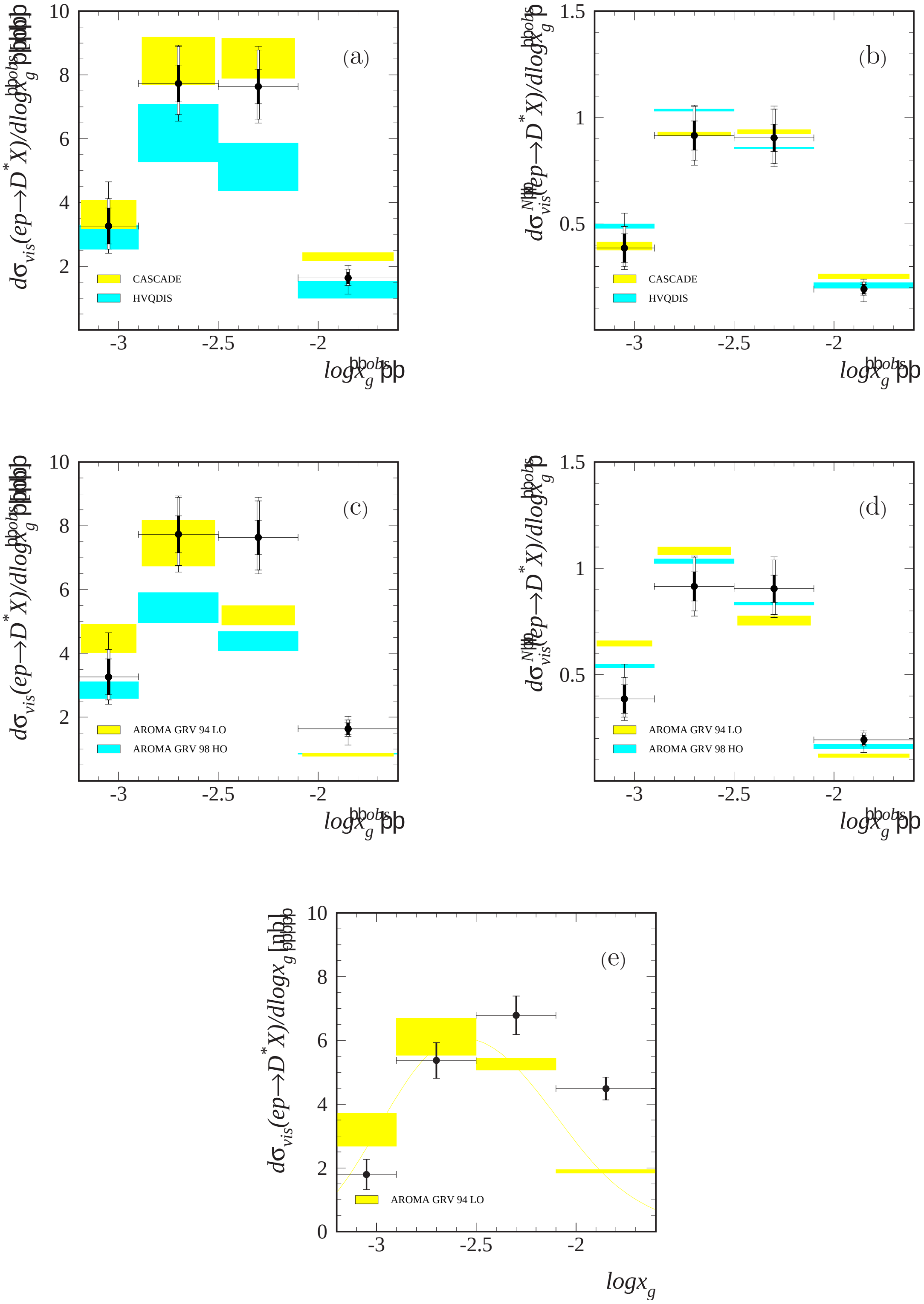

Figure 6.5: Inclusive D^{*+} single differential cross sections in the visible range as a function of x_g^{obs} (points) compared to (a) the HVQDIS and CASCADE predictions as described in the caption of figure 5.1 and compared to (c) the AROMA predictions using two different gluon densities as described in the caption of figure 5.4. The figures (b) and (d) give the normalised cross sections. The result of the unfolding is shown in figure (e) which gives the D^{*+} cross section as a function of x_g. In figure (e) the data error bars indicate the error given by the unfolding programme. On the same figure the AROMA predicted cross section is also shown as a function of x_g.

version of the AROMA generator used here. The gluon density is therefore given at the scale of 20 GeV^2 which also allows easy comparison with the indirect F_2 measurement. The resulting gluon density is shown in figure 6.6 together with the GRV 94 LO and GRV 98 HO parametrisation. The excess of experimental cross section compared to the AROMA prediction at large x_g appears clearly in an abnormal rather flat extracted gluon density.

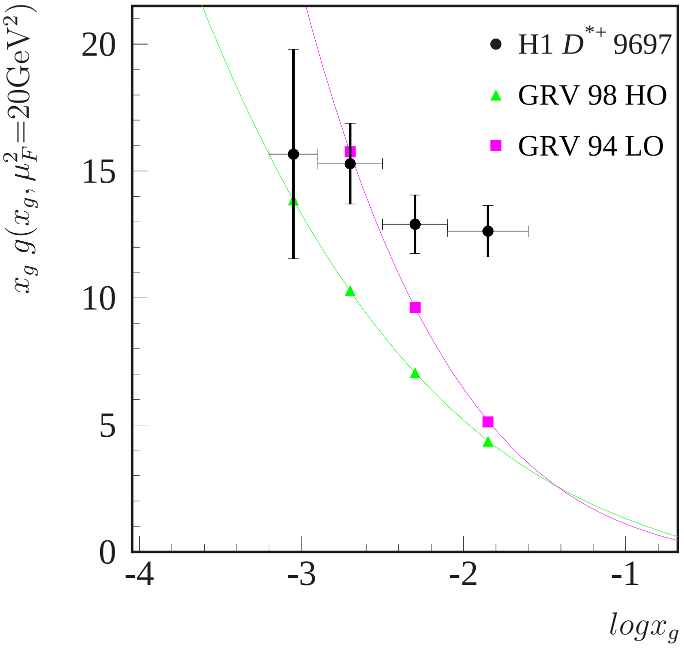

Figure 6.6: Measured $x_g\ g(x_g, \mu_F^2{=}20\mathrm{GeV}^2)$ as a result of the D^{*+} analysis. The error bars on the data points represent the error given by the unfolding programme. The line with the squares shows the GRV 94 LO parametrisation, and the line with the triangles the GRV 98 HO parametrisation.

In order to verify that the unfolding procedure as well as the data quality are not implicated, the following checks have been performed.

- The dependency of the unfolding result on the estimation of the background function was tested by performing the unfolding procedure with two other background samples:
  - D^{*+} candidates satisfying the m_{D^0} window cut but lying in the high Δm region 0.16 GeV/c^2 $< \Delta m <$0.17 GeV/c^2.
  - D^{*+} candidates lying in the high m_{D^0} region 2.05 GeV/c^2 $< m_{D^0} <$2.35 GeV/c^2.

  As shown in figure 6.7(a), the difference in the final results stays systematically bellow the error given by the unfolding programme.
- The signal to background ratio N_S/N_B in the m_{D^0} and Δm windows[3] varies with increasing x_g^{obs} from 1.0 to 3.2 for the combined 1996 and 1997 data. However, the

---

[3] The quantities N_S and N_B stand for the signal and background number of D^{*+} in the m_{D^0} and Δm mass windows.

result of the unfolding is not directly affected since the background is defined and subtracted for each x_g^{obs} bin. It has been checked that the normalisation factor between the background sample and the contribution in the Δm window can be taken as constant for the four x_g bins. For this, the error on the background contribution in the Δm window for the different x_g bins is estimated and given in table 6.1. The error on the total cross section due to the use of a constant background normalisation factor is lowered by the good signal to background ratio. Indeed, the relative error $\Delta N_S/N_S$ on the signal coming from the background estimation is given by:

$$\Delta N_S/N_S = -\frac{\Delta N_B/N_B}{(N_S/N_B)}. \tag{6.14}$$

After a simple parametrisation of the error on the estimation of the background contribution, each background event was reweighted. The resulting differences on the unfolded distribution are shown in figure 6.7.(b).

$log x_g^{obs}$	[-3.2;-2.9]	[-2.9;-2.5]	[-2.5;-2.1]	[-2.1;-1.6]
N_S/N_B: Signal to Background Ratio	1.0	1.3	1.3	3.2
$\Delta N_B/N_B$ Error on the Background Contribution	+12%	-3%	-6%	+36%

Table 6.1: Signal to background ratio (N_S/N_B) and error on the estimation of the background contribution ($\Delta N_B/N_B$) for the four x_g^{obs} bins of the combined 1996 and 1997 data. For each x_g^{obs} bin, the error on the background contribution is given by the difference of the number of background events estimated from the fit of the Δm distribution for D^{*+} candidates within the concerned x_g^{obs} bin and the number of background events estimated from the fit of the Δm distribution for all D^{*+} candidates with respect to the latter.

- The most relevant experimental precision in the reconstruction of the quantity x_g^{obs} is the precision on the kinematic variables. Therefore the unfolding programme was run using a data sample (signal and background) where the scattered electron energy was changed by ±1% at 27.5 GeV to ±3.0% at 8 GeV assuming a linear behaviour of the energy uncertainty (see section 2.3). The relative differences with respect to the reference measurement are shown in figure 6.7(c). The procedure was also performed with the sigma method instead of the electron method for the kinematics determination and the resulting differences are shown in figure 6.7(d). In both cases the changes in the unfolded cross section cannot be responsible for the cross section excess at large x_g.

- Using reconstructed D^{*+}, the four-momentum of the charm quark may be approximated by applying a correction factor $\langle Z_D \rangle$=1.2 to the D^{*+} momentum in formula 6.8 in order to take into account the effect of fragmentation, i.e. $\vec{p}_c = \vec{p}_{D^*}/\langle Z_D \rangle$ (the charm quark mass is fixed to 1.5 GeV/c^2). Running the unfolding with this other way of calculating x_g^{obs} changes the unfolded cross section. The relative difference is shown in figure 6.8(a). Again the effect stays within the error on the unfolded cross section.

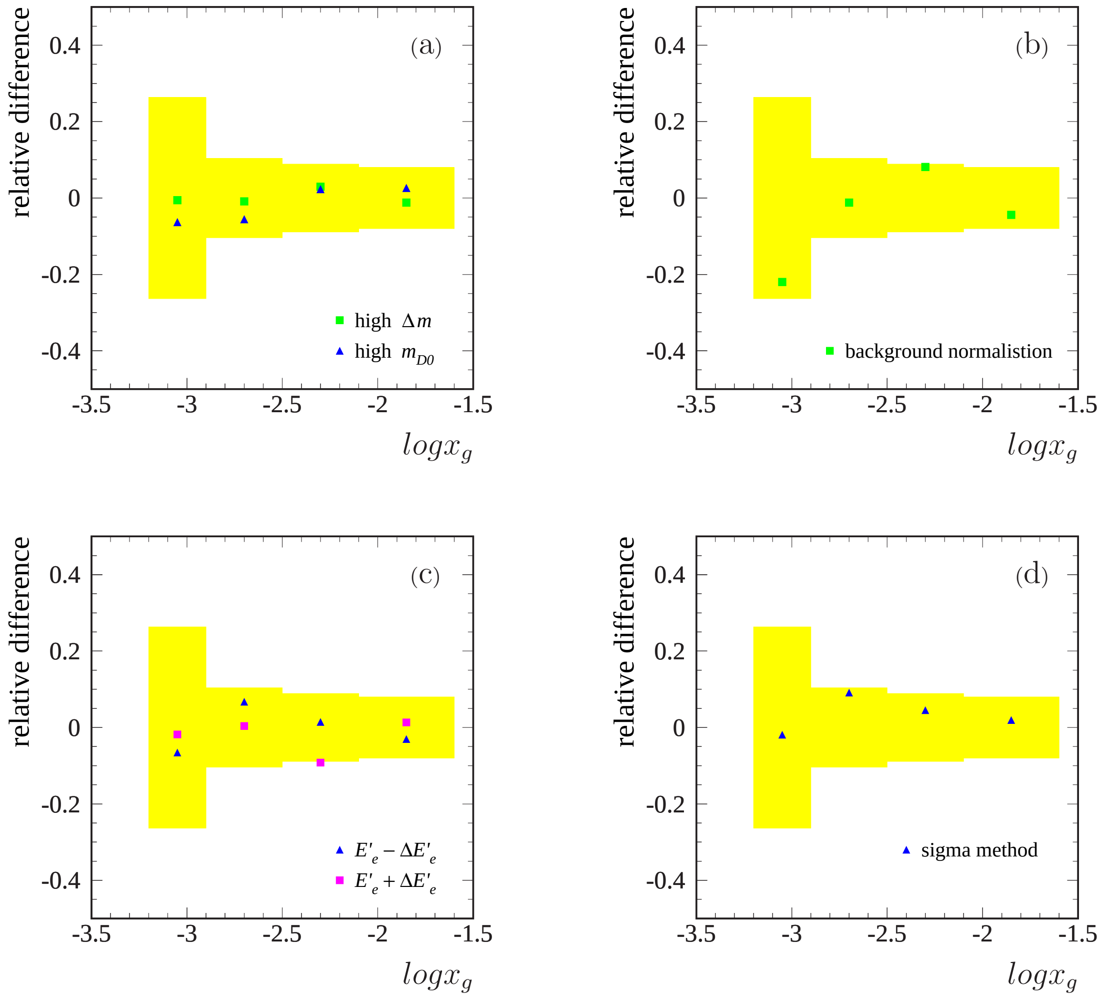

Figure 6.7: Relative difference for the unfolded D^{*+} visible cross section with regard to the reference result displayed in figure 6.5 as a function of x_g produced by:
- (a) the choice of different background samples
- (b) the normalisation of each background event with a weight depending of x_g^{obs} instead of an overall background normalisation factor
- (c) changing the measured scattered energy within the energy scale precision (see subsection 5.2.1)
- (d) the use of the sigma method instead of the electron method to reconstruct the kinematics.

In all figures the light shaded band indicates the error given by the unfolding programme in case of the reference result.

- In order to be sure that the result of the unfolding is not dependent of the Monte Carlo distristribution $d\sigma_{vis}^{MC}(ep \rightarrow eD^{*+}X)/dlogx_g$ the unfolding was run with the AROMA Monte Carlo events reweighted to the GRV 94 HO parametrisation. No changes in the unfolded cross section are observed in figure 6.8(b).

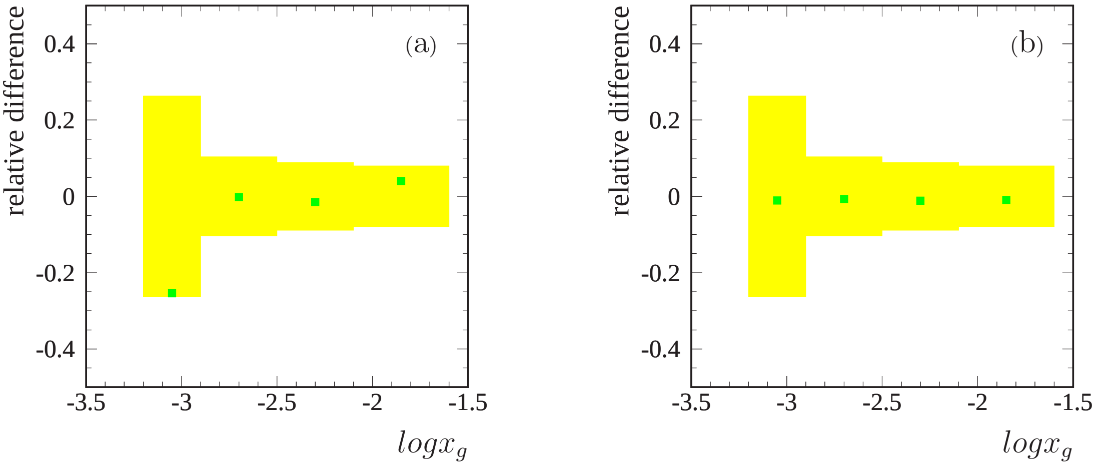

Figure 6.8: Relative difference for the unfolded D^{*+} visible cross section with regard to the reference result displayed in figure 6.5 as a function of x_g produced by:
- (a) the use of a correction factor $\langle Z_D \rangle$=1.2 instead of $\langle Z_D \rangle$=1.0 for the D^{*+} momentum when calculating x_g^{obs} (see text)
- (b) the use of GRV 94 HO instead of GRV 94 LO for the gluon density in AROMA.

In all figures the light shaded band indicates the error given by the unfolding programme in case of the reference result.

The results of the previous checks have demonstrated a very good data quality as well as the feasibility of the unfolding. However, the result of the unfolding is relevant only if the correlation matrix is understood. If the unfolding programme is used to deconvoluate detector effects the knowledge of the correlation matrix can be guaranteed. But in the present case the correlation matrix is dominated by the perturbative process and the charm fragmentation. The correctness of the unfolding result therefore requires a complete understanding of the evolution from the gluon to the measured D^{*+} meson. The results on the differential D^{*+} cross sections presented in chapter 5 have shown that the AROMA generator seems to prefer a steeper gluon density with respect to the kinematics behaviour and a flatter gluon density with respect to the behaviour in the D^{*+} quantities. This indicates that the AROMA generator is limited in the understanding of the physics processes taking place between the gluon and the D^{*+} meson which actually determines the correlation matrix $A(logx_g^{obs}, logx_g)$.

Another way to test the ability of the AROMA correlation matrix to describe the *real* correlation matrix which rules the measurement is to study the shape of the AROMA distributions after the unfolding. Indeed each D^{*+} candidate with given x_g, x_g^{obs}, E'_e, θ_e, x, Q^2, W, $p_{\perp D^*}$, η_{D^*}, x_{D^*} and $\hat{s}^{obs}$ carries, after the unfolding, a weight equals to $f_{mult}(logx_g)$. If the AROMA correlation is correct, its reweighted distributions should describe the measurement at least as good as the original distributions. Kolmogorov tests have been performed to compare, firstly the agreement between the AROMA original distributions and the measurement and secondly the agreement between the reweighted distributions after the unfolding and the measurement. The shapes of the AROMA distributions as a function of $p_{\perp D^*}$, η_{D^*}, and $\hat{s}^{obs}$ after the unfolding better agree with the measurement than before the unfolding. The contrary is observed for the distributions as a function of $E'_e, \theta_e, x, Q^2, W$ and x_{D^*}. This indicates again that the AROMA generator provides a wrong understanding of the correlation matrix $A(logx_g^{obs}, logx_g)$.

In figure 6.10 the relative differences due to the theoretical uncertainties for the unfolded cross section and for the extracted gluon density are displayed. The uncertainty on the charm fragmentation was studied by changing the value of ϵ(Peterson) between 0.035 and 0.100. The uncertainty on the charm mass was studied by changing its value between 1.3 GeV/c^2 and 1.7 GeV/c^2. Finally, the effects due to the next to leading order terms were studied by reweighting the AROMA correlation matrix $A(logx_g^{obs}, logx_g)$ in order to reproduce the correlation matrix predicted by the HVQDIS NLO calculations (see part (b) of figure 6.9). With respect to the three theoretical systematics studied, the differences for the unfolded cross section come from the changes in the correlation matrices used to perform the unfolding. The differences for the extracted gluon density come from:

- the changes in the predicted extrapolations from the D^{*+} visible range to the total range,
- the changes in the predicted ratios from the total cross section to the gluon density,
- the changes in the predicted bin centre corrections and scale corrections.

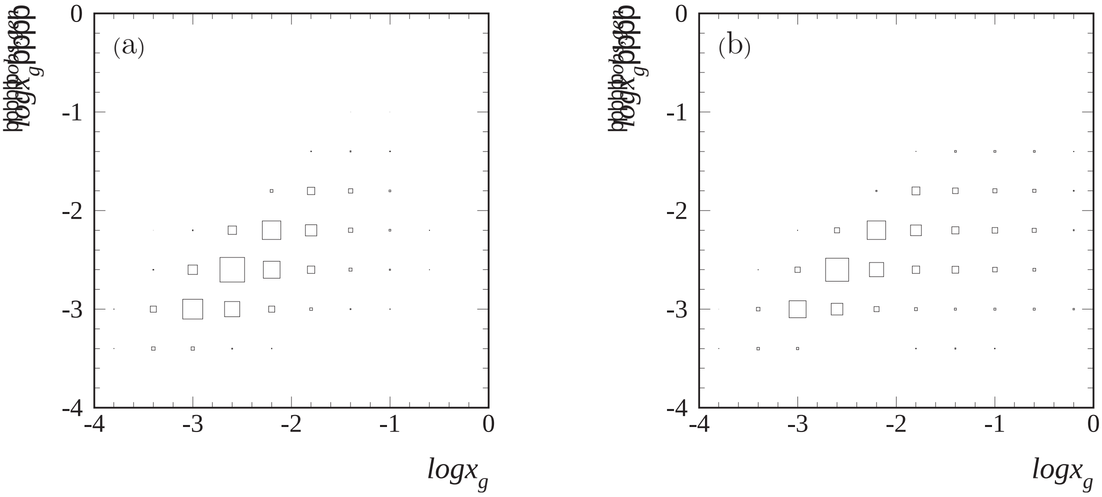

Figure 6.9: Correlation between the generated quantity $x_g^{obs,gen}$ and the generated x_g for (a) the LO AROMA D^{*+} events ($m_c = 1.5$ GeV/c^2, GRV 94 LO) and for (b) the NLO HVQDIS D^{*+} events ($m_c = 1.5$ GeV/c^2, GRV 98 HO). In both cases the D^{*+} events lay within the visible range

The influence of ϵ(Peterson) parameter is not negligible especially at large x_g. Moreover it seems that a more reasonable gluon density is extracted when ϵ(Peterson) is set to 0.035 which corresponds to a harder fragmentation. However, this effect is the result of a wrong description of the correlation between x_g^{obs} and x_{D^*}. This can be observed in figure 6.13 where the cross section is differentiated with respect to x_g^{obs} and x_{D^*}.

The systematics errors due to the charm mass on the gluon density extracted with the help of the AROMA generator is large but no tendency in the slope of the gluon density can be observed.

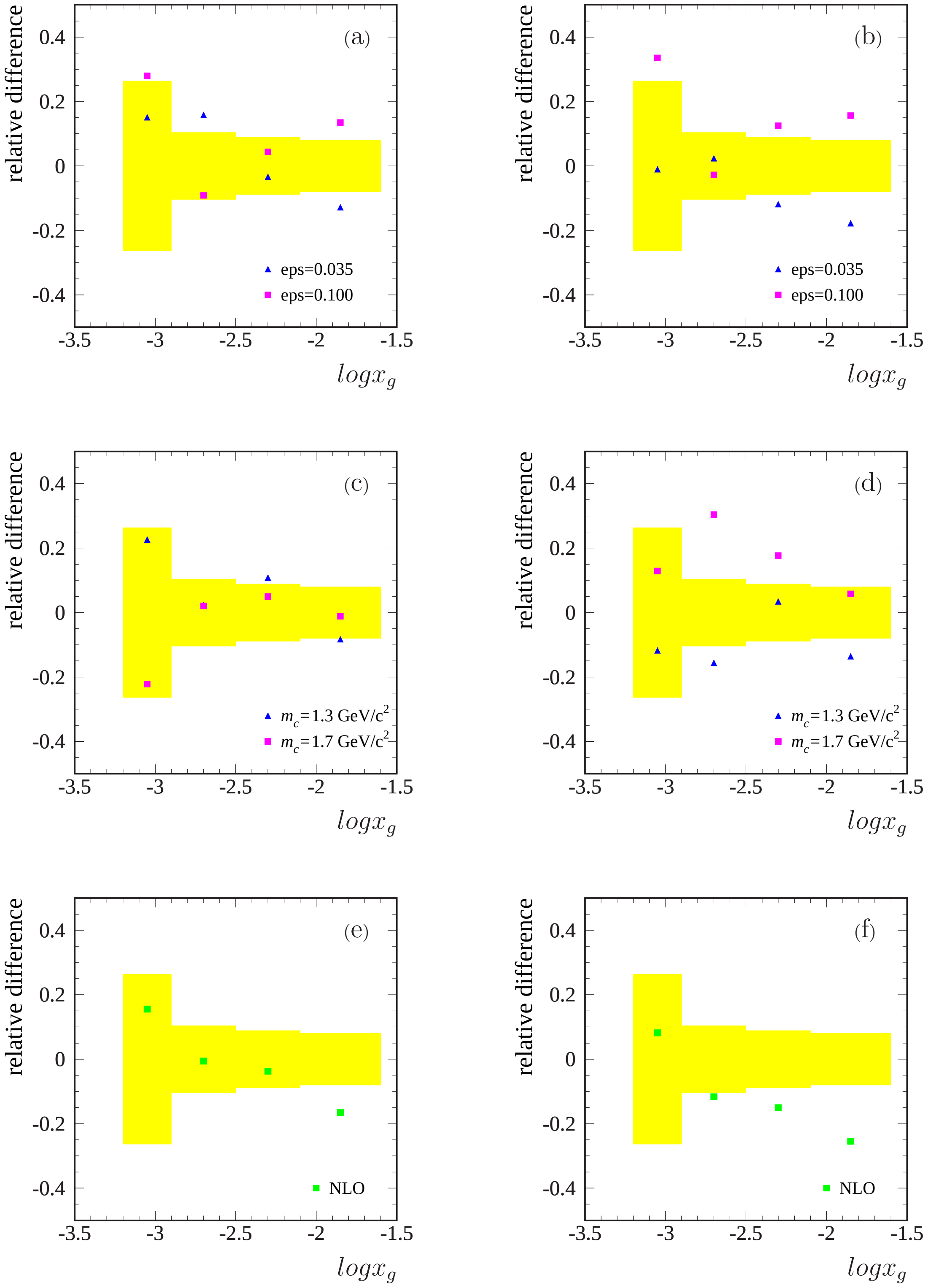

Figure 6.10: Relative differences for the unfolded D^{*+} visible cross section ((a), (c) and (e)) and for the extracted gluon density ((b), (d) and (f)) with regard to the reference result displayed in figure 6.5 and 6.6 as a function of x_g produced by :
- the use of different ϵ(Peterson) values
- the use of different charm mass
- the change in the correlation matrix $A(logx_g^{obs}, logx_g)$ to the one predicted by the HVQDIS NLO calculations. The extraction of the gluon density is done with the NLO prediction.
In all figures the light shaded band indicates the error given by the unfolding programme in case of the reference result.

A clear improvement in the unfolded cross section is observed when the unfolding is performed with the AROMA generator reweighted according to the correlation matrix $A(logx_g^{obs}, logx_g)$ predicted by the HVQDIS NLO calculations. As a consequence, the slope of the gluon density is definitely steeper when it is extracted from the cross section $d\sigma_{vis}(ep \rightarrow D^{*+}X)/dlogx_g$ unfolded with the NLO correlation matrix as observed in figure 6.11. In this figure the points represent the gluon density extracted with the prediction of the LO caculations whereas the prediction of the NLO caculations is used for the triangles. Both show the same tendency. However, a normalisation problem remains. This problems has its origin in the fact that both predictions underestimate the D^{*+} visible cross section as seen in chapter 5. Assuming the normalisation problem to be independent of the gluon dynamics, the extracted gluon density is scaled by the difference in the D^{*+} visible cross section between the measurement and the two predictions respectively (see table 5.3). This is displayed in the right plot of figure 6.11. In the same figure the result of the F_2 indirect measurement is shown. A good agreement is observed. The extraction of the gluon density using the D^{*+} cross section seems therefore to be feasible only if the NLO terms are taken into account in the correlation matrix $A(logx_g^{obs}, logx_g)$.

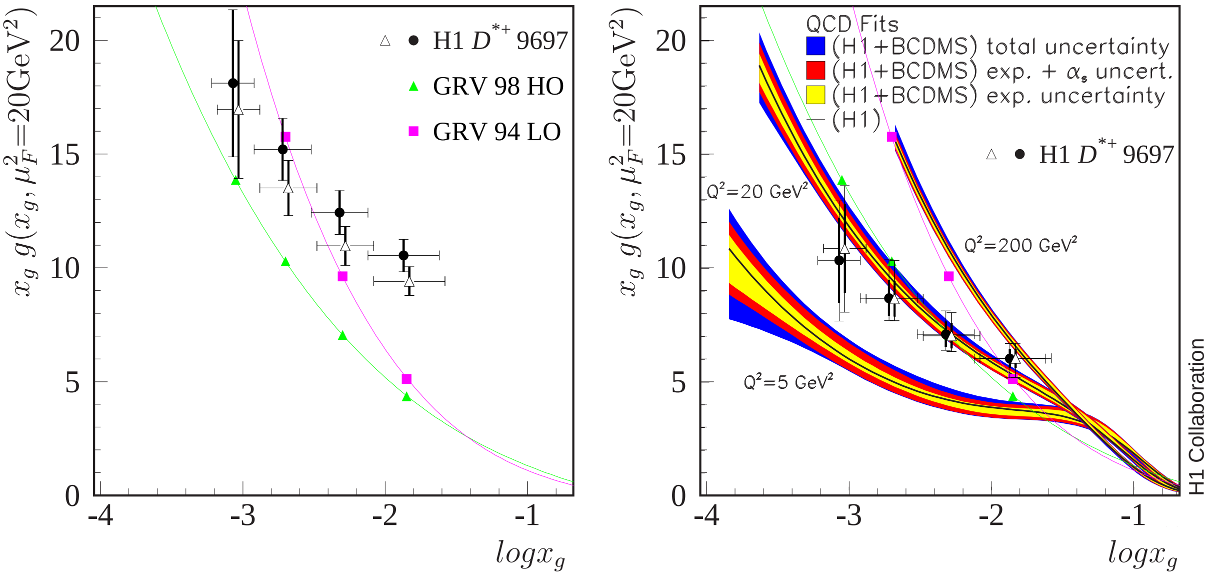

Figure 6.11: Measured $x_g\ g(x_g, \mu_F^2{=}20\text{GeV}^2)$ as a result of the D^{*+} analysis where the unfolding is performed with the correlation matrix $A(logx_g^{obs}, logx_g)$ reweighted to the one predicted by the HVQDIS NLO calculations. On both plots, the points represent the gluon density extracted from the unfolded cross section $d\sigma_{vis}(ep \rightarrow eD^{*+}X)/dlogx_g$ using the LO prediction whereas for the open triangles the NLO prediction was used. The thick error bars represent the error given by the unfolding programme. The line with the squares (triangles) shows the GRV 94 LO (GRV 98 HO) parametrisation. On the right plot the extracted gluon density was scaled to the difference in the D^{*+} total cross section between the data and the two predictions respectively. The total error bars additionally take into account the experimental systematics and theoretical systematics due to the fragmentation and the charm mass. In addition the results of the F_2 indirect measurement (bands) are shown.

The double differential cross sections displayed in figures 6.12 and 6.13 allow to have a better understanding of the success and weakness of the different calculations considered in this work. For three different ranges of the observed quantity x_g^{obs} the behaviours in $log\hat{s}^{obs}$ (where the quantity $\hat{s}^{obs}$ is given in GeV^2 and is implicitly divided by 1 GeV^2), x, η_{D^*} and x_{D^*} are displayed. Among the three different calculations, the predictions of the CASCADE generator describe the measurement at best. However, the predictions of the CASCADE generator seem to overestimate the cross section at large x_g^{obs} and large $log\hat{s}^{obs}$. CASCADE also shows an excess at low η_{D^*} for middle and large x_g^{obs}. The predictions of the HVQDIS NLO calculations are fairly good despite that they seem to prefer lower values of $log\hat{s}^{obs}$ than the measurement especially for intermediary values of x_g^{obs}. Moreover the agreement with the measurement for the η_{D^*} behaviour is deteriorated with increasing x_g^{obs}. The same effect is observed in the x_{D^*} distribution. The predictions of the AROMA event generator are the most apart from the measurement.

Like in the case of the HVQDIS predictions, the AROMA predictions favour lower values of $log\hat{s}^{obs}$ than the measurement but the effect is stronger and observed for the whole x_g^{obs} range. Moreover, the AROMA predictions are peaking at higher x than the measurement and this independently of x_g^{obs}. As a consequence, the use of the GRV 94 LO density parametrisation results in a better agreement in the x behaviour after integration over x_g^{obs}. The η_{D^*} and x_{D^*} distributions predicted by AROMA show the same behaviour than the HVQDIS prediction. The better agreement using the GRV 94 HO in the single differential cross section as a function of η_{D^*} comes from the fact that a flatter gluon density suppresses the cross section at negative η_{D^*} (backward D^{*+}). However, the correlation is softer in the predictions of AROMA than for the measurement. To conclude, the measurement has allowed to establish the weakness of the LO DGLAP calculations in describing the measured double differential cross sections. An improvement is observed in the predictions of the NLO DGLAP calculations. The CCFM formalism used in the CASCADE generator seems to be the most successful which indicates either the need of a better understanding on how to apply the DGLAP formalism or the need of NNLO DGLAP calculations.

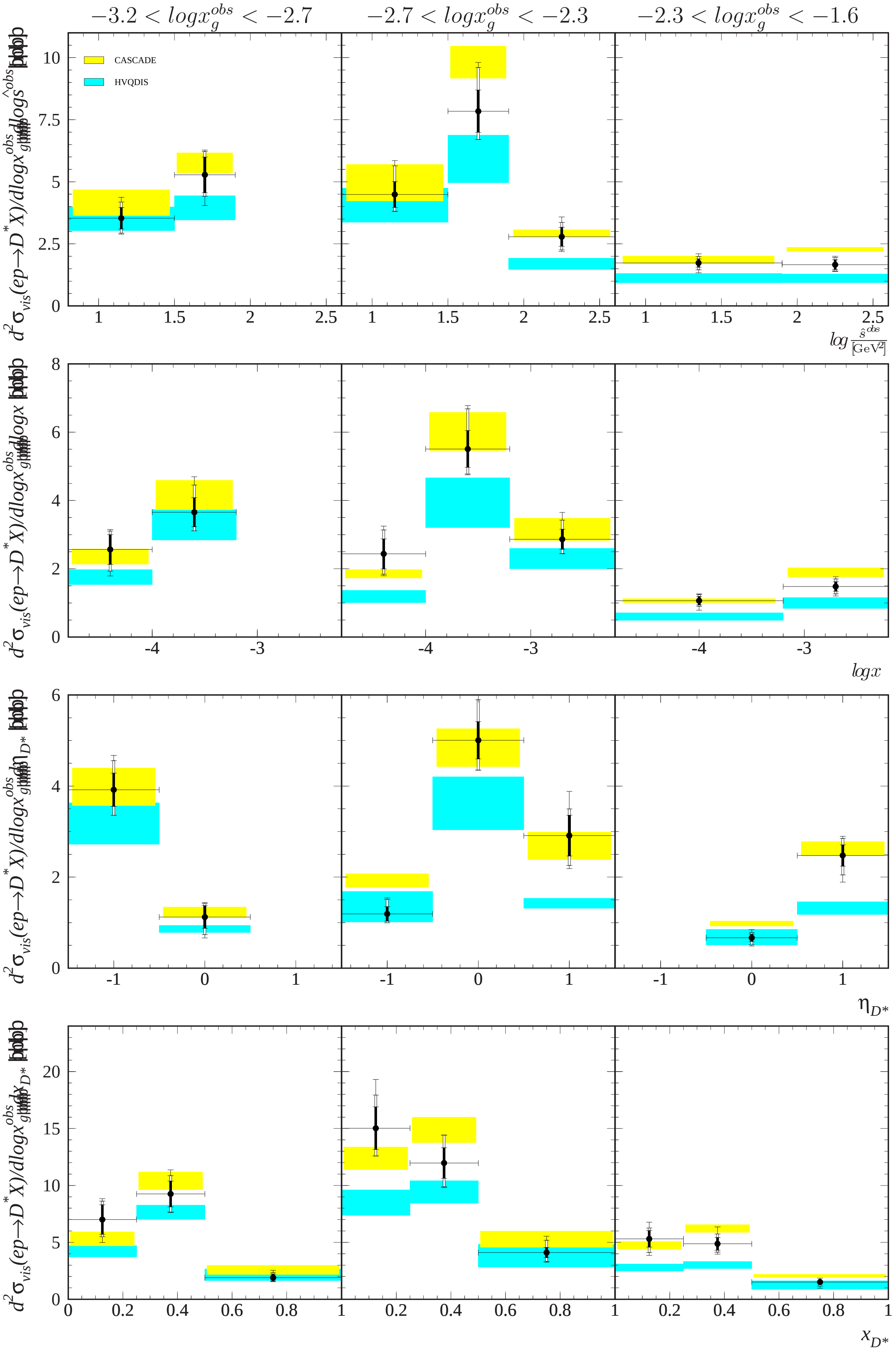

Figure 6.12: Inclusive D^{*+} double differential cross sections in the visible range: $d^2\sigma_{vis}(ep \to eD^{*+}X)/(dlogx_g^{obs}dlog\hat{s}^{obs}/[\mathrm{GeV}^2])$, $d^2\sigma_{vis}(ep \to eD^{*+}X)/(dlogx_g^{obs}dlogx)$, $d^2\sigma_{vis}(ep \to eD^{*+}X)/(dlogx_g^{obs}d\eta_{D^*})$, $d^2\sigma_{vis}(ep \to eD^{*+}X)/(dlogx_g^{obs}dx_{D^*})$. The dark and light shaded bands are described in the caption of figure 5.1

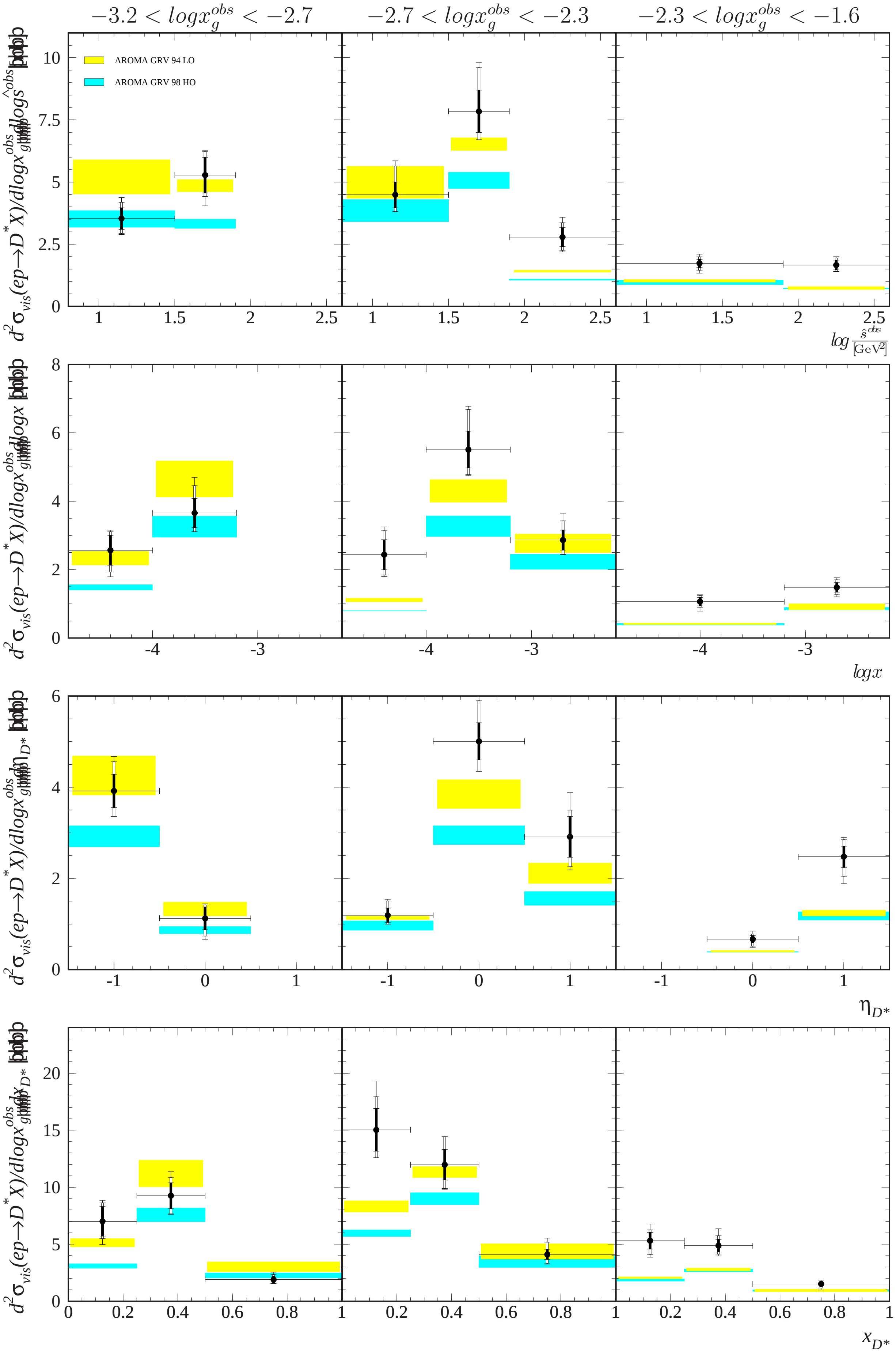

Figure 6.13: Inclusive D^{*+} double differential cross sections in the visible range: $d^2\sigma_{vis}(ep \to eD^{*+}X)/(dlogx_g^{obs}dlog\hat{s}^{obs}/[\mathrm{GeV}^2])$, $d^2\sigma_{vis}(ep \to eD^{*+}X)/(dlogx_g^{obs}dlogx)$, $d^2\sigma_{vis}(ep \to eD^{*+}X)/(dlogx_g^{obs}d\eta_{D^*})$, $d^2\sigma_{vis}(ep \to eD^{*+}X)/(dlogx_g^{obs}dx_{D^*})$. The dark and light shaded bands are described in the caption of figure 5.4

Conclusion

This thesis has been based on the data collected by the H1 experiment during the years 1996 and 1997. The selected event sample corresponds to an integrated luminosity of 18.55 pb^{-1}. Nearly one thousand D^{*+} events in the $D^0\pi_s^+ \rightarrow (K^-\pi^+)\pi_s^+$ decay channel have been reconstructed within the kinematic range 1 GeV^2 $< Q^2 <$ 100 GeV^2 and $0.05 < y < 0.7$ and within the visible range of the D^{*+} analysis $-1.5 < \eta_{D^*} < 1.5$ and $p_{\perp D^*} > 1.5$ GeV/c. Within the given ranges, the total D^{*+} cross section measured amounts to 8.44 ± 0.42(stat.) $^{+1.12}_{-0.83}$(exp. syst.) $^{+0.64}_{-0.41}$(theo.syst.) nb. The CASCADE generator predictions, based on the LO CCFM formalism, well agree in normalisation whereas both LO and NLO predictions based on the DGLAP formalism from the AROMA generator and HVQDIS programme respectively underestimate the measurement. The achieved statistics allows a precise measurement of single differential cross sections and - for the first time - a measurement of double differential cross sections. The CASCADE generator, with the setting as used here, predicts the measured single and double differential cross sections fairly well, especially the D^{*+} pseudorapidity behaviour which is hardly described by the predictions of the AROMA generator and the HVQDIS programme. The CASCADE predictions, however, seem to overestimate the cross section at high $p_{\perp D^*}$ especially when the D^{*+} meson is emitted into the backward region. The data x_{D^*} distribution, which is very sensible with regard to both the hard process and the charm fragmentation, reveals a softer behaviour than all the studied predictions. The double differential cross sections show that the excess of experimental cross section at large η_{D^*} with respect to the HVQDIS predictions corresponds to small $p_{\perp D^*}$ and small x_{D^*}. This excess is independent of Q^2 within the measurement uncertainties. At high $p_{\perp D^*}$, the HVQDIS predictions are nearly in line with the measurement and describe the Q^2 behaviour whereas the CASCADE predictions systematically overestimate the measurement.

In addition to the cross sections measurement, the gluon density within the LO DGLAP formalism was extracted after unfolding the cross section as a function of x_g, the fraction of proton momentum carried by the gluon. An abnormal, rather flat extracted gluon density shows that the LO pQCD calculations are not able to describe the relation between the behaviour at hard scattering and the final state behaviour. Indeed, the LO AROMA generator predictions cannot describe the Bjorken x behaviour in different regions of the observed variable x_g^{obs}. After reweighting the AROMA predictions with the NLO correlation between x_g^{obs} and x_g a clear improvement with regard to the extracted gluon density is observed, however with a persistent normalisation problem.

The presented results have demonstrated the need for a refined understanding of applying pQCD in charm quark production together with a better knowledge on charm fragmentation. The data taken between the years 1998 and 2000 will bring the experimental errors smaller than the theoretical uncertainties. Moreover HERA II, the second running period of HERA, with its accelerator and detector upgrades will allow even more precise measurements and maybe the challenging measurement in the forward direction. These improvements will require the need of a NLO Monte Carlo event generator in order to reduce the theoretical uncertainties on the cross sections measurement.

Appendix A

Detector

A.1 Pulse Profile (Q, t) Analysis

The pulse integral Q and the signal timing t are the relevant parameters of a drift chamber. The pulse profile (Q, t) analysis is performed to have access to the pulse integral and the drift time from the ionisation point[1] to the avalanche point on a wire.

The pulse integrals Q_L and Q_R are the results of the sum of a defined part of the digitalised signals coming from the left end and from the right end of the wire respectively as shown in figure A.1.

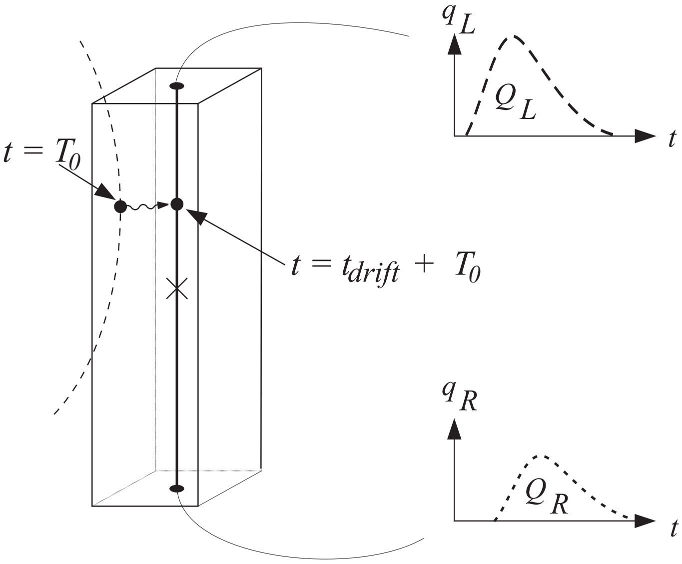

Figure A.1: Schematic view of a sense wire and the signals collected at both ends with the pulse integral Q_L and Q_R.

The determination of the drift time is more complicated. In the following the algorithm which is used for the H1 drift chambers is described. A schematic view is displayed in figure A.2. At a first step the times at half full amplitude $t_{L\,1/2}$ and $t_{R\,1/2}$ are determined

---

[1] The ionisation point or hit is the point on the particle trajectory with the shortest distance to the wire along the drift direction.

by linear interpolation of both left and right signals. The average of $t_{L\,1/2}$ and $t_{R\,1/2}$ represents the time at half maximum of the two signals as if they had been induced at the position on the wire which corresponds to equal travelling time t_{tot} of the left and right signals to reach the digitising electronic (to a good approximation, in case of equal cabling length, this position is at half of the wire). The average rise time of the left and right signal is used to extrapolate from $(t_{L\,1/2} + t_{R\,1/2})/2$ to the arrival time of the first electrons t_e. The time t_e is obtained by subtracting t_{tot} to the time $(t_L + t_R)/2$ taken at 10% of the pulse amplitude. Finally the drift time t_{drift} is given by $t_{drift} = t_e - T_0$, where T_0 is the collision time defined in subsection 2.2.3. From the drift time and the drift velocity the closest approach of the track trajectory in the (x, y) plane is deduced.

The z coordinate of the closest approach z_{ca} is determined with the charge division method.

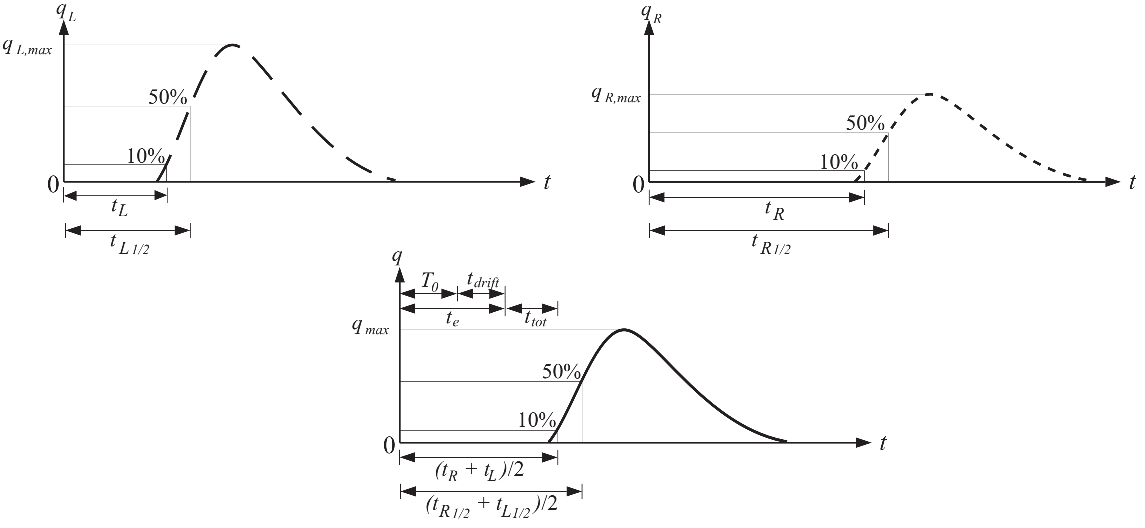

Figure A.2: Determination of t_{drift} from (Q, t) analysis.

A.2 Charge Division

In H1 the z coordinate of the closest approach z_{ca} is given with respect to the origin at the middle of the wire. The left end of the wire is in the positive z direction. From the pulse integral Q_L and Q_R the value of z_{ca} is determined as follows:

$$z_{ca} = L/2\,\frac{Q_L - Q_R}{Q_L + Q_R}, \tag{A.1}$$

where L represents the total wire length.

A.3 Time Evolution of the D^{*+} in DIS Subtrigger

The time evolution, in terms of trigger elements, of the D^{*+} in DIS subtrigger for the 1996 and 1997 data taking are given in tables A.1 and A.2. The definitions of the trigger elements are given in subsection 4.1.1.

<table>
<tr><th>ST 2</th><th></th><th></th><th></th><th></th><th></th><th></th></tr>
<tr><td>Run ≥ 146416 (03/07/96)</td><td>DCRPh_Tc</td><td>zVtx_sig</td><td>SPCLc_IET>1</td><td>!BToF_BG
&&
!VETO_inner_BG&&!VETO_Outer_BG</td><td>FToF_IA||!FToF_BG
&&
PToF_IA||!PToF_BG</td><td>!RZ_non_vtx||RZ_sig1</td></tr>
<tr><td>Run ≥ 147117 (05/07/96)</td><td>DCRPh_THig</td><td>zVtx_sig</td><td>SPCLc_IET>1</td><td>!BToF_BG
&&
!VETO_inner_BG&&!VETO_Outer_BG</td><td>FToF_IA||!FToF_BG
&&
PToF_IA||!PToF_BG</td><td>!RZ_non_vtx||RZ_sig1</td></tr>
<tr><td>Run ≥ 149557 (16/07/96)</td><td>DCRPh_THig</td><td>zVtx_sig</td><td>SPCLc_IET>1</td><td>!BToF_BG
&&
!VETO_inner_BG&&!VETO_Outer_BG</td><td>FToF_IA||!FToF_BG
&&
PToF_IA||!PToF_BG</td><td></td></tr>
<tr><td>Run ≥ 150509 (18/07/96)</td><td>DCRPh_THig</td><td>zVtx_sig</td><td>SPCLc_IET>1</td><td>!BToF_BG
&&
!VETO_inner_BG&&!VETO_Outer_BG</td><td></td><td></td></tr>
<tr><td>Run ≥ 151109 (21/07/96)</td><td>DCRPh_THig</td><td>zVtx_sig</td><td>SPCLc_IET>1</td><td>!BToF_BG
&&
!VETO_inner_BG&&!VETO_Outer_BG</td><td>FToF_IA||!FToF_BG
&&
PToF_IA||!PToF_BG</td><td></td></tr>
<tr><td>Run ≥ 151174 (22/07/96)</td><td>DCRPh_THig</td><td>zVtx_sig</td><td>SPCLc_IET>1</td><td>!BToF_BG
&&
!VETO_inner_BG&&!VETO_Outer_BG</td><td></td><td></td></tr>
<tr><td>Run ≥ 152130 (26/07/96)</td><td>DCRPh_THig</td><td>zVtx_sig</td><td>SPCLc_IET>1</td><td>!BToF_BG
&&
!VETO_inner_BG&&!VETO_Outer_BG</td><td>FToF_IA||!FToF_BG
&&
PToF_IA||!PToF_BG</td><td></td></tr>
<tr><td>Run ≥ 152566 (29/07/96)</td><td>DCRPh_THig</td><td>zVtx_sig</td><td>SPCLc_IET>1</td><td>!BToF_BG
&&
!VETO_inner_BG&&!VETO_Outer_BG</td><td>FToF_IA||!FToF_BG
&&
PToF_IA||!PToF_BG</td><td>!RZ_non_vtx||RZ_sig1</td></tr>
<tr><td>Run ≥ 152800 (30/07/96)</td><td>DCRPh_THig</td><td>zVtx_sig</td><td>SPCLc_IET>1</td><td>!BToF_BG
&&
!VETO_inner_BG&&!VETO_Outer_BG</td><td>FToF_IA||!FToF_BG
&&
PToF_IA||!PToF_BG</td><td></td></tr>
<tr><td>Run ≥ 154520 (10/08/96)</td><td>DCRPh_THig</td><td>zVtx_sig</td><td>SPCLc_IET>1</td><td>!BToF_BG
&&
!VETO_inner_BG&&!VETO_Outer_BG</td><td>FToF_IA||!FToF_BG</td><td></td></tr>
<tr><td>Run ≥ 157877 (05/09/96)</td><td>DCRPh_Ta</td><td>zVtx_sig</td><td>SPCLc_IET>1
||
SPCLc_IET_Cen_2</td><td>!BToF_BG
&&
!VETO_inner_BG&&!VETO_Outer_BG</td><td>FToF_IA||!FToF_BG</td><td></td></tr>
<tr><td>Run ≥ 163255 (12/10/96)</td><td>DCRPh_THig</td><td>zVtx_sig</td><td>SPCLc_IET>1
||
SPCLc_IET_Cen_2</td><td>!BToF_BG
&&
!VETO_inner_BG&&!VETO_Outer_BG</td><td>FToF_IA||!FToF_BG</td><td></td></tr>
<tr><td>Run ≥ 166213 (30/10/96)</td><td>DCRPh_THig</td><td>zVtx_sig</td><td>SPCLc_IET>1
||
SPCLc_IET_Cen_2</td><td>!BToF_BG
&&!
VETO_inner_BG&&!VETO_Outer_BG
&&
!SPCLh_AToF_E_1</td><td>FToF_IA||!FToF_BG</td><td></td></tr>
</table>

Table A.1: Time evolution of subtrigger ST2 in 1996.

<table>
<tr><td>ST 2</td><td colspan="6"></td></tr>
<tr><td>Run ≥ 177920 (03/03/97)</td><td>DCRPh_THig</td><td>zVtx_sig</td><td>SPCLe_IET>1
||
SPCLe_IET_Cen_2</td><td>!BToF_BG
&&
!VETO_inner_BG&&!VETO_Outer_BG
&&
!SPCLh_AToF_E_1</td><td>FToF_IA||!FToF_BG</td><td></td></tr>
<tr><td>Run ≥ 185990 (28/04/97)</td><td>DCRPh_THig</td><td>zVtx_sig</td><td>SPCLe_IET>1
||
SPCLe_IET_Cen_2</td><td>!BToF_BG
&&
!VETO_inner_BG&&!VETO_Outer_BG
&&
!SPCLh_AToF_E_1</td><td></td><td></td></tr>
<tr><td>Run ≥ 186001 (28/04/97)</td><td>DCRPh_THig</td><td>zVtx_sig</td><td>SPCLe_IET>1
||
SPCLe_IET_Cen_2</td><td>!BToF_BG
&&
!VETO_inner_BG&&!VETO_Outer_BG
&&
!SPCLh_AToF_E_1</td><td>FToF_IA||!FToF_BG</td><td></td></tr>
<tr><td>ST 61</td><td colspan="6"></td></tr>
<tr><td>Run ≥ 193433 (28/06/97)</td><td>DCRPh_THig</td><td>zVtx_sig</td><td>SPCLe_IET>2
||
SPCLe_IET_Cen_3</td><td>!BToF_BG
&&
!VETO_inner_BG&&!VETO_Outer_BG
&&
!SPCLh_AToF_E_1 && !SPCLh_ToF_E_2</td><td>FToF_IA||!FToF_BG</td><td>!(DCRPh_NL_many
&&
DCRPh_NH_many
&&
DCRPh_PL_many
&&
DCRPh_PH_many)</td></tr>
</table>

Table A.2: Time evolution of subtrigger ST2 and ST61 in 1997.

Appendix B

Charm Configuration in the Boson-Proton System

The c and $\bar{c}$ quarks which are back to back in the γg system have a very small opening angle in the γp system because of the strong boost between the two systems (on average $\vec{p}_g = 10^{-4}\vec{p}_p$). For this reason the charm mass is negligible in the $\gamma^* p$ system. The invariant mass of the two quarks can be written as follows:

$$\begin{aligned} m_{c\bar{c}}^2\mathrm{c}^4 &= (p_c + p_{\bar{c}})^2\mathrm{c}^2 = (E_c^{\gamma^*p} + E_{\bar{c}}^{\gamma^*p})^2 - (\vec{p}_c^{\,\gamma^*p} + \vec{p}_{\bar{c}}^{\,\gamma^*p})^2\mathrm{c}^2 \\ &\approx 2E_c^{\gamma^*p}E_{\bar{c}}^{\gamma^*p} - 2E_c^{\gamma^*p} * E_{\bar{c}}^{\gamma^*p} * \cos(\theta_{c\bar{c}}^{\gamma^*p}) \qquad m_c \approx m_{\bar{c}} \approx 0 \\ &\approx 0 \text{ in the } \gamma^*p \text{ system} \qquad \theta_{c\bar{c}}^{\gamma^*p} \approx 0. \end{aligned} \tag{B.1}$$

This means that the invariant mass of the $c\bar{c}$ pair can be neglected in the γp system.

Using the same arguments, the particles in the proton remnant also have a negligible total invariant mass in the hadronic final state system.

The hadronic centre of mass energy W is then only depending on the $c\bar{c}$ energy (or the proton remnant energy):

$$\begin{aligned} W &= (p_{c\bar{c}} + p_X)^2\mathrm{c}^2 \\ &= E_{c\bar{c}}^{\gamma^*p\,2} + E_X^{\gamma^*p\,2} + 2E_{c\bar{c}}^{\gamma^*p}E_X^{\gamma^*p} - |\vec{p}_{c\bar{c}}^{\,\gamma^*p}|^2\mathrm{c}^2 - |\vec{p}_X^{\,\gamma^*p}|^2\mathrm{c}^2 - 2\vec{p}_{c\bar{c}}^{\,\gamma^*p} \cdot \vec{p}_X^{\,\gamma^*p}\mathrm{c}^2 \\ &= m_{c\bar{c}}^2\mathrm{c}^4 + m_X^2\mathrm{c}^4 + 2E_{c\bar{c}}^{\gamma^*p}E_X^{\gamma^*p} - 2\vec{p}_{c\bar{c}}^{\,\gamma^*p} \cdot \vec{p}_X^{\,\gamma^*p}\mathrm{c}^2 \\ &\approx 4E_{c\bar{c}}^{\gamma^*p}E_X^{\gamma^*p} \approx 4E_{c\bar{c}}^{\gamma^*p\,2} \approx 4E_X^{\gamma^*p\,2} \qquad m_{c\bar{c}}^2 \approx m_X^2 \approx 0 \text{ and } \vec{p}_{c\bar{c}}^{\,\gamma^*p} + \vec{p}_X^{\,\gamma^*p} = 0. \end{aligned} \tag{B.2}$$

Therefore both the $c\bar{c}$ pair and the proton remnant are carrying half of the centre of mass energy W.

Appendix C

Correction for Downscaling of Subtriggers

In most of the cases the problem of the subtriggers downscaling is solved in two possible straightforward ways:

- only one subtrigger (for example the subtrigger i) is used and for each run k, the integrated luminosity L_k is corrected by the corresponding prescale factor d_{ik} according to:
$$L_k^{cor} = \frac{L_k}{d_{ik}}. \tag{C.1}$$
- a set of subtriggers is used but only runs where none of these subtriggers were downscaled.

The most general case, where several subtriggers with possible downscaling factors are requested, is precisely described in reference [18]. In this case each event j which is kept after the downscaling procedure has to carry a weight w_j in order to correctly estimate the cross section:

$$w_j = \frac{\sum_{k=1}^{N_{runs}} L_k}{\sum_{k=1}^{N_{runs}} L_k P_{jk}}. \tag{C.2}$$

The averaging over all runs is done to minimise the statistical error in case of prescale factors which are varying from run to run. P_{jk} represents the probability that at least one of the N_{subtr} subtriggers triggers the event j in a run k and is given by:

$$P_{jk} = 1 - (1 - \prod_{k=1}^{N_{subtr}} \frac{r_{ij}}{d_{ik}}) \tag{C.3}$$

where d_{ik} is the prescale factor of the subtrigger i in the run k and r_{ij} is one if the raw subtrigger i is set in the event j. The raw subtrigger bit is set as soon as the subtrigger condition is satisfied whereas the actual subtrigger bit is set only for subtriggers surviving the downscaling.

One should be aware that the correction of the integrated luminosity (like in equation C.1) is not possible as soon as more than one subtrigger is used.

Appendix D

Mass Fits, D^{*+} Rates and Efficiencies

D.1 Δm Fits

The number of reconstructed D^{*+} is obtained from the fit of the Δm distribution. The function is composed of a Gaussian distribution centred at the nominal Δm mass plus the two-body phase space background. The width and the mean value of the Gaussian distribution are determined from the fit to the total sample of D^{*+} candidates. The obtained values were used as constants for all Δm fits performed bin wise.

The fitted Δm distributions in bins of W, x, Q^2, $p_{\perp D^*}$, η_{D^*}, x_{D^*}, $(p_{\perp D^*}; \eta_{D^*})$, $(p_{\perp D^*}; x_{D^*})$, $(x_{D^*}; \eta_{D^*})$, $(\eta_{D^*}; Q^2)$, $(p_{\perp D^*}; Q^2)$, $(x_g^{obs}; \hat{s}^{obs})$, $(x_g^{obs}; x)$, $(x_g^{obs}; \eta_{D^*})$ and $(x_g^{obs}; x_{D^*})$ are shown in figures D.1 to D.15. The wrong charge background is displayed for $\Delta m + 0.4$ GeV/c^2. The results of the fits are given in the upper box where the number of D^{*+} is given by the parameter P4 (definition of the other free parameters can be found in equation 4.23). In the upper corner a χ^2 indicates that a χ^2 fit is performed. When the statistics are too poor a likelihood fitting procedure is applied.

D.2 D^{*+} Rates

The D^{*+} rates as a function of W, x, Q^2, $p_{\perp D^*}$, η_{D^*}, x_{D^*} are presented in figure D.16. The D^{*+} rates in bins of $(p_{\perp D^*}; \eta_{D^*})$, $(p_{\perp D^*}; x_{D^*})$, $(x_{D^*}; \eta_{D^*})$ are shown in figure D.17 and in bins of $(\eta_{D^*}; Q^2)$, $(p_{\perp D^*}; Q^2)$ in figure D.18. Finally, the D^{*+} rates as a function of $\hat{s}^{obs}$, x, η_{D^*}, x_{D^*} are displayed in figure D.19 for three different ranges of x_g^{obs}. The H1 data D^{*+} rates (points) are compared to the D^{*+} rates from the simulation (histograms). For the simulation the number of D^{*+} within one bin $N_{D^*}^{MC}(bin)$ is the luminosity normalised number of fitted D^{*+} expected by the Monte Carlo and scaled by the total number of D^{*+} found in the data $N_{D^*}^{data}$:

$$N_{D^*}^{MC}(bin) = \frac{\mathcal{L}^{96} N_{D^*}^{MC96}(bin) + \mathcal{L}^{97} N_{D^*}^{MC97}(bin)}{\mathcal{L}^{96} + \mathcal{L}^{97}} \cdot \frac{N_{D^*}^{data}}{N_{D^*}^{MC}}. \tag{D.1}$$

The Monte Carlo generator used for the simulation is AROMA 2.21 with $\mu_R = \mu_F = \hat{s}$, ϵ(Peterson) $= 0.078$, $m_c = 1.5$ GeV/c^2 and GRV 94 LO for the gluon density. The AROMA generator with these sets of parameters was used to get the efficiencies in the kinematic and visible ranges.

D.3 Efficiencies

The analysis efficiency ε_{vis}^{year} for one year is given by:

$$\varepsilon_{vis}^{\text{year}} = \frac{N_{D^*}^{MC,\text{year}}(rec)}{N_{D^*}^{MC,\text{year}}(gen)}. \tag{D.2}$$

The number $N_{D^*}^{MC,\text{year}}(rec)$ is the number of fitted D^{*+} events after subtrigger requirements and analysis cuts in the reconstructed kinematic, visible and bin ranges. The number $N_{D^*}^{MC,\text{year}}(gen)$ is the total number of D^{*+} in the generated kinematic, visible and bin ranges. In figures D.20 to D.23 the efficiency in bins of W, x, Q^2, $p_{\perp D^*}$, η_{D^*}, x_{D^*}, $(p_{\perp D^*};\, \eta_{D^*})$, $(p_{\perp D^*};\, x_{D^*})$, $(x_{D^*};\, \eta_{D^*})$, $(\eta_{D^*};\, Q^2)$, $(p_{\perp D^*};\, Q^2)$, $(x_g^{obs};\, \hat{s}^{obs})$, $(x_g^{obs};\, x)$, $(x_g^{obs};\, \eta_{D^*})$ and $(x_g^{obs};\, x_{D^*})$ are presented.

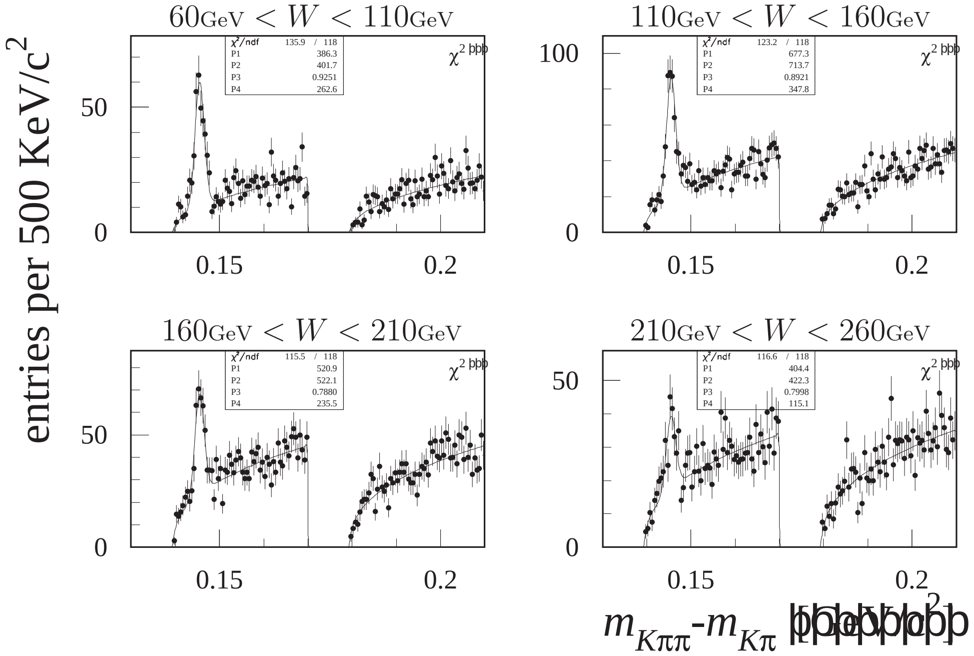

Figure D.1: Δm distributions with fits (curves) in bins of W. For details on the fit see text.

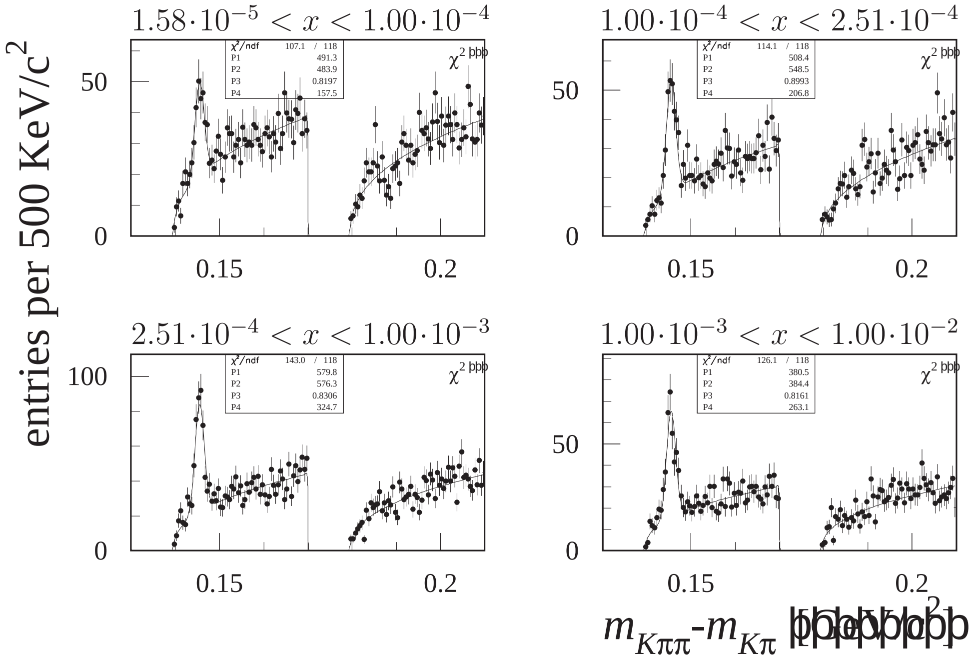

Figure D.2: Δm distributions with fits (curves) in bins of x. For details on the fit see text.

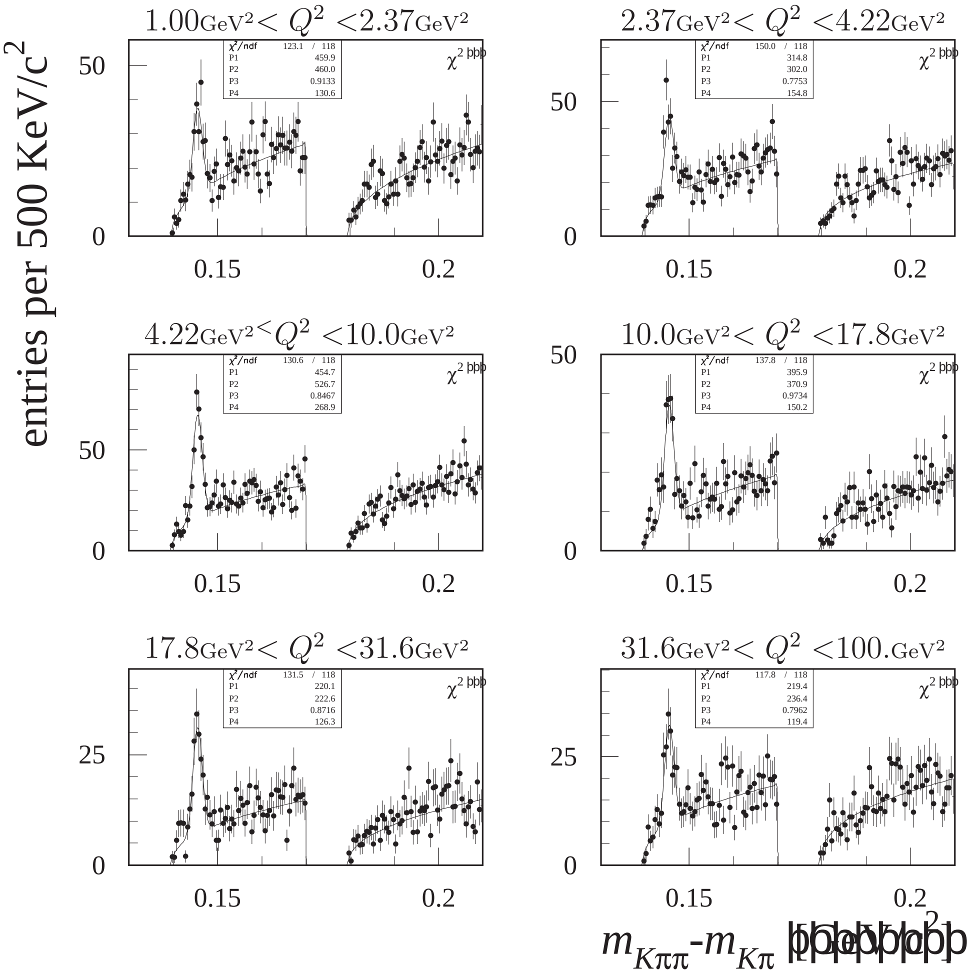

Figure D.3: Δm distributions with fits (curves) in bins of Q^2. For details on the fit see text.

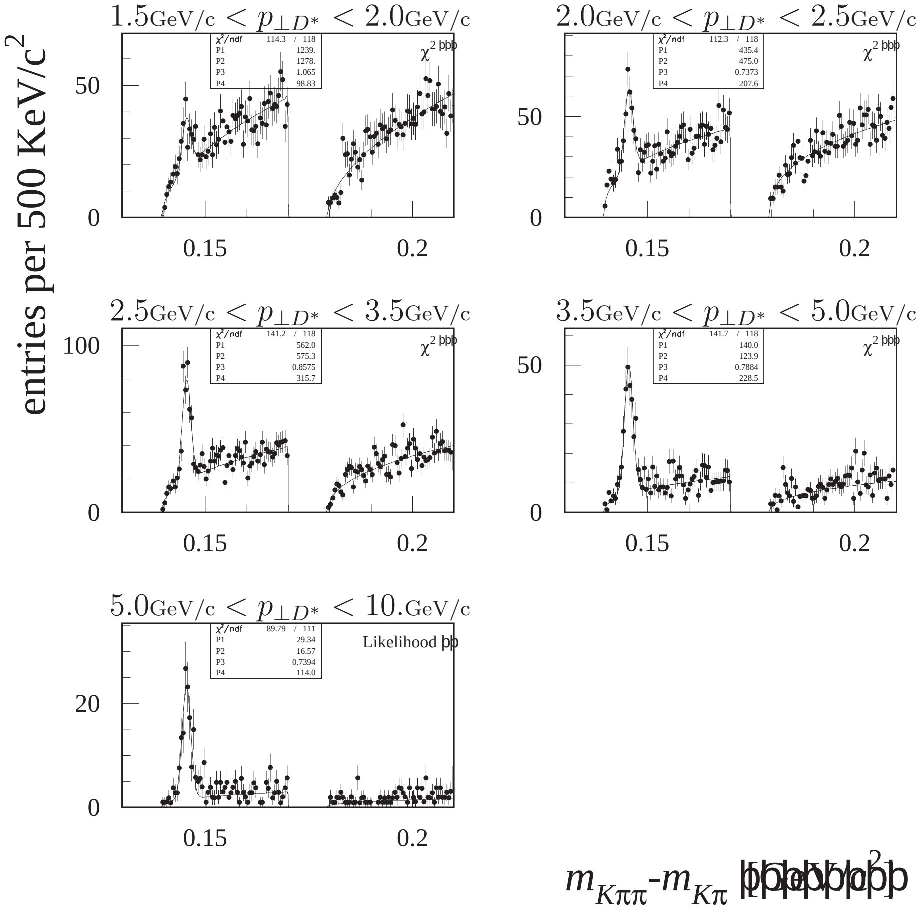

Figure D.4: Δm distributions with fits (curves) in bins of $p_{\perp D^*}$. For details on the fit see text.

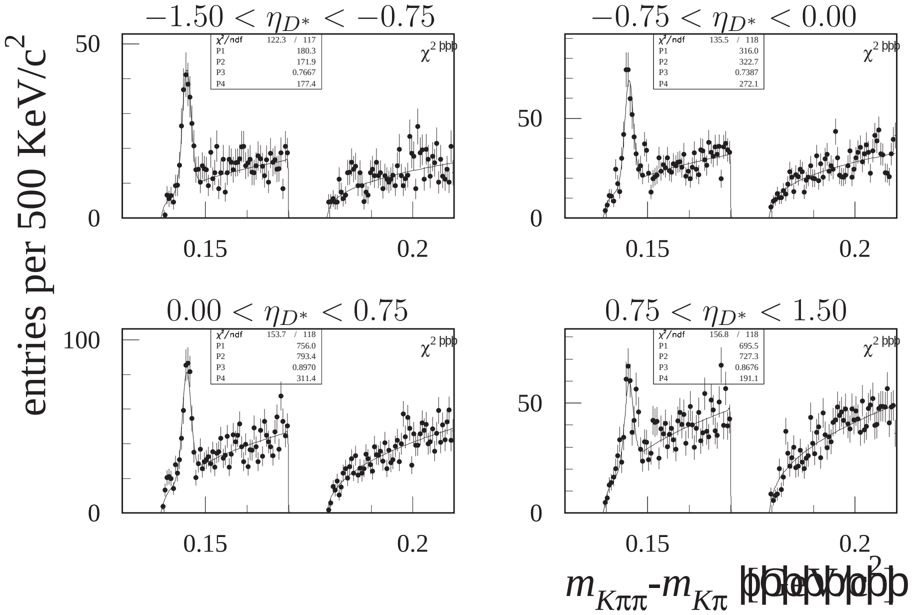

Figure D.5: Δm distributions with fits (curves) in bins of η_{D^*}. For details on the fit see text.

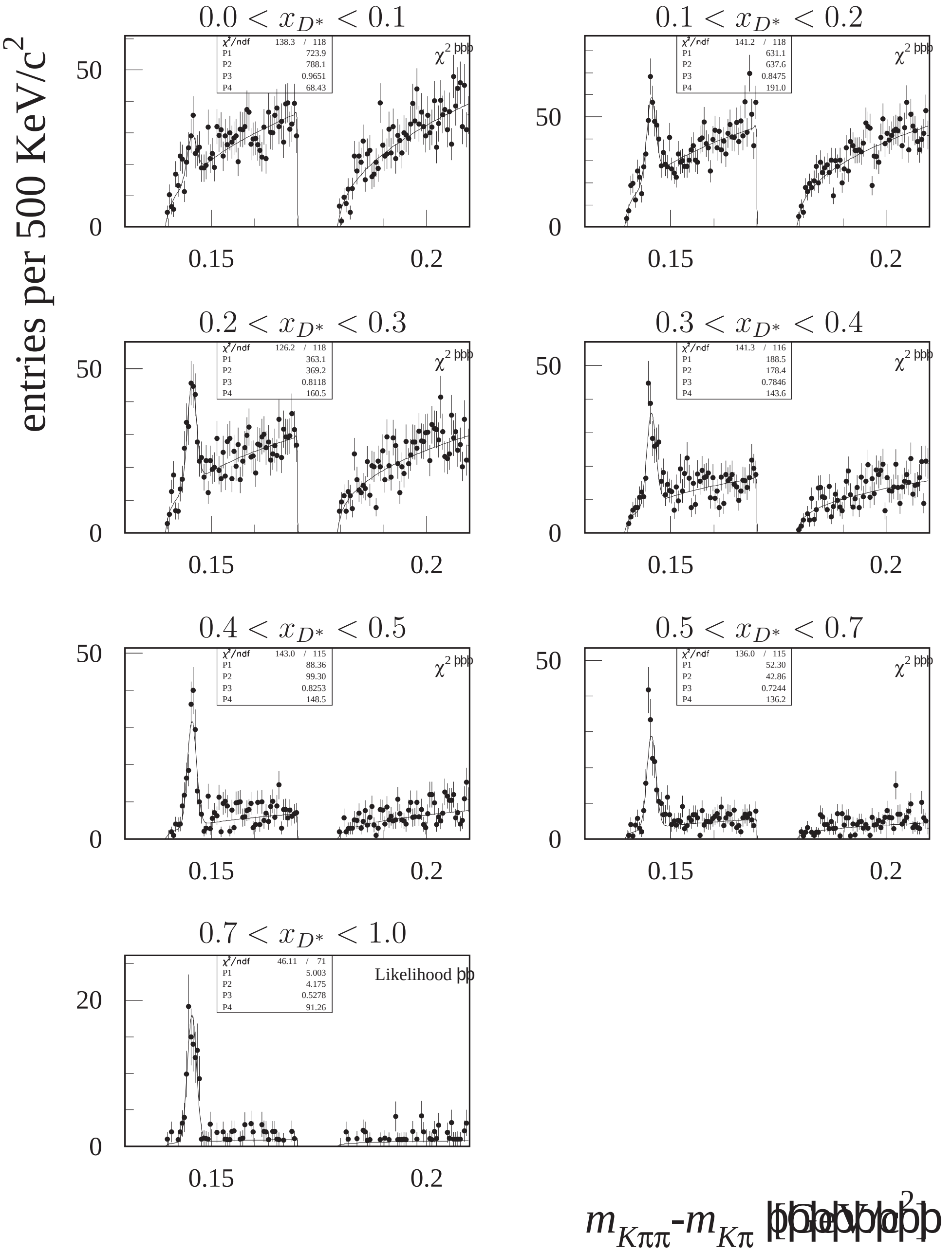

Figure D.6: Δm distributions with fits (curves) in bins of x_{D^*}. For details on the fit see text.

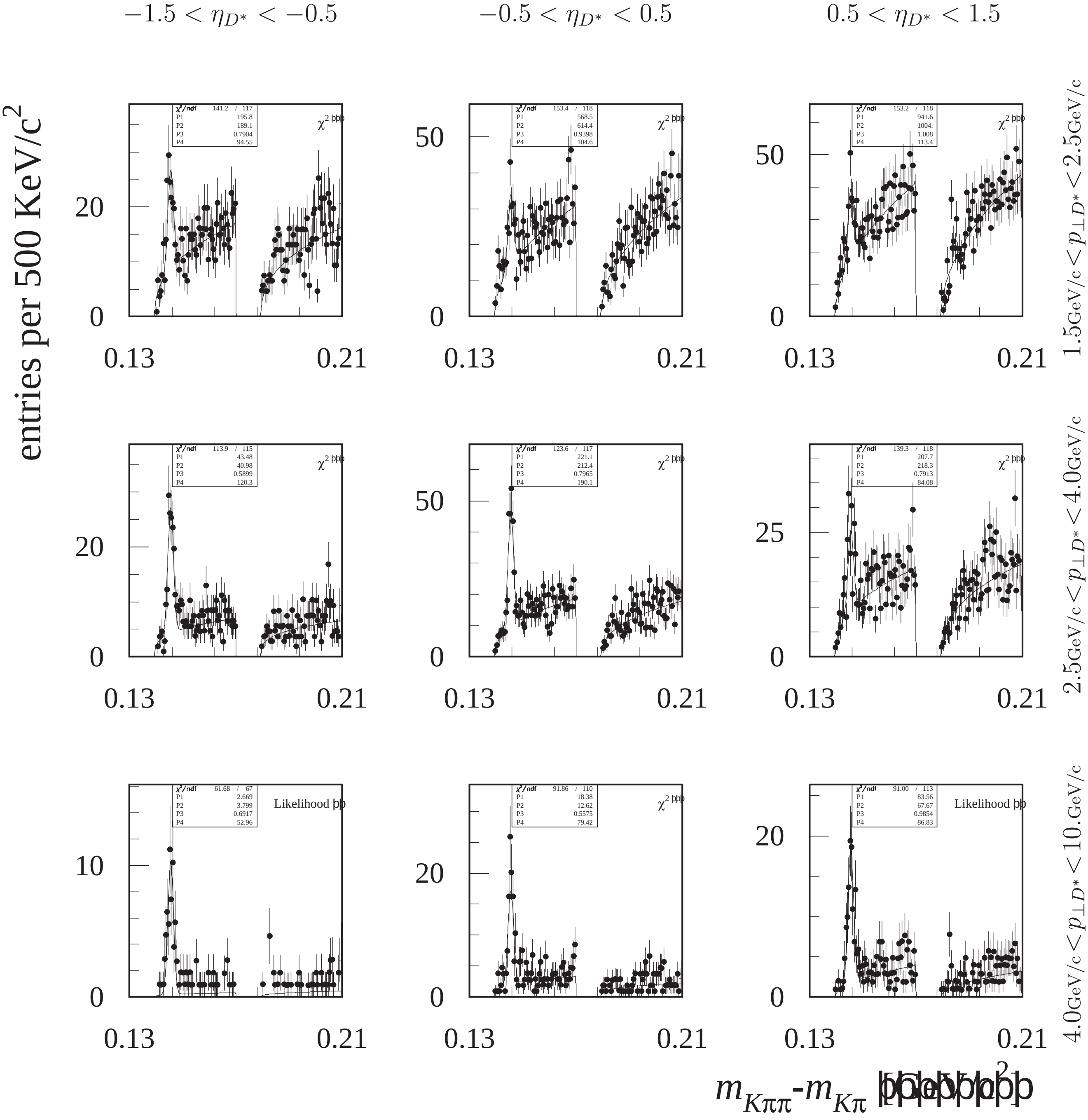

Figure D.7: Δm distributions with fits (curves) in bins of $(p_{\perp D^*}; \eta_{D^*})$. For details on the fit see text.

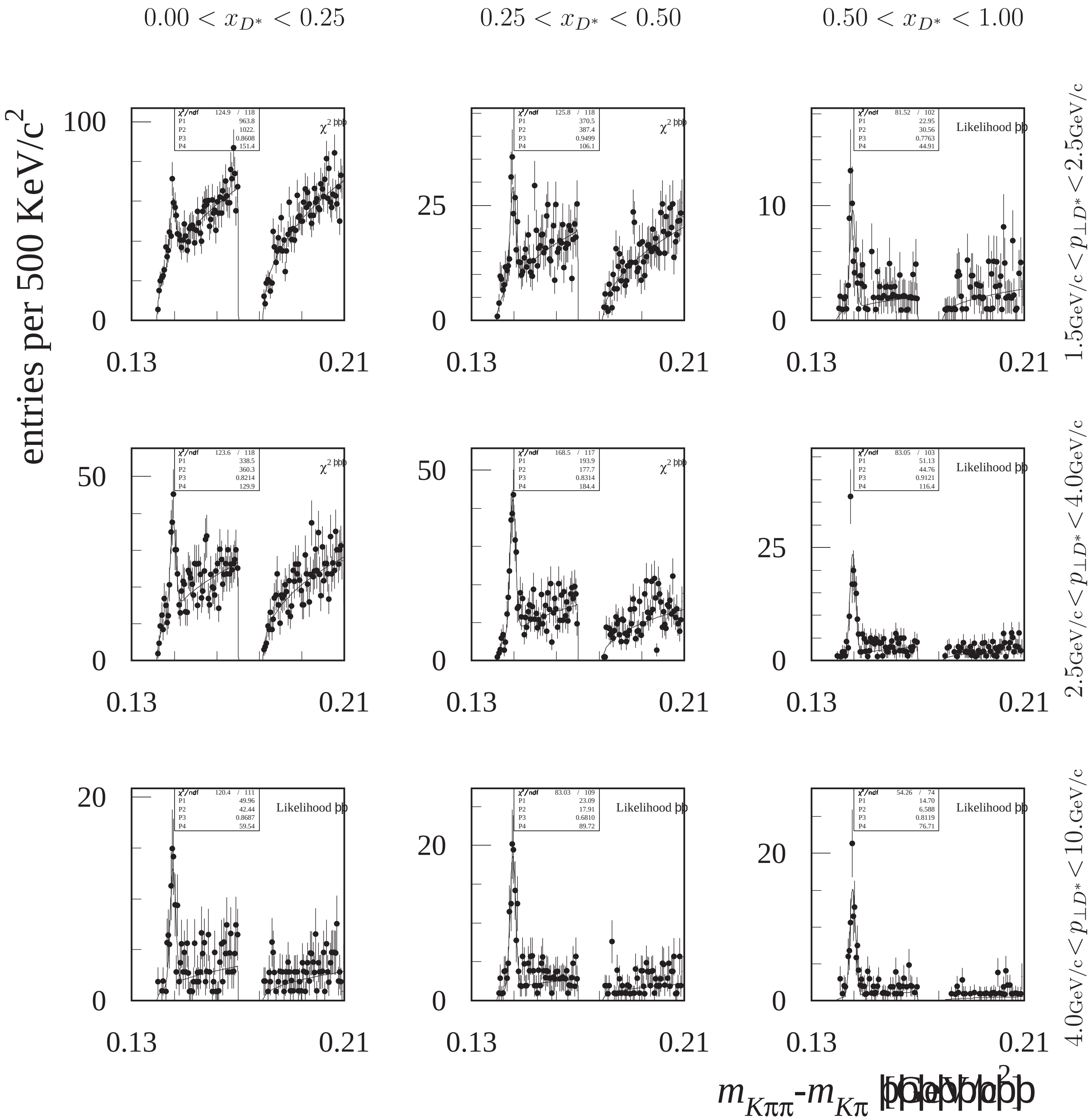

Figure D.8: Δm distributions with fits (curves) in bins of $(p_{\perp D^*}; x_{D^*})$. For details on the fit see text.

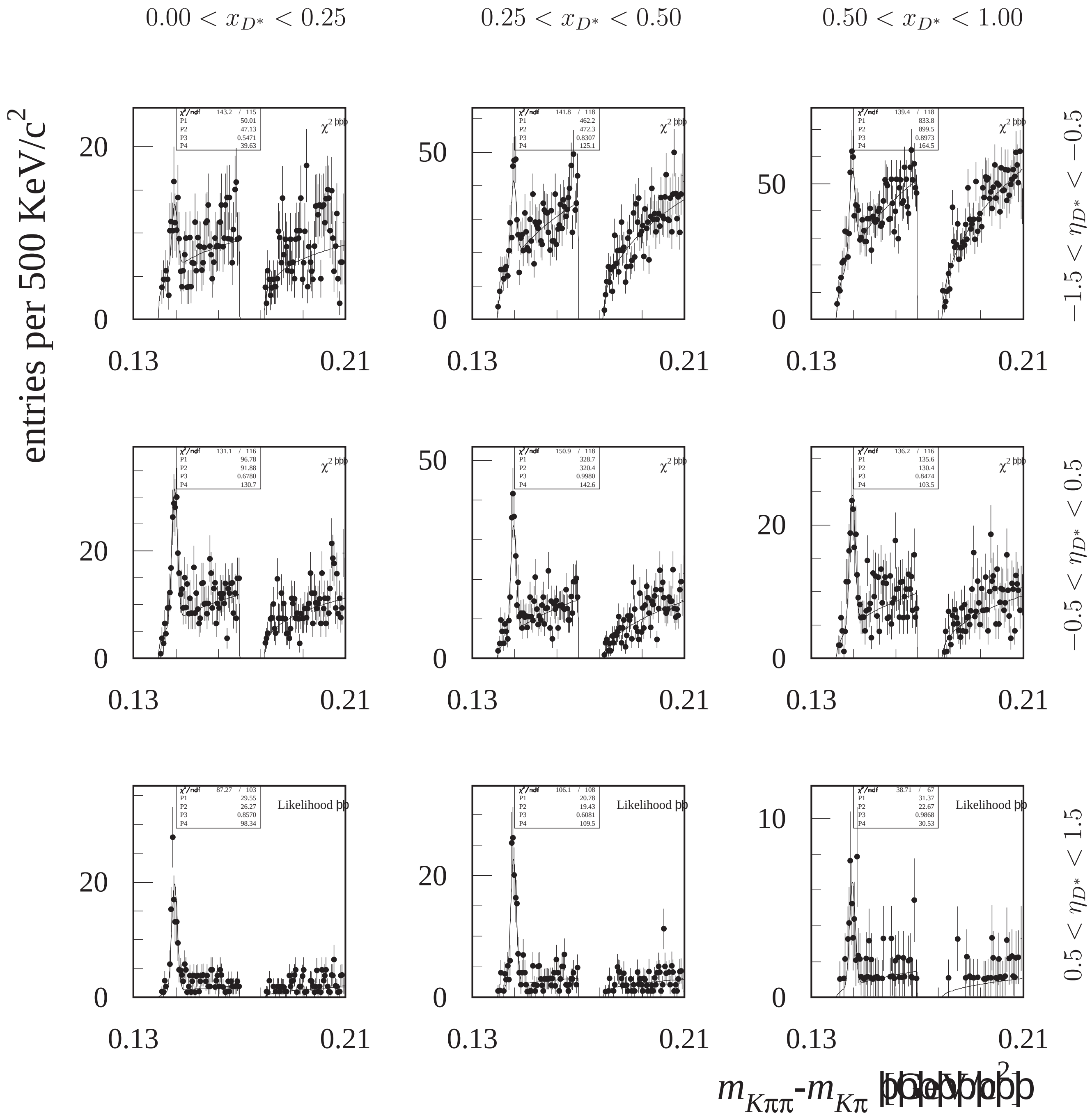

Figure D.9: Δm distributions with fits (curves) in bins of $(x_{D^*}; \eta_{D^*})$. For details on the fit see text.

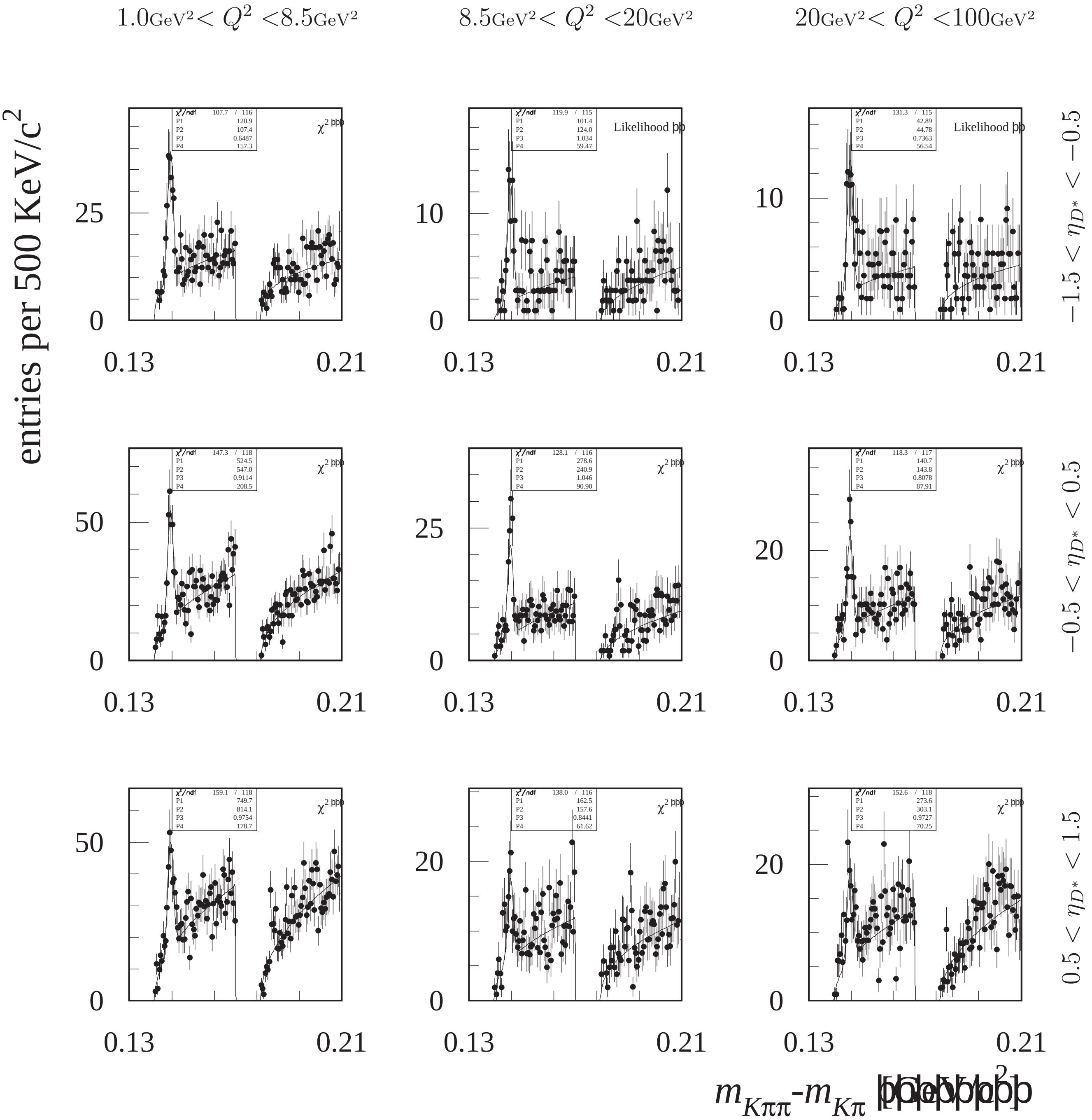

Figure D.10: Δm distributions with fits (curves) in bins of $(\eta_{D^*}; Q^2)$. For details on the fit see text.

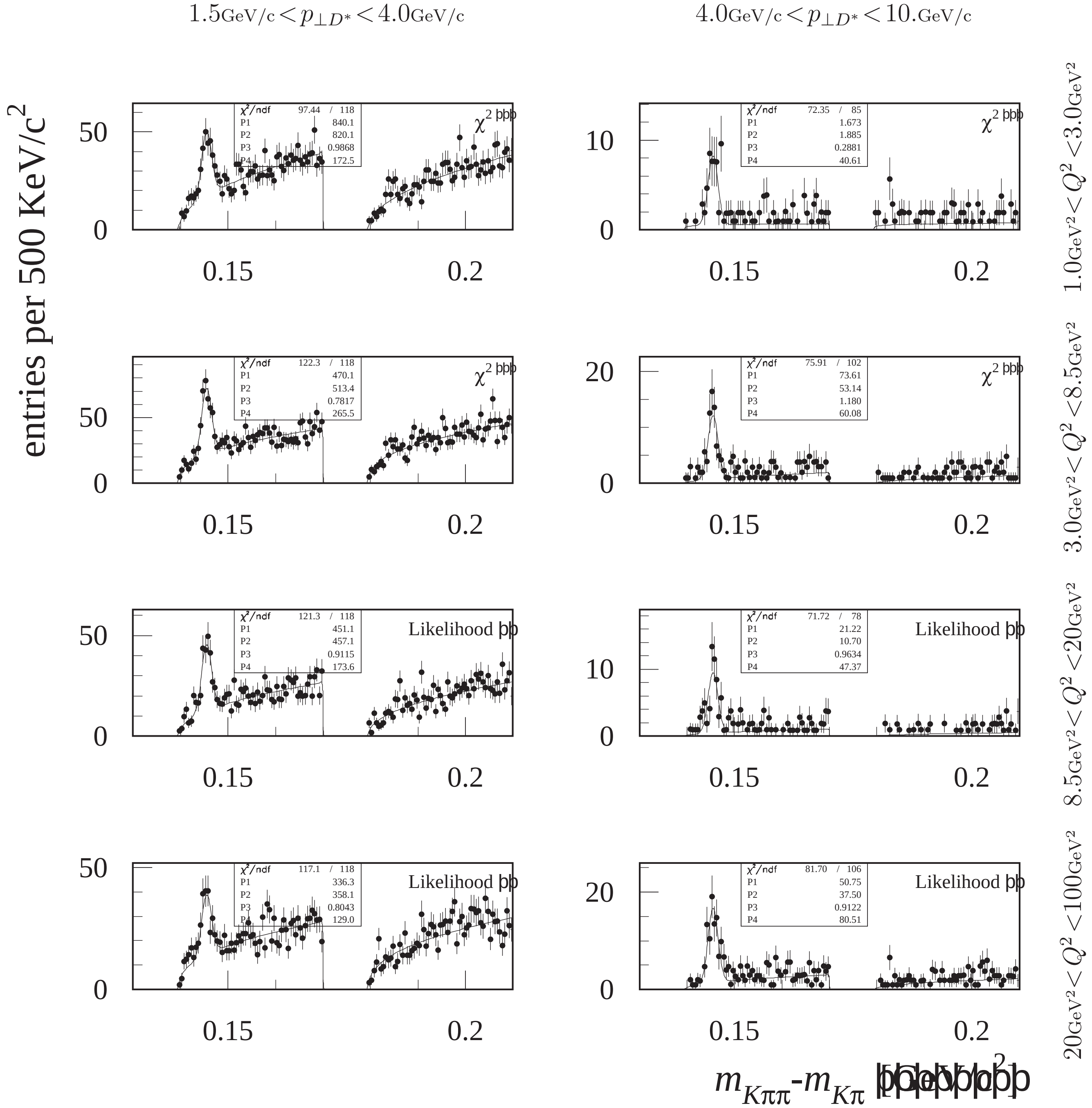

Figure D.11: Δm distributions with fits (curves) in bins of $(p_{\perp D^*}; Q^2)$. For details on the fit see text.

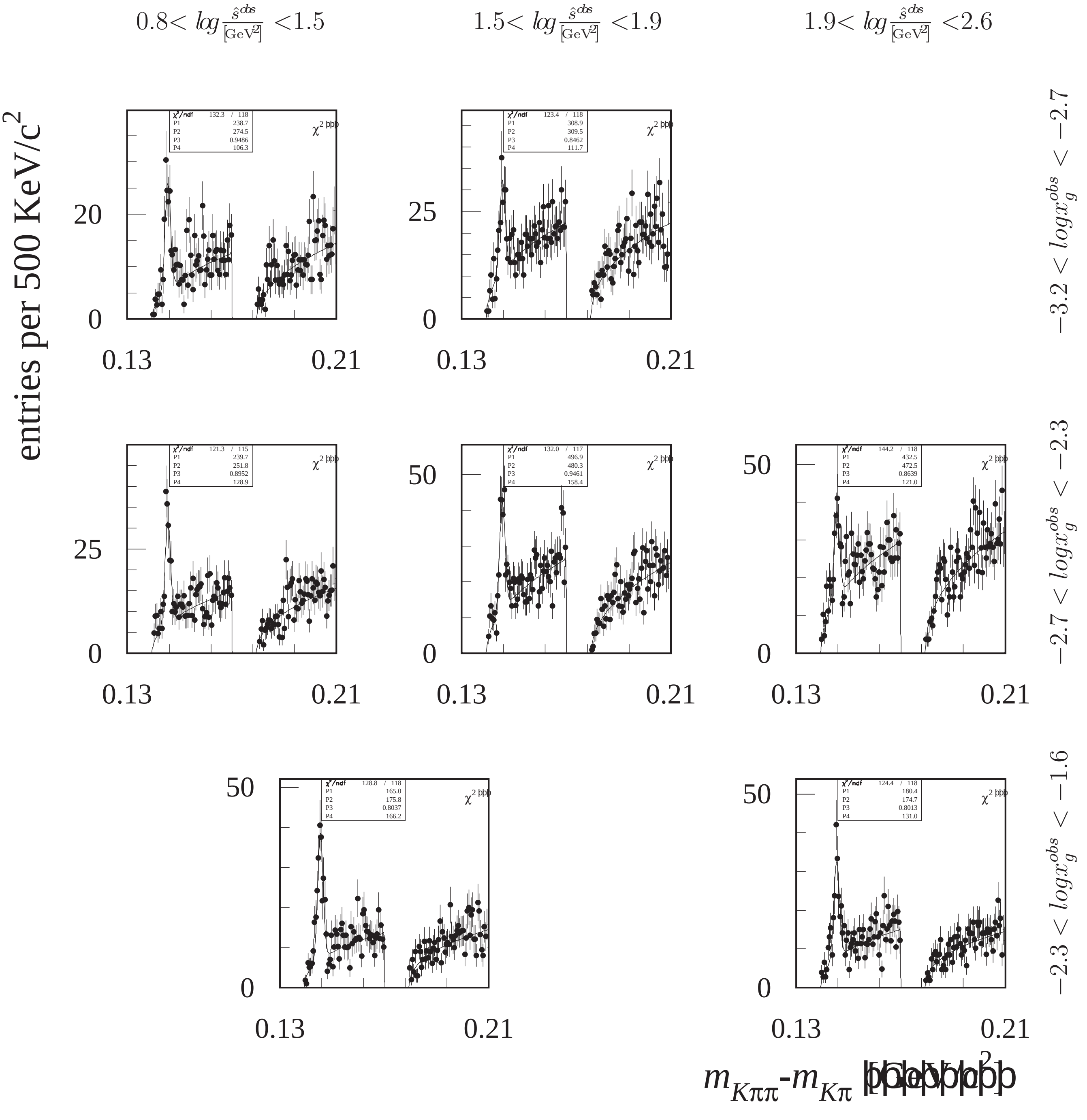

Figure D.12: Δm distributions with fits (curves) in bins of (x_g^{obs}; $\hat{s}^{obs}$), where $\hat{s}^{obs}$ is given in GeV^2 and is implicitly divided by 1 GeV^2. For details on the fit see text.

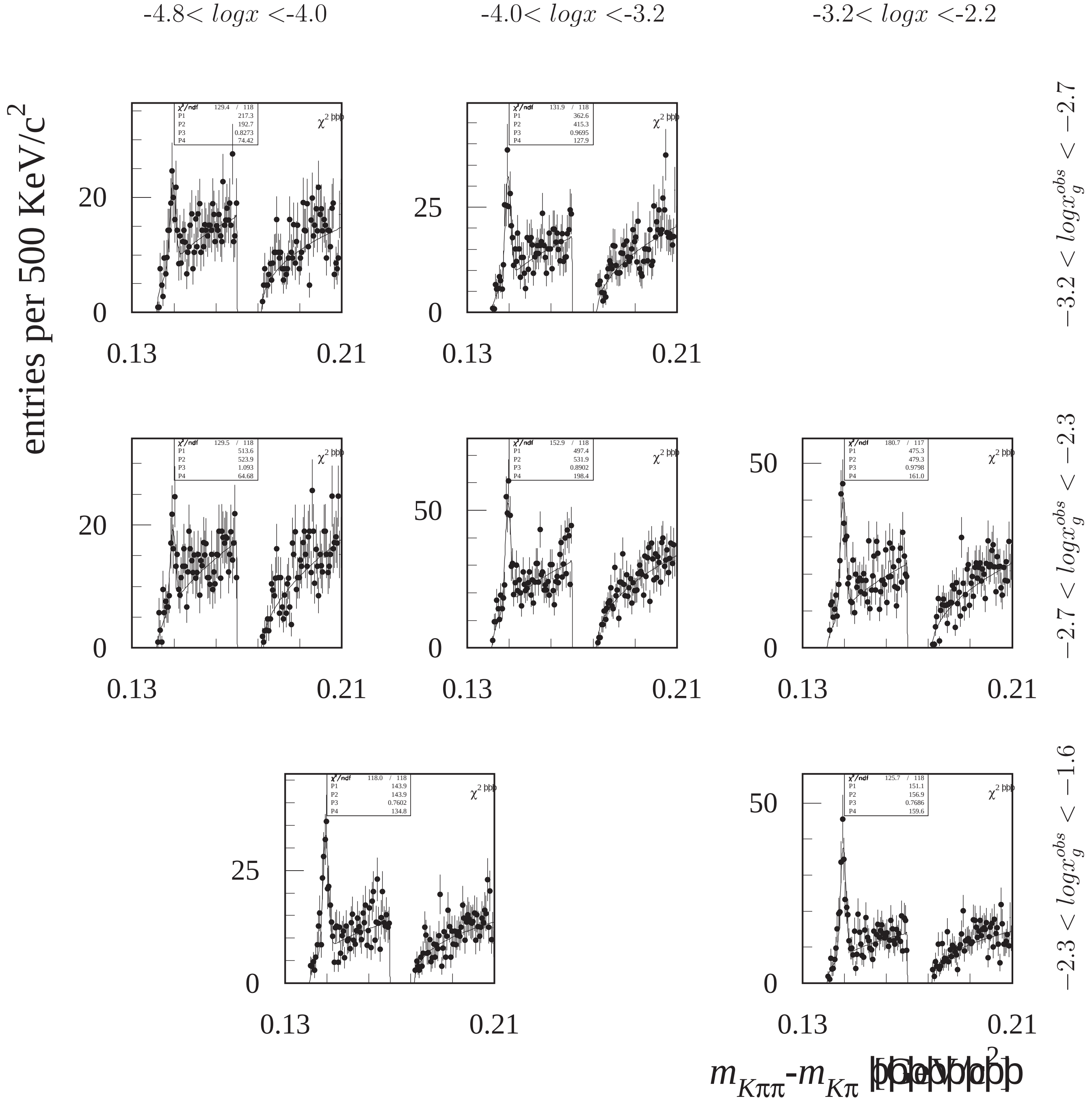

Figure D.13: Δm distributions with fits (curves) in bins of (x_g^{obs}; x). For details on the fit see text.

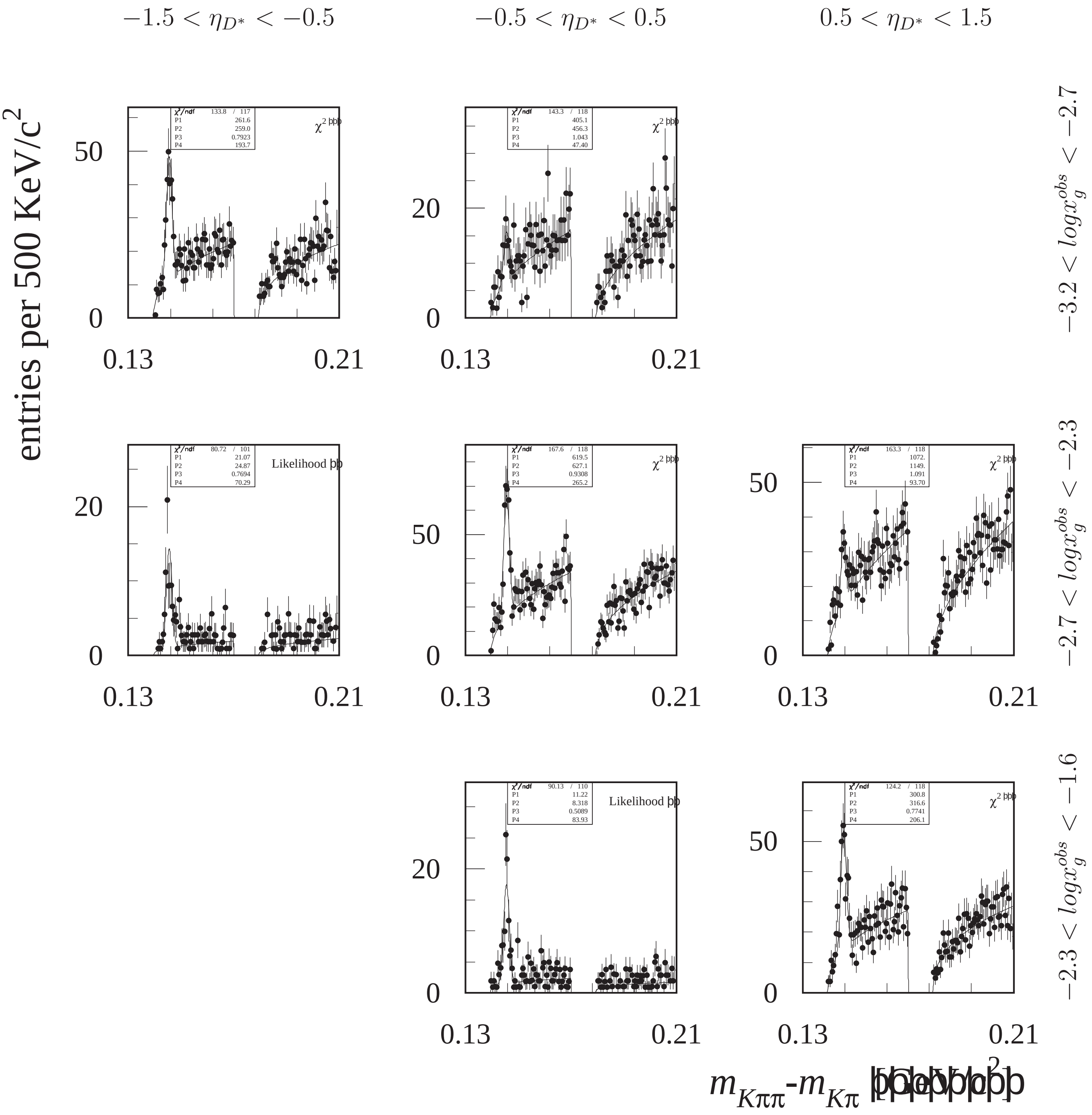

Figure D.14: Δm distributions with fits (curves) in bins of x_g^{obs}; η_{D^*}). For details on the fit see text.

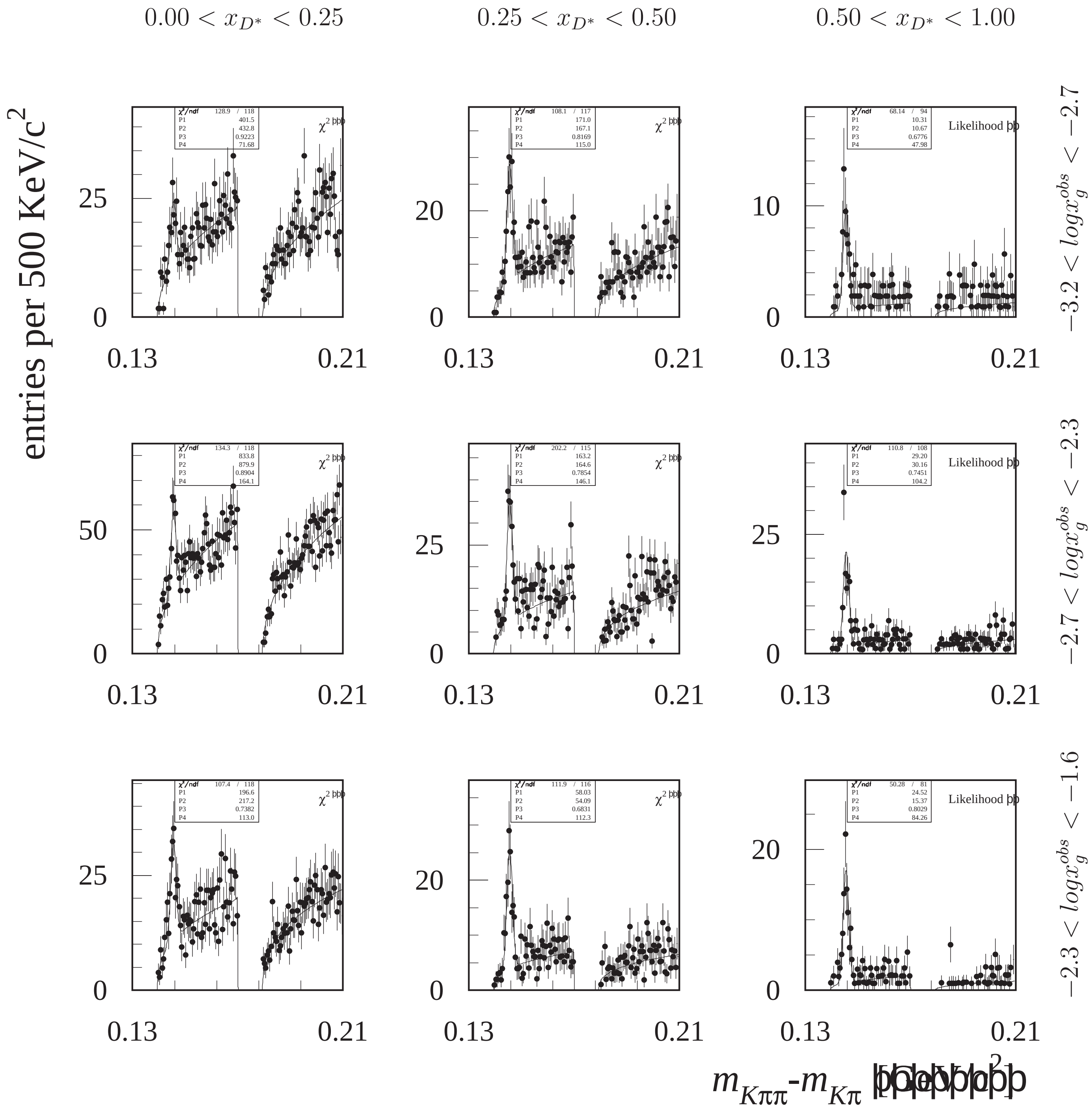

Figure D.15: Δm distributions with fits (curves) in bins of (x_g^{obs}; x_{D^*}). For details on the fit see text.

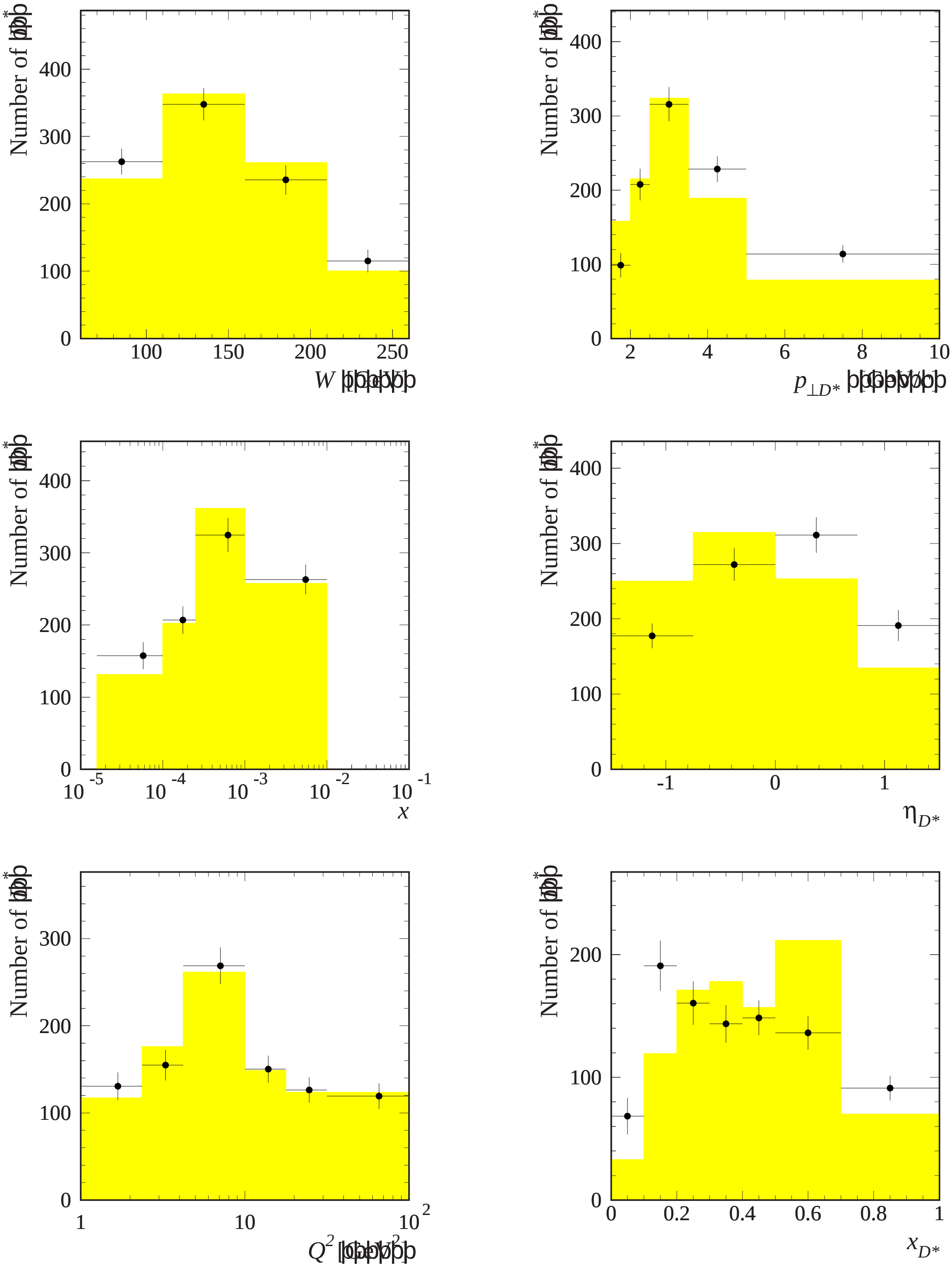

Figure D.16: Number of fitted D^{*+} for the 1996 and 1997 data as a function of W, x, Q^2, $p_{\perp D^*}$, η_{D^*} and x_{D^*}. The data (points) are compared to the luminosity normalised number of fitted D^{*+} expected by the Monte Carlo (histograms) scaled by the total number of D^{*+} found in the data according to equation D.1.

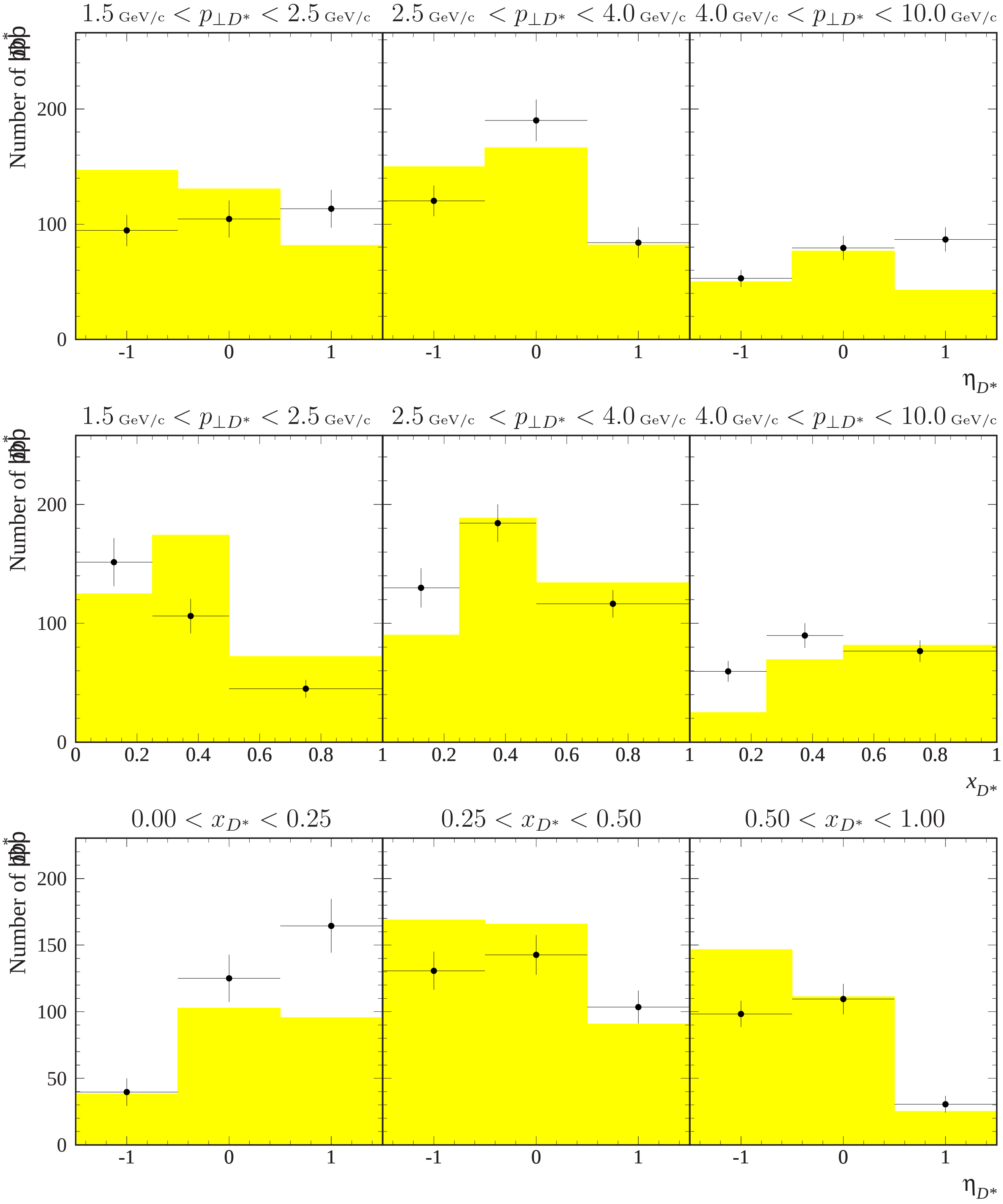

Figure D.17: Number of fitted D^{*+} for the 1996 and 1997 data as a function of ($p_{\perp D^*}$; η_{D^*}), ($p_{\perp D^*}$; x_{D^*}) and (x_{D^*}; η_{D^*}). The data (points) are compared to the luminosity normalised number of fitted D^{*+} expected by the Monte Carlo (histograms) scaled by the total number of D^{*+} found in the data according to equation D.1.

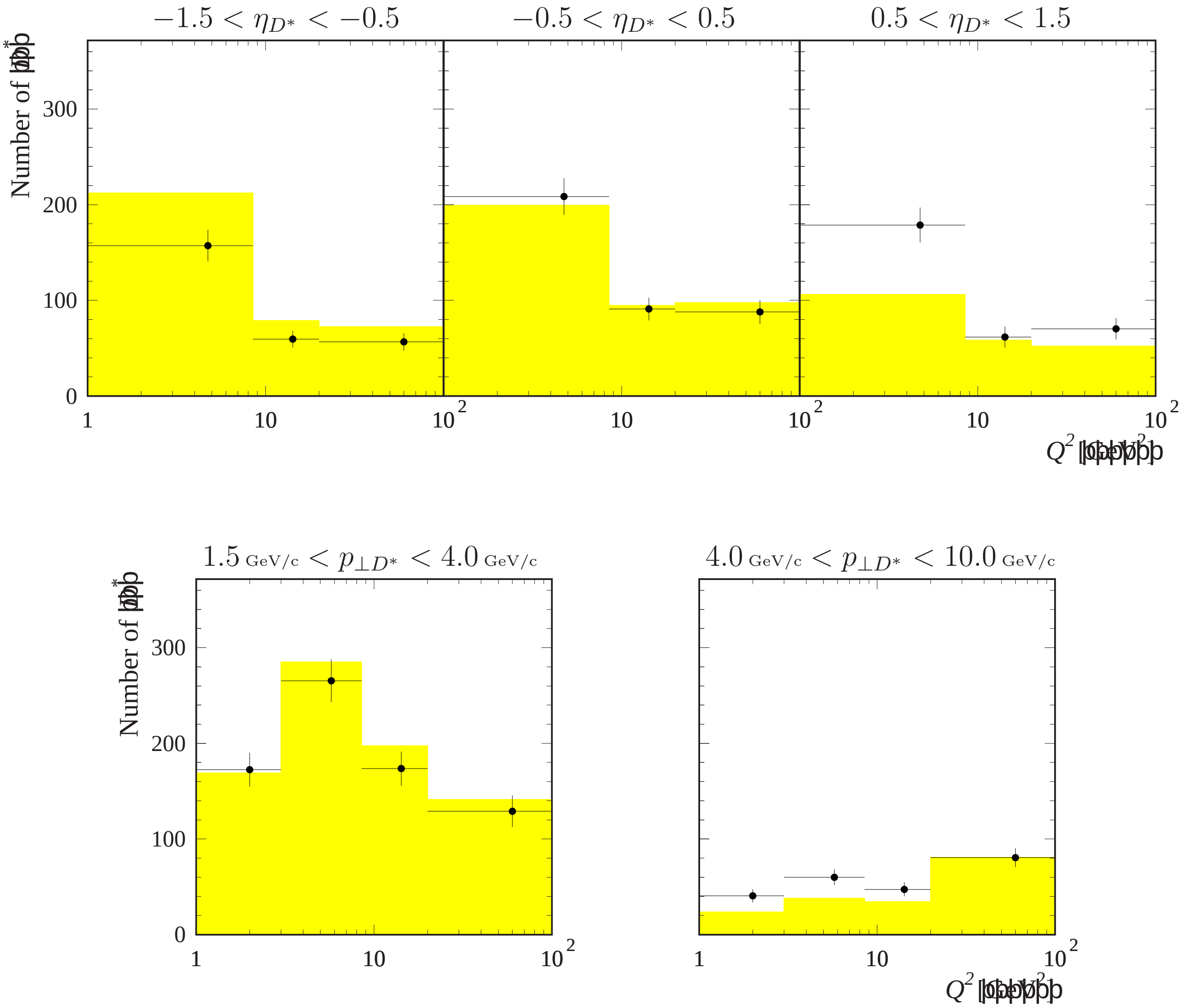

Figure D.18: Number of fitted D^{*+} for the 1996 and 1997 data as a function of $(\eta_{D^*}; Q^2)$ and $(p_{\perp D^*}; Q^2)$. The data (points) are compared to the luminosity normalised number of fitted D^{*+} expected by the Monte Carlo (histograms) scaled by the total number of D^{*+} found in the data according to equation D.1.

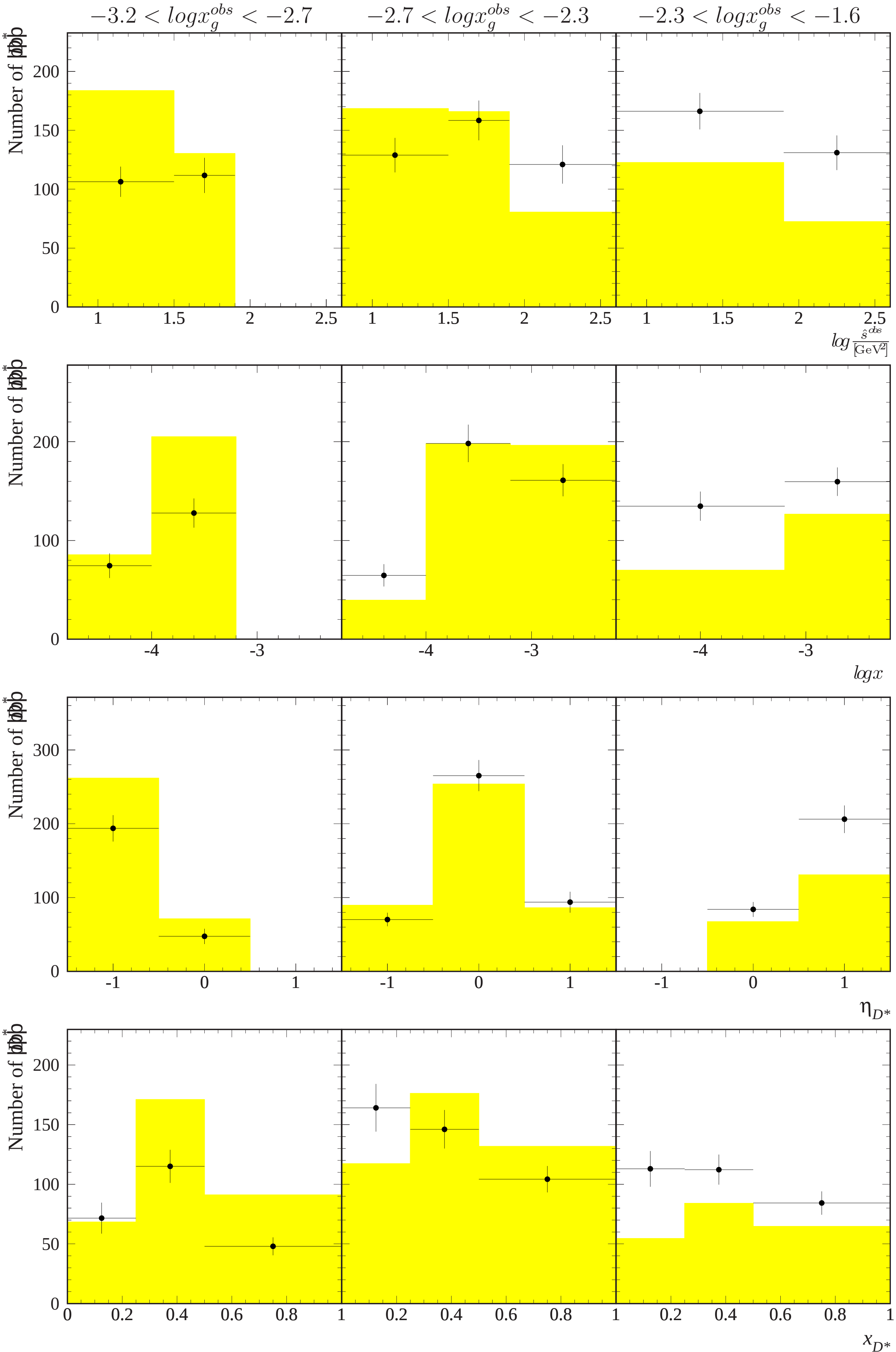

Figure D.19: Number of fitted D^{*+} for the 1996 and 1997 data as a function of $(x_g^{obs}; \hat{s}^{obs})$, $(x_g^{obs}; x)$, $(x_g^{obs}; \eta_{D^*})$ and $(x_g^{obs}; x_{D^*})$. The data (points) are compared to the luminosity normalised number of fitted D^{*+} expected by the Monte Carlo (histograms) scaled by the total number of D^{*+} found in the data according to equation D.1.

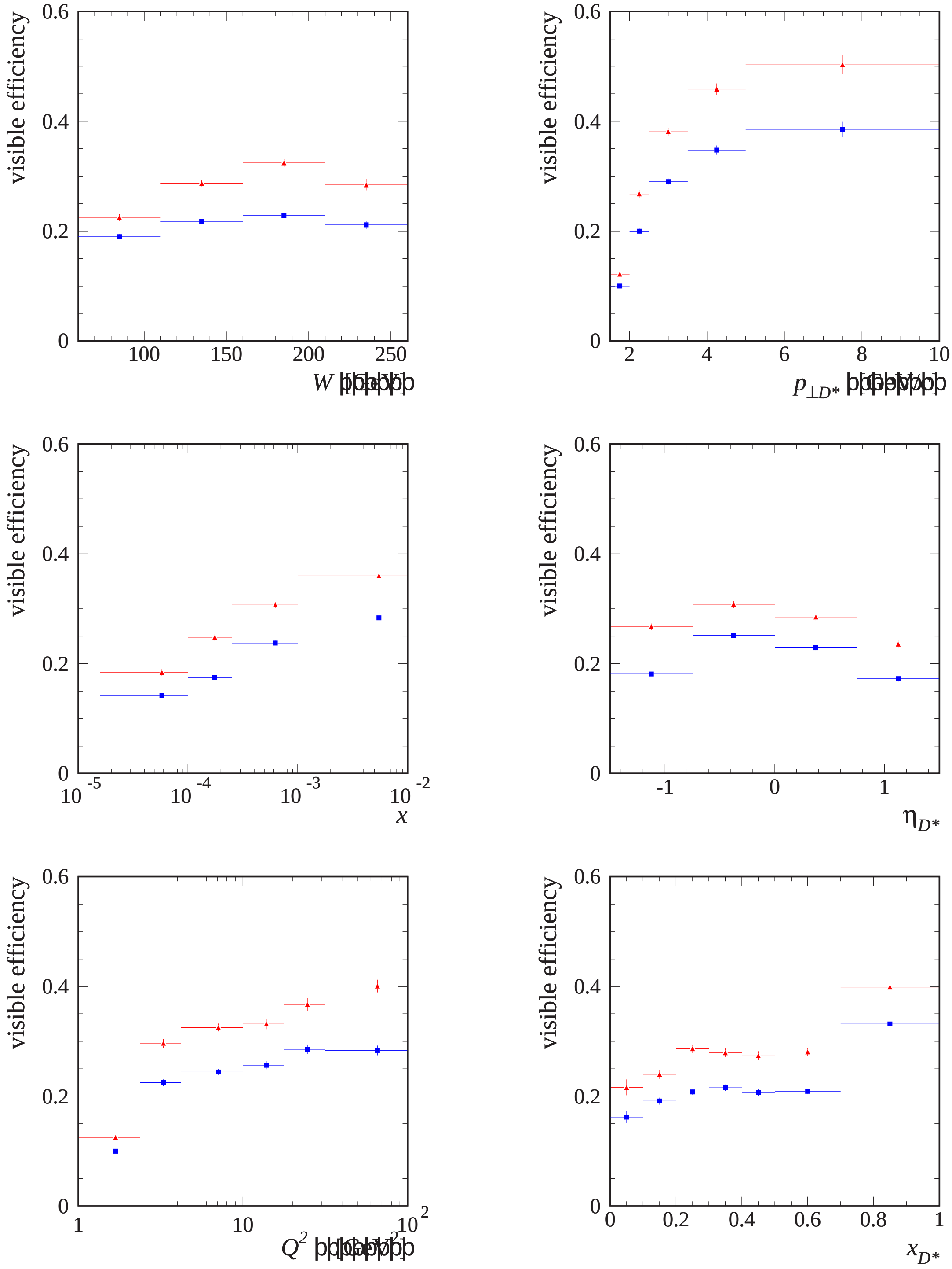

Figure D.20: Efficiencies of the D^{*+} selection cuts within the visible rangle predicted by the AROMA Monte Carlo generator and after detector simulation for the year 1996 (triangles) and 1997 (squares) as a function of W, x, Q^2, $p_{\perp D^*}$, η_{D^*} and x_{D^*}.

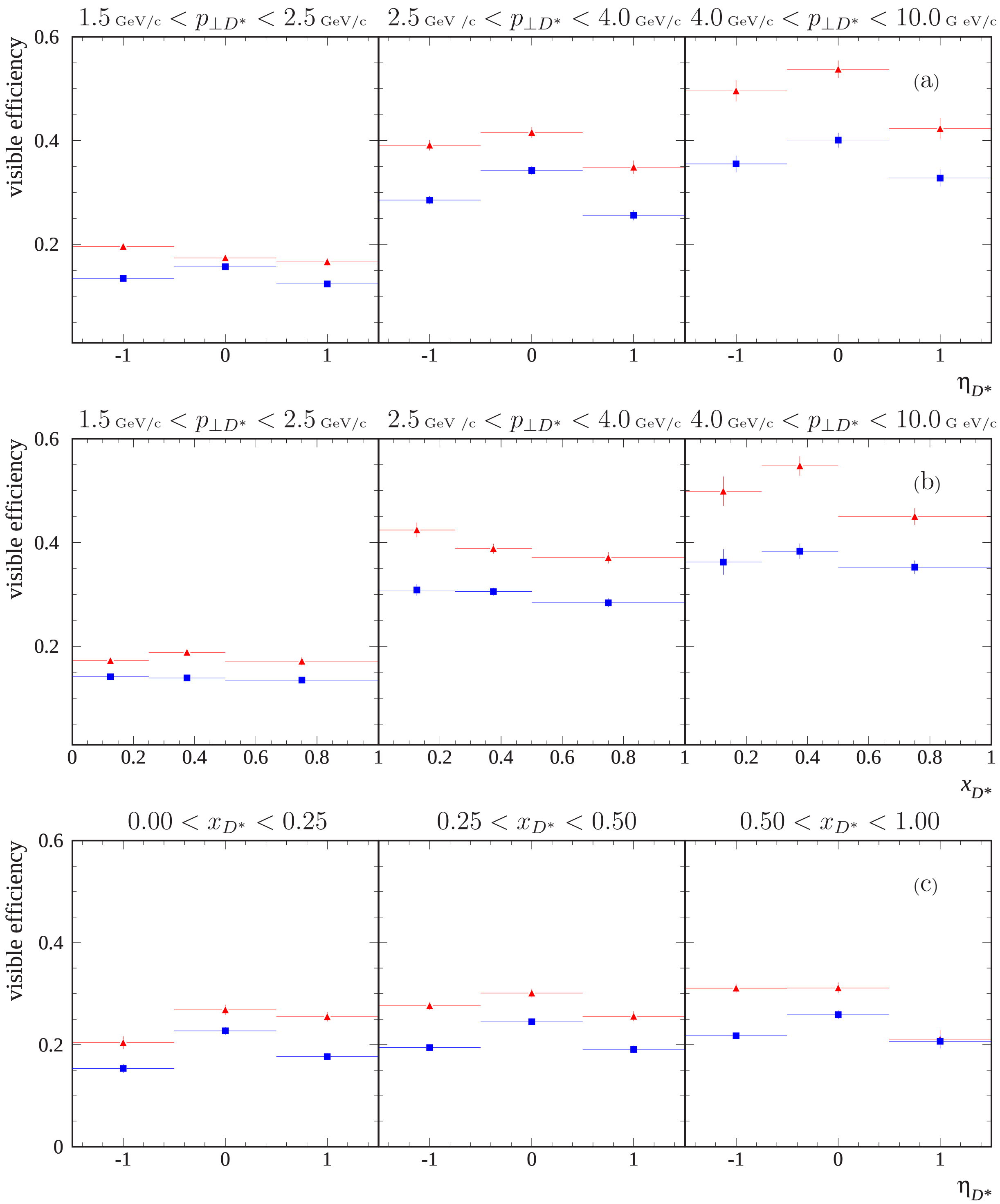

Figure D.21: Efficiencies of the D^{*+} selection cuts within the visible rangle predicted by the AROMA Monte Carlo generator and after detector simulation for the years 1996 (triangles) and 1997 (squares) in bins of ($p_{\perp D^*}$; η_{D^*}), ($p_{\perp D^*}$; x_{D^*}), (x_{D^*}; η_{D^*}) and (η_{D^*}; Q^2).

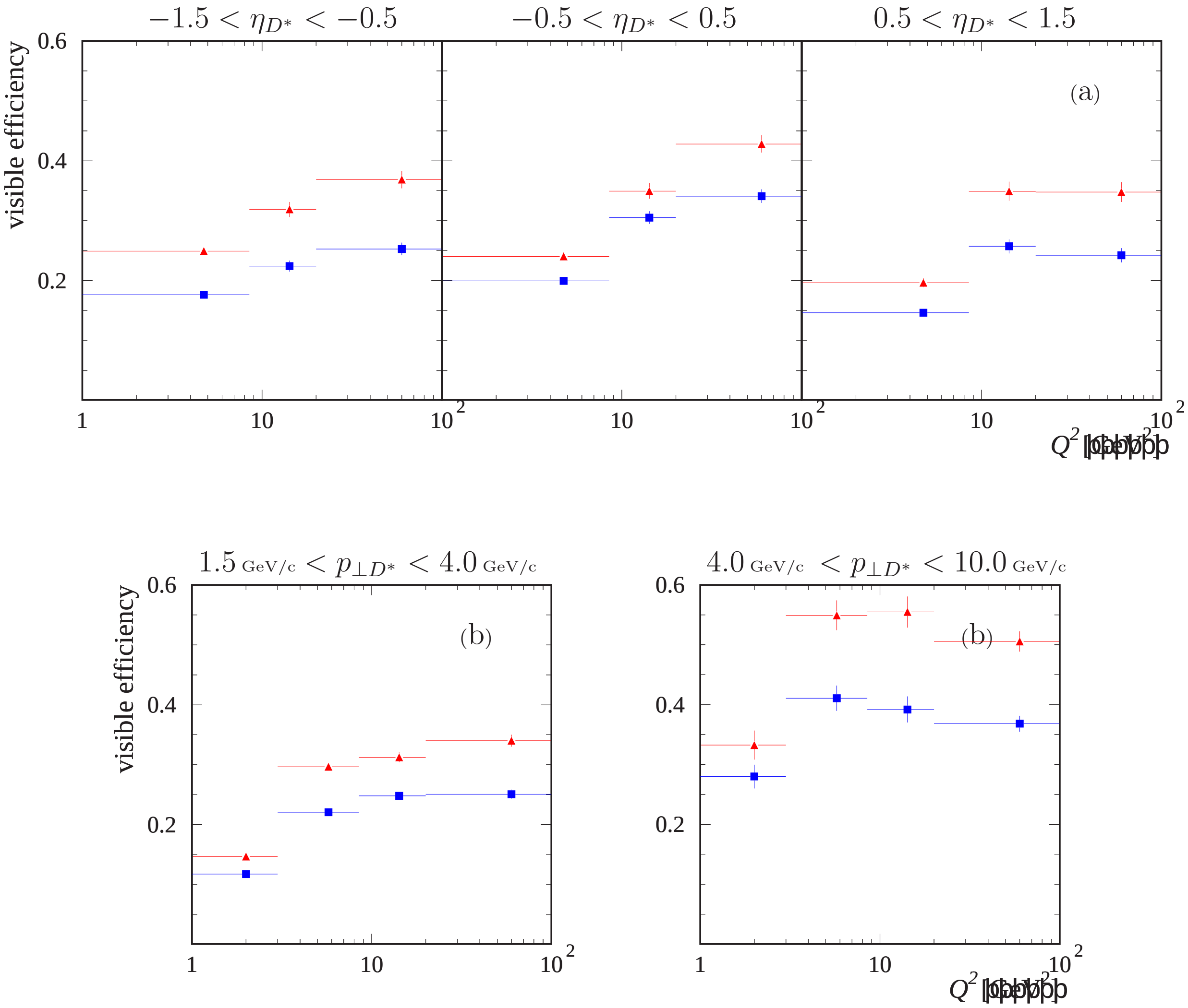

Figure D.22: Efficiencies of the D^{*+} selection cuts within the visible rangle predicted by the AROMA Monte Carlo generator and after detector simulation for the years 1996 (triangles) and 1997 (squares) in bins of (η_{D^*}; Q^2) and ($p_{\perp D^*}$; Q^2).

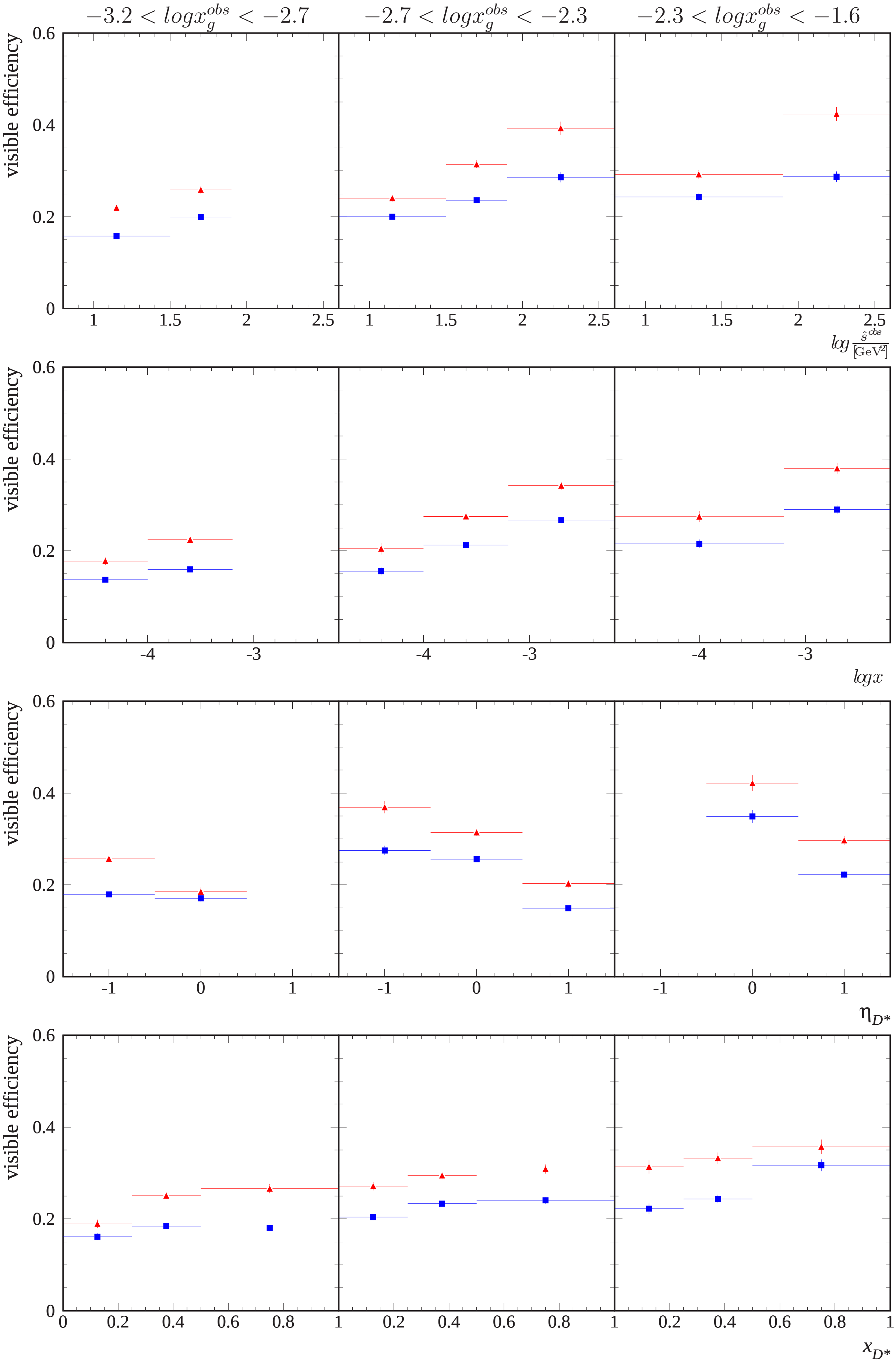

Figure D.23: Efficiencies of the D^{*+} selection cuts within the visible rangle predicted by the AROMA Monte Carlo generator and after detector simulation for the years 1996 (triangles) and 1997 (squares) in bins of $(x_g^{obs}; \hat{s}^{obs})$, $(x_g^{obs}; x)$, $(x_g^{obs}; \eta_{D^*})$ and $(x_g^{obs}; x_{D^*})$.

Appendix E

Normalised D^{*+} Cross Sections

In order to confront the shapes of the D^{*+} differential cross sections measured in the data and those predicted by models, the normalised cross sections are more appropriate. To achieve this, the data differential cross sections are normalised to the D^{*+} total cross section measured in the kinematic and D^{*+} visible range. The predicted differential cross sections for each model are also normalised to their respective predicted total D^{*+} cross sections. The D^{*+} total cross sections which are used for the normalisation can be found in section 5.3.1.

The inclusive normalised D^{*+} single differential cross sections in the visible range versus W, x, Q^2 and $p_{\perp D^*}$, η_{D^*}, x_{D^*} are shown in figure E.1 (together with the HVQDIS and CASCADE predictions) and in figure E.5 (together with the AROMA predictions). The normalised double differential cross sections

$$d^2\sigma^N_{vis}(ep \to eD^{*+}X)/(dp_{\perp D^*}d\eta_{D^*})$$
$$d^2\sigma^N_{vis}(ep \to eD^{*+}X)/(dp_{\perp D^*}dx_{D^*})$$

are shown in figure E.2 (together with the HVQDIS and CASCADE predictions) and in figure E.6 (together with the AROMA predictions). The normalised double differential cross sections

$$d^2\sigma^N_{vis}(ep \to eD^{*+}X)/(dx_{D^*}d\eta_{D^*})$$
$$d^2\sigma^N_{vis}(ep \to eD^{*+}X)/(d\eta_{D^*}dQ^2)$$
$$d^2\sigma^N_{vis}(ep \to eD^{*+}X)/(dp_{\perp D^*}dQ^2)$$

are shown in figure E.3 (together with the HVQDIS and CASCADE predictions) and in figure E.7 (together with the AROMA predictions).

The double differential cross sections in terms of x_g^{obs} presented in chapter 6 are shown in figure E.4 (together with the HVQDIS and CASCADE predictions) and in figure E.8 (together with the AROMA predictions) after normalisation:

$$d^2\sigma^N_{vis}(ep \to eD^{*+}X)/(dlogx_g^{obs}dlog\hat{s}^{obs}/[\mathrm{GeV}^2])$$
$$d^2\sigma^N_{vis}(ep \to eD^{*+}X)/(dlogx_g^{obs}dlogx)$$
$$d^2\sigma^N_{vis}(ep \to eD^{*+}X)/(dlogx_g^{obs}d\eta_{D^*})$$
$$d^2\sigma^N_{vis}(ep \to eD^{*+}X)/(dlogx_g^{obs}dx_{D^*}).$$

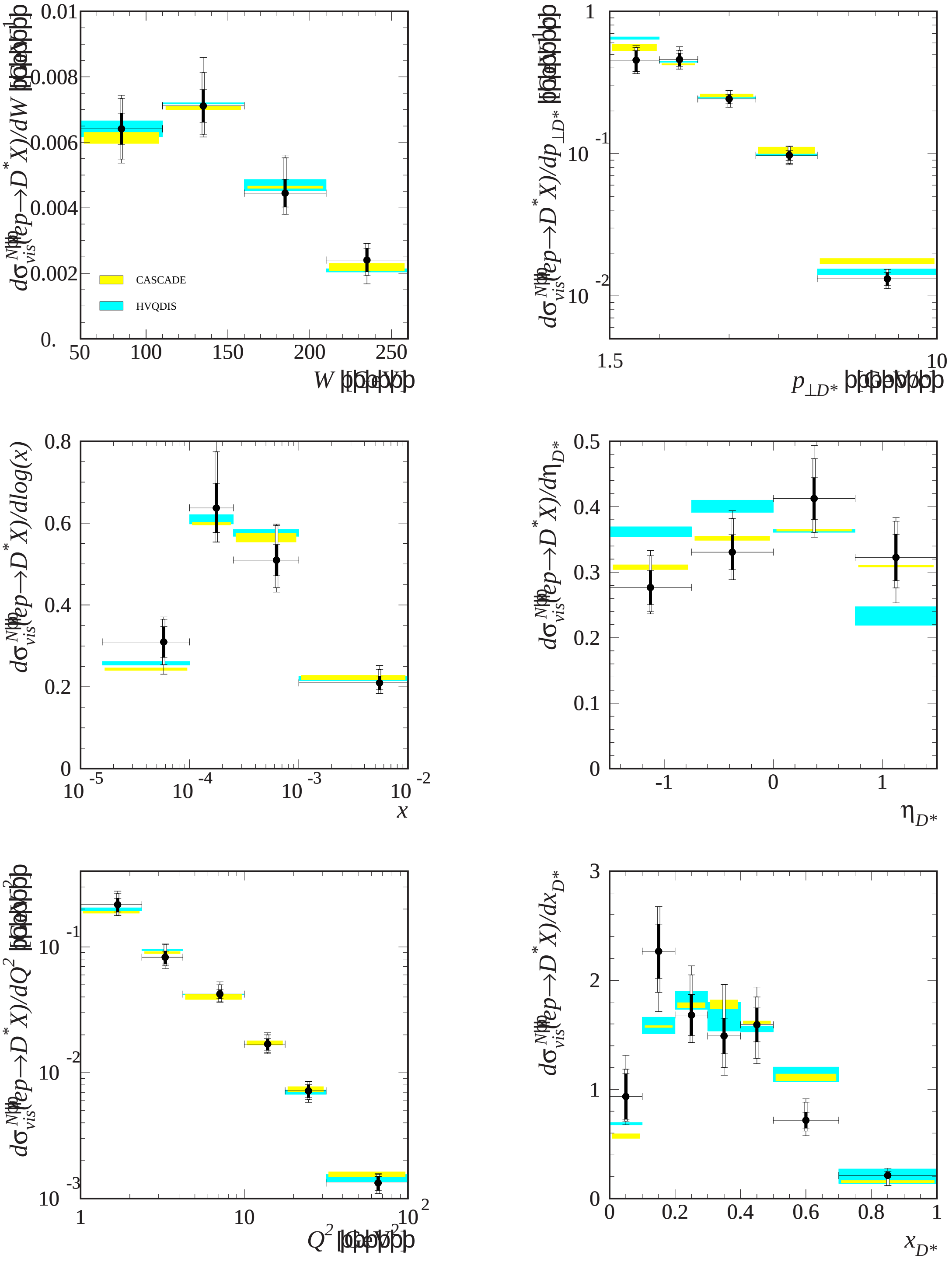

Figure E.1: Inclusive D^{*+} normalised single differential cross sections in the visible range versus W, x , Q^2 and $p_{\perp D^*}$, η_{D^*}, x_{D^*}. The innermost error bars correspond to the statistical error. The experimental systematical errors are added in quadrature for the middle error bars and the total error bars additionally take the Monte Carlo systematics into account. The dark shaded band is the prediction of the HVQDIS NLO DGLAP calculations for $m_c = 1.3$ GeV/c^2, ϵ(Peterson) $= 0.035$ (upper limit) and $m_c = 1.5$ GeV/c^2, ϵ(Peterson) $= 0.10$ (lower limit). The light shaded band is the prediction of the CASCADE LO CCFM calculations for $m_c = 1.3$ GeV/c^2 (upper limit) and $m_c = 1.5$ GeV/c^2 (lower limit); ϵ(Peterson) has been fixed to 0.078.

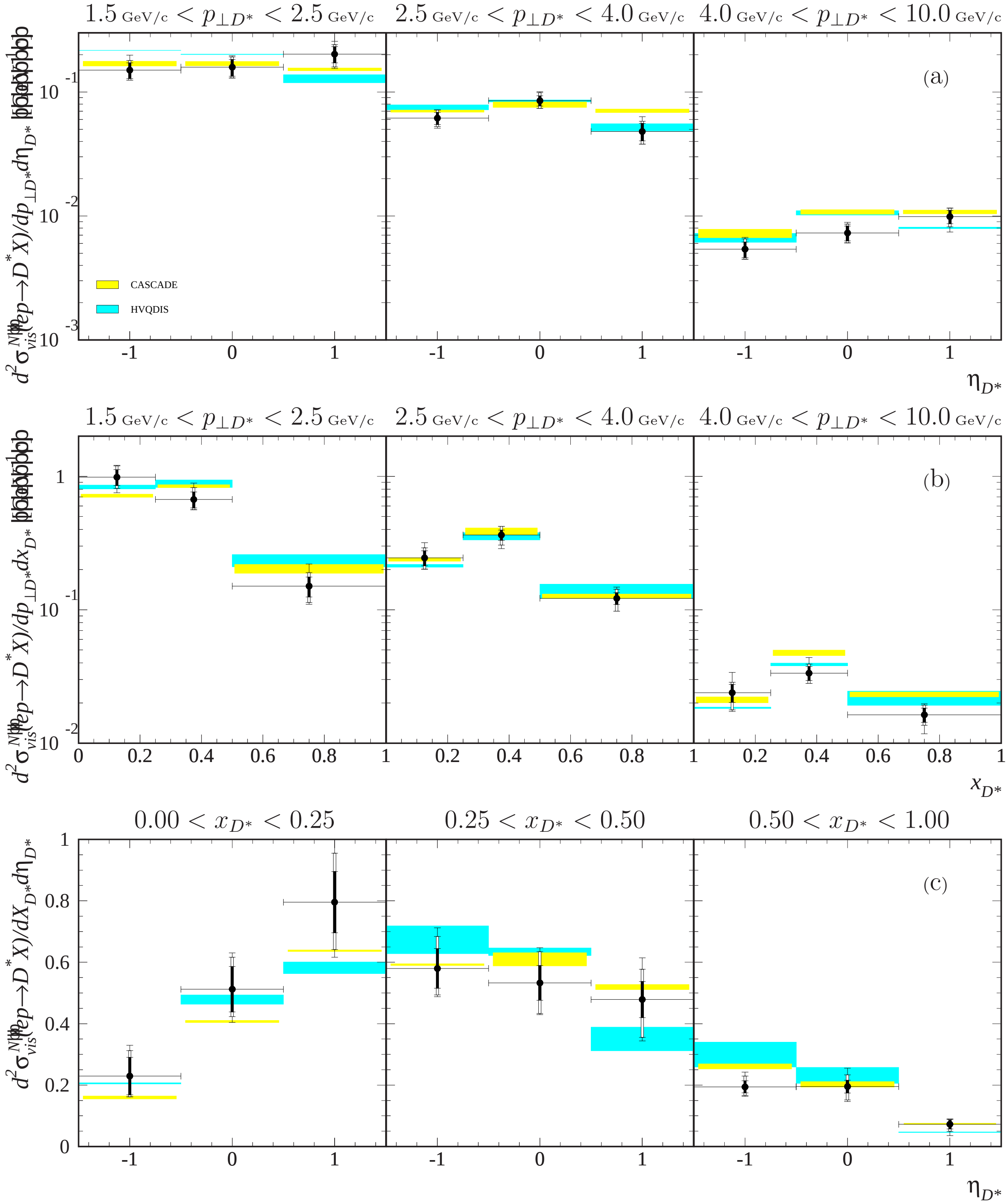

Figure E.2: Inclusive D^{*+} normalised double differential cross sections in the visible range for D^{*+} quantities $d^2\sigma_{vis}^N(ep \to eD^{*+}X)/(dp_{\perp D^*}d\eta_{D^*})$, $d^2\sigma_{vis}^N(ep \to eD^{*+}X)/(dp_{\perp D^*}dx_{D^*})$, $d^2\sigma_{vis}^N(ep \to eD^{*+}X)/(dx_{D^*}d\eta_{D^*})$. The dark and light shaded bands are described in the caption of figure E.1.

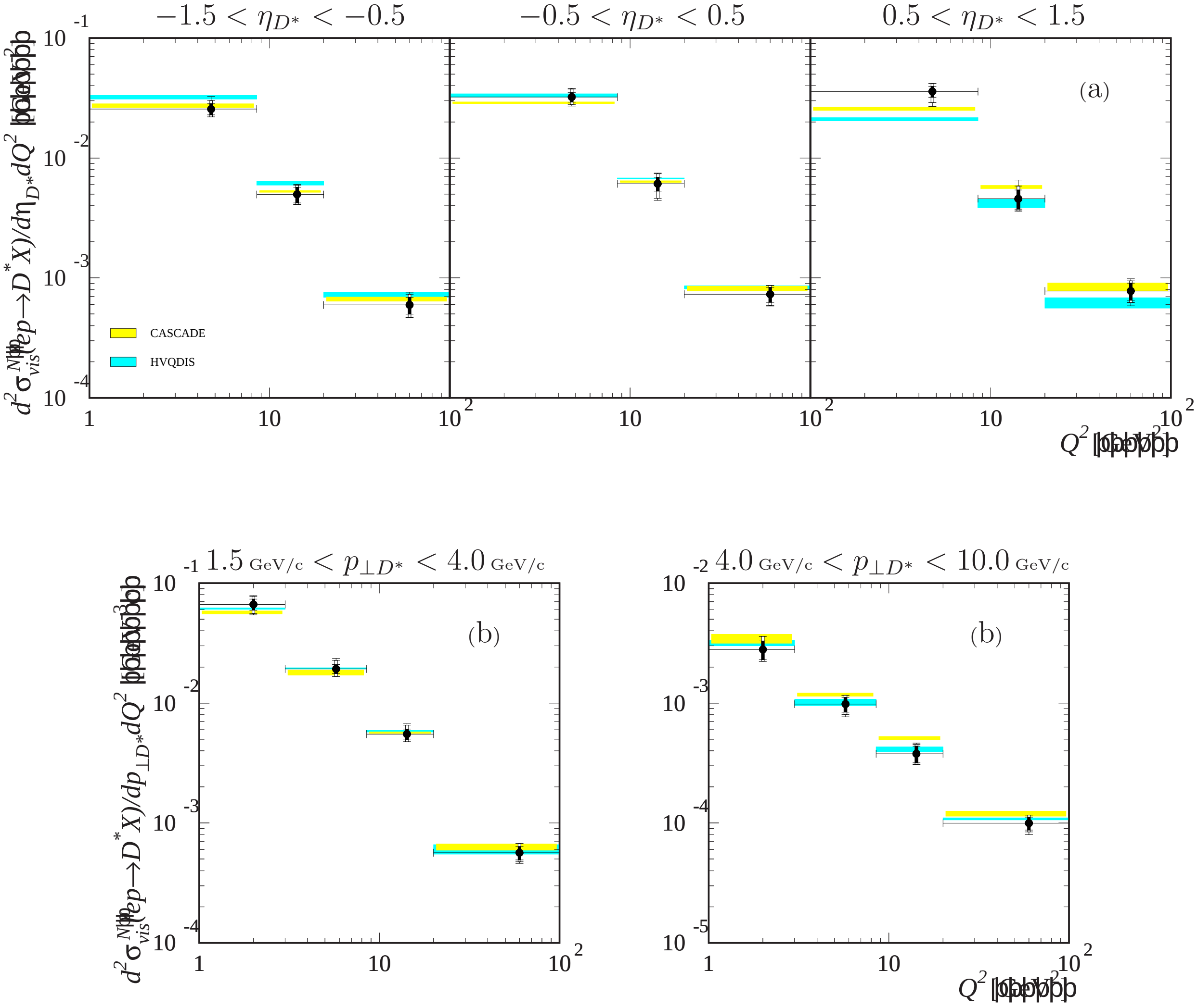

Figure E.3: Inclusive D^{*+} normalised double differential cross sections in the visible range $d^2\sigma^N_{vis}(ep \to eD^{*+}X)/(d\eta_{D^*}dQ^2)$ and $d^2\sigma^N_{vis}(ep \to eD^{*+}X)/(dp_{\perp D^*}dQ^2)$. The dark and light shaded bands are described in the caption of figure E.1.

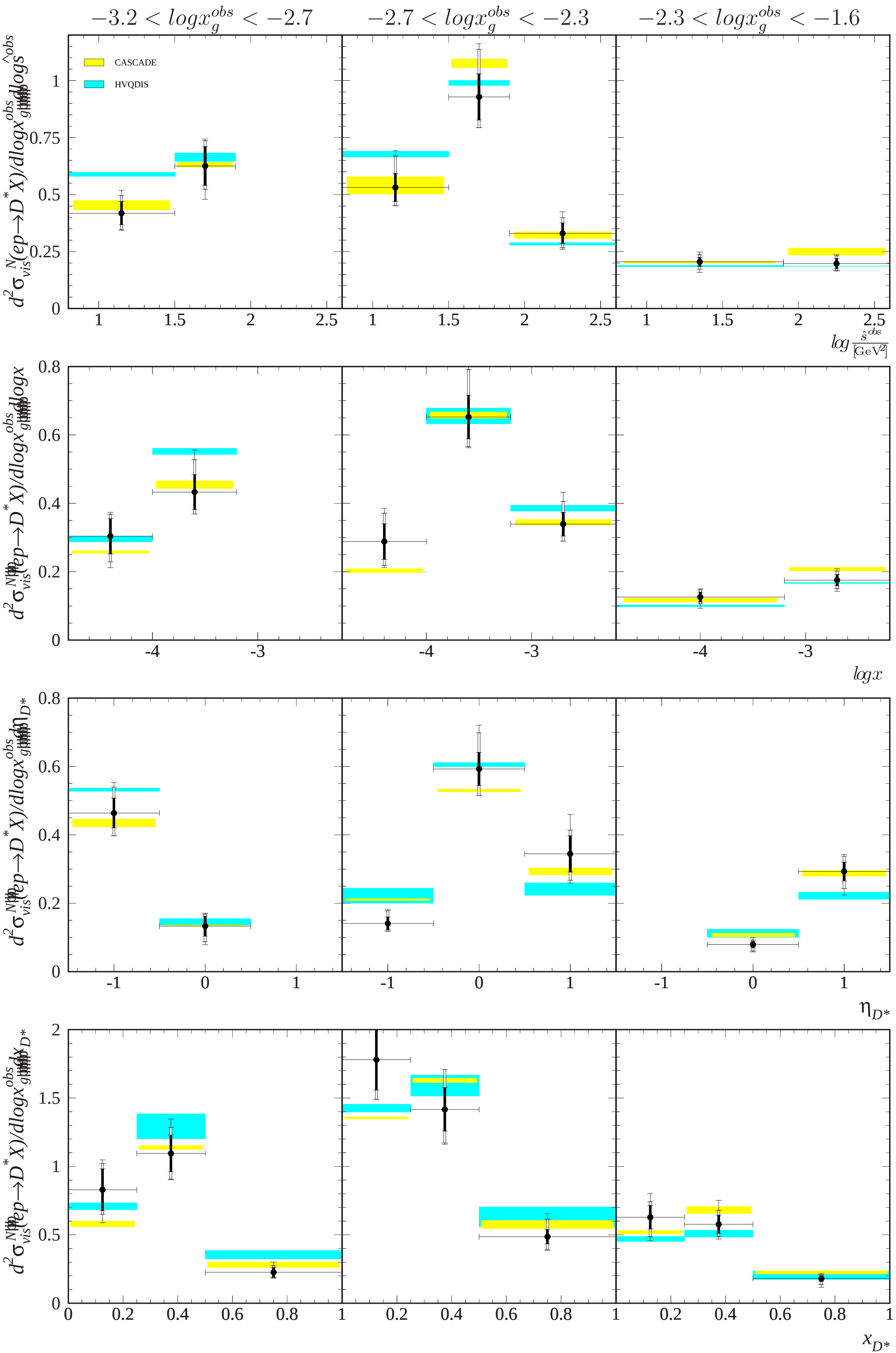

Figure E.4: Inclusive D^{*+} normalised double differential cross sections in the visible range: $d^2\sigma_{vis}^N(ep \to eD^{*+}X)/(dlogx_g^{obs}dlog\hat{s}^{obs}/[\text{GeV}^2])$, $d^2\sigma_{vis}^N(ep \to eD^{*+}X)/(dlogx_g^{obs}dlogx)$, $d^2\sigma_{vis}^N(ep \to eD^{*+}X)/(dlogx_g^{obs}d\eta_{D^*})$, $d^2\sigma_{vis}^N(ep \to eD^{*+}X)/(dlogx_g^{obs}dx_{D^*})$. The dark and light shaded bands are described in the caption of figure E.1

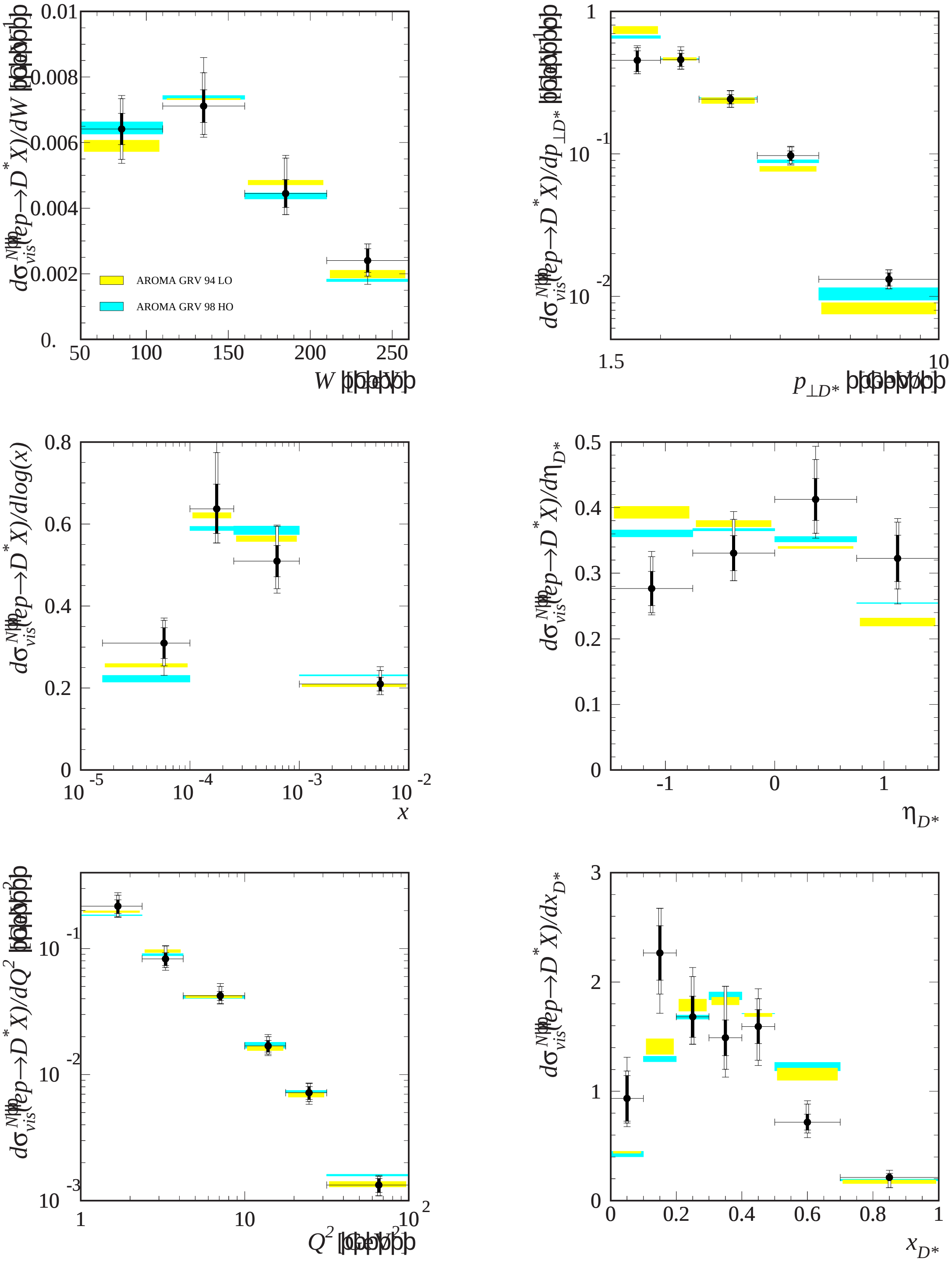

Figure E.5: Inclusive D^{*+} normalised single differential cross sections in the visible range versus W, x , Q^2 and $p_{\perp D^*}$, η_{D^*}, x_{D^*}. The innermost error bars correspond to the statistical error. The experimental systematical errors are added in quadrature for the middle error bars and the total error bars additionally take the Monte Carlo systematics into account. The dark shaded band is the prediction of the LO DGLAP AROMA event generator for $m_c = 1.3$ GeV/c^2 (upper limit) and $m_c = 1.5$ GeV/c^2 (lower limit) with GRV 98 HO for the parton density set. The light shaded band is the prediction of the LO DGLAP AROMA event generator for $m_c = 1.3$ GeV/c^2 (upper limit) and $m_c = 1.5$ GeV/c^2 (lower limit) with GRV 94 LO for the parton density set. In both cases ϵ(Peterson) has been fixed to 0.078.

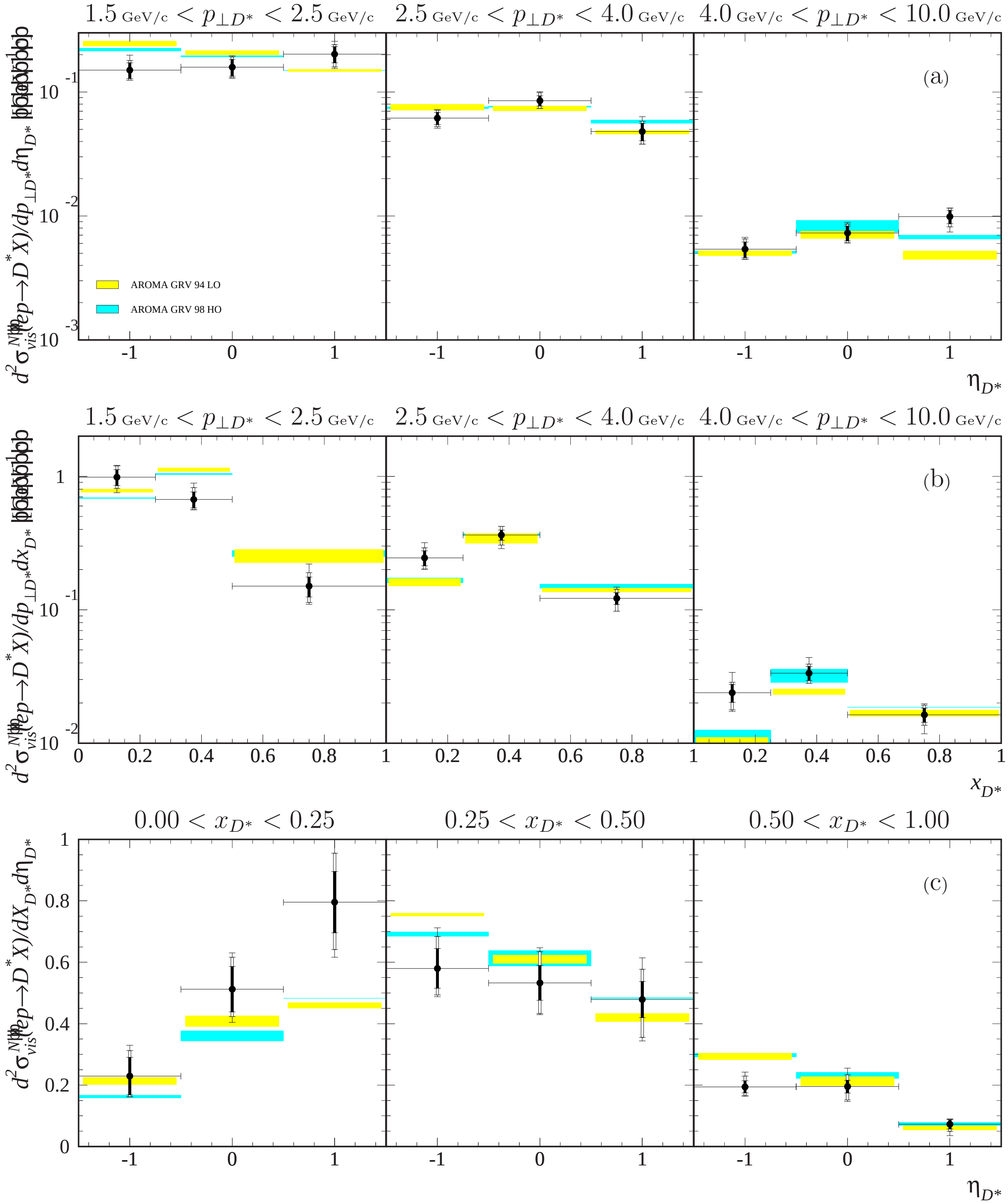

Figure E.6: Inclusive D^{*+} normalised double differential cross sections in the visible range for D^{*+} quantities $d^2\sigma^N_{vis}(ep \to eD^{*+}X)/(dp_{\perp D^*}d\eta_{D^*})$, $d^2\sigma^N_{vis}(ep \to eD^{*+}X)/(dp_{\perp D^*}dx_{D^*})$, $d^2\sigma^N_{vis}(ep \to eD^{*+}X)/(dx_{D^*}d\eta_{D^*})$. The dark and light shaded bands are described in the caption of figure E.5.

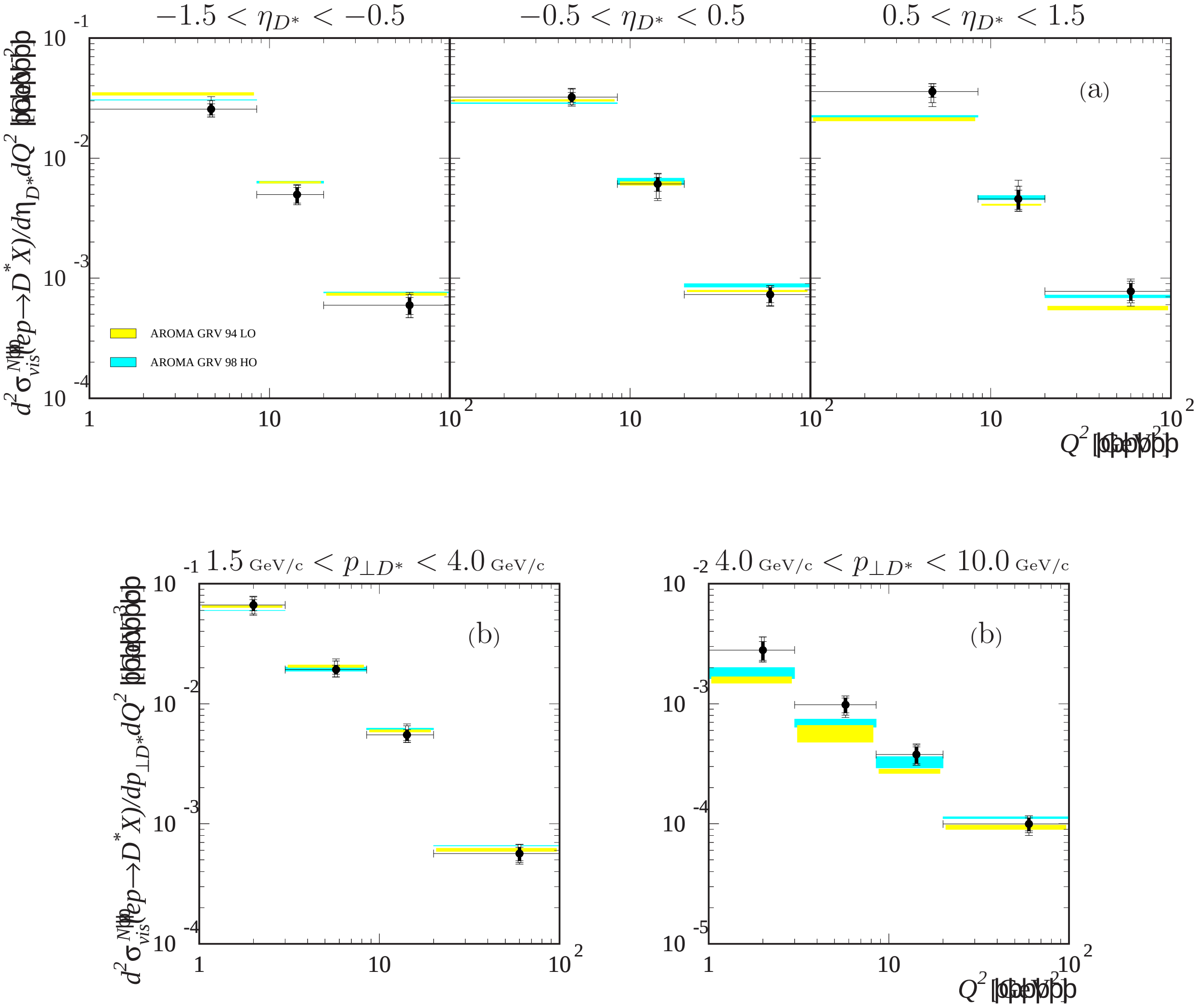

Figure E.7: Inclusive D^{*+} normalised double differential cross sections in the visible range $d^2\sigma^N_{vis}(ep \to eD^{*+}X)/(d\eta_{D^*}dQ^2)$ and $d^2\sigma^N_{vis}(ep \to eD^{*+}X)/(dp_{\perp D^*}dQ^2)$. The dark and light shaded bands are described in the caption of figure E.5.

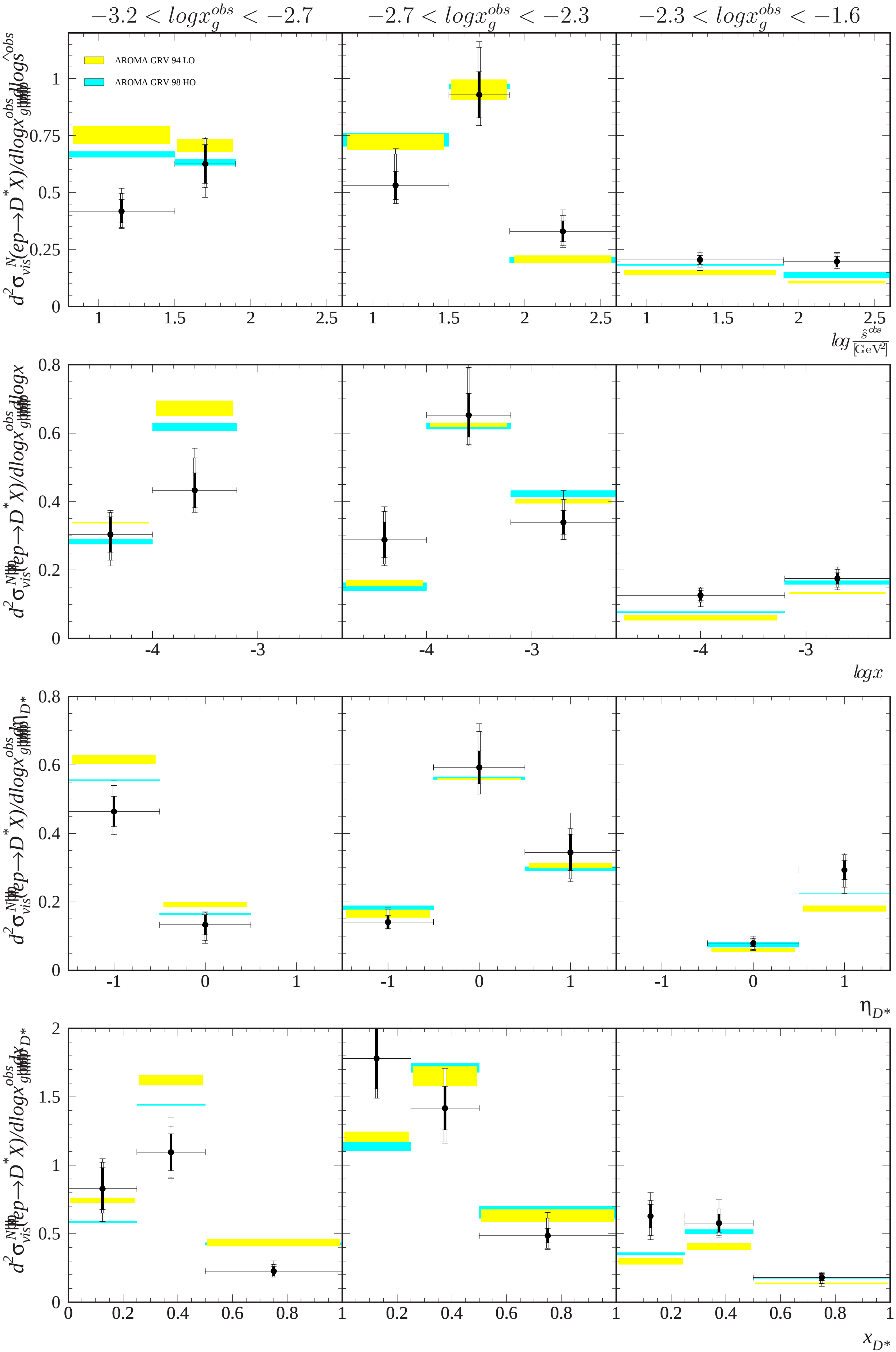

Figure E.8: Inclusive D^{*+} normalised double differential cross sections in the visible range: $d^2\sigma_{vis}^N(ep \to eD^{*+}X)/(dlogx_g^{obs}dlog\hat{s}^{obs}/[\mathrm{GeV}^2])$, $d^2\sigma_{vis}^N(ep \to eD^{*+}X)/(dlogx_g^{obs}dlogx)$, $d^2\sigma_{vis}^N(ep \to eD^{*+}X)/(dlogx_g^{obs}d\eta_{D^*})$, $d^2\sigma_{vis}^N(ep \to eD^{*+}X)/(dlogx_g^{obs}dx_{D^*})$. The dark and light shaded bands are described in the caption of figure E.5

Abbreviations

ALEPH ..: **A**pparatus for **LEP P**hysics
ARGUS .: **ARGUS**, magnetic detector installed at the storage ring DORIS II at DESY
AROMA .: **AROMA**, a Monte Carlo Generator for Heavy Flavour Events in *ep* collisions
BDC ....: **B**ackward **D**rift **C**hamber
BEMC ...: **B**ackward **E**lectro**M**agnetic **C**alorimeter
BGF .....: **B**oson-**G**luon **F**usion
BST .....: **B**ackward **S**ilicon **T**racker
CC ......: **C**harged **C**urrent
CERN ...: **C**onseil **E**uropéen pour la **R**echerche **N**ucléaire
CIP .....: **C**entral **I**nner **P**roportional Chamber
CIZ ......: **C**entral **I**nner z-Chamber
CJC .....: **C**entral **J**et **C**hamber
COP .....: **C**entral **O**uter **P**roportional Chamber
COZ .....: **C**entral **O**uter z-Chamber
CST .....: **C**entral **S**ilicon **T**racker
CTD ....: **C**entral **T**racking **D**evice
CTL .....: **C**entral **T**rigger **L**ogic
DELPHI .: **DE**tector for **L**epton, **P**hoton and **H**adron **I**dentification
DESY ...: **D**eutsches **E**lektronen-**Sy**nchrotron
DORIS ..: **DO**ppel-**RI**ng-**S**peicher, the alleged mother country of the Dorian conquerors of the Peloponnese
DIS ......: **D**eep **I**nelastic **S**cattering
EMC ....: **E**uropean **M**uon **C**ollaboration
ET ......: **E**lectron **T**racker
FTD .....: **F**orward **T**racking **D**evice
FWPC ..: **F**orward Multi-**W**ire **P**roportional **C**hamber
HECTOR : **HECTOR**, a programme for the calculation of QED, QCD and electroweak corrections to *ep*, and $l^{\pm}N$ deep inelastic neutral and charged current scattering, in greek legend HECTOR was the eldest son of the Troyan king Priam.
HERA ...: **H**adron-**E**lektron-**R**ing-**A**nlage, in greek religion queen of the Olympian gods
HERWIG : **H**adron **E**mission **R**eactions **W**ith **I**nterfering **G**luons
HQSEL ..: **H**eavy **Q**uark **Sel**ection

IET .....: **I**nclusive **E**lectron-**T**rigger
ITEP ...: **I**nstitute of **T**heoretical and **E**xperimental **P**hysics
JETSET : **JETSET**, a programme for event generation in high energy physics assuming “jet universality”.
LEP ....: **L**arge **E**lectron **P**ositron **C**ollider
LO .....: **L**eading **O**rder
LST ....: **L**imited **S**treamer **T**ube
MC .....: **M**onte **C**arlo
MWPC .: **M**ulti **W**ire **P**roportional **C**hamber
NC .....: **N**eutral **C**urrent
NLO ....: **N**ext to **L**eading **O**rder
NMC ...: **N**ew to **M**uon **C**ollaboration
PD .....: **P**hoton **D**etector
PETRA .: **P**ositron-**E**lektron-**T**andem-**R**ing-**A**nlage, an ancient city which was the centre of an Arab kingdom in Hellenistic and Roman times. Nowadays its ruins are in southwest Jordan.
PHYTIA : **PYTHIA**, a programme to generate hadronic physics at very high energy, an ancient Greek medium who delivered oracles at Delphi.
PS ......: **P**roton **S**ynchrotron
QCD ...: **Q**uantum **C**hromo **D**ynamic
QED ....: **Q**uantum **E**lectro **D**ynamic
QPM ...: **Q**uark **P**arton **M**odel
RISC ...: **R**educed **I**nstruction **S**et **C**omputer
SpaCal .: **Spa**ghetti **Cal**orimeter
SPS .....: **S**uper **P**roton **S**ynchrotron
ST ......: **S**ub**T**rigger
TC .....: **T**ail **C**atcher
ToF .....: **T**ime **o**f **F**light
TR .....: **T**ransition **R**adiator

Bibliography

[1] A. Ali *et al.,* in *Proc. of the HERA Workshop*, Hamburg, **Vol. 1**(1988)393
A. Ali and D. Wyler, in *Proc. of the Workshop "Physics at HERA"*, Hamburg, **Vol. 2**(1991)669
M.A.G. Aivazis *et al.*, *Phys. Rev.* **D50**(1994)3085, *Phys. Rev.* **D50**(1994)3102.

[2] S. Riemersma *et al.*, *Phys. Lett.* **B347**(1995)143.

[3] H1 Collab., C. Adloff *et al.*, *Z. Phys.* **C72**(1996)593.

[4] ZEUS Collab., J. Breitweg *et al.*, *Phys. Lett.* **B407**(1997)402.

[5] EMC Collab., J.J. Aubert *et al.*, *Nucl. Phys.* **B213**(1983)31.

[6] F. Sefkow, *Measurement of the Beauty Production Cross Section at HERA Using Lifetime Information*, submitted to the 30th International Conference of High Energy Physics ICHEP2000, Osaka, July 2000;
H1 Collab., C. Adloff *et al.*, *Phys. Lett.* **B467**(1999)156.

[7] T. Sloan, *Beauty Production in Deep Inelastic Scattering*, talk presented at the XXXVI th Rencontres de Moriond session devoted to QCD AND HIGH ENERGY HADRONIC INTERACTIONS, March 2001, H1prelim-01-072.

[8] S. Frixione, M. L. Mangano, P. Ridolfi, *Phys. Lett.* **B348**(1995)633.

[9] H1 Collab., I. Abt *et al.*, *Nucl. Instr. Meth.* **A386**(1997)310.

[10] H1 SpaCal Group, R.-D Appuhn *et al.*, *Nucl. Instr. Meth.* **A386**(1997)397.

[11] H1 SPACAL Group, T. Nicholls *et al.*, *Nucl. Instr. Meth.* **A374**(1996)149.

[12] A. Meyer, Measurement of the Structure Function $F_2(x, q^2)$ of the Proton at low Q^2 with the H1-Detector at HERA using the new Detector Components SpaCal and BDC, Ph.D. Thesis, Hamburg 1997.

[13] R. Maraček, A study of Quasi-Real QED Compton Events at HERA, Ph.D. Thesis, Košice 1998.

[14] H1 SpaCal Group, R.-D Appuhn *et al.*, DESY Red Report 96-013.

[15] B. Schwab, Das Rückwärtsdriftkammersystem des H1-Experiments, Ph.D. Thesis, Heidelberg 1996.

[16] L. Favart, H1 note H1-06/94-366.

[17] H1 Collab., S. Aid *et al.*, submitted to the 28th International Conference of High Energy Physics, ICHEP'96, Warsaw, Poland, pa17-026.

[18] S. Egli *et al.*, H1 note H1-04/97-517.

[19] J.D. Bjorken, *Phys. Rev. Lett.***16**(1966)408;
J.D. Bjorken, *Phys. Rev.* **179**(1969)1547.

[20] E. D. Bloom *et al.*, *Phys. Rev. Lett.***23**(1969)930;
M. Breidenbach *et al.*, *Phys. Rev. Lett.* **23**(1969)935.

[21] F.Halzen and AD. Martin, *Quarks and Lepton*, John Wiley and Sons (1984)163.

[22] L. W. Mo, Proceeding of the 4th International Symposium on Lepton Proton Interaction at High Energies, Stanford 1975, published in Lepton-Photon Symp. (1975) 651.

[23] R.E. Taylor, Proceeding of the 4th International Symposium on Lepton Proton Interaction at High Energies, Stanford 1975, published in Lepton-Photon Symp. (1975) 679.

[24] V.N. Gribov and L.N. Lipatov, *Sov. J. Nucl. Phys.* **15**(1972)438 and 675;
G. Altarelli and G. Parisi, *Nucl. Phys.* **B126**(1977)298.

[25] R.G Roberts, *The Structure of the Proton*, Cambridge University Press (1990).

[26] J. Breitweg *et al.*, *Eur. Phys. J.* **C7**(1999)609

[27] C. Adloff *et al.*, DESY Red Report 00-181, accepted by *Eur. Phys. J.*

[28] Yu.L. Dokshitzer, *Sov. Phys.* JETP **46**(1977)641

[29] E.A. Kuraev, L.N. Lipatov and V.S. Fadin, *Sov. Phys.* JETP **45**(1977)199;
Y.Y. Balitski and L.N. Lipatov, *Sov. J. Nucl. Phys.* **28**(1978)822.

[30] I. Bojak and M. Ernst, *Phys. Rev.* **D53**(1996)80.

[31] J. R. Forshaw and P.J. Sutton, *Eur. Phys. J.* **C1**(1998)285.

[32] V. S. Fadin and L.N. Lipatov, *Phys. Lett.* **B429**(1998)127;
M. Ciafaloni, and G. Camini, *Phys. Lett.* **B430**(1998)349.

[33] M. Ciafaloni, *Nucl. Phys.* **B296**(1988)49;
S. Catani, F. Fiorani and G. Marchesini, *Phys. Lett.* **B234**(1990)339;
S. Catani, F. Fiorani and G. Marchesini, *Nucl. Phys.* **B336**(1990)18;
G. Marchesini, *Nucl. Phys.* **B445**(1995)49.

[34] M.A.G. Aivazis *et al.*, *Nucl. Phys.* **B50**(1994)3102;
J.C. Collins, *Phys. Rev.* **D58**(1998)094002;
A.D. Martin *et al.*, *Eur. Phys. J.* **C4**(1998)463.

[35] H. Jung, HERA Monte Carlo Workshop, Hamburg, Germany, 1998-1999, hep-ph/9908497 ;
H. Jung et G.P. Salam, DESY Red Report 00-0151.

[36] S. Kretzer *et al.*, *Phys. Rev.* **D59**(1998)463.

[37] S. J. Brodsky, P. Hoyer, C. Peterson, N. Sakai, *Phys. Lett.* **B93**(1980)445;
S. J. Brodsky, C. Peterson, *Phys. Rev.* **D23**(1981)2745.

[38] T. Sjöstrand, *Comp. Phys. Comm.* **82**(1994)74.

[39] C. Peterson, D. Schlatter, I. Schmitt and P. Zerwas, *Phys. Rev.* **D27**(1983)105.

[40] D.E. Groom *et al.,* (Particle Data Group), *Eur. Phys. J.* **C15**(2000)1-878.

[41] P. Abreu *et al.*, *Z. Phys.* **C73**(1996)11.

[42] R. Barate *et al.*, *Eur. Phys. J.* **C16**(2000)597.

[43] G.Marchesini *et al.*, *Comp. Phys. Comm.* **67**(1992)465.

[44] K. Daum *et al.*, DESY Red Report 96-205.

[45] G.Ingelman, J. Rathmann, G.A Schuler *Comp. Phys. Comm.* **101**(1997)135.

[46] H. Jung, *Comp. Phys. Comm.* **86**(1995)147.

[47] L. Lönnblad, *Comp. Phys. Comm.* **71**(1992)15.

[48] B.R. Webber, *Nucl. Phys.* **B238**(1984)492.

[49] B. Anderson *et al.*, *Phys. Rep.* **97**(1983)31.

[50] A. Kwiatkowski, H. Spiesberger and H-J. Möring, *Comp. Phys. Comm.* **69**(1992)155.

[51] G. Marchesini and B. Webber, *Nucl. Phys.* **B349**(1991)617;
G. Marchesini and B. Webber, *Nucl. Phys.* **B386**(1992)215.

[52] S. Aid *et al.*, *Nucl. Phys.* **B470**(1996)3.

[53] C. Adloff *et al.*, *Nucl. Phys.* **B538**(1999)3.

[54] J. Breitweg *et al.*, *Eur. Phys. J.* **C6**(1999)239.

[55] J. Breitweg *et al.*, *Phys. Lett.* **B474**(1999)223.

[56] B. W. Harris and J. Smith, *Phys. Rev.* **D57**(1998)2806.

[57] ALEPH Collab., R. Barate *et al.*, HEP-EX/9909032, submitted to *Eur. Phys. J.*

[58] C. Caso *et al.,* (Particle Data Group), *Eur. Phys. J.* **C3**(1998)1-794.

[59] S. Bentvelsen, J. Engelen and P. Kooijman, in *Proc. of the Workshop "Physics at HERA"*, Hamburg, **Vol. 1**(1991)23;
K. C. Hoeger, in *Proc. of the Workshop "Physics at HERA"*, Hamburg, **Vol. 1**(1991)43.

[60] A. Meyer, H1 note H1-12/97-532.

[61] A. Alimovich Glazov, H1 note H1-12/97-532.

[62] Judith Katzy, Messung der Strukturfunktion F2 bei kleinen Bjorken-x und kleinen Impulsüberträgen am H1 Experiment bei HERA, Ph.D. Thesis, Heidelberg 1997.

[63] A. Arbuzov *et al.*, *Comp. Phys. Comm.* **94**(1996)128.

[64] A. Kuepper, Messung des Charm Beitrags zur Protonstrukturfunktion F_2 in der tiefinelastischen Streuung bei H1 über den Zerfall $D^{*+} \to (K^- \pi^+)\pi_s^+$, Ph.D. Thesis, to be published.

[65] Jörn Steinhart, Die Messung des totalen $c\bar{c}$-Photoproduktion-Wirkungsquerschnittes durch die Rekonstruction von Λ_c-Barionen unter Verwendung der verbesserten dE/dx-Teilchenindentifikation am H1 Experiment bei HERA , Ph.D. Thesis, Hamburg 1999.

[66] W.Erdmann, Untersuchung der Photoproduktion von D^*-Mesonen am ep-Speichering HERA, Ph.D. Thesis, ETH Zürich 1996.

[67] F. Lehner, Bestimmung und QCD-Analyse der Protonstrukturfunktion $F_2(x, q^2)$ bei kleinen Bjorken-x und Q^2 mit Hilfe des verbesserten Rückwärtsbereichs des H1-Detektors. , Ph.D. Thesis, Hamburg 1998.

[68] N. Gogitidze, S Levonian, H1 note H1-02/96-471.

[69] H1 Collab., C. Adloff *et al.*, *Nucl. Phys.* **B545**(1999)21.

[70] H1 Collab., I. Abt *et al.*, *Nucl. Phys.* **B449**(1995)3.

[71] H1 Collab., C.Adloff *et al.*, DESY Red Report 00-145, submitted to *Eur. Phys. J.*

[72] C.Adloff *et al.*, *Eur. Phys. J.* **C13**(2000)609.

[73] V.Blobel, OPAL Technical Note TN361, March 1996.

Acknowledgements

First of all I wish to express my gratitude and thanks to Prof. Hinrich Meyer who offered me the possibility to work in the H1 collaboration at DESY and who supported and advised me especially in the harder times. Beside this, his wide scientific and human experience made the moments with him enriching and pleasant.

I would like to thanks Dr. Karin Daum who was at the origin of my PhD position in H1. Special thanks go to her for her insistence in holding meeting in German instead of the usual English which forced me to learn German.

During my time at DESY I appreciated the time spent with the team of the Wuppertal University especially with Prof. Schmidt and Stephan Wiesand. Stephan Wiesand deserves also heartfelt thanks for his introduction to the H1 software and his continuous help in solving computer problems.

The physics analysis presented in this thesis would not have been possible without the work of a lot of people in H1. I would like to especially thanks Andreas Kuepper for his great experience in the D^{*+} analysis, for his work on the CJC reweighting procedure and for his tremendous work in running over the raw data of H1. For their understanding in the new backward calorimeter of H1 as well as in the scattered electron analysis I would like to thanks E. Tzamariudaki, R. Wallny and V. Arkadov.

At the time I was in charge of the D^{*+} in DIS data quality check I attended the regular data quality meeting. It is very important to show here my admiration for all the people, and especially Jan Olson, who work very hard on behalf of the H1 data reliability.

I would also like to thanks my friends and family for their encouragement and for their faithfulness despite the lack of time I had for them. I would like especially to thanks my parents who supported me in finishing writing this thesis. Finally, I would like to thanks wholeheartedly my friend, Thomas Schilcher, for his infinite patience and help. Now, we will be able to look ahead together in the same direction.